FORMULATION, CHARACTERIZATION, AND *IN VIVO* REMODELING MECHANISMS OF POLYURETHANE BIOCOMPOSITES FOR BONE TISSUE ENGINEERING

By

Edna Margarita Prieto-Ballengee

Dissertation

Submitted to the Faculty of the

Graduate School of Vanderbilt University

in partial fulfillment of the requirements

for the degree of

DOCTOR OF PHILOSOPHY

in

Chemical Engineering

December, 2013

Nashville, Tennessee

Approved:

Professor Scott A. Guelcher

Professor Jamey Young

Professor Matthew Lang

Professor Hak-Joon Sung

To my family, the engine of my life:

both the family that made me who I am,

and the family we have just started.

ACKNOWLEDGEMENTS

I would like to start by gratefully acknowledging the different funding sources that have supported the work presented in this dissertation. These include the Orthopaedic Extremity Trauma Research Program, the National Science Foundation, the National Institutes of Health, the Center for Military Biomaterials Research, and the Armed Forces Institute of Regenerative Medicine.

I also want to express great gratitude to my research advisor Dr. Scott A. Guelcher who allowed me to be part of an exciting research field by welcoming me in his lab. His support has provided me with opportunities to explore different professional avenues, and participate in several collaborative teams to develop not only my research, but also many other professional skills. Thank you for believing in my work and mentoring me to become a better researcher and team player. In a similar way, I want to acknowledge the help I have received from my committee members over these years: Dr. Jamey Young, Dr. Matthew Lang, and Dr. Hak-Joon Sung. Their advice after each meeting, and support in the lab also enabled me to accomplish my research objectives.

Vanderbilt has been an excellent place to conduct interdisciplinary research. I want to thank our collaborators at the Vanderbilt Center for Bone Biology, especially Dr. Julie Sterling and Dr. James Edwards, for guiding me through the biology of bone; to Alyssa Merkel for always having a helping hand with the mice and cell culture techniques; and to Javier Esparza for teaching me how to work with animals. Also thank you to the people at the Biomechanics Lab (Dr. Jeffrey Nyman, Sasidhar Uppuganti, Matthew Murry), the Vanderbilt Institute of Nanoscale Science and Engineering (VINSE, Dr. Tony Hmelo and Dr. Ben Schmidt), the National Research Resource for Imaging Mass Spectroscopy (Dr. Jeremy Norris), the Vanderbilt University Institute of Imaging Science (VUIIS, Dr. Daniel Perrien), the Flow Cytometry Shared Resource (David

Flaherty), and to the Cell Imaging Shared Resource (CISR, Carol Ann Bonner) for providing access to and training on instruments used in this work. I am also very grateful to our external collaborators who have brought views from outside academia into our research, in this way keeping us focused on the patients that need improved treatments. Thank you in particular to Dr. Joseph Wenke (USAISR) for his support and for introducing me to the interesting problem of infection.

So many other people have supported my work along the way. Thank you to the Chemical and Biomolecular Engineering staff (Mary Gilleran, Rae Uson, and Mark Holmes) for helping me to successfully navigate administrative and laboratory hurdles. I am infinitely grateful for the help and friendships I have found in my fellow lab members (past and present). Thank you to Katarzyna Zienkiewicz for being incredibly supportive, always our right hand in the lab, and a great example of dedicated hard work. Thank you also to the undergraduates (Nicholas Gould, Erica Von Stein, Brian Shen, David Harris), high school students (Anna Claire Brakefield, Jonathan Davies), and teacher (Melinda Higgins) who made contributions to this research along the way.

Leaving the most important for last, I must acknowledge the help and support I have received from my family and friends. Thank you to my parents, Edna Margarita and Gabriel Omar, and my siblings, Camila, Gabriel, and Omar, for their love, support, and for always believing and being part of my dreams and goals. Thank you also to my grandparents, aunts and uncles, cousins, and friends back in Colombia, who even far away have always managed to be next to me every step of the way. I am immensely grateful to all the friends I met while in Vanderbilt; in particular thank you to Stijn, Will, Doris, Svenja, Silvia, Carlos, Sebastian, Juan, Angela, Juanita, Christi, Elizabeth, Neil, and Taylor for becoming my Nashville family! And of course, thank you to my best friend and husband Jason Ballengee. You have been there from the first day of the PhD journey, and all this work would not have been possible without your unconditional support, constructive feedback, and loving care.

TABLE OF CONTENTS

Page

LIST OF TABLES

LIST OF FIGURES

CHAPTER I

INTRODUCTION

The treatment of bone defects remains a challenging clinical problem. Trauma, disease, primary tumor resection, and/or congenital deformation often result in large bone losses requiring bone grafting procedures.[1-4] Bone is the second most commonly transplanted tissue after blood.[5] As shown in Figure 1.1, in the US alone, the number of bone grafting procedures has continuously increased since 1990, and in 2005 it surpassed 1.6 million procedures per year.[6] As a result, tissue engineering can impact millions of patients' lives by developing bone substitute materials which promote bone-defect healing.

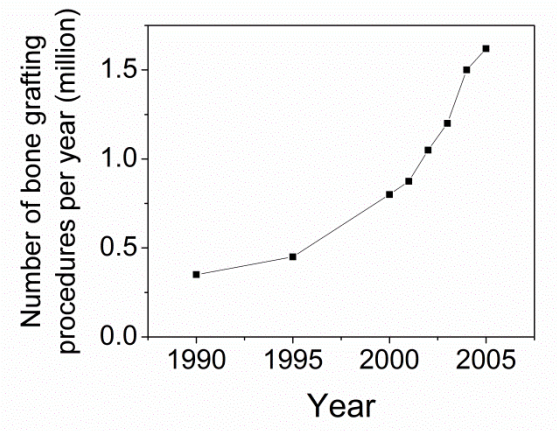

Figure 1.1. Number of bone grafting procedures in the US in the last 20 years.[6]

Established clinical approaches to treat critical-sized bone defects include the implantation of autograft or allograft bone, ceramic scaffolds, or metallic devices.[7] These materials offer a temporal solution to large bone loss, however, none of them fulfills all the requirements for successful bone scaffolds, namely being osteoconductive, biocompatible, resorbable, porous, and having mechanical properties comparable to the

surrounding host bone.[8-10] Biomaterials research continues to focus on developing alternative bone graft formulations that satisfy these characteristics with the dual objectives of reducing revision surgeries' frequency and the rate of secondary complications in the clinic.[11]

Biodegradable, lysine-derived polyurethane (PUR) networks have been developed for regenerative medicine applications.[12] When implanted *in vivo*, these materials generate a minimal and transient inflammatory response, support cellular infiltration, and degrade to non-cytotoxic compounds.[13, 14] Porous, injectable formulations have been used as delivery vehicles for biologically active small molecules such as growth factors,[15, 16] antibiotics,[17] and small molecule drugs.[18] For bone applications, porous and non-porous composites incorporating mineralized fillers into a polyurethane (PUR) network have been developed and tested in femoral plug bone defects in rats,[19, 20] rabbits,[21-23] and sheep.[24] The mineralized matrix provides osteoconductivity to the polymer by acting as a porogen that guides cellular infiltration[21], and the polymer reduces the brittle behavior of the ceramics. While pre-clinical testing positioned PUR composites as suitable biomaterials for bone regeneration, further formulation development was needed for moldable scaffolds to approach weight-bearing capabilities.

The goal of this dissertation was to formulate and characterize PUR biocomposites that participate actively and predictably in the bone healing process. Building on previous work in the Guelcher lab, high and low porosity formulations were developed to improve the healing outcomes of contaminated and femoral plug bone defects. *In vitro* characterization of the formulations included physical, rheological, mechanical and cell culture analyses. *In vivo* implantation and analysis of healing

progression provided information about the remodeling mechanisms of the different PUR formulations. In order to fully characterize the resorptive component of graft remodeling, an *in vitro* osteoclastic culture protocol was developed to enable quantitation and direct comparison between volumetric resorptive rates of synthetic matrices. Each chapter in this dissertation focuses on a different PUR formulation and its detailed characterization. Combined, they offer design guidelines for the development of PUR scaffolds that a) protect scaffolds from contamination, and b) maintain bone-like strength while actively remodeling.

Chapter III describes the formulation, characterization, and *in vivo* evaluation of a PUR biofilm-dispersive graft.[25] Infectious complications in open fractures are a major factor contributing to osseous non-union and extremity amputation.[26] The persistence of bacteria within biofilms, despite meticulous debridement and antibiotic therapy, is believed to be a major cause of chronic infection.[27] As a therapeutic strategy for the reduction and prevention of biofilm-associated infections, D-Amino Acids (D-AA) with biofilm dispersal capabilities were incorporated into porous PUR scaffolds. Detailed *in vitro* characterization of the D-AA effect over the formation and dispersal of clinical bacterial strain biofilms is presented. The scaffold's porosity, mechanical properties and D-AA release profile are reported. The *in vivo* biofilm dispersal potential of the augmented PUR scaffolds was evaluated in contaminated rat segmental bone defects.

Chapter IV continues to present a settable PUR biocomposite formulation containing surface modified β-tricalcium phosphate (TCP) particles. Previous studies in our lab have developed compression molded TCP-PUR composites that supported cellular infiltration and remodeling when implanted in femoral condyle defects in rats.[20]

Due to the brittle nature of TCP, high pressure was required to obtain final mechanical properties matching those of bone. However, since the compressed composites are molded outside the body, their application is limited by the defect geometry. As a result, Chapter IV describes the development of a settable TCP-PUR formulation in which the surface of the ceramic filler was modified to improve the interactions with the PUR binder. The effect of surface modification was evaluated on the mechanical and *in vitro* biological performance of the biocomposites.

In contrast to slow resorbing TCP, allograft bone particles (ABP) remodel by osteoclastic resorption followed by osteoblastic new bone deposition.[28] Thus, ABPs were included in PUR composites to study the effect of design parameters on the healing of settable bone grafts *in vivo*. The design parameters, studied in Chapter V, are the rates of new bone formation, matrix resorption, and polymer degradation. Biocomposites were augmented with recombinant human bone morphogenetic protein-2 (rhBMP-2) to modulate the rates of new bone formation and polymer degradation. Instead, in Chapter VI, the influence of filler particle size, loading, and mineral content on the ABP-PUR biocomposites' remodeling mechanisms are considered. Each chapter reports the handling and mechanical properties of the appropriate formulations. The composites were delivered to cylindrical defects in the femoral condyle of New Zealand White rabbits, and the remodeling progression was evaluated by X-ray microcomputed tomography (□CT) and histomorphometry at 0, 6, and 12 weeks.

In order for biocomposites to be effectively integrated into the bone remodeling cycle they must undergo active resorption at a similar rate to that of new bone formation.[29] Consequently, detailed understanding of the osteoclastic effect on different

materials is valuable information for the designing functional biocomposites which promote bone regeneration. Chapter VII introduces an *in vitro* cell culture protocol to study the differentiation and resorptive activity of murine bone marrow cells in the presence of biomaterials. Implementation of the protocol is described to quantify the volumetric resorption rate of dentin in the presence and absence of rhBMP-2.

To conclude, Chapter VIII summarizes the main findings of this dissertation and Chapter IX presents suggestions for future work. As a whole, this dissertation presents a compelling argument for wider use and further development of PUR biocomposites.

References

1 Timothy A. Lew, John A. Walker, Joseph C. Wenke, Lorne H. Blackbourne, and Robert G. Hale, 'Characterization of Craniomaxillofacial Battle Injuries Sustained by United States Service Members in the Current Conflicts of Iraq and Afghanistan', *Journal of Oral and Maxillofacial Surgery*, 68 (2010), 3-7.

2 D. Ghysen, L. Ozsarlak, L. van den Hauwe, J. Van Goethem, AM. De Schepper, and PM. Parizel, 'Maxillo-Facial Trauma', *JBR-BTR*, 83 (2000), 181-97.

3 BB. Ward, SE. Brown, and PH. Krebsbach, 'Bioengineering Strategies for Regeneration of Craniofacial Bone: A Review of Emerging Technologies', *Oral diseases*, doi:10.1111/j.1601-0825.2010.01682.x (2010).

4 BJ. Costello, G. Shah, P. Kumta, and CS. Sfeir, 'Regenerative Medicine for Craniomaxillofacial Surgery', *Oral Maxillofac Surg Clin North Am.*, 22 (2010), 33-42.

5 P. Giannoudis, H. Dinopoulos, and E. Tsiridis, 'Bone Substitues: An Update', *Injury, Int. J. Care Injured*, 36S (2005), S20-S27.

6 United States Census Bureau, 'Organ Transplants and Grafts: 1990 to 2007', (2007).

7 M. A. Woodruff, C. Lange, J. Reichert, A. Berner, F. L. Chen, P. Fratzl, J. T. Schantz, and D. W. Hutmacher, 'Bone Tissue Engineering: From Bench to Bedside', *Materials Today*, 15 (2012), 430-35.

8 K. Rezwan, Q. Z. Chen, J. J. Blaker, and A. R. Boccaccini, 'Biodegradable and Bioactive Porous Polymer/Inorganic Composite Scaffolds for Bone Tissue Engineering', *Biomaterials*, 27 (2006), 3413-31.

9 S. Scaglione, E. Lazzarini, C. Ilengo, and R. Quarto, 'A Composite Material Model for Improved Bone Formation', *Journal of Tissue Engineering and Regenerative Medicine*, 4 (2010), 505-13.

10 S. Bose, M. Roy, and A. Bandyopadhyay, 'Recent Advances in Bone Tissue Engineering Scaffolds', *Trends in Biotechnology*, 30 (2012), 546-54.

11 MS. Gilardino, DS. Cabiling, and SP. Bartlett, 'Long-Term Follow-up Experience with Carbonated Calcium Phosphate Cement (Norian) for Cranioplasty in Children and Adults.', *Plast Reconstr Surg.*, 123 (2009), 983-94.

12 S. A. Guelcher, 'Biodegradable Polyurethanes: Synthesis and Applications in Regenerative Medicine', *Tissue Engineering Part B-Reviews*, 14 (2008), 3-17.

13 A. Hafeman, K. Zienkiewicz, A. Zachman, H.J. Sung, L.B. Nanney, J.M. Davidson, and S.A. Guelcher, 'Characterization of the Degradation Mechanisms of Lysine-Derived and Aliphatic Poly(Ester Urethane) Scaffolds', *Biomaterials*, In review (2010).

14 J. M. Page, E. M. Prieto, J. E. Dumas, K. J. Zienkiewicz, J. C. Wenke, P. Brown-Baer, and S. A. Guelcher, 'Biocompatibility and Chemical Reaction Kinetics of Injectable, Settable Polyurethane/Allograft Bone Biocomposites', *Acta Biomaterialia*, 8 (2012), 4405-16.

15 B. Li, T. Yoshii, A. E. Hafeman, J. S. Nyman, J. C. Wenke, and S. A. Guelcher, 'The Effects of Rhbmp-2 Released from Biodegradable Polyurethane/Microsphere Composite Scaffolds on New Bone Formation in Rat Femora', *Biomaterials*, 30 (2009), 6768-79.

16 AE Hafeman, B Li, T Yoshii, KL Zienkiewicz, JM Davidson, and SA Guelcher, 'Injectable Biodegradable Polyurethane Scaffolds with Release of Platelet-Derived Growth Factor for Tissue Repair and Regeneration', *Pharm Res*, 25 (2008), 2387-99.

17 B. Li, K. V. Brown, J. C. Wenke, and S. A. Guelcher, 'Sustained Release of Vancomycin from Polyurethane Scaffolds Inhibits Infection of Bone Wounds in a Rat Femoral Segmental Defect Model', *Journal of Controlled Release,* 145 (2010), 221-30.

18 T Yoshii, A. Hafeman, J Nyman, J Esparza, K Shinomiya, D. M. Spengler, Gregory R. Mundy, G. Gutierrez, and S A Guelcher 'A Sustained Release of Lovastatin from Biodegradable, Elastomeric Polyurethane Scaffolds for Enhanced Bone Regeneration', *Tissue Eng Part A,* 16 (2010).

19 J. E. Dumas, K. Zienkiewicz, S. A. Tanner, E. M. Prieto, S. Bhattacharyya, and S. A. Guelcher, 'Synthesis and Characterization of an Injectable Allograft Bone/Polymer Composite Bone Void Filler with Tunable Mechanical Properties', *Tissue Engineering Part A,* 16 (2010), 2505-18.

20 T. Yoshii, J. E. Dumas, A. Okawa, D. M. Spengler, and S. A. Guelcher, 'Synthesis, Characterization of Calcium Phosphates/Polyurethane Composites for Weight-Bearing Implants', *Journal of Biomedical Materials Research Part B-Applied Biomaterials,* 100B (2012), 32-40.

21 J. E. Dumas, T. Davis, G.E. Holt, T. Yoshii, D. S. Perrien, J. S. Nyman, T. Boyce, and S.A. Guelcher, 'Synthesis, Characterization, and Remodeling of Weight-Bearing Allograft Bone/Polyurethane Composites in the Rabbit', *Acta Biomaterialia,* 6 (2010), 2394-406.

22 J. E. Dumas, E. M. Prieto, K.J. Zienkiewicz, T. Guda, J. C. Wenke, J. Bible, G.E. Holt, and S.A. Guelcher, 'Balancing the Rates of New Bone Formation and Polymer Degradation Enhances Healing of Weight-Bearing Allograft/Polyurethane Composites in Rabbit Femoral Defects', *Tissue Eng Part A,* Not available - ahead of print (2013).

23 J.E. Dumas, P.B. BrownBaer, E.M. Prieto, T. Guda, R.G. Hale, J.C. Wenke, and S.A. Guelcher, 'Injectable Reactive Biocomposites for Bone Healing in Critical-Size Rabbit Calvarial Defects', *Biomedical Materials,* 7 (2012), 024112.

24 R. Adhikari, P. A. Gunatillake, I. Griffiths, L. Tatai, M. Wickramaratna, S. Houshyar, T. Moore, R. T. M. Mayadunne, J. Field, M. McGee, and T. Carbone, 'Biodegradable Injectable Polyurethanes: Synthesis and Evaluation for Orthopaedic Applications', *Biomaterials,* 29 (2008), 3762-70.

25 Carlos J. Sanchez Jr, Edna M. Prieto, Chad A. Krueger, Katarzyna J. Zienkiewicz, Desiree R. Romano, Catherine L. Ward, Kevin S. Akers, Scott A. Guelcher, and Joseph C. Wenke, 'Effects of Local Delivery of D-Amino Acids from Biofilm-Dispersive Scaffolds on Infection in Contaminated Rat Segmental Defects', *Biomaterials,* 34 (2013), 7533-43.

26 J. Huh, D. J. Stinner, T. C. Burns, and J. R. Hsu, 'Infectious Complications and Soft Tissue Injury Contribute to Late Amputation after Severe Lower Extremity Trauma', *J Trauma,* 71 (2011), S47-51.

27 D. P. Lew, and F. A. Waldvogel, 'Osteomyelitis', *Lancet,* 364 (2004), 369-79.

28 Leandro Eduardo Klüppel, Fernando Antonini, Sérgio Olate, Frederico Felipe Nascimento, José Ricardo Albergaria-Barbosa, and Renato Mazzonetto, 'Bone Repair Is Influenced by Different Particle Sizes of Anorganic Bovine Bone Matrix: A Histologic and Radiographic Study in Vivo', *Journal of Craniofacial Surgery,* 24 (2013), 1074-77 10.97/SCS.0b013e318286a0a3.

29 ArndtF Schilling, Sandra Filke, Silja Brink, Heike Korbmacher, Michael Amling, and JohannesM Rueger, 'Osteoclasts and Biomaterials', *European Journal of Trauma,* 32 (2006), 107-13.

CHAPTER II

BACKGROUND

General principles of bone tissue engineering

Tissue engineering is "an interdisciplinary field of research that applies the principles of engineering and the life sciences towards the development of biological substitutes that restore, maintain, or improve tissue function''.[1] As such, bone tissue engineering aims to develop scaffolds that promote the healing of bone defects generated by trauma, disease, primary tumor resection, and/or congenital deformation.[2-5]

Bone is a dynamic tissue under constant remodeling in the body. This is achieved by the combined action of 3 cell types: osteoblasts (bone forming cells), osteoclasts (bone resorbing cells), and osteocytes (mechanosensor cells entrapped in bone). As a material, bone is a natural composite of an organic phase (mainly collagen) and hydroxycarbonate apatite.[6] It is organized in two architectural forms: trabecular or porous bone, and cortical or compact bone.[7] Depending on the location in the body, the architectural organization determines target bone mechanical properties.

Several requirements have been identified for bone tissue engineering scaffolds. These focus on achieving mechanical as well as biological properties that will favor scaffold replacement by new and functional bone in time. As a result, successful bone scaffolds must:

(a) be *biocompatible*, or support normal cellular activity without any local and systematic toxic effects to the host tissue,[6]

(b) be *osteoconductive*, or provide a surface for bone cells to adhere, proliferate, migrate, and deposit new bone,

(c) be *osteoinductive*, or capable of inducing new bone formation through the recruitment of osteoprogenitor cells,

(d) have *mechanical properties* similar to those of the surrounding host bone,

(e) have *interconnected pores* to facilitate diffusion of nutrients and oxygen required for the survival of cells, and

(f) be *bioresorbable* or *degradable* in a controlled manner such that they are replaced by new bone.

Characterization of bone scaffolds

Proper characterization of bone scaffolds encompasses multiple strategies from several design perspectives. Table 2.1 lists various design perspectives, corresponding parameters, and utilized methods to characterize bone scaffolds. The list is organized generally as proceeding from fabrication (top) to implementation (bottom). This section provides a summary of some techniques and protocols listed. A detailed discussion about how the techniques work is not provided since this falls outside the scope of the chapter, but citations to previous work applying these techniques have been included as reference.

Characterization of polymer scaffolds often requires analysis of polymer composition and structure since these parameters influence scaffold processability and final performance. Molecular weight distribution is usually quantified using gas permeation chromatography.[34, 35] Differential Scanning Calorimetry (DSC) is used to identify thermal transitions such as the glass transition and melting temperatures.

Table 2.1. Characterization methods for bone scaffolds

Type	Category	Parameter(s)	Method(s)
Handling	Viscosity	Shear rate profile, Injectability	Rheometer, Viscometer [8], MTS [9, 10]
	Cure profile	Working time (storage and loss modulus)	Rheometer, Gillmore needle [9, 11, 12]
Reaction conditions	Thermodynamics	Exotherm	DSC, Thermal couple [13, 14]
	Conversion	Composition	NMR [15], FTIR [16, 17], XRD [18]
Static	Volumetric properties	Architecture: porosity, size, shape	SEM [8, 19, 20, 16, 21, 13, 22, 18, 9, 11, 15, 23], mCT [15], Stereological approach [13], Gravimetric [19, 20, 24, 16, 9, 11, 12, 25], Mercury intrusion [16]
	Aqueous interaction	Swelling (volume), absorption (mass)	Gravimetric [21, 13, 15, 14]
Biocompatibility	Cellular interaction	*In vitro*: cell proliferation, viability, morphology	MTT [26, 22, 27], live/dead [19, 28, 21, 29, 22, 30, 15, 10, 27], SEM [30], Microscopy [15, 27]
		In vivo: cell identification	Histology [28, 26, 17, 31]
Biomechanics	Rheology	Shear rate (Yield stress), Elastic modulus	Rheometer [21]
	Compression [24], torsion, fatigue, tensile, three-point bending	Stress vs. strain, strength, modulus, energy to failure	DMA [25], Instron [19, 20, 32, 18, 15] MTS [16, 9, 12, 33, 23, 14], Universal Testing Machine [10]
Degradation	*In vitro*	Composition	Gravimetric [26, 9, 11], HPLC
	In vivo	Presence	Histology [26]

Standard thermal analysis protocols include a combination of heat-cool-heat cycles with heating and cooling rates of 5-10 °C min^{-1}, and identification of the thermal transitions from the second heating cycle.[36, 37] DSC can also be used to quantify the crystalline content of the polymeric phases,[38, 34] although more detailed information about crystallinity can be obtained using X-ray diffraction techniques.[39] Rotational rheometers have been used to measure viscosity as well as the storage (G') and loss (G") moduli of

flowable formulations.[40] Additional protocols to measure viscosity include the use of more traditional Ubbelohde viscometers.[41, 42]

The porous architecture of bone scaffolds has a direct impact on the mechanical properties, degradation rates, and cellular infiltration of the materials. Although high porosity and interconnectivity are desired to support cellular infiltration, mechanical properties decrease with porosity squared, while the effect on degradation rates varies depending on the material. Pore size distribution and morphology can be evaluated using Scanning Electron Microscopy (SEM). To do so, a thin section of the material is gold sputter-coated and imaged at different locations. Images are used to measure pore diameter which is reported either as an average (n>100) or after applying a statistical correction to account for non-ideal spherical pores.[40,42,43] Porosity is commonly determined gravimetrically by comparing dry scaffold density (ρ_F) with the density of bulk material (ρ) according to: $\text{Porosity} = 1 - \frac{\rho_F}{\rho}$.[44, 45] X-Ray microtomography (μCT) has also been used to accurately quantify porosity. In this case, dry scaffolds are scanned in a μCT system at high resolution modes, and porosity values are obtained after thresholding the reconstructed image.[46-48] Pore size distribution, total pore volume, surface area, and density can also be obtained using mercury intrusion porosimetry (MIP),[49, 34] although interconnected pores are required in order to obtain representative results using this technique.

In vitro degradation profiles of scaffolds are determined by incubating samples at 37°C in phosphate-buffered saline (PBS) at various pH levels, enzyme-containing media, or oxidative media.[34,50,47,39] At each time point, the media with degradation products is collected and the dry sample mass is measured and compared to the initial sample mass.

In addition to reporting the mass loss in time, the media collected can be analyzed with techniques such as high-performance liquid chromatography (HPLC) to determine the nature and concentration of the degradation products.

Depending on the specific application of the bone scaffold, specific mechanical requirements must be achieved under tension, compression, and/or torsion. Mechanical testing of the samples resulting in stress-strain data is conducted with protocols modeled by standard methods.[51-53] Reported properties usually include compressive and tensile modulus and strength.[50,37,44,38,34]

Scaffolding materials for bone tissue engineering

Autologous bone remains the standard of care for the treatment of bone defects due to its ideal osteogenic, osteoinductive and osteoconductive properties for bone defect healing. However, limited availability, postsurgical morbidity at the donor site, increased lengths of surgery and higher costs associated with autograft use[54] have increased the demand for alternative materials, such as allograft bone. In 2002, more than 980,000 bone allografts were distributed in the US and their usage was reported to be increasing.[55] Even though sterilization and viral inactivation of allograft bone render the material suitable for clinical use, the available shapes are limited by the donor source.[56] As a result, bone tissue engineering efforts have focused on the development of synthetic grafts that promote healing of bone defects. The following sections discuss the characteristics and performance of several of these formulations.

Low porosity calcium phosphate cements

Since their initial discovery in 1982,[57] injectable calcium phosphate cements (CPCs) have been successfully introduced into the clinic for a number or orthopaedic and craniomaxillofacial applications, including repair of tibial plateau fractures and calvarial defects. CPCs have been investigated extensively as injectable bone replacement biomaterials due to their similar chemical composition to the mineral component of bone, biocompatibility,[58] osteoconductivity, and fast setting times (< 5 min).[59] These biomaterials set at a physiological pH with minimal reaction exotherm and do not release toxic monomers or solvents.[60, 18] Apatite, which has low solubility and resorbs slowly, and brushite, which has higher solubility than apatite and resorbs more rapidly, comprise the two primary classes of CPCs.[61] While CPCs set by an acid/base reaction that can reduce the pH of the paste to values as low as 3,[32] a number of *in vivo* studies have reported favorable host responses after setting.[24, 17] In a recent study, the mechanism of cell-mediated degradation of brushite CPCs was investigated by culturing RAW264.7 cells on the cements *in vitro*.[30] The RAW264.7 cells differentiated to macrophages, multinucleated giant cells, as well as osteoclast-like cells, on the brushite CPCs. SEM analysis of the ultra-structure of osteoclast-like cells revealed characteristics associated with the osteoclast phenotype, such as formation of a sealing zone and ruffled border. Furthermore, osteoclast-like cells were observed to penetrate deep into the interior of the cements, which suggests that brushite CPCs are demineralized by osteoclast-mediated resorption *in vivo*.

In a promising area of new research, the effects of nanometer-scale calcium phosphate (CaP) crystals on cellular interactions are under investigation.[62] Coating of

mesenchymal stem cells with CaP nanorods has been reported to exhibit enhanced osteoblastic differentiation and production of extracellular matrix production relative to uncoated cells,[63] which suggests that nanoscale injectable CPCs may be desirable carriers for stem cells. However, while nanostructured CaPs enhance osteoblast differentiation, the rate of cellular infiltration into monolithic cements is limited by osteoclast-mediated resorption. This rate of infiltration is relatively slow (i.e., 0.02 μm^3 μm^{-2} day^{-1}), in contrast to migration and proliferation of cells through interconnected pores.[64] Thus, a number of recent studies have investigated new methods for introducing macropores into injectable CPCs to enhance cellular infiltration and remodeling.

Porous calcium phosphate cements

Primary limitations of first-generation low porosity CPCs restricting their use in the clinic include brittle mechanical properties, which lead to low shear strength and fracture toughness; slow degradation *in vivo*;[65] and the small pore size (0.1 – 10 μm), which results in slow cellular infiltration and ingrowth of new bone.[58,66] Both low porosity as well as small pore size in CPCs contribute to slow remodeling and ingrowth of new bone, and have thus been suggested as a root cause for the failure of CPCs in periodontal bone repair.[67] Slow remodeling of CPCs has also been suggested to contribute to their failure in cranioplasty applications.[68] Therefore, recent studies have focused on introducing macropores into CPCs and improving their mechanical properties while preserving their favorable biocompatibility in order to improve their clinical performance.

Interconnected macropores >10 μm are essential for promoting infiltration of cells and ingrowth of blood vessels and new bone into CPCs,[69, 70] as well as for polymeric scaffolds such as hydrogels.[15] In order to preserve the excellent biocompatibility and osteoconductivity of CPCs, adjuvants added to create macropores must be non-cytotoxic. In one approach, multi-phasic cements have been prepared by combining soluble ceramic particles, such as calcium sulphate, with less soluble particles, such as triccalcium phosphate or hydroxyapatite.[71,23] A bi-phasic CPC was fabricated by mixing α-tricalcium phosphate (α-TCP), calcium sulphate hemihydrate (CSH), and an aqueous solution containing 2.5 wt% Na_2HPO_4.[33] The resulting cement comprised an apatitic phase (calcium-deficient hydroxyapatite, CDHA) and a soluble phase (calcium sulphate dihydrate, CSD). After setting, the soluble CSD and CSH phases dissolved, resulting in pores that facilitated the ingrowth of new bone in a rat on-lay graft model.[31] The technology has been licensed to BoneSupport and is marketed as CERAMENT**™** bone void filler for spinal and orthopaedic indications. Recent clinical studies have highlighted the potential of the partially resorbable biphasic (60% calcium sulphate/40% hydroxyapatite) CERAMENT**™** CPC as an effective substitute for non-resorbable poly(methyl methacrylate) (PMMA) for treatment of osteoporotic and traumatic vertebral fractures.[72, 73]

Composites with calcium phosphates

A number of other strategies have been investigated for fabricating injectable macroporous CPCs. Foaming agents such as surfactants,[12] hydrogen peroxide solution,[16] carbon dioxide,[74] or hydrophobic liquids,[75] have been utilized to fabricate injectable

calcium phosphate foams. In one study, the surfactant sodium dodecyl sulphate (SDS) was used as an air-entraining agent to create macroporous CPCs.[12] Micro- and macroporosity were controlled by the liquid-to-powder ratio and the concentration of SDS, which stabilized the bubbles formed by the setting reaction of the cement. Alternatively, biocompatible and degradable polymeric microspheres such as poly(lactic-co-glycolic acid) (PLGA),[76] poly(trimethyl carbonate), or gelatin[9, 11] have been investigated to synthesize macroporous CPCs. CPCs incorporating degradable porogens offer the additional advantage of local delivery of drugs or growth factors, since biologics can be encapsulated in the porogens prior to embedding in the calcium phosphate matrix.[77] While incorporation of PLGA microspheres in CPCs has been suggested to improve the initial strength of the composites, the strength decreases upon dissolution of the microspheres and does not increase until new bone starts to grow into the macropores.[78] To improve the injectability of CPC incorporating 30 wt% PLGA microspheres, sodium citrate was added to the aqueous solution, which reduced the viscosity of the paste. Due to their macroporosity, injectable CPCs incorporating a porogen have significant advantages compared to monolithic CPCs. Thus, macroporous CPCs are anticipated to be considered a preferred choice for healing of bony defects after regulatory approval.[65] In an alternative approach, CaP granules suspended in aqueous solutions of hydroxy-propylmethyl-cellulose promoted faster initial ingrowth of new bone at the surface of the material, relative to macroporous CPCs.[28, 79] It has been suggested that the observed early apposition of new bone could potentially enhance the interfacial bonding between host bone and the CPC, thus reinforcing the material for weight-bearing applications.[65]

Polymeric bone scaffolds

Polyesters are among the most studied biodegradable materials for biomedical applications.[80-83] The degradation profiles and mechanical properties of polyesters can be tailored according to the final application by modifying the backbone composition. Due to this versatility, polyester scaffolds have been developed for bone, cartilage, and meniscus among other applications.[84, 82] The main degradation mechanism of polyesters is hydrolytic chain scission of the ester bonds in the backbone.[85, 82, 86, 80] Degradation products *in vivo* are incorporated into the tricarboxylic acid cycle (TCA) and secreted from the body.[82, 85]

Poly(propylene fumarate) (PPF) is a linear, unsaturated, cross-linkable, and biodegradable polyester.[87, 88, 35, 42] used in bone scaffolds. Physical, mechanical, and degradation properties of PPF networks can be tuned by modifying one or several formulation parameters such as macromer molecular weight, cross-linking density, nature of the cross-linking agents, and porosity. Increased molecular weight of the linear PPF has been suggested to increase glass transition temperatures and viscosity.[88] Increased viscosity allows PPF to be injected into irregular shaped defects to later be cross-linked *in situ*. PPF networks exhibit a wide range of mechanical properties, which increase with higher cross-linking densities.[89] PPF degrades by hydrolysis of the ester bonds into propylene glycol and fumaric acid.[87] Fumaric acid is incorporated into the TCA cycle, while propylene glycol, which is a commonly used food additive, can be secreted by the body without generating any toxic reaction. Techniques to produce porous PPF-based scaffolds include crosslinking in combination with salt-leaching,[90] emulsion templating,[44, 42] gas foaming,[91] and a combination of 3D printing and injection molding.[92]

Tyrosine-derived polymers have been developed as materials with significant biological compatibility due to the presence of naturally occurring building blocks and degradable bonds, as well as high mechanical properties provided by the aromatic rings in their backbone. The main building block of these polymers is the diphenolic monomer Desaminotyrosyl-L-Tyrosine alkyl ester (DTR, where R represents the alkyl pendant group) which is obtained from the carbodiimide-mediated reaction between L-tyrosine alkyl ester and desaminotyrosine (DAT).[93] DTR can be polymerized with different reagents to create tyrosine derived polymers with a range of mechanical properties and degradation profiles. Reaction with phosgene, dicarboxylic acids, or alkyl or aryl dichlorophosphates generates poly(DTR carbonates),[36] poly(DTR arylates), or poly(DTR phosphate esters) respectively.[93] Tyrosine-derived polycarbonate foams have been prepared using a combination of solvent casting/porogen leaching techniques.[36]

Polymeric scaffolds for bone tissue engineering have been developed incorporating the materials described above. PPF foams prepared by solvent casting followed by salt leaching have been tested in calvarial defects *in vivo* and shown to be biocompatible and support new bone formation after 8 weeks.[90] Tyrosine-derived polycarbonates containing DTR, DT, and PEG, prepared using a combination of solvent casting, porogen leaching, and phase separation techniques have also been tested both *in vitro* and *in vivo*. The scaffolds had 85% porosity, a bimodal pore size distribution with macropores >200 μm and micropores <20 μm,[36] and a compressive modulus >0.5 MPa (minimal requirement for bone graft substitutes) after 6 weeks of incubation in PBS at 37°C.[94] When tested *in vivo* using a critical size calvarial defect in New Zealand White rabbits, the materials generated minimal inflammatory response and degraded faster than

under *in vitro* conditions. New bone formation was promoted when the scaffolds were loaded with 50 μg of recombinant human bone morphogenetic protein-2 (rhBMP-2) or coated with calcium phosphate.[94] Recently, PLGA porous scaffolds with pore sizes in the range of 200-600 μm were prepared via thermal sintering of PLGA spheres and porogen leaching.[48] The scaffolds had initial mechanical properties in the range of human trabecular bone, and improved oxygen diffusion across the scaffold. This last property is of interest for the treatment of large-area bone defects to support cellular infiltration deep into the scaffolds. In general, the *in vivo* performance of polymeric scaffolds in bone defects has shown to be improved with the incorporation of ceramic fillers or biologics which provide osteoinductive properties to the already biocompatible and osteoconductive materials. Examples of ceramic fillers include calcium phosphates,[95-97] allograft bone,[98] and bioactive glass,[99, 100] while biologics include rhBMP-2,[94, 101] lovastatin,[102] and TGF-β.[103]

Biodegradable polyurethanes

Polyurethanes (PUR[104]) comprise a diverse family of materials including cast elastomers, thermoplastic elastomers, and flexible foams. Due to their toughness, durability, biocompatibility, and improved biostability, they have been incorporated in a wide variety of implantable biomedical devices. Biodegradable polyurethanes prepared from biocompatible intermediates, such as polyester polyols and aliphatic and lysine-derived polyisocyanates, have attracted considerable interest recently for use as tissue scaffolds and drug delivery systems.[104, 105] Their ability to be processed by reactive liquid molding renders polyurethanes useful as injectable biomaterials for minimally invasive

surgeries, in which the material is injected as a reactive viscous liquid that cures *in situ* to form a viscoelastic solid scaffold. Furthermore, macropores that facilitate cellular infiltration can be generated within the scaffold by the process of gas foaming through the reaction of isocyanate groups with water[106-108] or by encapsulation of porogens.[109]

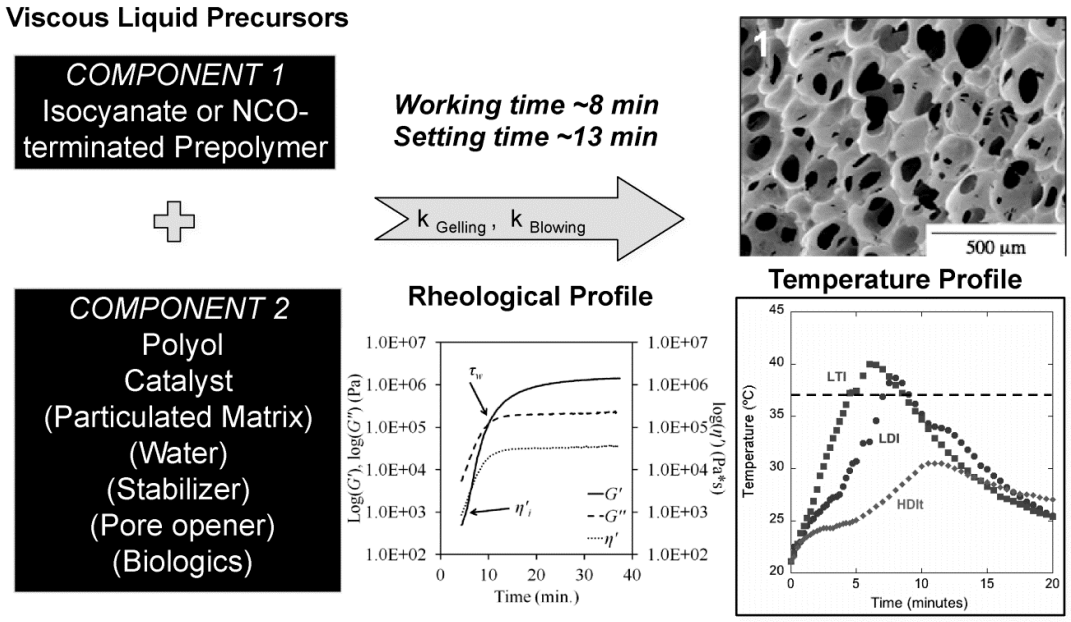

Figure 2.1. Schematic summarizing the synthesis of injectable polyurethane (PUR) foams from viscous liquid precursors.

The synthesis of injectable PUR scaffolds is shown in Figure 2.1. Component 1 comprises either an isocyanate or an isocyanate-terminated prepolymer, while Component 2 includes all components with active hydrogen groups that react with the isocyanate (NCO) groups. The polyol component, which comprises a hydroxyl-terminated macromer with a polyester, polyether, or polycarbonate backbone, reacts with the prepolymer to form a polymer network linked by urethane groups (the gelling reaction). The NCO groups also react with water, either added to the formulation or present in the wound environment, to yield a di-substituted urea and gaseous carbon dioxide, which acts as a blowing agent to form interconnected macropores within the

PUR network [107, 108, 106] as shown in the SEM image (Figure 2.1). The working time, identified by the G'-G" crossover point (rheological profile in Figure 2.1) where the foam transitions from a viscous liquid to an elastic solid, can be tuned to targeted values using urethane catalysts, such as tertiary amines[110] or organometallic compounds. Amine-based catalysts have low cytotoxicity[111] and selectively catalyze the water-isocyanate blowing reaction,[112] while the more cytotoxic organometallic catalysts selectively catalyze the polyol-isocyanate gelling reaction. In contrast to the temperatures during cure exceeding 100^{o}C observed for aromatic isocyanates, the exotherm for lysine-derived PUR foams is <20^{o}C (temperature profile in Figure 2.1). Other additives, such as stabilizers and pore openers to control miscibility and pore size,[106] matrix particles to control expansion and increase mechanical properties, or biologics to enhance bioactivity,[113] can also be included in component 2.

While biodegradable PUR foams have been synthesized from aliphatic polyisocyanates,[114] lysine-derived polyisocyanates have shown the greatest promise for injectable and settable systems.[107, 115-117, 108, 110, 112, 118] Reactive PUR scaffolds prepared from lysine-derived polyisocyanates, including lysine methyl ester diisocyanate (LDI) and lysine triisocyanate (LTI), and tertiary amine catalysts, have been reported to induce a minimal inflammatory response on host tissue in both cutaneous and bone defects *in vivo*.[115, 108, 112, 118] Furthermore, *in vitro* cytotoxicity testing of the leachates from the reactive PUR has shown that the reactive PUR components are non-toxic.[112] These studies highlight the potential of injectable and settable lysine-derived PURs for both soft and hard tissue regeneration.

Polyurethane scaffolds for bone regeneration

PUR biocomposites derived from LDI[108, 119] and LTI[110, 120, 121] have been investigated as injectable bone void fillers and cements. An extracellular matrix component, such as demineralized bone matrix (DBM), calcium phosphate particles, or allograft bone particles, is blended with the reactive PUR to increase the osteoconductivity and mechanical properties of the graft and also to reduce its volumetric expansion *in situ*. Lysine-derived PUR composites are injectable, set within clinically relevant working times (e.g., 5-10 min) to form grafts with mechanical strength approaching that of host bone, and remodel and heal to form new bone. In an early study, a four-armed poly(dioxanone-*co*-glycolide) prepolymer capped with LDI was mixed with calcium phosphate particles in the presence of an diethanolamine catalyst and water to form a reactive putty that expanded to form a foam with interconnected pores.[108] When implanted into the pectoralis muscles of rats for up to 42 days, the putty exhibited a transient inflammatory response that resolved after 3 days. At longer time points, the foams were well integrated with host tissue and showed no evidence of a chronic inflammatory reaction.

In a similar study in bony defects, a settable foam was prepared by reacting an LDI-pentaerythritol prepolymer with a poly(lactide-*co*-glycolide) polyol (functionality of 4).[119] The two reactive liquid components were mixed with stannous octoate catalyst, water, and β-tricalcium phosphate particles (10 μm) and injected into femoral condyle plug defects in sheep, where they cured in ~10 min and expanded for form porous foam. Defects showed progressive healing from 6 to 24 weeks, characterized by the formation of new cortex, polymer degradation, and appositional bone growth with no signs of acute

or chronic inflammation. Cells infiltrated the foam through the processes of migration into open pores as well as polymer degradation.

In an alternative approach, injectable foams prepared from an LTI-PEG prepolymer, a poly(ε-caprolactone-co-lactide-co-glycolide) triol, allograft bone particles (180 μm), and the low-toxicity tertiary amine catalyst triethylene diamine were evaluated in femoral condyle plug defects in rats[110] and rabbits.[112] Compared to LDI prepolymers, the LTI-PEG prepolymer has reduced viscosity (20,000 cSt versus 80,000 cSt for LDI-pentaerythritol) and higher reactivity.[112] Cells infiltrated the scaffold through migration into open pores, surface degradation of the PUR to non-cytotoxic breakdown products, and osteoclast-mediated resorption of the allograft bone particles, with no signs of chronic inflammation.

While challenges including controlling expansion due to the gas blowing reaction and matching the rate of new bone formation to polymer degradation need to be addressed, the ability of PUR grafts to cure *in situ* without adversely affecting host tissue, degrade to non-cytotoxic breakdown products, and support infiltration of cells and new tissue underscores their potential as scaffolds for bone repair.

Polyurethane scaffolds as drug delivery systems

Lysine-derived PUR scaffolds have also been investigated as drug delivery systems to support both diffusion-controlled release of biologics added as labile powders[121-125] as well as degradation-controlled release of drugs covalently bound to the polymer.[117, 126, 127, 116, 128] An example of diffusion-controlled drug delivery is presented in Figure 2.2. SEM (Figure 2.2.A) and confocal (Figure 2.2.B) images of an LTI-polyester

foam augmented with FITC-labeled BSA as a labile powder show discrete BSA-FITC particles distributed throughout the scaffold.

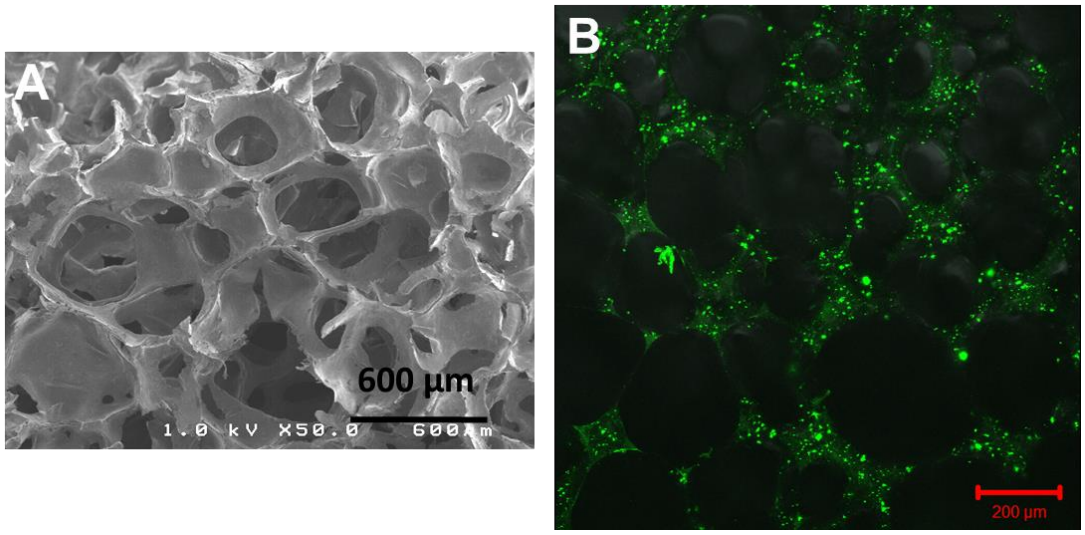

Figure 2.2. Drug delivery from PUR scaffolds. (A) SEM image of an LTI-polyester foam. (B) Confocal image of LTI-polyester foam augmented with FITC-labeled BSA as a labile powder. Discrete BSA-FITC particles can be observed uniformly distributed throughout the material.

In a recent study, injectable LTI-derived PUR/allograft bone composites augmented with recombinant human bone morphogenetic protein-2 (rhBMP-2) as a labile powder enhanced new bone formation at 6 weeks in a critical-size rabbit calvarial defect model[120]. In other studies, diffusion-controlled release of the antibiotic vancomycin and rhBMP-2 controlled infection[123] and enhanced bone healing[129] in critical-size defects contaminated with 10^5 Colony Forming Units (CFUs) *S. aureus*. Release of other biologics, such as nanoparticles delivering siRNA,[124] added to injectable PUR bone grafts as a labile powder has also been reported to be diffusion-controlled, with sustained release for up to 3 – 8 weeks.

In an alternative approach, drugs with active hydrogen groups (e.g., primary hydroxyl groups and amines), such as ascorbic acid,[130] naphthalene compounds,[117] and

the anti-tumor drug 7-*tert*-butyldimethylsilyl-10-hydroxy-camptothecin (DB-67),[128] were dissolved in the reactive PUR prior to injection and subsequently released in biologically active form by degradation of the polymer. Recent studies have reported that the release kinetics can be controlled by the composition of the drug,[117] the choice of catalyst,[116] or the addition of ionic ligands,[126] which offer greater tunability compared to diffusion-controlled release. Potential advantages of covalently binding drugs to PUR scaffolds include the ability to increase drug loading and control release to achieve therapeutically relevant doses. For example, clinical evaluation of DB-67 has been limited by the inability to deliver it in sufficient quantities to slow tumor growth and disease progression. When DB-67 was covalently incorporated into LDI-glycerol PUR scaffolds, it was released *in vitro* at a rate suitable for delivering therapeutic concentrations of the drug and inhibited cellular proliferation by 50% for several malignant glioma cell lines.[128, 126] While the degradation-controlled release mechanism has proven successful for small molecule synthetic drugs, another study has reported that recombinant human proteins dissolved in the aqueous phase prior to foaming are not released from the cured foam in a biologically active form.[121]

References

1 Robert Langer, and Joseph P. Vacanti, 'Tissue Engineering', *Science*, 260 (1993), 920-26.

2 Timothy A. Lew, John A. Walker, Joseph C. Wenke, Lorne H. Blackbourne, and Robert G. Hale, 'Characterization of Craniomaxillofacial Battle Injuries Sustained by United States Service Members in the Current Conflicts of Iraq and Afghanistan', *Journal of Oral and Maxillofacial Surgery*, 68 (2010), 3-7.

3 D. Ghysen, L. Ozsarlak, L. van den Hauwe, J. Van Goethem, AM. De Schepper, and PM. Parizel, 'Maxillo-Facial Trauma', *JBR-BTR*, 83 (2000), 181-97.

4 BB. Ward, SE. Brown, and PH. Krebsbach, 'Bioengineering Strategies for Regeneration of Craniofacial Bone: A Review of Emerging Technologies', *Oral diseases*, doi:10.1111/j.1601-0825.2010.01682.x (2010).

5 BJ. Costello, G. Shah, P. Kumta, and CS. Sfeir, 'Regenerative Medicine for Craniomaxillofacial Surgery', *Oral Maxillofac Surg Clin North Am.*, 22 (2010), 33-42.

6 S. Bose, M. Roy, and A. Bandyopadhyay, 'Recent Advances in Bone Tissue Engineering Scaffolds', *Trends in Biotechnology*, 30 (2012), 546-54.

7 António J. Salgado, Olga P. Coutinho, and Rui L. Reis, 'Bone Tissue Engineering: State of the Art and Future Trends', *Macromolecular Bioscience*, 4 (2004), 743-65.

8 Elizabeth M. Christenson, Wafa Soofi, Jennifer L. Holm, Neil R. Cameron, and Antonios G. Mikos, 'Biodegradable Fumarate-Based Polyhipes as Tissue Engineering Scaffolds', *Biomacromolecules*, 8 (2007), 3806-14.

9 W. J. Habraken, L. T. de Jonge, J. G. Wolke, L. Yubao, A. G. Mikos, and J. A. Jansen, 'Introduction of Gelatin Microspheres into an Injectable Calcium Phosphate Cement', *J Biomed Mater Res A*, 87 (2008), 643-55.

10 Liang Zhao, Michael D Weir, and Hockin HK Xu, 'An Injectable Calcium Phosphate-Alginate Hydrogel-Umbilical Cord Mesenchymal Stem Cell Paste for Bone Tissue Engineering', *Biomaterials*, 31 (2010), 6502-10.

11 W. J. Habraken, Z. Zhang, J. G. Wolke, D. W. Grijpma, A. G. Mikos, J. Feijen, and J. A. Jansen, 'Introduction of Enzymatically Degradable Poly(Trimethylene Carbonate) Microspheres into an Injectable Calcium Phosphate Cement', *Biomaterials*, 29 (2008), 2464-76.

12 S. Sarda, M. Nilsson, M. Balcells, and E. Fernandez, 'Influence of Surfactant Molecules as Air-Entraining Agent for Bone Cement Macroporosity', *J Biomed Mater Res A*, 65 (2003), 215-21.

13 E. Behravesh, S. Jo, K. Zygourakis, and A. G. Mikos, 'Synthesis of in Situ Cross-Linkable Macroporous Biodegradable Poly(Propylene Fumarate-Co-Ethylene Glycol) Hydrogels', *Biomacromolecules*, 3 (2002), 374-81.

14 Shulin He, Michael J. Yaszemski, Alan W. Yasko, Paul S. Engel, and Antonios G. Mikos, 'Injectable Biodegradable Polymer Composites Based on Poly(Propylene Fumarate) Crosslinked with Poly(Ethylene Glycol)-Dimethacrylate', *Biomaterials*, 21 (2000), 2389-94.

15 Sidi A Bencherif, R Warren Sands, Deen Bhatta, Praveen Arany, Catia S Verbeke, David A Edwards, and David J Mooney, 'Injectable Preformed Scaffolds with Shape-Memory Properties', *Proceedings of the National Academy of Sciences*, 109 (2012), 19590-95.

16 A. Almirall, G. Larrecq, J. A. Delgado, S. Martinez, J. A. Planell, and M. P. Ginebra, 'Fabrication of Low Temperature Macroporous Hydroxyapatite Scaffolds by Foaming and Hydrolysis of an Alpha-Tcp Paste', *Biomaterials,* 25 (2004), 3671-80.

17 B. R. Constantz, B. M. Barr, I. C. Ison, M. T. Fulmer, J. Baker, L. McKinney, S. B. Goodman, S. Gunasekaren, D. C. Delaney, J. Ross, and R. D. Poser, 'Histological, Chemical, and Crystallographic Analysis of Four Calcium Phosphate Cements in Different Rabbit Osseous Sites', *J Biomed Mater Res,* 43 (1998), 451-61.

18 E. Fernandez, M. P. Ginebra, M. G. Boltong, F. C. Driessens, J. Ginebra, E. A. De Maeyer, R. M. Verbeeck, and J. A. Planell, 'Kinetic Study of the Setting Reaction of a Calcium Phosphate Bone Cement', *J Biomed Mater Res,* 32 (1996), 367-74.

19 Robert S. Moglia, Jennifer L. Holm, Nicholas A. Sears, Caitlin J. Wilson, Dawn M. Harrison, and Elizabeth Cosgriff-Hernandez, 'Injectable Polyhipes as High-Porosity Bone Grafts', *Biomacromolecules,* 12 (2011), 3621-28.

20 J. M. Williams, A. J. Gray, and M. H. Wilkerson, 'Emulsion Stability and Rigid Foams from Styrene or Divinylbenzene Water-in-Oil Emulsions', *Langmuir,* 6 (1990), 437-44.

21 E. Hill, T. Boontheekul, and D. J. Mooney, 'Designing Scaffolds to Enhance Transplanted Myoblast Survival and Migration', *Tissue Engineering,* 12 (2006), 1295-304.

22 Jun Liu, Hockin H. K. Xu, Hongzhi Zhou, Michael D. Weir, Qianming Chen, and Carroll Ann Trotman, 'Human Umbilical Cord Stem Cell Encapsulation in Novel Macroporous and Injectable Fibrin for Muscle Tissue Engineering', *Acta Biomaterialia,* 9 (2013), 4688-97.

23 E. Fernandez, M. D. Vlad, M. M. Gel, J. Lopez, R. Torres, J. V. Cauich, and M. Bohner, 'Modulation of Porosity in Apatitic Cements by the Use of Alpha-Tricalcium Phosphate-Calcium Sulphate Dihydrate Mixtures', *Biomaterials,* 26 (2005), 3395-404.

24 P. Frayssinet, L. Gineste, P. Conte, J. Fages, and N. Rouquet, 'Short-Term Implantation Effects of a Dcpd-Based Calcium Phosphate Cement', *Biomaterials,* 19 (1998), 971-7.

25 Diederik H. R. Kempen, Lichun Lu, Choll Kim, Xun Zhu, Wouter J. A. Dhert, Bradford L. Currier, and Michael J. Yaszemski, 'Controlled Drug Release from a Novel Injectable Biodegradable Microsphere/Scaffold Composite Based on Poly(Propylene Fumarate)', *Journal of Biomedical Materials Research Part A,* 77A (2006), 103-11.

26 Jaclyn A. Shepard, Farrukh R. Virani, Ashley G. Goodman, Timothy D. Gossett, Seungjin Shin, and Lonnie D. Shea, 'Hydrogel Macroporosity and the Prolongation of Transgene Expression and the Enhancement of Angiogenesis', *Biomaterials,* 33 (2012), 7412-21.

27 Qingchun Zhang, Ke Tan, Zhaoyang Ye, Yan Zhang, Wensong Tan, and Meidong Lang, 'Preparation of Open Porous Polycaprolactone Microspheres and Their Applications as Effective Cell Carriers in Hydrogel System', *Materials Science and Engineering: C,* 32 (2012), 2589-95.

28 C. Trojani, F. Boukhechba, J. C. Scimeca, F. Vandenbos, J. F. Michiels, G. Daculsi, P. Boileau, P. Weiss, G. F. Carle, and N. Rochet, 'Ectopic Bone Formation Using an Injectable Biphasic Calcium Phosphate/Si-Hpmc Hydrogel Composite Loaded with Undifferentiated Bone Marrow Stromal Cells', *Biomaterials,* 27 (2006), 3256-64.

29 Hongzhi Zhou, and Hockin H. K. Xu, 'The Fast Release of Stem Cells from Alginate-Fibrin Microbeads in Injectable Scaffolds for Bone Tissue Engineering', *Biomaterials,* 32 (2011), 7503-13.

30 Z Xia, L M Groverb, Y Huang, I E Adamopoulosa, U Gbureck, J T Triffitt, R M Sheltone, and J E Barralet, 'In Vitro Biodegradation of Three Brushite Calcium Phosphate Cements by a Macrophage Cell-Line', *Biomaterials*, 27 (2006), 4557-65.

31 A. Truedsson, J. S. Wang, P. Lindberg, M. Gordh, B. Sunzel, and G. Warfvinge, 'Bone Substitute as an on-Lay Graft on Rat Tibia', *Clin Oral Implants Res*, 21 (2010), 424-9.

32 M. Bohner, P. Van Landuyt, H. P. Merkle, and J. Lemaitre, 'Composition Effects on the Ph of a Hydraulic Calcium Phosphate Cement', *J Mater Sci Mater Med*, 8 (1997), 675-81.

33 M. Nilsson, E. Fernandez, S. Sarda, L. Lidgren, and J. A. Planell, 'Characterization of a Novel Calcium Phosphate/Sulphate Bone Cement', *J Biomed Mater Res*, 61 (2002), 600-7.

34 Lichun Lu, Susan J. Peter, Michelle D. Lyman, Hui Lai, Lin, Susan M. Leite, Janet A. Tamada, Joseph Vacanti, P., Rober Langer, and Antonios G. Mikos, 'In Vitro Degradation of Porous Poly(L-Lactic Acid) Foams', *Biomaterials*, 21 (2000), 1595-605.

35 F Kurtis Kasper, Kazuhiro Tanahashi, John P. Risher, and Antonios G. Mikos, 'Synthesis of Poly(Propylene Fumarate)', *Nature Protocols*, 4 (2009), 518-25.

36 MHR. Magno, J Kim, A Srinivasan, S McBride, D Bolikal, A Darr, JO Hollinger, and J Kohn, 'Synthesis, Degradation and Biocompatibility of Tyrosine-Derived Polycarbonate Scaffolds', *Journal of Materials Chemistry*, 20 (2010), 8885-93.

37 A.S. Rowlands, S.A. Lim, D. Martin, and J.J. Cooper-White, 'Polyurethane/Poly(Lactic-Co-Glycolic) Acid Composite Scaffolds Fabricated by Thermally Induced Phase Separation', *Biomaterials*, 28 (2007), 2109-21.

38 Peter X. Ma, and Ji-Won Choi, 'Biodegradable Polymer Scaffolds with Well-Defined Interconnected Spherical Pore Network', *Tissue Engineering*, 7 (2001), 23-49.

39 F Carfi Pavia, V La Carrubba, S Piccarolo, and V Brucato, 'Polymeric Scaffolds Prepared Via Thermally Induced Phase Separation: Tuning of Structure and Morphology', *J Biomed Mater Res Part A*, 86A (2008), 459-66.

40 Aurelio Salerno, Salvatore Iannace, and Paolo A. Netti, 'Open-Pore Biodegradable Foams Prepared Via Gas Foaming and Microparticulate Templating', *Macromolecular Bioscience*, 8 (2008), 655-64.

41 ASTM, 'D445: Standard Test Method for Kinematic Viscosity of Transparent and Opaque Liquids (and Calculation of Dynamic Viscosity)', (1997).

42 Elizabeth M. Christenson, Wafa Soofi, Jennifer Holm, L., Neil Cameron, R., and Antonios G. Mikos, 'Biodegradable Fumarate-Based Polyhipes as Tissue Engineering Scaffolds', *Biomacromolecules*, 8 (2007), 3806-14.

43 ASTM, 'D3576: Standard Test Method for Cell Size of Rigid Cellular Plastics', (2004).

44 Robert S. Moglia, Jennifer L. Holm, Nicholas A. Sears, Caitlin J. Wilson, Dawn Harrison, and Cosgriff-Hernandez, 'Injectable Polyhipes as High-Porosity Bone Grafts', *Biomacromolecules*, 12 (2011), 3621-28.

45 SA Guelcher, V Patel, K Gallagher, S Connonlly, JE Didier, JS Doctor, and JO Hollinger, 'Synthesis and in Vitro Biocompatibility of Injectable Polyurethane Foam Scaffolds', *Tissue engineering*, 12 (2006b), 1247-59.

46 Leon J.M. Jacobs, Maartje F. Kemmere, and Jos T.F. Keurentjes, 'Sustainable Polymer Foaming Using High Pressure Carbon Dioxide: A Review on Fundamentals, Processes and Applications', *Green Chemistry,* 10 (2008), 731-38.

47 Joanne. E McBane, Soroor Sharifpoor, Cai Kuihua, Rosalind S. Labow, and J. Paul Santerre, 'Biodegradation and in Vivo Biocompatibility of a Degradable, Polar/Hydrophobic/Ionic Polyurethane for Tissue Engineering Applications', *Biomaterials,* 32 (2011), 6034-44.

48 AR. Amini, DJ. Adams, CT. Laurencin, and SP Nukavarapu, 'Optimally Porous and Biomechanically Compatible Scaffolds for Large-Area Bone Regeneration', *Tissue Engineering: Part A,* 18 (2012), 1376-88.

49 Yoon Sung Nam, and Tae Gwan Park, 'Porous Biodegradable Polymeric Scaffolds Prepared by Thermally Induced Phase Separation', *J Biomed Mater Res,* 47 (1999), 8-17.

50 AE Hafeman, KJ Zienkiewicz, AL Zachman, HJ Sung, LB Nanney, JM Davidson, and SA Guelcher, 'Characterization of the Degradation Mechanisms of Lysine-Derived Aliphatic Poly(Ester Urethane) Scaffolds', *Biomaterials,* 32 (2010), 419-29.

51 ASTM, 'D-3574: Standard Test Methods for Flexible Cellular Materials- Slab, Bonded, and Molded Urethane Foams', (2001).

52 ASTM, 'D695: Standard Test Method for Compressive Properties of Rigid Plastics', (2002).

53 ASTM, 'D-1621: Standard Test Method for Compressive Properties of Rigid Cellular Plastics', (2010).

54 S.N. Khan, F.P. Cammisa, H.S. Sandbu, A.D. Diwan, F.P. Girardi, and J.M. Lane, 'The Biology of Bone Grafting', *Journal of the American Academy of Orthopaedic Surgeons,* 13 (2005), 77-86.

55 K.S. Beebe, J. Benevenia, B.E. Tuy, C.A. DePaula, R.D. Harten, and W.F. Enneking, 'Effects of a New Allograft Processing Procedure on Garfting Healing in a Canine Model', *Clin Orthop Relat Res,* 467 (2009), 273-80.

56 J. E. Dumas, K. Zienkiewicz, S. Tanner, E.M. Prieto, S. Battacharyya, and S.A. Guelcher, 'Synthesis and Characterization of an Injectable Allograft Bone/Polymer Composite Bone Void Filler with Tunable Mechanical Properties', *Tissue Engineering: Part A,* 16 (2010), 2505-18.

57 R. Z. Legeros, A. Chohayeb, and A. Schulman, 'Apatitic Calcium Phosphates Possible Dental Restorative Materials', *Journal of Dental Research,* 61 (1982), 343.

58 K. L. Low, S. H. Tan, S. H. Zein, J. A. Roether, V. Mourino, and A. R. Boccaccini, 'Calcium Phosphate-Based Composites as Injectable Bone Substitute Materials: A Review', *J Biomed Mater Res B Appl Biomater*.

59 Harvey Chim, and Arun K. Gosain, 'Biomaterials in Craniofacial Surgery Experimental Studies and Clinical Application', *Journal of Craniofacial Surgery,* 20 (2009), 29-33.

60 C. Liu, W. Wang, W. Shen, T. Chen, L. Hu, and Z. Chen, 'Evaluation of the Biocompatibility of a Nonceramic Hydroxyapatite', *J Endod,* 23 (1997), 490-3.

61 M Bohner, 'Calcium Orthophosphates in Medicine: From Ceramics to Calcium Phosphate Cements', *Injury,* 31 (2000), S-D37-47.

62 Thomas J. Webster, Celaletdin Ergun, Robert H. Doremus, Richard W. Siegel, and Rena Bizios, 'Enhanced Functions of Osteoblasts on Nanophase Ceramics', *Biomaterials,* 21 (2000), 1803-10.

63 R Gonzalez-McQuire, D W Green, K. A. Partridge, R. O. Oreffo, S Mann, and S A Davis, 'Coating of Human Mesenchymal Cells in 3d Culture with Bioinorganic Nanoparticles Promotes Osteoblastic Differentiation and Gene Transfection', *Adv Mater*, 19 (2007), 2236-40.

64 T. Winkler, E. Hoenig, R. Gildenhaar, G. Berger, D. Fritsch, R. Janssen, M. M. Morlock, and A. F. Schilling, 'Volumetric Analysis of Osteoclastic Bioresorption of Calcium Phosphate Ceramics with Different Solubilities', *Acta Biomaterialia*, 6 (2010), 4127-35.

65 J. D. Kretlow, S. Young, L. Klouda, M. Wong, and A. G. Mikos, 'Injectable Biomaterials for Regenerating Complex Craniofacial Tissues', *Adv Mater Deerfield*, 21 (2009), 3368-93.

66 M. L. Shindo, P. D. Costantino, C. D. Friedman, and L. C. Chow, 'Facial Skeletal Augmentation Using Hydroxyapatite Cement', *Arch Otolaryngol Head Neck Surg*, 119 (1993), 185-90.

67 G. D. Brown, B. L. Mealey, P. V. Nummikoski, S. L. Bifano, and T. C. Waldrop, 'Hydroxyapatite Cement Implant for Regeneration of Periodontal Osseous Defects in Humans', *J Periodontol*, 69 (1998), 146-57.

68 C S Goldberg, O Antonyshyn, R Midha, and J A Fialkov, 'Measuring Pulsatile Forces on the Human Cranium', *J Craniofacial Surgery*, 16 (2005), 134 - 39.

69 T. Livingston, P. Ducheyne, and J. Garino, 'In Vivo Evaluation of a Bioactive Scaffold for Bone Tissue Engineering', *J Biomed Mater Res*, 62 (2002), 1-13.

70 R. M. Pilliar, M. J. Filiaggi, J. D. Wells, M. D. Grynpas, and R. A. Kandel, 'Porous Calcium Polyphosphate Scaffolds for Bone Substitute Applications -- in Vitro Characterization', *Biomaterials*, 22 (2001), 963-72.

71 J. E. Barralet, L. Grover, T. Gaunt, A. J. Wright, and I. R. Gibson, 'Preparation of Macroporous Calcium Phosphate Cement Tissue Engineering Scaffold', *Biomaterials*, 23 (2002), 3063-72.

72 S. Marcia, C. Boi, M. Dragani, S. Marini, M. Marras, E. Piras, G. C. Anselmetti, and S. Masala, 'Effectiveness of a Bone Substitute (Cerament) as an Alternative to Pmma in Percutaneous Vertebroplasty: 1-Year Follow-up on Clinical Outcome', *Eur Spine J*, 21 Suppl 1 (2012), S112-8.

73 S. Masala, G. Nano, S. Marcia, M. Muto, F. P. Fucci, and G. Simonetti, 'Osteoporotic Vertebral Compression Fracture Augmentation by Injectable Partly Resorbable Ceramic Bone Substitute (Cerament|Spinesupport): A Prospective Nonrandomized Study', *Neuroradiology*, 54 (2012), 1245-51.

74 W. Chen, Hongzhi Zhou, M. Tang, Michael D Weir, C. Bao, and Hockin H. K. Xu, 'Gas-Foaming Calcium Phosphate Cement Scaffold Encapsulating Human Umbilical Cord Stem Cells.', *Tissue Engineering Part A*, 18 (2012), 816-27.

75 M Bohner, 'Calcium Phosphate Emulsions: Possible Applications', *Key Eng Mater*, 192-195 (2001), 765-68.

76 D. P. Link, J. van den Dolder, W. J. Jurgens, J. G. Wolke, and J. A. Jansen, 'Mechanical Evaluation of Implanted Calcium Phosphate Cement Incorporated with Plga Microparticles', *Biomaterials*, 27 (2006), 4941-7.

77 P. Q. Ruhe, O. C. Boerman, F. G. Russel, P. H. Spauwen, A. G. Mikos, and J. A. Jansen, 'Controlled Release of Rhbmp-2 Loaded Poly(Dl-Lactic-Co-Glycolic Acid)/Calcium Phosphate Cement Composites in Vivo', *J Control Release*, 106 (2005), 162-71.

78 R B Martin, M W Chapman, R E Holmes, D J Sartoris, E C Shors, J E Gordon, D O Heitter, N A Sharkey, and A G Zissimos, 'Effects of Bone Ingrowth on the Strength and Non-Invasive Assessment of a Coralline Hydroxyapatite Material', *Biomaterials*, 10 (1989), 481-88.

79 O. Gauthier, R. Muller, D. von Stechow, B. Lamy, P. Weiss, J. M. Bouler, E. Aguado, and G. Daculsi, 'In Vivo Bone Regeneration with Injectable Calcium Phosphate Biomaterial: A Three-Dimensional Micro-Computed Tomographic, Biomechanical and Sem Study', *Biomaterials,* 26 (2005), 5444-53.

80 C. Mauli Agrawal, and Robert B. Ray, 'Biodegradable Polymeric Scaffolds for Musculoskeletal Tissue Engineering', *Journal of Biomed Mater Res,* 55 (2001), 141-50.

81 Zhen Pan, and Jiandong Ding, 'Poly(Lactide-Co-Glycolide) Porous Scaffolds for Tissue Engineering and Regenerative Medicine', *Interface Focus,* 2 (2012), 366-77.

82 Lakshimi S. Nair, and Cato T. Laurencin, 'Biodegradable Polymers as Biomaterials', *Progress in Polymer Science,* 32 (2007), 762-98.

83 Xiaohua Liu, and Peter X. Ma, 'Polymeric Scaffolds for Bone Tissue Engineering', *Annals of Biomedical Engineering,* 32 (2004), 477-86.

84 E Farng, and O Sherman, 'Meniscal Repair Devices: A Clinical and Biomechanical Literature Review', *J Arthrosc Relat Surg,* 20 (2004), 273-86.

85 C. Vaca-Garcia, 'Biomaterials', in *Introduction to Chemicals from Biomass*, ed. by JH Clark and FEI Deswarte (Chichester: Wiley, 2008), pp. 103-42.

86 L. Brannon-Peppas, and M. Vert, 'Polylactic and Polyglycolic Acids as Drug Delivery Carriers', in *Handbook of Pharmaceutical Controlled Release Technology*, ed. by DL Wise (New York: Marcel Dekker, 2000), pp. 99-130.

87 X Shi, and AG Mikos, 'Poly(Propylene Fumarate)', in *An Introduction to Biomaterials*, ed. by SA Guelcher and JO Hollinger (Boca Raton: CRC Press, 2006), pp. 205-18.

88 Shanfeng Wang, Lichun Lu, and Michael J. Yaszemski, 'Bone Tissue-Engineering Material Poly(Propylene Fumarate): Correlation between Molecular Weight, Chain Dimensions, and Physical Properties', *Biomacromolecules,* 7 (2006), 1976-82.

89 MD Timmer, C Carter, CG Ambrose, and AG Mikos, 'Fabrication of Poly(Propylene Fumarate)-Based Orthopaedic Implants by Photo-Crosslinking through Transparent Silicone Molds', *Biomaterials,* 24 (2003), 4707.

90 JP Fisher, JWM Vehof, D Dean, JPCM van der Waerden, TA Holland, A Mikos, and JA Jansen, 'Soft and Hard Tissue Response to Photocrosslinked Poly(Propylene Fumarate) Scaffolds in a Rabbit Model', *J Biomed Mater Res,* 59 (2002), 547-56.

91 D.H. Kempen, L Lu, C. Kim, X. Zhu, W.J.A. Dhert, B.L. Currier, and M.J. Yaszemski, 'Controlled Drug Release from a Novel Injectable Biodegradable Microsphere/Scaffold Composite Based on Poly(Propylene Fumarate)', *J Biomed Mater Res A.,* 77 (2006), 103-11.

92 K.W. Lee, S. Wang, L. Lu, E. Jabbari, B.L. Currier, and M.J. Yaszemski, 'Fabrication and Characterization of Poly(Propylene Fumarate) Scaffolds with Controlled Pore Structures Using 3-Dimensional Printing and Injection Molding', *Tissue engineering,* 12 (2006), 2801-11.

93 J Kohn, and J Schut, 'Polymers Derived from L-Tyrosine', in *An Introduction to Biomaterials*, ed. by SA Guelcher and JO Hollinger (Boca Raton: CRC Press, 2006), pp. 185-204.

94 J Kim, MHR Magno, H Waters, B Doll, S McBride, P Alvarez, A Darr, A Vasanji, J Kohn, and JO Hollinger, 'Bone Regeneration in a Rabbit Critical-Sized Calvarial Model Using Tyrosine-Derived Polycarbonate Scaffolds', *Tissue Engineering: Part A,* 18 (2012), 1132-39.

95 R Adhikari, PA Gunatillake, I Griffiths, L Tatai, M Wickramaratna, S Houshyar, T Moore, RTM Mayadunne, J Field, M McGee, and T Carbone, 'Biodegradable Injectable Polyurethanes: Synthesis and Evaluation for Orthopaedic Applications', *Biomaterials,* 29 (2008), 3762-70.

96 S Bennett, K Connolly, DR Lee, Y Jiang, D Buck, JO Hollinger, and EA Gruskin, 'Initial Biocompatibility Studies of a Novel Degradable Polymeric Bone Substitute That Hardens in Situ', *Bone,* 19 (1996), 1015.

97 MJ Yaszemski, RG Payne, WC Hayes, R Langer, TB Aufdemorte, and AG Mikos, 'The Ingrowth of New Bone Tissue and Initial Mechanical Properties of a Degrading Polymeric Composite Scaffold', *Tissue engineering,* 1 (1995), 41.

98 JE Dumas, K Zienkiewicz, SA Tanner, EM Prieto, S Battacharyya, and SA Guelcher, 'Synthesis and Characterization of an Injectable Allograft Bone/Polymer Composite Bone Void Filler with Tunable Mechanical Properties', *Tissue engineering: Part A,* 16 (2010), 2505-18.

99 P Gentile, M Mattioli-Belmonte, V Chiono, C Ferretti, F Baino, C Tonda-Turo, C Vitale-Brovarone, I Pashkuleva, RL Reis, and G Ciardelli, 'Bioactive Glass/Polymer Composite Scaffolds Mimicking Bone Tissue', *J Biomed Mater Res Part A,* 100A (2012), 2654-67.

100 HH Lu, SF El-Amin, KD Scott, and CT Laurencin, 'Three-Dimensional, Bioactive, Biodegradable, Polymer-Bioactive Glass Composite Scaffolds with Improved Mechanical Properties Support Collagen Synthesis and Mineralization of Human Osteoblast-Like Cells in Vitro', *J Biomed Mater Res A,* 64 (2003), 465-74.

101 B Li, T Yoshii, AE Hafeman, JS Nyman, JC Wenke, and SA Guelcher, 'The Effects of Rhbmp-2 Released from Biodegradable Polyurethane/Microsphere Composite Scaffolds on New Bone Formation in Rat Femora', *Biomaterials,* 30 (2009), 6768-79.

102 T Yoshii, AE Hafeman, JS Nyman, JM Esparza, K Shinomiya, DM Spengler, GR Mundy, GE Gutierrez, and SA Guelcher, 'A Sustained Release of Lovastatin from Biodegradable, Elastomeric Polyurethane Scaffolds for Enhanced Bone Regeneration', *Tissue engineering: Part A,* 16 (2010), 2396-79.

103 SJ Peter, L Lu, DJ Kim, GN Stamatas, MJ Miller, MJ Yaszemski, and AG Mikos, 'Effects of Transforming Growth Factor B1 Released from Biodegradable Polymer Microparticles on Marrow Stromal Osteoblasts Cultured on Poly(Propylene Fumarate) Substrates', *J. Biomed. Mater. Res.,* 50 (2000), 452-62.

104 S. A. Guelcher, 'Biodegradable Polyurethanes: Synthesis and Applications in Regenerative Medicine', *Tissue Engineering Part B-Reviews,* 14 (2008), 3-17.

105 J. P. Santerre, K. Woodhouse, G. Laroche, and R. S. Labow, 'Understanding the Biodegradation of Polyurethanes: From Classical Implants to Tissue Engineering Materials', *Biomaterials,* 26 (2005), 7457-70.

106 S. Guelcher, A. Srinivasan, A. Hafeman, K. Gallagher, J. Doctor, S. Khetan, S. McBride, and J. Hollinger, 'Synthesis, in Vitro Degradation, and Mechanical Properties of Two-Component Poly(Ester Urethane)Urea Scaffolds: Effects of Water and Polyol Composition', *Tissue Engineering,* 13 (2007), 2321-33.

107 J. Y. Zhang, E. J. Beckman, N. P. Piesco, and S. Agarwal, 'A New Peptide-Based Urethane Polymer: Synthesis, Biodegradation, and Potential to Support Cell Growth in Vitro', *Biomaterials,* 21 (2000), 1247-58.

108 S. Bennett, K. Connolly, D. R. Lee, Y. Jiang, D. Buck, J. O. Hollinger, and E. A. Gruskin, 'Initial Biocompatibility Studies of a Novel Degradable Polymeric Bone Substitute That Hardens in Situ', *Bone,* 19 (1996), S101-S07.

109 P. Bruin, G. J. Veenstra, A. J. Nijenhuis, and A. J. Pennings, 'Design and Synthesis of Biodegradable Poly(Ester-Urethane) Elastomer Networks Composed of Non-Toxic Building-Blocks', *Makromolekulare Chemie-Rapid Communications,* 9 (1988), 589-94.

110 J. E. Dumas, K. Zienkiewicz, S. A. Tanner, E. M. Prieto, S. Bhattacharyya, and S. A. Guelcher, 'Synthesis and Characterization of an Injectable Allograft Bone/Polymer Composite Bone Void Filler with Tunable Mechanical Properties', *Tissue Engineering Part A,* 16 (2010), 2505-18.

111 M. C. Tanzi, P. Verderio, M. G. Lampugnani, M. Resnati, E. Dejana, and E. Sturani, 'Cytotoxicity of Some Catalysts Commonly Used in the Synthesis of Copolymers for Biomedical Use', *Journal of Materials Science-Materials in Medicine,* 5 (1994), 393-96.

112 J. M. Page, E. M. Prieto, J. E. Dumas, K. J. Zienkiewicz, J. C. Wenke, P. Brown-Baer, and S. A. Guelcher, 'Biocompatibility and Chemical Reaction Kinetics of Injectable, Settable Polyurethane/Allograft Bone Biocomposites', *Acta Biomaterialia,* 8 (2012), 4405-16.

113 J. Y. Zhang, B. A. Doll, E. J. Beckman, and J. O. Hollinger, 'A Biodegradable Polyurethane-Ascorbic Acid Scaffold for Bone Tissue Engineering', *Journal of Biomedical Materials Research Part A,* 67A (2003), 389-400.

114 K. Gorna, and S. Gogolewski, 'Biodegradable Porous Polyurethane Scaffolds for Tissue Repair and Regeneration', *Journal of Biomedical Materials Research Part A,* 79A (2006), 128-38.

115 J. Y. Zhang, E. J. Beckman, J. Hu, G. G. Yang, S. Agarwal, and J. O. Hollinger, 'Synthesis, Biodegradability, and Biocompatibility of Lysine Diisocyanate-Glucose Polymers', *Tissue Engineering,* 8 (2002), 771-85.

116 W. N. Sivak, I. F. Pollack, S. Petoud, W. G. Zamboni, J. Y. Zhang, and E. J. Beckman, 'Catalyst-Dependent Drug Loading of Ldi-Glycerol Polyurethane Foams Leads to Differing Controlled Release Profiles', *Acta Biomaterialia,* 4 (2008), 1263-74.

117 W. N. Sivak, J. Y. Zhang, S. Petoud, and E. J. Beckman, 'Degradative-Release as a Function of Drug Structure from Ldi-Glycerol Polyurethanes', *Bio-Medical Materials and Engineering,* 20 (2010), 269-81.

118 E. J. Adolph, A. E. Hafeman, J. M. Davidson, L. B. Nanney, and S. A. Guelcher, 'Injectable Polyurethane Composite Scaffolds Delay Wound Contraction and Support Cellular Infiltration and Remodeling in Rat Excisional Wounds', *Journal of Biomedical Materials Research Part A,* 100A (2012), 450-61.

119 R. Adhikari, P. A. Gunatillake, I. Griffiths, L. Tatai, M. Wickramaratna, S. Houshyar, T. Moore, R. T. M. Mayadunne, J. Field, M. McGee, and T. Carbone, 'Biodegradable Injectable Polyurethanes: Synthesis and Evaluation for Orthopaedic Applications', *Biomaterials,* 29 (2008), 3762-70.

120 J.E. Dumas, P.B. BrownBaer, E.M. Prieto, T. Guda, R.G. Hale, J.C. Wenke, and S.A. Guelcher, 'Injectable Reactive Biocomposites for Bone Healing in Critical-Size Rabbit Calvarial Defects', *Biomedical Materials,* 7 (2012), 024112.

121 B. Li, T. Yoshii, A. E. Hafeman, J. S. Nyman, J. C. Wenke, and S. A. Guelcher, 'The Effects of Rhbmp-2 Released from Biodegradable Polyurethane/Microsphere Composite Scaffolds on New Bone Formation in Rat Femora', *Biomaterials,* 30 (2009), 6768-79.

122 K. V. Brown, B. Li, T. Guda, D. S. Perrien, S. A. Guelcher, and J. C. Wenke, 'Improving Bone Formation in a Rat Femur Segmental Defect by Controlling Bone Morphogenetic Protein-2 Release', *Tissue Engineering Part A,* 17 (2011), 1735-46.

123 B. Li, K. V. Brown, J. C. Wenke, and S. A. Guelcher, 'Sustained Release of Vancomycin from Polyurethane Scaffolds Inhibits Infection of Bone Wounds in a Rat Femoral Segmental Defect Model', *Journal of Controlled Release,* 145 (2010), 221-30.

124 C. E. Nelson, M. K. Gupta, E. J. Adolph, J. M. Shannon, S. A. Guelcher, and C. L. Duvall, 'Sustained Local Delivery of Sirna from an Injectable Scaffold', *Biomaterials,* 33 (2012), 1154-61.

125 Carlos J. Sanchez Jr, Edna M. Prieto, Chad A. Krueger, Katarzyna J. Zienkiewicz, Desiree R. Romano, Catherine L. Ward, Kevin S. Akers, Scott A. Guelcher, and Joseph C. Wenke, 'Effects of Local Delivery of D-Amino Acids from Biofilm-Dispersive Scaffolds on Infection in Contaminated Rat Segmental Defects', *Biomaterials,* 34 (2013), 7533-43.

126 W. N. Sivak, J. Y. Zhang, S. Petoud, and E. J. Beckman, 'Incorporation of Ionic Ligands Accelerates Drug Release from Ldi-Glycerol Polyurethanes', *Acta Biomaterialia,* 6 (2010), 144-53.

127 W.N Sivak, J. Zhang, S. Petroud, and E. J. Beckman, 'Simultaneous Drug Release at Different Rates from Biodegradable Polyurethane Foams', *Acta Biomaterialia,* 5 (2009), 2398-408.

128 W. N. Sivak, I. F. Pollack, S. Petoud, W. C. Zamboni, J. Y. Zhang, and E. J. Beckman, 'Ldi-Glycerol Polyurethane Implants Exhibit Controlled Release of Db-67 and Anti-Tumor Activity in Vitro against Malignant Gliomas', *Acta Biomaterialia,* 4 (2008), 852-62.

129 S. A. Guelcher, K. V. Brown, B. Li, T. Guda, B. H. Lee, and J. C. Wenke, 'Dual-Purpose Bone Grafts Improve Healing and Reduce Infection', *Journal of Orthopaedic Trauma,* 25 (2011), 477-82.

130 J. Y. Zhang, B. A. Doll, E. J. Beckman, and J. O. Hollinger, 'Three-Dimensional Biocompatible Ascorbic Acid-Containing Scaffold for Bone Tissue Engineering', *Tissue Engineering,* 9 (2003), 1143-57.

CHAPTER III

EFFECTS OF LOCAL DELIVERY OF D-AMINO ACIDS FROM BIOFILM-DISPERSIVE SCAFFOLDS ON INFECTION IN CONTAMINATED RAT SEGMENTAL DEFECTS

Introduction

Despite meticulous treatment, infectious complications of open bone fractures continue to be a significant factor contributing to patient morbidity and poor healing outcomes. The ensuing infection of bone by bacteria (osteomyelitis) is characterized by high levels of inflammation and destruction of viable bone tissue. Often the infection becomes chronic, resulting in increased rates of surgical revisions, non-union, and extremity amputation [1-3]. Among the pathogenic microorganisms associated with chronic osteomyelitis, *Staphylococcus aureus* is the most frequently isolated organism, accounting for >50% of all cases [4-8]. In addition to the increasing trend of antimicrobial resistance among clinical isolates, biofilm formation is a significant contributing factor in the development of both device and non-device related chronic orthopaedic infections and a major barrier to wound healing [6, 4].

Bacterial biofilms are an association of single or multiple species attached to a surface surrounded by an extracellular polymeric matrix (EPM), which constitutes a protected mode of growth. Compared to their planktonic counterparts, biofilm-derived bacteria have distinctive phenotypes in regards to growth, gene expression, and protein production that confer resistance to antimicrobial agents as well as host mechanisms of clearance [5, 9]. Importantly, bacterial biofilms have been associated with a broad range of human infections, including chronic non-device-related infections such as osteomyelitis[10,

[11]. Previous studies have reported that staphylococcal biofilms are present within infected bone of patients with chronic osteomyelitis [6-8], and that clinical osteomyelitis isolates of *S. aureus* are capable of forming biofilms *in vitro* [12-14]. Furthermore, staphylococcal biofilms have been implicated as a major cause of osseous non-union [15]. These studies suggest that staphylococcal biofilms play a critical role in both the development of chronic osteomyelitis and the sequelae of infectious complications.

Biofilm development is a highly coordinated and reversible process beginning with the attachment and proliferation of cells on a surface and culminating in the dispersal of cells from the biofilm into the surrounding environment. The dispersal of cells is an essential stage of the biofilm life cycle that contributes to survival of the organism and disease transmission. For both Gram-positive and Gram-negative microorganisms, biofilm dispersion is mediated by self-produced diffusible factors [16, 17]. Considering the specificity and effectiveness of these molecules for dispersing biofilms, the use of biofilm dispersal agents has attracted considerable interest for the treatment of biofilm-associated infections [18, 19]. Recent studies have shown that use of biofilm dispersal agents, including bismuth thiols [20], recombinant DNAses [21], and diffusible soluble factors [22, 23], can disperse biofilms *in vitro* and improve healing of biofilm-associated infections *in vivo* [24, 25]. However, toxicity to viable host tissues (as observed for bismuth thiols and xylitol), as well as the specificity of these agents for certain bacterial species and/or strains, may preclude their use as broad therapeutic strategies.

Recent studies have shown that the D-isomers of amino acids (D-AAs) can prevent and disperse biofilms formed by a diverse range of bacterial species, including *S. aureus* and *P. aeruginosa* [26, 27]. In contrast to other biofilm dispersal agents, D-AAs

promote the disassembly of biofilms through multiple mechanisms and have minimal cellular toxicity [28]. In this study, we investigated the ability of biofilm-dispersive polyurethane (PUR) scaffolds augmented with D-AAs to protect the scaffold from contamination from the contiguous wound environment and to reduce microbial burden within segmental defects *in vivo*. A mixture of D-AAs with optimal *in vitro* anti-biofilm activity was evaluated in a rat contaminated segmental defect model to test our hypothesis that local delivery of D-AAs would reduce the extent of infection within the defect. We also investigated the cytotoxicity of D-AAs on host mammalian cells to further evaluate their therapeutic potential.

Experimental

Materials

D- and L-isomers of amino acids (free base form), including alanine, isoleucine, leucine, methionine, phenylalanine, proline, tryptophan, tyrosine, and valine, were purchased from Sigma Aldrich (St. Louis, MO, USA). For use in bacterial and cell cultures, D-AA stocks were prepared by dissolving powders in 0.5 M HCl at concentrations between 150-200 mM. Stocks were then diluted into cation-adjusted Mueller Hinton (MHB-II) broth neutralized to pH 7.4 and stored at -80°C. For polyurethane scaffold synthesis, ε-caprolactone and stannous octoate were supplied by Sigma-Aldrich, and glycolide and D,L-lactide were purchased from Polysciences. An isocyanate-terminated prepolymer (22.7% NCO) comprising polyethylene glycol (PEG) end-capped with lysine triisocyanate (LTI) at a 2:1 molar ratio of LTI:PEG was supplied

by Medtronic (Memphis, TN, USA). Triethylene diamine was purchased from Evonik (TEGOAMIN 33, Hopewell, VA, USA).

Table 3.1. Description of *S. Aureus* strains investigated in this study

Strain	Strain characteristics	Biofilm formation[a]
UAMS-1	ATCC strain 49230. Methicillin-susceptible strain of the USA200 clonal group and a well-characterized osteomyelitis isolate	Strong
Xen36	Bioluminescent strain modified with the *luxABCDE* operon derived from a methicillin-sensitive clinical bacteremia isolate of *S. Aureus* subsp. Wright (ATCC 49525)	Weak
S.Aureus Clinical Isolate 1	Methicillin-resistant strain of the USA300 clonal group; wound isolate	Strong
S.Aureus Clinical Isolate 2	Methicillin-resistant strain of the USA300 clonal group; blood isolate	Weak
S.Aureus Clinical Isolate 3	Methicillin-resistant strain of the USA700 clonal group; cultured from deep wound	Strong
S.Aureus Clinical Isolate 4	Methicillin-resistant strain of the USA200 clonal group; cultured from deep wound	Strong

[a] Biofilm formation classification is based on previous studies comparing the biofilm forming capacity compared to a biofilm positive control, *S. epidermidis* ATCC 12228; Strong indicates biofilm ≥ *S. epidermidis* and weak biofilm former ≤ than the control as determined by microtiter plate assay. [14]

Bacterial strains and growth conditions

Four clinical isolates of *S. aureus* from a repository collected from patients admitted for treatment not related to research at the San Antonio Military Medical Center (SAMMC, Ft. Sam Houston, TX, USA) were used in this study [14]. Characteristics of the clinical isolates used in this study, which were previously confirmed to be positive for biofilm formation, are described in Table 3.1. UAMS-1 (ATCC strain 49230) is a methicillin-susceptible *S. aureus* strain of the USA200 clonal group and a well-characterized osteomyelitis isolate [29, 30]. Xen36 is a bioluminescent strain modified with the *luxABCDE* operon (Caliper Life Sciences Inc.) derived from a methicillin-sensitive

clinical bacteremia isolate of *S. aureus* subsp. Wright (ATCC 49525). All bacterial strains were cultured in tryptic soy broth (TSB) with agitation or on blood agar plates overnight at 37°C.

Biofilm formation in 96 well plates and dispersal assays

Biofilm formation was assessed under static conditions using polystyrene 96-well plates (Corning, Inc., Corning, NY, USA) as described previously [31, 32]. Briefly, overnight bacterial cultures were diluted to an OD_{600} of 0.1 in TSB (~10^7 CFU/mL), and 20 µL were added to individual wells filled with 180 µl of media and incubated at 37°C for 48 h. To assess the biofilm dispersal activity of D-AAs, the culture medium from biofilms was removed after 48 h and 200 µL fresh medium containing either an individual D-AA or an equimolar mixture of D-AAs (1:1:1: D-Met:D-Pro:D-Trp) were added at the indicated concentrations. We chose this particular combination because of the individual D-AAs broad activity in the *in vitro* evaluation against clinical isolates. After treatment with D-AA(s) for 24 h, plates were gently washed with 1X phosphate buffered saline (PBS) to remove unattached cells, stained with 0.1% (w/v) crystal violet (Sigma Aldrich, St. Louis, MI, USA) for 10 min, rinsed with PBS, and then solubilized with 80% (v/v) ethanol. Biofilm biomass was determined by measuring the absorbance of solubilized stain at 570 nm using a microtiter plate reader. For assays measuring the ability of D-AA to block biofilm formation, cells were grown under biofilm conditions as above in the presence of media containing D-AAs. Representative images of the plates of CV-stained biofilms following treatment with D-AA prior to solubilization were taken using a digital camera. All assays were repeated in triplicate with a minimum of four technical replicates.

Cell viability assays

Human dermal fibroblasts and osteoblasts (PromoCell, Heidelberg, Germany) were maintained in Dulbecco's Modified Eagle Medium (DMEM; Invitrogen, Grand Island, NY, USA) supplemented with 10% Fetal Bovine Serum (FBS) and 1X penicillin/streptomycin at 37°C in 5% CO_2. Prior to each assay, cells were seeded at 100% confluence in black-clear bottom 96-well plates. After 24 h cells were exposed to media containing D-AA (1 nM-50 mM) and incubated for 24 h. Following treatment, cells were washed, re-suspended in 100 µL of sterile saline, and assessed for viability using the CellTiter-Fluor Cell Viability Assay (Promega, Madison, WI, USA) following the manufacturer's instructions. Viability assays were performed in triplicate with a minimum of four replicates. Viability was reported as the percentage of viable cells relative to untreated controls.

Synthesis of polyurethane (PUR) scaffolds

Polyester triols with a molecular weight of 900 g mol^{-1} and a backbone comprising 60 wt% ε-caprolactone, 30% glycolide, and 10% lactide (T6C3G1L900) were synthesized using published techniques [33, 34]. Appropriate amounts of dried glycerol and ε-caprolactone, glycolide, DL-lactide, and stannous octoate (0.1 wt-%) were mixed in a 100-ml flask and heated under an argon atmosphere with mechanical stirring to 140^{o}C for 24 h. The polyester triol was subsequently washed with hexane and dried. The appropriate amounts of each D-AA (as received from the vendor) were pre-mixed. Next, the polyester triol, LTI-PEG prepolymer (excess isocyanate 15%), 2.0 parts per hundred parts polyol (pphp) tertiary catalyst, 3.0 pphp water, 4.0 pphp calcium stearate pore

opener, and the equimolar mixture of D-AAs (0 – 10 wt% total D-AA, 1:1:1 mixture of D-Met:D-Pro:D-Trp) were loaded into a 20 ml cup and mixed for 1 min using a Hauschild SpeedMixer DAC 150 FVZ-K vortex mixer (FlackTek). The reactive mixture was allowed to cure and foam at room temperature for 24 h. Cylindrical samples for *in vivo* testing (~3mm diameter x 6.5mm height) were cut using a coring tool and then sterilized by treating with ethylene oxide (EO).

Characterization of PUR scaffolds

Scaffold density was determined from mass and volume measurements of cured samples, from which the gravimetric porosity was calculated as the volume fraction of pores as described previously [35]. After curing, PUR sections were sputter-coated with gold and imaged using a Hitachi 4200 SEM. Pore size was determined from the SEM images using MetaMorph 7.1 Image Analysis software (MDS Analytical Technologies). Compressive mechanical properties of the scaffolds were measured using a TA Instruments Q800 Dynamic Mechanical Analyzer (DMA, New Castle, DE). Samples were tested after 24 h or 7 days of incubation in PBS. Stress–strain curves were generated by compressing wet cylindrical 6 mm x 6 mm samples at 37°C at a rate of 0.1 N/min until they reached 60% strain. The compressive modulus was determined from the slope of the initial linear region of each stress–strain curve. Since the scaffolds could not be compressed to failure due to their elasticity, the compressive stress was reported at 50% strain [36].

Scanning electron microscopy (SEM) analysis of biofilm formation on PUR scaffold.

SEM analysis was performed to examine the effect of augmentation with D-AAs on bacterial attachment and biofilm formation on the scaffold *in vitro* and *in vivo*. PUR scaffolds were fixed with 2% (w/v) glutaraldehyde, 2% (w/v) paraformaldehyde (PFA), 0.15M sodium cacodylate, 0.15% (w/v) alcian blue for 3 h, rinsed 3X with 0.15M sodium cacodylate buffer, and incubated in 1% (v/v) osmium tetroxide in sodium cacodylate for 1 h. Samples were dehydrated with a stepwise gradient of ethanol and then treated with hexamethyldisilizane prior to drying in a desiccator overnight. Samples were sputter-coated with gold palladium and viewed with a Hitachi 4200 or JEOL-6610 scanning electron microscope.

D-AA release kinetics

PUR scaffolds incorporating 10 wt% of a 1:1:1 mixture of D-Met:D-Pro:D-Trp were incubated in PBS for up to 8 weeks. The medium was sampled twice weekly and analyzed for D-AAs by HPLC using a system equipped with a Waters 1525 binary pump and a 2487 Dual-Absorbance Detector at 200 nm. Samples of released D-AAs were eluted through an Atlantis HILIC Silica column (5 µm particle size, 4.6 mm diameter x 250 mm length) using an isocratic mobile phase flowing at 1mL/min [37]. The mobile phase contained 2.5 mM potassium dihydrogen phosphate with pH = 2.85 (A) and Acetonitrile (B) at a ratio of A25:B75. The column oven temperature was maintained at 30°C. Sample concentration was determined in reference to an external standard curve using the Waters Breeze system. Standard curves were prepared in the following

concentration ranges: (1) 7.8 µg/mL to 1 mg/mL for D-Met and D-Pro and (2) 0.78 µg/mL to 100 µg/mL for D-Trp.

Table 3.2. Study design investigating the ability of biofilm-dispersive scaffolds to reduce bacterial contamination *in vitro*. Scaffolds were contaminated with 10^7 CFU/ml *S. aureus* for 2 h and outcomes were assessed after 24 h incubation time in PBS.

Group	Description
PUR (-)	Sterile blank PUR scaffold with no D-AAs
PUR	Contaminated blank PUR scaffold with no D-AAs
PUR + D-AA-0.1	Contaminated PUR scaffold augmented with 0.1% D-AAs
PUR + D-AA-1	Contaminated PUR scaffold augmented with 1% D-AAs
PUR + D-AA-5	Contaminated PUR scaffold augmented with 5% D-AAs
PUR + D-AA-10	Contaminated PUR scaffold augmented with 10% D-AAs

Bacterial adhesion to PUR scaffolds

Bacterial adherence and biofilm formation on scaffolds with or without D-AAs was evaluated as described previously [38]. The study design is listed in Table 3.2. Sterile blank PUR scaffolds with no D-AAs were utilized as a negative control (PUR (-)). Blank scaffolds (denoted as PUR) or scaffolds augmented with an equimolar mixture of D-AAs (denoted as PUR+D-AA-x, where x = 0.1, 1.0, 5.0, or 10 wt% 1:1:1 mixture of D-Met:D-Pro:D-Trp) were placed into 24-well polystyrene plates containing sterile PBS for 2 h at room temperature, which allowed the scaffolds to become saturated. Samples were then transferred into a bacterial suspension of UAMS-1 (10^7 CFU/mL) in PBS and exposed for an additional 2 h at 37°C with agitation in 24-well plates. Following exposure, scaffolds were rinsed with PBS to remove non-attached bacteria and incubated overnight in PBS at 37°C to allow adequate time for attached bacteria to develop biofilms. Following incubation, scaffolds were then placed in 1 mL PBS and sonicated for 10 min

using a low-power bath sonicator. Bacterial CFUs per gram of scaffold were determined by plating serial dilutions on blood agar plates. Bacterial attachment and biofilm formation on scaffolds following incubation was also evaluated by SEM analysis. The sample size was 3 with duplicate runs.

Table 3.3. *In vivo* study design investigating the ability of biofilm-dispersive scaffolds to reduce contamination in 6-mm segmental defects in rat femora contaminated with 10^2 CFU of *S.aureus* UAMS-1 or Xen36. Outcomes were assessed at 2 weeks.

Group	Description	No infection	UAMS-1	Xen36
PUR (-)	Blank PUR scaffold in a sterile defect	10	0	0
Empty	Contaminated defect not grafted with a scaffold	0	10	10
PUR	Blank PUR scaffold in a contaminated defect	0	10	10
PUR + D-AA-1	PUR scaffold with 1% D-AAs in a contaminated defect	0	10	0
PUR + D-AA-5	PUR scaffold with 5% D-AAs in a contaminated defect	0	10	0
PUR + D-AA-10	PUR scaffold with 10% D-AAs in a contaminated defect	0	10	10

Rat femoral 6-mm segmental defect model

This study was conducted in compliance with the Animal Welfare Act, the implementing Animal Welfare Regulations, and the principles of the Guide for the Care and Use of Laboratory Animals. A previously characterized contaminated critical size defect in rat (Sprague–Dawley; 373 ± 4.15 g) femurs was utilized as the *in vivo* model of infection [39-41]. The study design is listed in Table 3.3. Briefly**,** a 6-mm segmental defect was created using a small reciprocating saw blade (MicroAire 1025, MicroAire, Charlottesville, VA), stabilized with a polyacetyl plate (length 25 mm, width 4 mm and height 4 mm) and fixed to the surface of the femur using threaded K-wires. Blank PUR scaffolds implanted in a sterile defect were utilized as a negative control (PUR (-)) and for SEM analysis to distinguish between host cellular and bacterial infiltration of the

scaffolds. The defects in all other animals were then implanted with 30 mg of type I bovine collagen (Stryker Biotech, Hopkinton, MA, USA) wetted with 10^2 CFU of *S. aureus* strain Xenogen-36 (Xen36 - Caliper Life Science, Hopkinton, MA) or *S. aureus* strain UAMS-1. The Xen36 strain is a weak biofilm producer and was used as a negative control. Six hours after contamination, the wounds were opened, debrided, and irrigated with saline. PUR or PUR+D-AA-x (1.0, 5.0, or 10 wt% 1:1:1 mixture of D-Met:D-Pro:D-Trp) scaffolds were then implanted into the wounds. Since cefazolin is recommended for primary prevention of infections associated with open fractures [42], rats received systemic antimicrobial treatment with cefazolin (5 mg/kg) administered subcutaneously for 3-days post-surgery. Two weeks following surgery, the rats were euthanized and the femurs were weighed, snap-frozen in liquid nitrogen, ground to a fine powder, and re-suspended in saline. CFUs (expressed as $\log_{10}$ CFU/g tissue) were determined by plating serial dilutions onto blood agar plates and incubated at 37°C for 24 h. Scaffolds from PUR (-), PUR and PUR+D-AA-10 groups were evaluated by SEM.

Statistical analysis

For *in vitro* comparisons of groups, statistical analyses were performed using a One-Way ANOVA with a Bonferroni test to determine statistical differences between groups. Non-parametric statistical methods were used to analyze the results from the *in vivo* study. Contingency tables analyzed with a Fisher's exact test were used to compare the number of infected and non-infected samples between groups. The CFU counts of the different treatment groups were compared using the Kruskal-Wallis test followed by a Dunn's multiple comparison test to identify differences between groups. Non-parametric

analyses were performed using GraphPad InStat Version 3.0 (GraphPad software, San Diego California, USA). $P<0.05$ was considered statistically significant.

Results

D-amino acids activity in vitro

To initially evaluate the feasibility of local delivery of D-AAs as a strategy for biofilm-dispersive scaffolds, the activity of D-AAs on biofilm dispersal and prevention was tested *in vitro* on a panel of four clinical isolates (described in detail in Table 3.1) of *S. aureus*. Pre-screening of eight individual D-AAs identified four amino acids, D-Met, D-Phe, D-Pro, and D-Trp, as highly effective at dispersing biofilms formed by the four clinical isolates (Figure 3.1), whereas the other four D-AAs had minimal effects. D-AAs dispersed biofilms in a dose-responsive manner and were most effective at concentrations ≥5mM. Thus, 5mM was chosen as the concentration for future studies. The efficacy of D-AAs varied between different bacterial strains, although for each strain tested more than one of the four D-AAs was effective at dispersing biofilms.

Consistent with previous studies, the anti-biofilm effect was isomer-specific, as no dispersal activity was observed with L-isomers of D-AAs (data not shown). When tested against the panel of clinical isolates of methicillin-resistant *S. aureus* (n=5), D-Phe, D-Met, D-Trp, and D-Pro were effective at dispersing established biofilms *in vitro* as determined by the measurement of the biofilm biomass (Figure 3.2A, C).

In addition to dispersing established biofilms, the four identified D-AAs also significantly blocked formation of biofilms by the clinical strains when bacteria were cultured in the presence of D-AAs (Figure 3.2B).

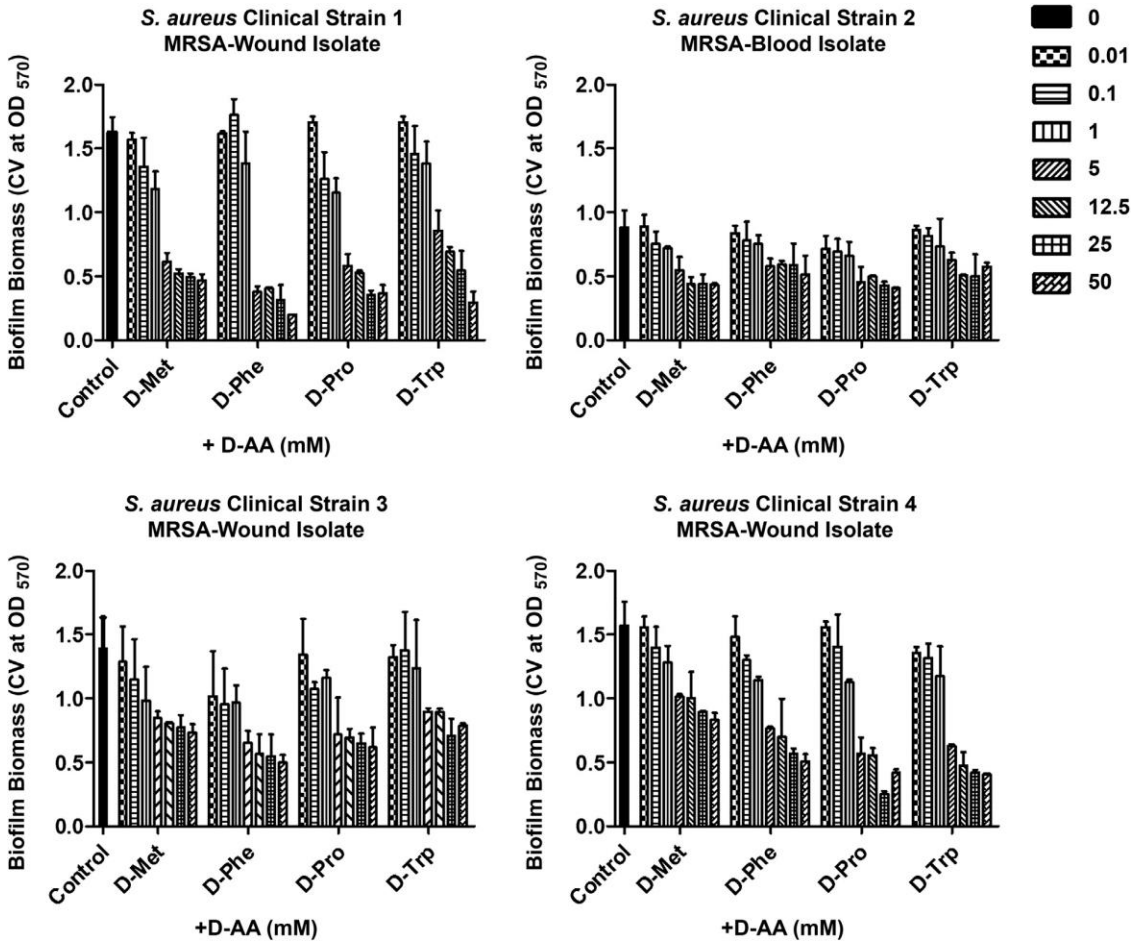

Figure 3.1. Screening of D-amino acids against clinical strains of *S.* aureus. Screening of D-Met, D-Phe, D-Pro, and D-TRP at concentrations ranging from 0.001 mM to 50 mM against preformed biofilms of four representative clinical isolates (described in Table 3.1). Biofilm dispersal was assessed by quantitating the remaining biofilm biomass following treatement with D-AAs by measuring the absorbance of solubilized CV from the stained biofilms at 570 nm.

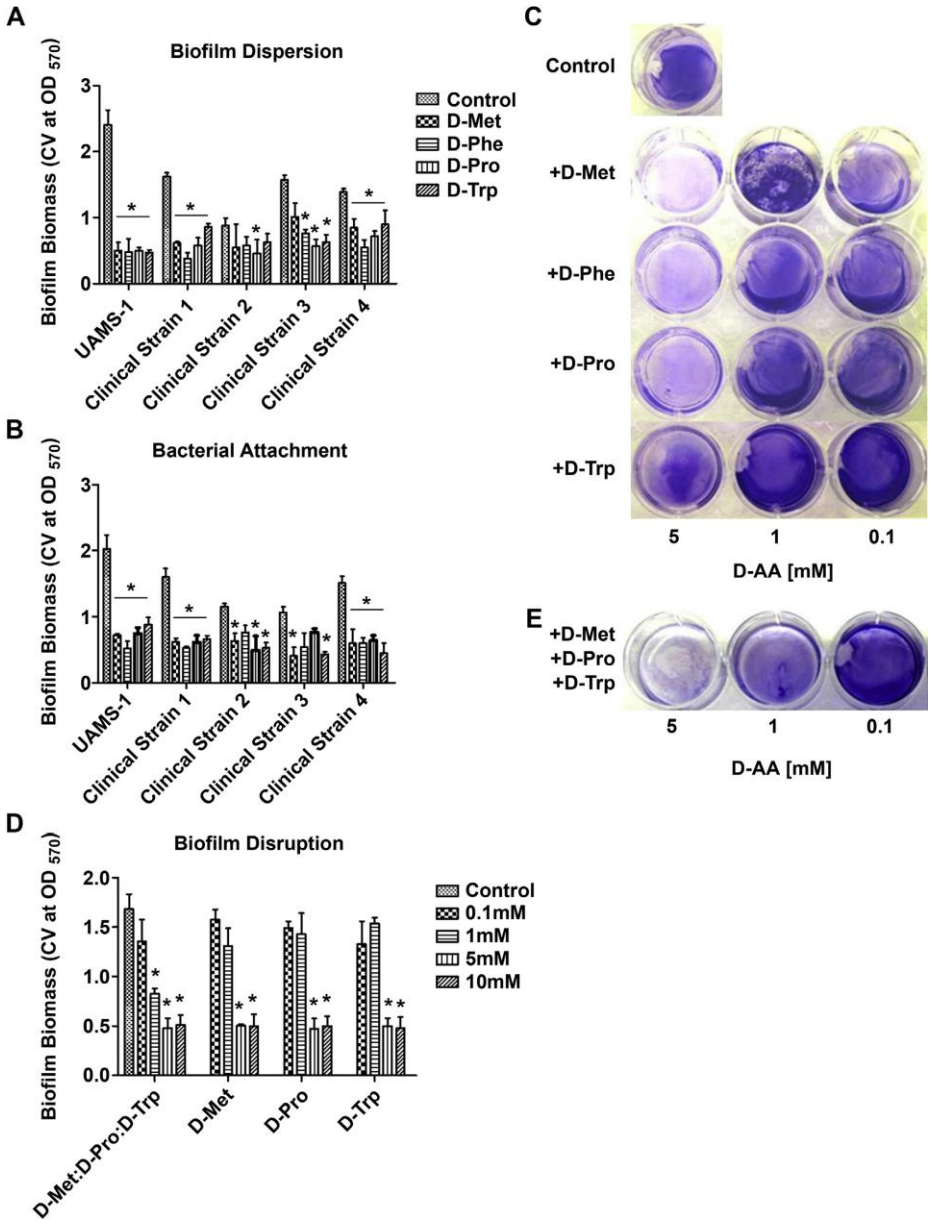

Figure 3.2. D-amino acids disperse biofilms and prevent biofilm formation in clinical isolates of S. aureus. (A) Dispersion of pre-formed biofilms: Biofilm biomass (OD570) following treatment of pre-formed biofilms of four representative clinical isolates of S. aureus (described in Table 1) with 5 mM of each individual D-AA for 24 h at 37^{o}C. (B) Prevention of biofilm formation: Biofilm biomass for the same clinical isolates as above following co-incubation of the bacteria with 5 mM of D-AA. (C) Representative images of CV-stained biofilms from S. aureus UAMS-1 (bone isolate) following overnight treatment with individual D-AAs. (D) An equimolar mixture ofD AAs is more effective at dispersing biofilms than individual D-AAs. Biofilm biomass (OD570) following treatment of pre-formed biofilms of S. aureus UAMS-1 with an equimolar mixture (0.1 e5 mM total concentration) of D-Met, D-Pro, and D-Trp for 24 h at 37^{o}C. (E) Representative images of CV-stained biofilms from S. aureus UAMS-1 following overnight treatment with the mixture of D-AAs (0.1 - 5mM). Averages are representative of three independent experiments, error bars signify standard deviation. Statistical analysis was performed using a One-Way ANOVA followed by a Bonferroni test to identify differences between groups; $p < 0.05$ was considered to be statistically different from the control group.

When combined as an equimolar mixture of D-Met, D-Pro, and D-Trp, biofilm-dispersive activity was enhanced (Figure 3.2D-E), as suggested by the decrease in biofilm biomass observed at D-AA concentrations <5mM **(**which was not observed for the individual D-AAs). Importantly, D-AAs had no significant effect on the growth of the bacteria, indicating that biofilm dispersal was a specific property and not the result of growth inhibition (data not shown).

Cytotoxicity of D-AAs in vitro

While Figures 3.1 and 3.2 show that D-AAs both block biofilm formation as well as disperse established biofilms, the toxicity of D-AAs toward mammalian cells have not been extensively investigated. Thus, we evaluated the cytotoxicity of D-AAs *in vitro* using human osteoblasts and dermal fibroblasts that are relevant to bone and wound healing, respectively. Osteoblasts and fibroblasts exposed to up to 50 mM of D-Met, D-Phe, D-Pro showed >70% viability after 24 h. Cytotoxicity was observed in mammalian cells exposed to D-Trp at concentrations exceeding 12.5 mM (~60% viability) (Figure 3.3). Importantly, these studies indicate that the D-AAs have minimal cytotoxic effects on mammalian cells at concentrations observed to be effective for preventing and disrupting biofilms *in vitro*.

Scaffold characteristics and in vitro release

Previous experiments investigating the feasibility of biofilm dispersion by exogenous D-AAs have focused on 2D surfaces. As an initial step toward the creation of a biofilm-dispersive scaffold, two-component PUR scaffolds prepared by reactive liquid

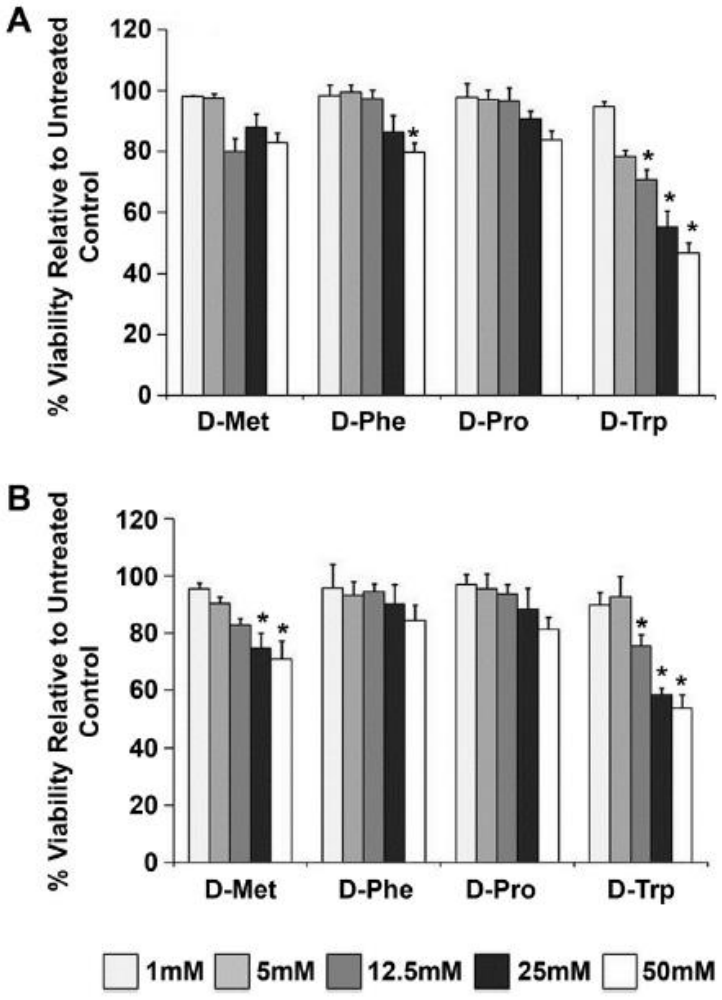

Figure 3.3. D-amino acids have limited cytotoxicity *in vitro*. Viability of human osteoblasts (A) and dermal fibroblasts (B) exposed to media supplemented with D-Met, D-Phe, DPro, and D-Trp (1-50 mM) for 24 h at 37^{o}C in 5% CO_2. Cell viability was determined using the Cell-Titer Flour assay by measuring fluorescence 405ex/505em and is represented as a percentage viability relative to non-treated controls. Values represent the average of three independent experiments, and error bars indicate standard deviation. Statistical analysis was performed using a One-Way ANOVA followed by a Bonferroni test to identify differences between groups; $p < 0.05$ was considered to be statistically different from controls (*)

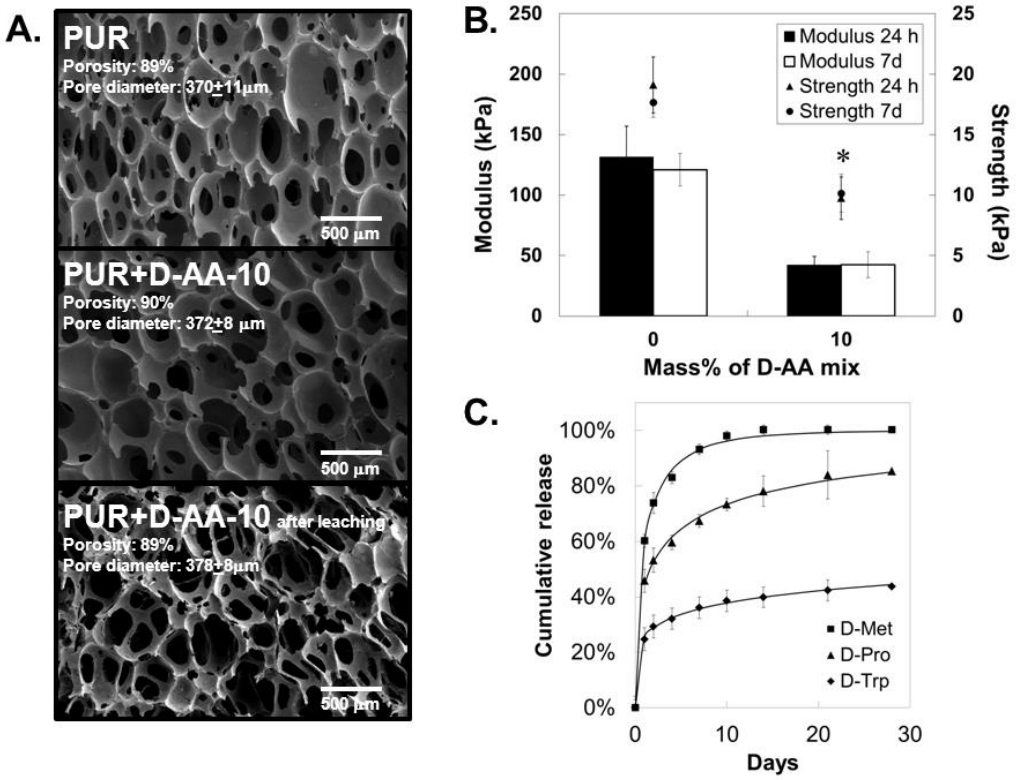

Figure 3.4. Characterization of PUR + D-AA scaffolds. (A) SEM images of PUR, PUR + D-AA-10 (before leaching), and PUR + D-AA-10 (after 24 h leaching) scaffolds. Porosity and pore size remain relatively constant with increasing wt% D-AA. (B) Compressive mechanical properties of dry and wet (soaked in PBS for 24 h) PUR and PUR + D-AA-10 samples; $p < 0.05$ was considered to be statistically different from controls (*). (C) Cumulative % release of D-Pro, D-Met, and D-Trp versus time (symbols). The solid lines represent the fit to the Weibull model.

molding were augmented with a mixture of D-AAs (1:1:1 wt% D-Met:D-Pro:D-Trp) as a labile powder. Prior to *in vivo* testing, the PUR+D-AA scaffolds were characterized *in vitro*.

Scaffolds containing 0 (PUR) or 10 wt% D-AA mixture (PUR+D-AA-10) had similar values of density, porosity, and pore size before and after leaching overnight in PBS. Representative SEM images of the PUR and PUR+D-AA-10 scaffolds show inter-connected pores and a mean pore diameter ranging from 370 to 378 μm (Figure 3.4A). While the addition of 10% D-AA mix to the PUR scaffolds did not affect the porosity, the wet mechanical properties were significantly reduced compared to the empty scaffold

(Figure 3.4B). There were no differences in the properties of the scaffolds incubated in PBS for 24 hours or 7 days.

The release kinetics of D-Pro, D-Met, and D-Trp were characterized by an initial burst followed by a sustained release for up to 21 days (Figure 3.4C). D-Met released the fastest, characterized by a 60% burst on day 1 and nearly 100% release by day 14. The release of D-Pro was somewhat slower (45% burst and 85% release by day 28), while D-Trp released slowly, with only a 25% burst and 44% release after 28 days. The Weibull equation has been used to identify the mechanism controlling drug release from polymeric materials [39, 43]:

$$\frac{M_t}{M_\infty} = 1 - exp(-at^b) \quad (3.1)$$

where M_t corresponds to the mass of drug released in time t, M_∞ is the mass of drug released at infinite time (which corresponds to the initial loading of drug), and a and b are constants. When $b<0.75$, Fickian diffusion controls drug release, while a more complex mechanism involving both diffusion and swelling controls release when $b>0.75$ [44]. The D-AA release data were fit to the Weibull model and the values of the b parameter for D-Met, D-Pro, and D-Trp were calculated as 0.56, 0.35, and 0.21 respectively, suggesting that the release of each D-AA from the scaffolds was diffusion-controlled.

Effects of biofilm-dispersive scaffolds on bacterial contamination in vitro

The effect of local delivery of D-AAs from biofilm-dispersive scaffolds on bacterial contamination was evaluated *in vitro* prior to *in vivo* testing. Incorporation of D-AA into PUR scaffolds at concentrations ≥ 1 wt% D-AA significantly reduced the amount of attached bacteria and biofilm formation on the surface compared to the

scaffolds without D-AA. PUR scaffolds with 1, 5, and 10 wt% D-AA had a ≥ 4-log reduction in the number of bacteria (Figure 3.5A), while PUR scaffolds with 0.1% showed a more moderate (~1-log reduction) but significant reduction in bacteria attached to the scaffold surface. Consistent with the bacterial counts, SEM images of PUR scaffolds augmented with D-AA also demonstrated the dramatic reduction in surface-attached bacteria within biofilms on scaffolds augmented with the D-AA mixture (Figure 3.5B). However, as indicated by the bacterial counts, PUR scaffolds without D-AA as well PUR scaffolds with 0.1% D-AA had extensive bacterial colonization and the presence of biofilms on the surface.

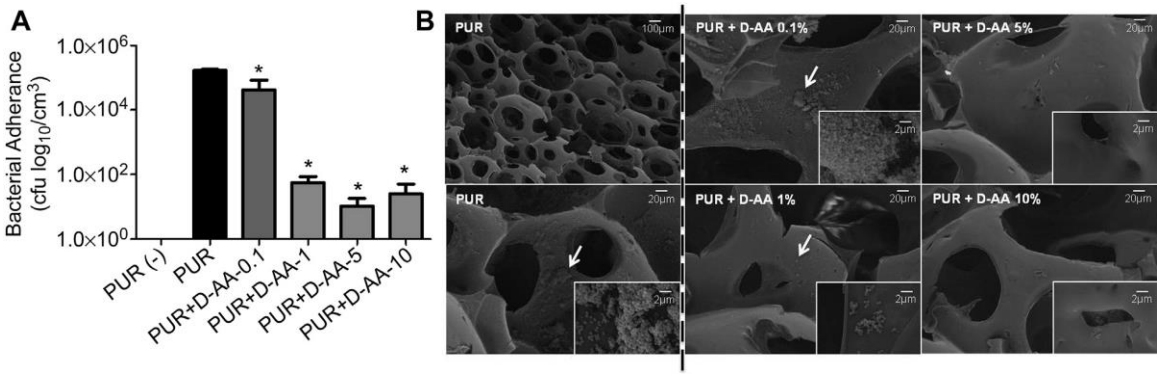

Figure 3.5. Augmentation of PUR scaffolds with an equimolar mixture of D-AAs reduces bacterial adherence in vitro. (A) $\log_{10}$ CFU/cm^3 UAMS-1 bacteria adhered to PUR scaffolds augmented with D-AAs after 24 h incubation time decrease ~4 orders of magnitude for >1 wt% equimolar D-AA mixture. The PUR negative control (PUR (-)) incubated in sterile medium shows no contamination. (B) SEM images of PUR + D-AA scaffolds exhibiting decreased biofilm with increasing D-AA concentration.

Effects of biofilm-dispersive scaffolds in vivo

For the *in vivo* studies, 6-mm segmental defects in rats were contaminated with 10^2 CFUs *S. aureus* XEN-36, a bioluminescent, septicemic isolate forming weak biofilms, or 10^2 CFUs *S. aureus* UAMS-1, an osteomyelitis isolate and a strong biofilm producer. Treatment of femoral UAMS-1-contaminated defects with PUR+D-AA-5 or PUR+D-

AA-10 significantly reduced bacterial contamination within the homogenized bone ($p<0.05$) (Figure 3.6A), while lower doses did not reduce contamination compared to the empty (untreated) defect control. Similarly, PUR+D-AA-5 and PUR+D-AA-10 reduced the number of contaminated samples compared to the PUR scaffold (Figure 3.6B), although the difference did not reach statistical significance ($p=0.087$).

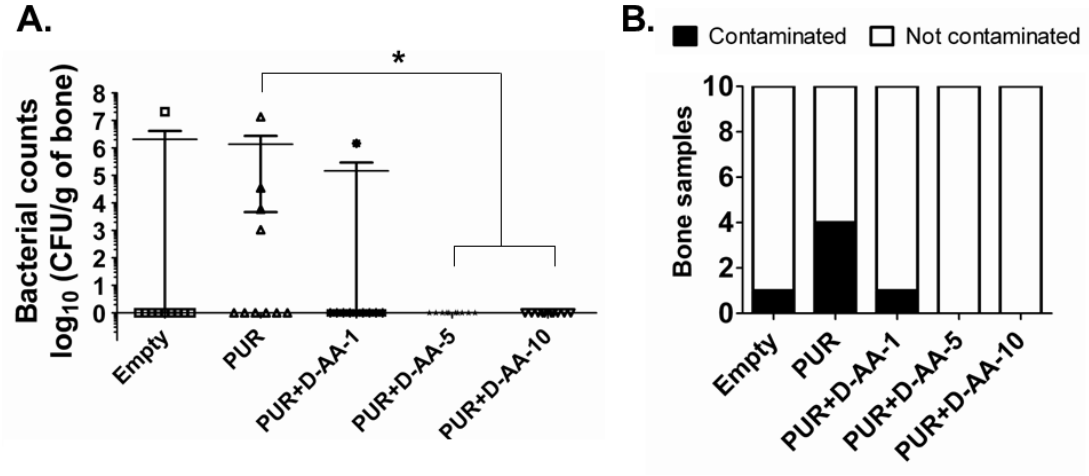

Figure 3.6. Augmentation of PUR scaffolds with an equimolar mixture ofD-AAs reduces bacterial contamination of segmental defects contaminated with 102 CFU *S. aureus* UAMS-1 *in vivo*. (A) Bacterial counts (log_{10} CFU/g) in homogenized bone from segmental defects of rats contaminated with 102 CFU of S. aureus UAMS-1 followed by implantation of no scaffold (Empty, n ¼ 10), PUR blank scaffold (PUR, n ¼ 10), or PUR scaffold + equimolar D-AA mixture (n ¼ 10 per group) for two weeks post-wounding. Bars represent the mean value and error bars are the standard error of the mean. Statistical analysis was performed using a Kruskal Wallis test followed by a Dunn's multiple comparisons test to identify differences between groups (* significantly different than PUR, $p < 0.05$) (B) Distribution of contaminated and non-contaminated bone samples from the segmental defects. Fewer samples were contaminated when the PUR scaffold was augmented with D-AA content >5 wt%, although the differences were not statistically significant (p ¼ 0.087). Statistical analysis was performed using contingency tables analyzed with a Fisher exact test comparing the number of contaminated bone samples for each PUR + D-AA treatment group to the PUR blank scaffold.

Consistent with these observations, SEM analysis of scaffolds removed from rats following infection also showed a dramatic reduction of biofilm attached to the surface of the scaffolds (Figure 3.7). Blank PUR scaffolds implanted in contaminated defects

exhibited extensive bacterial adhesion and biofilm formation on the majority of the surface, whereas PUR+D-AA-10 showed a substantial reduction in the amount of attached bacteria. In contrast, PUR+D-AA scaffolds implanted in defects contaminated with 10^2 CFUs Xen-36 strain, an extremely weak biofilm producer, did not significantly reduce bacterial contamination or the number of contaminated samples compared to the empty defect (data not shown).

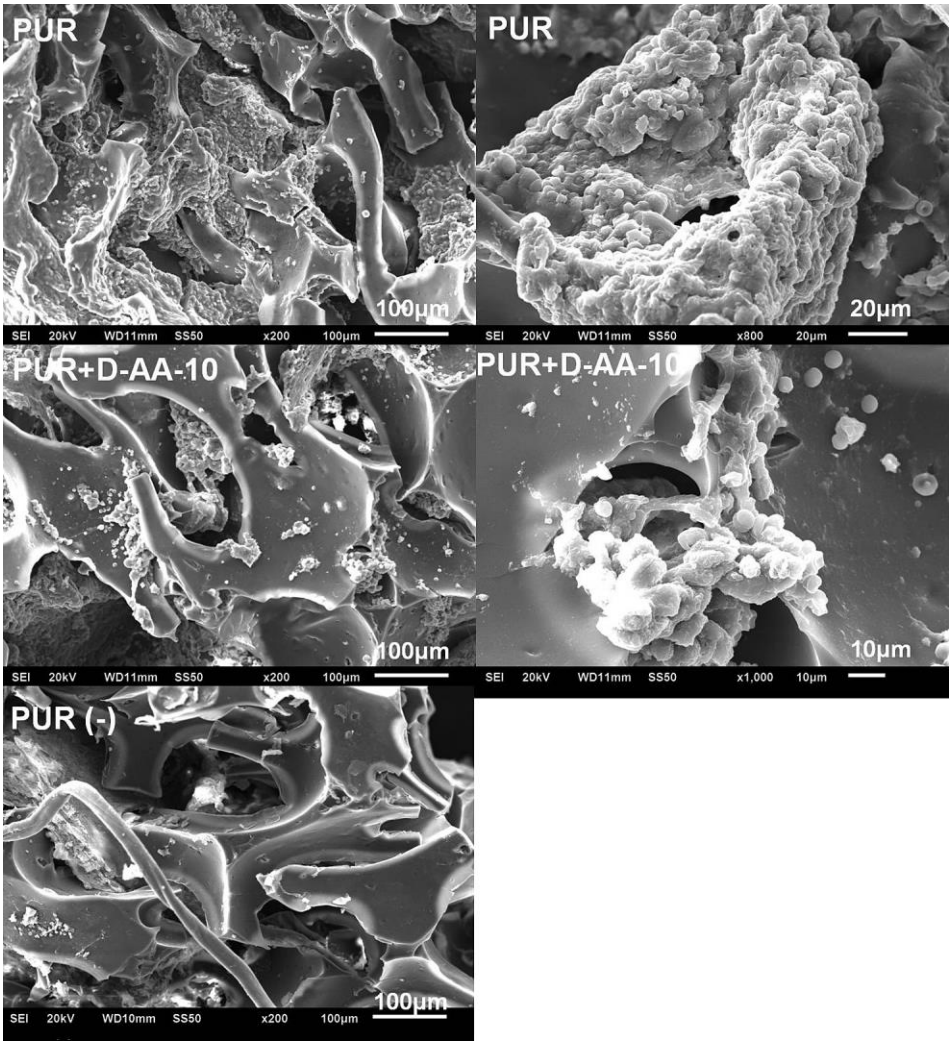

Figure 3.7. Low- and high-magnification SEM images of biofilms on PUR and PUR + D-AA-10 scaffolds implanted in contaminated femoral segmental defects in rats for 2 weeks show reduced bacterial adhesion for the scaffold augmented with 10 wt% of the equimolar mixture of D-AAs. PUR scaffolds implanted in sterile defects (PUR (-) negative control) show minimal bacterial adhesion

Discussion

Despite meticulous clinical management including surgical debridement and the use of systemic antibiotics, contamination rates of open fractures continue to be a significant cause of non-osseous union, potentially leading to extremity amputation. Local delivery of antibiotics from bone grafts has been investigated as a strategy to reduce bacterial contamination and promote osseous union [39, 45-52]. However, the efficacy of antibiotics against the surface-attached communities of bacteria known as biofilms, which are considered a major virulence factor in chronic disease [6, 4], is limited due to the slow metabolic and growth rates of bacteria within the biofilm [53]. Furthermore, the avascular bone graft may itself serve as a substrate for bacterial colonization and a nidus for recurrent infections [54]. Finally, a small population (i.e., 0.1–10%) of "persister cells" survives antimicrobial therapy and rapidly grows after the cessation of antibiotic therapy, potentially resulting in recurrent infections [55]. Recent studies have highlighted the potential of bacterial signaling molecules that trigger biofilm dispersal, such as bismuth thiols [56, 20], quorum-sensing inhibitors and analogs [57], and D-AAs [27, 26], as therapeutic agents for treatment of chronic infections. In this study, we have shown that local delivery of D-AAs from PUR scaffolds inhibits biofilm formation by clinical isolates of *S. aureus* both *in vitro* and *in vivo*. Dose-response experiments showed that D-AAs inhibited biofilm formation and dispersed existing biofilms at concentrations ≥5 mM *in vitro*. A PUR scaffold augmented with ≥5 wt% D-AAs significantly reduced bacterial contamination and biofilm formation by the strong biofilm-producing strain *S. aureus* UAMS-1 compared to the control scaffold with no D-AAs in a contaminated segmental defect in rats. Interestingly, with careful scanning of the scaffolds with D-AAs, small

colonies of bacteria within a biofilm could be found. Conversely, biofilm formation could easily be found on the scaffolds without D-AAs that were retrieved from contaminated defects. Almost the entire scaffold was covered with biofilm, and the colonies were very robust. Furthermore, D-AAs exhibited relatively low cytotoxicity to mammalian cells at doses effective at inhibiting biofilm formation.

Considering the many human chronic diseases involving biofilms, the use of biofilm dispersal agents has gained considerable interest for the treatment of biofilm-mediated infections. A previous study has reported that D-Phe, D-Pro, and D-Tyr prevent biofilm formation and trigger biofilm dispersion in *S. aureus* WT strain SC01 at concentrations as low as 0.5 mM *in vitro* [27]. In this study, we have shown that D-Met, D-Phe, D-Pro, and D-Trp inhibit biofilm formation and disperse established biofilms of clinical strains of *S. aureus* at concentrations ≥5 mM (Figure 3.1), which is ~10 times greater than the previously reported dose. The activity of individual D-AAs varied in previous studies, with D-Tyr requiring the lowest concentration (3 μM), and D-Met (2 mM), D-Trp (5 mM) and D-Leu (8.5 mM) requiring higher concentrations for anti-biofilm activity against *Bacillus subtilis* strain NCIB 3610 and for *S. aureus* strain SC01 [26]. Differences between bacterial species as well as strain heterogeneity are likely contributing factors to the observed discrepancies between studies. Importantly, from our studies we identified concentrations having effective biofilm-dispersive activity active against a number of clinical strains. Consistent with a previous study showing that the equimolar mixture of D-Phe:D-Pro:D-Tyr lowered the effective dose [27], the data in Figure 3.2D-E show that an equimolar mixture of D-Met:D-Pro:D-Trp shifted the dose-response curve toward lower doses compared to the individual D-AAs. Other than for *B.*

subtilis, the mechanisms by which D-AAs disrupt biofilms are not known. However, the enhanced anti-biofilm activity of the D-AA mixture is suggestive of multiple mechanisms acting on the bacteria, which warrants further investigation.

In order to be useful as a clinical therapy, D-AAs must exhibit minimal cytotoxicity at concentrations that are effective at dispersing biofilms. As shown in Figure 3.3, osteoblasts and fibroblasts treated with D-Phe, D-Pro, or D-Met for 24 h exhibited >70% viability at concentrations ≤50 mM, while D-Trp exhibited cytotoxic effects (i.e., <70% viability) at concentrations >12.5 mM. While these data suggest that individual D-AAs are non-cytotoxic to mammalian cells at concentrations efficacious against biofilms, they contrast with a previous study reporting cytotoxicity of D-Phe, D-Met, and D-Trp toward Chinese Hamster Ovary (CHO) and HeLa cells at concentrations ≥10 mM [28]. The discrepancies in D-AA toxicities between the present study and that reported previously may be attributed to differences among cell lines. In another study, D-Phe and D-Trp reportedly elicited a chemotactic response in human neutrophils via activation of GPR109B [58]. Additional *in vivo* studies investigating the biocompatibility of D-AAs in sterile defects are needed to further assess their safety, and these studies are currently ongoing in our laboratories.

As a first step toward the development of a biofilm-dispersive bone graft for clinical applications, we evaluated the effects of local delivery of D-AAs from biodegradable PUR scaffolds on infection in a contaminated segmental defect model in rats. The scaffold investigated in this study has a half-life of 14 weeks *in vitro* [36], and degrades to non-cytotoxic breakdown products such as lysine and α-hydroxy acids [59]. PUR scaffolds are effective delivery vehicles for sustained released of biologics, such as

antibiotics [60, 39] and recombinant human bone morphogenic protein-2 (rhBMP-2) [61, 44, 40]. Furthermore, PUR scaffolds are injectable [62, 63] and thus can be delivered using minimally invasive surgical techniques. As shown in Figure 3.4, while D-AAs had minimal effects on the porosity and pore size, PUR+D-AA scaffolds exhibited approximately 2-3-fold decreases in both Young's modulus and compressive stress at 50% strain. A previous study reported that PUR scaffolds augmented with 8 wt% tobramycin had significantly higher porosity and lower modulus than blank PUR scaffolds after 24 h incubation time in PBS, which was attributed to rapid leaching of tobramycin and consequent formation of new pores [60]. Surprisingly, in the present study the modulus decreased significantly even after 24 h, at which time only a fraction of the D-AAs had released, and did not decrease further for up to 7 days of incubation. These observations suggest that the decrease in modulus with addition of D-AAs results from defects in the pore walls of the scaffold caused by the presence of the particles rather than from the formation of new pores due to leaching of the D-AAs.

As shown in Figure 3.4C, PUR+D-AA scaffolds supported diffusion-controlled sustained release of the biologically active drug for up to 4 weeks, which is consistent with previous studies reporting diffusion-controlled release of active antibiotics [60, 39], recombinant human growth factors [64, 44], and siRNA nanoparticles [65]. At each time point, the order of cumulative release was D-Met>D-Pro>D-Trp, while the order of solubility was D-Pro>>D-Met>D-Trp [66]. At 4 weeks, >85% of D-Pro and D-Met had been released and <10% of the scaffold had degraded [36], which is consistent with the notion that the D-AA release was diffusion-controlled at early time points. However, <40% of the D-Trp had been released by 4 weeks, suggesting that degradation of the scaffold may control D-

Trp release kinetics at later (>4 weeks) time points. Since the free base form of each D-AA was used in this study, the release kinetics could be increased by using the more soluble hydrochloride as reported previously for vancomycin [39]. While antibiotic therapy for up to 8 weeks is recommended for effective treatment of MRSA osteomyelitis [67], the optimal release profile for D-AAs is unknown and thus merits further investigation.

In a proof-of-concept study, we evaluated the ability of biofilm-dispersive PUR scaffolds augmented with D-AAs to prevent biofilm formation and reduce CFUs in a contaminated rat segmental defect model. Several recent studies have evaluated the effects of local delivery of antibiotics on infection using an acute contamination model, in which the bone graft was placed immediately after contamination of the defect with bacteria [68, 69]. However, preclinical models with an established chronic infection [40, 70] represent a more rigorous test for the efficacy of biofilm-dispersive grafts, since they ensure that the bacteria are able to adhere to the surface of the wound and form biofilms [71]. In the present study, rat segmental defects were contaminated with 10^2 CFU for 6 h prior to implantation of the PUR+D-AA scaffolds. Augmentation of the scaffolds with ≥5 wt% D-AAs significantly reduced bacterial contamination within the segmental defects treated with UAMS-1, an osteomyelitis strain. In contrast, the D-AAs had no significant effect on defects contaminated with Xen36, which is a weak biofilm producer [14]. These observations are consistent with the notion that D-AAs reduce contamination in the defect by preventing the formation of and/or dispersing biofilms, thus limiting the application of D-AAs as a treatment for biofilm infections. However, numerous studies indicate that the majority of staphylococcal clinical isolates *in vitro* as well as those found in human tissues are strong biofilm producers.

Because D-AAs are not bactericidal, they are anticipated to be most effective as an adjuvant therapy to conventional treatment with systemic antibiotics. In this study, rats were treated with cefazolin (5 mg/kg) administered subcutaneously for 3-days post surgery to simulate the clinical scenario [42]. Despite the presence of systemic antibiotics, one of the untreated rats developed an infection, which increased to four rats when treated with blank PUR scaffolds. This suggests that placement of an avascular graft into an open fracture potentiates infection. Treatment with PUR+D-AA-5 or PUR+D-AA-10 scaffolds reduced the number of infected rats to zero, which underscores the potential clinical utility of biofilm-dispersive bone grafts as an adjuvant therapy to systemic antibiotics. The broad spectrum of D-AAs will allow their use for preventing infection without the need of knowing the nature of contaminating bacteria. For chronic infections such as MRSA osteomyelitis, treatment with systemic antibiotics is recommended for a minimum of 8 weeks [67]. Importantly, for most patients, the extended duration of systemic treatment is associated with a number of risks to the patient's health, including renal toxicity, and is an economic burden to the patient and healthcare system. Our results suggest that local delivery of a biofilm dispersion agent alone or co-delivered with antimicrobial agents represents a potentially efficacious therapy for treatment of chronic infections, which, when combined with the standard systemic antimicrobial treatment may reduce the time of treatment and resulting complications and cost for chronic orthopedic infections.

Conclusions

The ability of bacteria to establish biofilms substantially hinders the treatment of orthopedic infections and is implicated as a significant contributing factor in the sequelae associated with open fractures. Biofilm-dispersive scaffolds augmented with D-AAs can be used as a novel therapeutic strategy to reduce microbial burden within wounds and improve healing outcomes.

References

1 D. P. Lew, and F. A. Waldvogel, 'Osteomyelitis', *Lancet,* 364 (2004), 369-79.

2 L. O. Conterno, and C. R. da Silva Filho, 'Antibiotics for Treating Chronic Osteomyelitis in Adults', *Cochrane Database Syst Rev* (2009), CD004439.

3 J. Huh, D. J. Stinner, T. C. Burns, and J. R. Hsu, 'Infectious Complications and Soft Tissue Injury Contribute to Late Amputation after Severe Lower Extremity Trauma', *J Trauma,* 71 (2011), S47-51.

4 J. W. Costerton, 'Biofilm Theory Can Guide the Treatment of Device-Related Orthopaedic Infections', *Clin Orthop Relat Res* (2005), 7-11.

5 J. W. Costerton, P. S. Stewart, and E. P. Greenberg, 'Bacterial Biofilms: A Common Cause of Persistent Infections', *Science,* 284 (1999), 1318-22.

6 R. A. Brady, J. G. Leid, J. H. Calhoun, J. W. Costerton, and M. E. Shirtliff, 'Osteomyelitis and the Role of Biofilms in Chronic Infection', *FEMS Immunol Med Microbiol,* 52 (2008), 13-22.

7 T. J. Marrie, and J. W. Costerton, 'Mode of Growth of Bacterial Pathogens in Chronic Polymicrobial Human Osteomyelitis', *J Clin Microbiol,* 22 (1985), 924-33.

8 A. G. Gristina, M. Oga, L. X. Webb, and C. D. Hobgood, 'Adherent Bacterial Colonization in the Pathogenesis of Osteomyelitis', *Science,* 228 (1985), 990-3.

9 J. W. Costerton, 'Introduction to Biofilm', *Int J Antimicrob Agents,* 11 (1999), 217-21; discussion 37-9.

10 J. L. del Pozo, and R. Patel, 'The Challenge of Treating Biofilm-Associated Bacterial Infections', *Clin Pharmacol Ther,* 82 (2007), 204-9.

11 L. Hall-Stoodley, J. W. Costerton, and P. Stoodley, 'Bacterial Biofilms: From the Natural Environment to Infectious Diseases', *Nat Rev Microbiol,* 2 (2004), 95-108.

12 J. Esteban, D. Molina-Manso, I. Spiliopoulou, J. Cordero-Ampuero, R. Fernandez-Roblas, A. Foka, and E. Gomez-Barrena, 'Biofilm Development by Clinical Isolates of Staphylococcus Spp. From Retrieved Orthopedic Prostheses', *Acta Orthop,* 81 (2010), 674-9.

13 E. O'Neill, C. Pozzi, P. Houston, D. Smyth, H. Humphreys, D. A. Robinson, and J. P. O'Gara, 'Association between Methicillin Susceptibility and Biofilm Regulation in Staphylococcus Aureus Isolates from Device-Related Infections', *J Clin Microbiol,* 45 (2007), 1379-88.

14 C. J. Sanchez, Jr., K. Mende, M. L. Beckius, K. S. Akers, D. R. Romano, J. C. Wenke, and C. K. Murray, 'Biofilm Formation by Clinical Isolates and the Implications in Chronic Infections', *BMC Infect Dis,* 13 (2013), 47.

15 M. Palmer, W. Costerton, J. Sewecke, and D. Altman, 'Molecular Techniques to Detect Biofilm Bacteria in Long Bone Nonunion: A Case Report', *Clin Orthop Relat Res,* 469 (2011), 3037-42.

16 D. McDougald, S. A. Rice, N. Barraud, P. D. Steinberg, and S. Kjelleberg, 'Should We Stay or Should We Go: Mechanisms and Ecological Consequences for Biofilm Dispersal', *Nat Rev Microbiol,* 10 (2012), 39-50.

17 L. Hall-Stoodley, and P. Stoodley, 'Biofilm Formation and Dispersal and the Transmission of Human Pathogens', *Trends Microbiol,* 13 (2005), 7-10.

18 J. B. Kaplan, 'Biofilm Dispersal: Mechanisms, Clinical Implications, and Potential Therapeutic Uses', *J Dent Res*, 89 (2010), 205-18.

19 A. S. Lynch, and D. Abbanat, 'New Antibiotic Agents and Approaches to Treat Biofilm-Associated Infections', *Expert Opin Ther Pat*, 20 (2010), 1373-87.

20 J. P. Folsom, B. Baker, and P. S. Stewart, 'In Vitro Efficacy of Bismuth Thiols against Biofilms Formed by Bacteria Isolated from Human Chronic Wounds', *J Appl Microbiol*, 111 (2011), 989-96.

21 J. B. Kaplan, K. LoVetri, S. T. Cardona, S. Madhyastha, I. Sadovskaya, S. Jabbouri, and E. A. Izano, 'Recombinant Human Dnase I Decreases Biofilm and Increases Antimicrobial Susceptibility in Staphylococci', *J Antibiot (Tokyo)*, 65 (2012), 73-7.

22 J. M. Dow, L. Crossman, K. Findlay, Y. Q. He, J. X. Feng, and J. L. Tang, 'Biofilm Dispersal in Xanthomonas Campestris Is Controlled by Cell-Cell Signaling and Is Required for Full Virulence to Plants', *Proc Natl Acad Sci U S A*, 100 (2003), 10995-1000.

23 J. A. Jennings, H. S. Courtney, and W. O. Haggard, 'Cis-2-Decenoic Acid Inhibits S. Aureus Growth and Biofilm in Vitro: A Pilot Study', *Clin Orthop Relat Res*, 470 (2012), 2663-70.

24 O. Simonetti, O. Cirioni, R. Ghiselli, G. Goteri, A. Scalise, F. Orlando, C. Silvestri, A. Riva, V. Saba, K. D. Madanahally, A. Offidani, N. Balaban, G. Scalise, and A. Giacometti, 'Rnaiii-Inhibiting Peptide Enhances Healing of Wounds Infected with Methicillin-Resistant Staphylococcus Aureus', *Antimicrob Agents Chemother*, 52 (2008), 2205-11.

25 G. Brackman, P. Cos, L. Maes, H. J. Nelis, and T. Coenye, 'Quorum Sensing Inhibitors Increase the Susceptibility of Bacterial Biofilms to Antibiotics in Vitro and in Vivo', *Antimicrob Agents Chemother*, 55 (2011), 2655-61.

26 I. Kolodkin-Gal, D. Romero, S. Cao, J. Clardy, R. Kolter, and R. Losick, 'D-Amino Acids Trigger Biofilm Disassembly', *Science*, 328 (2010), 627-9.

27 A. I. Hochbaum, I. Kolodkin-Gal, L. Foulston, R. Kolter, J. Aizenberg, and R. Losick, 'Inhibitory Effects of D-Amino Acids on Staphylococcus Aureus Biofilm Development', *J Bacteriol*, 193 (2011), 5616-22.

28 N. Ercal, X. Luo, R. H. Matthews, and D. W. Armstrong, 'In Vitro Study of the Metabolic Effects of D-Amino Acids', *Chirality*, 8 (1996), 24-9.

29 M. S. Smeltzer, J. R. Thomas, S. G. Hickmon, R. A. Skinner, C. L. Nelson, D. Griffith, T. R. Parr, Jr., and R. P. Evans, 'Characterization of a Rabbit Model of Staphylococcal Osteomyelitis', *J Orthop Res*, 15 (1997), 414-21.

30 E. C. Weiss, A. Zielinska, K. E. Beenken, H. J. Spencer, S. J. Daily, and M. S. Smeltzer, 'Impact of Sara on Daptomycin Susceptibility of Staphylococcus Aureus Biofilms in Vivo', *Antimicrob Agents Chemother*, 53 (2009), 4096-102.

31 J. E. Cassat, C. Y. Lee, and M. S. Smeltzer, 'Investigation of Biofilm Formation in Clinical Isolates of Staphylococcus Aureus', *Methods Mol Biol*, 391 (2007), 127-44.

32 G. D. Christensen, W. A. Simpson, J. J. Younger, L. M. Baddour, F. F. Barrett, D. M. Melton, and E. H. Beachey, 'Adherence of Coagulase-Negative Staphylococci to Plastic Tissue Culture Plates: A Quantitative Model for the Adherence of Staphylococci to Medical Devices', *J Clin Microbiol*, 22 (1985), 996-1006.

33 S. A. Guelcher, V. Patel, K. M. Gallagher, S. Connolly, J. E. Didier, J. S. Doctor, and J. O. Hollinger, 'Synthesis and in Vitro Biocompatibility of Injectable Polyurethane Foam Scaffolds', *Tissue Eng*, 12 (2006), 1247-59.

34 A. S. Sawhney, and J. A. Hubbell, 'Rapidly Degraded Terpolymers of Dl-Lactide, Glycolide, and Epsilon-Caprolactone with Increased Hydrophilicity by Copolymerization with Polyethers', *J Biomed Mater Res*, 24 (1990), 1397-411.

35 S. Guelcher, A. Srinivasan, A. Hafeman, K. Gallagher, J. Doctor, S. Khetan, S. McBride, and J. Hollinger, 'Synthesis, in Vitro Degradation, and Mechanical Properties of Two-Component Poly(Ester Urethane)Urea Scaffolds: Effects of Water and Polyol Composition', *Tissue Engineering*, 13 (2007), 2321-33.

36 AE Hafeman, B Li, T Yoshii, KL Zienkiewicz, JM Davidson, and SA Guelcher, 'Injectable Biodegradable Polyurethane Scaffolds with Release of Platelet-Derived Growth Factor for Tissue Repair and Regeneration', *Pharm Res*, 25 (2008), 2387-99.

37 P Bhandare, P Madhavan, B M Rao, and N Someswar Rao, 'Determination of Amino Acid without Derivatization by Using Hplc-Hilic Column', *J. Chem. Pharm. Res.*, 2 (2010), 372-80.

38 T. J. Kinnari, J. Esteban, N. Z. Martin-de-Hijas, O. Sanchez-Munoz, S. Sanchez-Salcedo, M. Colilla, M. Vallet-Regi, and E. Gomez-Barrena, 'Influence of Surface Porosity and Ph on Bacterial Adherence to Hydroxyapatite and Biphasic Calcium Phosphate Bioceramics', *J Med Microbiol*, 58 (2009), 132-7.

39 B. Li, K. V. Brown, J. C. Wenke, and S. A. Guelcher, 'Sustained Release of Vancomycin from Polyurethane Scaffolds Inhibits Infection of Bone Wounds in a Rat Femoral Segmental Defect Model', *J Control Release*, 145 (2010), 221 - 30.

40 S. A. Guelcher, K. V. Brown, B. Li, T. Guda, B. H. Lee, and J. C. Wenke, 'Dual-Purpose Bone Grafts Improve Healing and Reduce Infection', *Journal of orthopaedic trauma*, 25 (2011), 477-82.

41 J.G. Penn-Barwell, C.K. Murray, and J.C. Wenke, 'Early Antibiotics and Debridement Independently Reduce Infection in an Open Fracture Model', *J Bone Joint Sur Br*, 94-B (2012), 1-6.

42 D. R. Hospenthal, C. K. Murray, R. C. Andersen, R. B. Bell, J. H. Calhoun, L. C. Cancio, J. M. Cho, K. K. Chung, J. C. Clasper, M. H. Colyer, N. G. Conger, G. P. Costanzo, H. K. Crouch, T. K. Curry, L. C. D'Avignon, W. C. Dorlac, J. R. Dunne, B. J. Eastridge, J. R. Ficke, M. E. Fleming, M. A. Forgione, A. D. Green, R. G. Hale, D. K. Hayes, J. B. Holcomb, J. R. Hsu, K. E. Kester, G. J. Martin, L. E. Moores, W. T. Obremskey, K. Petersen, E. M. Renz, J. R. Saffle, J. S. Solomkin, D. E. Sutter, D. R. Tribble, J. C. Wenke, T. J. Whitman, A. R. Wiesen, and G. W. Wortmann, 'Guidelines for the Prevention of Infections Associated with Combat-Related Injuries: 2011 Update: Endorsed by the Infectious Diseases Society of America and the Surgical Infection Society', *J Trauma*, 71 (2011), S210-34.

43 V. Papadopoulou, K. Kosmidis, M. Vlachou, and P. Macheras, 'On the Use of the Weibull Function for the Discernment of Drug Release Mechanisms', *Int J Pharm*, 309 (2006), 44-50.

44 B. Li, T. Yoshii, A. E. Hafeman, J. S. Nyman, J. C. Wenke, and S. A. Guelcher, 'The Effects of Rhbmp-2 Released from Biodegradable Polyurethane/Microsphere Composite Scaffolds on New Bone Formation in Rat Femora', *Biomaterials*, 30 (2009), 6768-79.

45 A. A. Beardmore, D. E. Brookds, J. C. Wenke, and D. B. Thomas, 'Effectiveness of Local Antibiotic Delivery with an Osteoinductive and Osteoconductive Bone-Graft Substitute', *J Bone Joint Sur*, 87A (2005), 107-12.

46 MD McKee, LM Wild, EH Schemitsch, and JP Waddell, 'The Use of an Antibioticimpregnated, Osteoconductive, Bioabsorbable Bone Substitute in the Treatment of Infected Long Bone Defects: Early Results of a Prospective Trial. ', *J Orthop Trauma,* 16 (2002), 622-7.

47 S. Radin, P. Ducheyne, T. Kamplain, and B. H. Tan, 'Silica Sol-Gel for the Controlled Release of Antibiotics. I. Synthesis, Characterization, and in Vitro Release', *J Biomed Mater Res,* 57 (2001), 313-20.

48 S. P. Noel, H. S. Courtney, J. D. Bumgardner, and W. O. Haggard, 'Chitosan Sponges to Locally Deliver Amikacin and Vancomycin: A Pilot in Vitro Evaluation', *Clin Orthop Relat Res,* 468 (2010), 2074-80.

49 K. Feng, H. Sun, M. A. Bradley, E. J. Dupler, W. V. Giannobile, and P. X. Ma, 'Novel Antibacterial Nanofibrous Plla Scaffolds', *J Control Release,* 146 (2010), 363-9.

50 M. R. Virto, B. Elorza, S. Torrado, L. Elorza Mde, and G. Frutos, 'Improvement of Gentamicin Poly(D,L-Lactic-Co-Glycolic Acid) Microspheres for Treatment of Osteomyelitis Induced by Orthopedic Procedures', *Biomaterials,* 28 (2007), 877-85.

51 S. Radin, T. Chen, and P. Ducheyne, 'The Controlled Release of Drugs from Emulsified, Sol Gel Processed Silica Microspheres', *Biomaterials,* 30 (2009), 850-8.

52 X. Shi, Y. Wang, L. Ren, N. Zhao, Y. Gong, and D. A. Wang, 'Novel Mesoporous Silica-Based Antibiotic Releasing Scaffold for Bone Repair', *Acta Biomater,* 5 (2009), 1697-707.

53 E. Tuomanen, R. Cozens, W. Tosch, O. Zak, and A. Tomasz, 'The Rate of Killing of Escherichia Coli by Beta-Lactam Antibiotics Is Strictly Proportional to the Rate of Bacterial Growth', *J Gen Microbiol,* 132 (1986), 1297-304.

54 A. G. Gristina, P. Naylor, and Q. Myrvik, 'Infections from Biomaterials and Implants: A Race for the Surface', *Med Prog Technol,* 14 (1988), 205-24.

55 S. L. Percival, K. E. Hill, S. Malic, D. W. Thomas, and D. W. Williams, 'Antimicrobial Tolerance and the Significance of Persister Cells in Recalcitrant Chronic Wound Biofilms', *Wound Repair Regen,* 19 (2011), 1-9.

56 M. Alipour, Z. E. Suntres, R. M. Lafrenie, and A. Omri, 'Attenuation of Pseudomonas Aeruginosa Virulence Factors and Biofilms by Co-Encapsulation of Bismuth-Ethanedithiol with Tobramycin in Liposomes', *J Antimicrob Chemother,* 65 (2010), 684-93.

57 M. Hentzer, and M. Givskov, 'Pharmacological Inhibition of Quorum Sensing for the Treatment of Chronic Bacterial Infections', *J Clin Invest,* 112 (2003), 1300-7.

58 Y. Irukayama-Tomobe, H. Tanaka, T. Yokomizo, T. Hashidate-Yoshida, M. Yanagisawa, and T. Sakurai, 'Aromatic D-Amino Acids Act as Chemoattractant Factors for Human Leukocytes through a G Protein-Coupled Receptor, Gpr109b', *Proc Natl Acad Sci U S A,* 106 (2009), 3930-4.

59 A. E. Hafeman, K. J. Zienkiewicz, A. L. Zachman, H. J. Sung, L. B. Nanney, J. M. Davidson, and S. A. Guelcher, 'Characterization of the Degradation Mechanisms of Lysine-Derived Aliphatic Poly(Ester Urethane) Scaffolds', *Biomaterials,* 32 (2011), 419-29.

60 A. E. Hafeman, K. J. Zienkiewicz, E. Carney, B. Litzner, C. Stratton, J. C. Wenke, and S. A. Guelcher, 'Local Delivery of Tobramycin from Injectable Biodegradable Polyurethane Scaffolds', *J Biomater Sci Polym Ed,* 21 (2010), 95-112.

61 K. V. Brown, B. Li, T. Guda, D. S. Perrien, S. A. Guelcher, and J. C. Wenke, 'Improving Bone Formation in a Rat Femur Segmental Defect by Controlling Bone Morphogenetic Protein-2 Release', *Tissue engineering. Part A,* 17 (2011), 1735-46.

62 J. E. Dumas, K. Zienkiewicz, S. A. Tanner, E. M. Prieto, S. Bhattacharyya, and S. Guelcher, 'Synthesis and Characterization of an Injectable Allograft Bone/Polymer Composite Bone Void Filler with Tunable Mechanical Properties', *Tissue Eng Part A*, 16 (2010), 2505-18.

63 J. E. Dumas, P. B. Brownbaer, E. M. Prieto, T. Guda, R. G. Hale, J. C. Wenke, and S. A. Guelcher, 'Injectable Reactive Biocomposites for Bone Healing in Critical-Size Rabbit Calvarial Defects', *Biomed Mater*, 7 (2012), 024112.

64 B. Li, J. M. Davidson, and S. A. Guelcher, 'The Effect of the Local Delivery of Platelet-Derived Growth Factor from Reactive Two-Component Polyurethane Scaffolds on the Healing in Rat Skin Excisional Wounds', *Biomaterials*, 30 (2009), 3486-94.

65 C. E. Nelson, M. K. Gupta, E. J. Adolph, J. M. Shannon, S. A. Guelcher, and C. L. Duvall, 'Sustained Local Delivery of Sirna from an Injectable Scaffold', *Biomaterials*, 33 (2012), 1154-61.

66 Y. Nozaki, and C. Tanford, 'The Solubility of Amino Acids and Two Glycine Peptides in Aqueous Ethanol and Dioxane Solutions. Establishment of a Hydrophobicity Scale', *J Biol Chem*, 246 (1971), 2211-7.

67 C. Liu, A. Bayer, S. E. Cosgrove, R. S. Daum, S. K. Fridkin, R. J. Gorwitz, S. L. Kaplan, A. W. Karchmer, D. P. Levine, B. E. Murray, J. Rybak M, D. A. Talan, and H. F. Chambers, 'Clinical Practice Guidelines by the Infectious Diseases Society of America for the Treatment of Methicillin-Resistant Staphylococcus Aureus Infections in Adults and Children: Executive Summary', *Clin Infect Dis*, 52 (2011), 285-92.

68 R. L. Stewart, J. T. Cox, D. Volgas, J. Stannard, L. Duffy, K. B. Waites, and T. M. Chu, 'The Use of a Biodegradable, Load-Bearing Scaffold as a Carrier for Antibiotics in an Infected Open Fracture Model', *J Orthop Trauma*, 24 (2010), 587-91.

69 Z. Zheng, W. Yin, J. N. Zara, W. Li, J. Kwak, R. Mamidi, M. Lee, R. K. Siu, R. Ngo, J. Wang, D. Carpenter, X. Zhang, B. Wu, K. Ting, and C. Soo, 'The Use of Bmp-2 Coupled - Nanosilver-Plga Composite Grafts to Induce Bone Repair in Grossly Infected Segmental Defects', *Biomaterials*, 31 (2010), 9293-300.

70 J. C. Wenke, and S. A. Guelcher, 'Dual Delivery of an Antibiotic and a Growth Factor Addresses Both the Microbiological and Biological Challenges of Contaminated Bone Fractures', *Expert Opin Drug Deliv*, 8 (2011), 1555-69.

71 K. V. Brown, J. A. Walker, D. S. Cortez, C. K. Murray, and J. C. Wenke, 'Earlier Debridement and Antibiotic Administration Decrease Infection', *Journal of Surgical Orthopaedic Advances*, 19 (2010), 18-22.

CHAPTER IV

SURFACE MODIFICATION OF B-TRI-CALCIUM PHOSPHATE IMPROVES THE MECHANICAL PERFORMANCE OF SETTABLE CALCIUM PHOSPHATE/POLYURETHANE BIOCOMPOSITES FOR BONE TISSUE ENGINEERING

Introduction

Due to their natural presence in bone [1], calcium phosphate cements (CPCs) and scaffolds have been investigated extensively for the treatment of osseous defects. β-tricalcium phosphate (β-TCP) is an osteoconductive [2] and biocompatible ceramic which has been reported to bond directly to bone [3, 4]. However, injectable CPCs derived from β-TCP are susceptible to brittle fracture and graft migration [5-7]. These conditions limit their application in weight-bearing defects, and increase the probability of additional revision surgeries for patients.

As alternative materials to overcome the mechanical limitations of CPCs, β-TCP/polymer composites have been investigated. A wide range of polymers have been used to fabricate composites with calcium phosphates resulting in materials with varying porosities and mechanical properties [8]. In a previous study, we reported that compression-molded β-TCP/polyurethane composites implanted in femoral condyle defects in rats supported cellular infiltration and appositional remodeling [9]. However, few β-TCP/polymer composites are moldable and settable, which precludes their use in minimally invasive surgical procedures.

Lysine-derived polyurethane (PUR) scaffolds are biocompatible, degrade to non-cytotoxic compounds [10-15], and have tunable working times which make them suitable for injectable applications [16, 17, 14]. The reactive nature of the polyurethane gelling process enables interfacial bonding between the polymer and filler phases with functional hydroxyl or amine groups at the surface [13]. Low porosity allograft bone/PUR molded composites with high filler loading (>64 vol.%) have also been shown to support cellular infiltration and remodel by creeping substitution as cells follow the path provided by the interconnected particles [18]. The limited availability and risks of disease transmission associated with allograft bone [19] have generated interest in the development of composites with similar properties using synthetic matrix particles.

In the present study, we investigated the effects of β-TCP particle loading and surface composition on the mechanical and biological properties of β-TCP/PUR composites. A composite with completely interconnected phases may offer increased resistance to crack growth and consequently extend the effective loading range supported by the materials [8]. Thus, we hypothesized that surface modification of the β-TCP particles with grafted polymeric chains would improve the compatibility of the ceramic and polymeric phases by promoting chain entanglements and/or reactivity between the phases, resulting in enhanced mechanical properties. Poly(ε-caprolactone) (PCL - a polymer also present in the backbone of the polyurethane) was covalently grafted to protonated β-TCP particles via ring-opening-polymerization [20], and composite mechanical properties were evaluated under dry and wet conditions. Effects of surface modification on cellular attachment and differentiation were evaluated *in vitro*.

Experimental

Materials

Lysine triisocyanate (LTI) was purchased from Kyowa Hakko USA (New York) and polyethylene glycol (PEG, MW 200 Da) from Alfa Aesar (Ward Hill, MA). Glycerol, ε-caprolactone, stannous octoate, phosphoric acid, chloroform, the reagents for the alkaline phosphatase assay, and the chemicals for intracellular (Sigma kit 387A) and extracellular staining of tartrate resistance acid phosphatase (TRAP) were obtained from Sigma-Aldrich (St. Louis, MO). Glycolide and D,L-lactide were purchased from Polysciences (Warrington, PA). The tertiary amine catalyst (TEGOAMIN33) was obtained as a gift from Goldschmidt (Hopewell, VA). β-TriCalcium Phosphate particles (TCP, grain size distribution 100-300 μm) were purchased from Berkeley Advanced Biomaterials (Berkeley, CA). MC3T3 osteoprogenitor cells and c57bl wild type mice were obtained from Javier Esparza and Dr. James Edwards, respectively, at the Vanderbilt Center for Bone Biology (VCBB). Dentin pieces were kindly provided by Dr. Julie Sterling also at the VCBB, and were cut into thin chips as controls for osteoclastic cell culture. α-minimal essential medium (α-MEM), fetal bovine serum (FBS), Penicillin/Streptomycin solution (P/S), Dulbecco's phosphate-buffered salt without calcium and magnesium (PBS), and the Pierce BCA Protein kit were purchased from Fisher Scientific (Pittsburgh, PA). The Live/Dead Viability/Cytotoxicity and CyQUANT Cell proliferation Assay kits were purchased from Invitrogen. Osteoclast growth factors (recombinant mouse Macrophage Colony Stimulating Factor [MCSF] and Receptor Activator of NF-kB Ligand [RANKL]) were purchased from R&D Systems (Minneapolis, MN). cD11b Microbeads used in the purification of osteoclast precursors were obtained

from Miltenyi Biotec (Auburn, CA). Prior to use, glycerol and PEG were dried at 10 mmHg overnight at 80°C, and ε-caprolactone was dried over anhydrous magnesium sulfate [21]. All other materials were used as received.

Surface modification of TCP

PCL was covalently grafted to TCP particles following the method proposed by Kunze et. al. [20]. Briefly, the surface of the particles was activated by stirring in 5% aqueous phosphoric acid for 1 hr, followed by washing with distilled water and vacuum-drying at 40ºC overnight. The resulting protonated material (p-TCP) was then reacted with ε-caprolactone at 150°C for 4 days. The molar ratio of TCP to ε-caprolactone was 1:10. The product (TCP-PCL) was washed with chloroform, filtered, and dried under vacuum at 60°C for 24 h.

Characterization of matrix particles

The skeletal density, which accounts for both the volume of the solid as well as the blind (e.g., inaccessible) pores of the particles, was measured by gas pycnometry using nitrogen as the penetrating gas (Micromeritics, Norcross, GA). Particle size distribution was measured by static image analysis using a Morphologi G3 (Malvern Instruments). Specific surface area was determined using a Micromeritics ASAP 2020 porosimeter with nitrogen as the adsorbing gas.

Gel Permeation Chromatography (GPC)

Previous studies grafting polystyrene on cellulose surfaces have shown minimal differences between the molecular weight of resulting grafted and non-grafted polymers [22]. Thus, to obtain an approximate molecular weight of the PCL grafted to the surface of TCP-PCL, the polymer collected after washing with chloroform (non-grafted PCL) was analyzed using a Waters Breeze GPC (Milford, MA). Two MesoPore 300x7.5 mm columns (Polymer Laboratories) were used in series with stabilized tetrahydrofuran (THF) as the mobile phase at a flow rate of 1 mL min^{-1} at 35°C.

Thermogravimetric Analysis (TGA)

The amount of polymer grafted to the surface of TCP-PCL particles was quantified using a TGA Q500 (TA Instruments). As a reference material, non-grafted PCL was analyzed by TGA to identify its degradation temperature. TCP-PCL and non-grafted PCL samples (~10 mg) were heated from 20ºC to 550ºC at a rate of 20ºC min^{-1} under a purge flow of nitrogen. The mass loss taking place at temperatures above the PCL degradation temperature was determined to be the polymer content on the particles.

X-Ray Photoelectron Spectroscopy (XPS)

The surface composition of the matrix particles was assessed using a PHI 5000 VersaProbe X-Ray Photoelectron Spectrometer with a 25 W monochromatic Al K-α X-ray source and a 100 µm spot size. The matrix particles were compressed (12,000lbs) into 14 mm diameter pellets before analysis. Survey spectra were collected using 187.85 pass energy. All measurements were performed using a 45º take-off angle and charge

neutralization under ultra-high vacuum. Analysis of the data was performed using the software CasaXPS Version 2.3.14 (© 1999-2008 Neal Fairley).

Contact angle measurements

In order to track changes in wetting properties of the matrix, contact angles between TCP or TCP-PCL particles and unreactive polymer mixture (no catalyst added) were measured. Contact angle measurements were completed using sintered TCP pellets with further surface modification. Compressed pellets (as prepared as for XPS analysis) were sintered at 1100 ºC for 2 hours. The surface modification method described before was used to graft PCL to the surface of the pellets. Sessile drops of the polyol-prepolymer mixture (without catalyst) were placed on the surface of the pellets and the contact angle was measured using a Rame-Hart (Succasunna, NJ) goniometer.

Prepolymer and polyol synthesis

Previously published techniques were applied to prepare the polyol [23, 21] and the NCO-terminated prepolymer [13]. A trifunctional polyester polyol (target molecular weight: 300 g/mol, measured OH number: 429) was prepared from a glycerol starter and a 60% ε-caprolactone, 30% glycolide, 10% D,L-lactide backbone using stannous octoate catalyst (0.1 wt%). LTI-PEG prepolymer was prepared from LTI and PEG (200 g/mol) with a molar ratio of 2:1 (NCO:OH equivalent ratio = 3:1) and NCO number of 22.2%. The OH number of the polyol (used to verify the molecular weight) and the NCO number of the pre-polymer were measured by titration using a Metrohm 798 MPT Titrino according to

ASTM D4274-99 Method C [24], and ASTM D2572-97 [25], respectively. The properties of the prepolymer have been reported previously [14].

Matrix/PUR biocomposite synthesis

The polyol and prepolymer described above were used to synthesize the composites. To investigate the effect of PUR composition on the mechanical performance of the composites, samples with target index (the ratio of isocyanate and hydroxyl equivalents multiplied by 100) of 105 and 140 were prepared. The actual index was calculated from the measured OH number for the polyol and %NCO for the prepolymer. The polyol and the amine catalyst were mixed in a 10 mL cup at 3300 rpm for 1 min using a Hauschild SpeedMixer mixer. The particles (either unmodified or modified) were then added and the components hand-mixed for 3 min, followed by addition of the prepolymer and hand-mixing for another 3 min. The resulting reactive paste was cast into cylindrical molds (6 mm diameter) and a pressure of 330 kPa was applied for a period exceeding the setting time of the material. The green composite was subsequently cured at 37°C for 15 hr.

Scanning electron microscopy (SEM)

SEM was used to observe the morphology of the composites, in particular near the interface between the matrix and polyurethane phases. After curing, disks were cut from the cylindrical composites and mounted on conductive carbon tape. Samples were sputter-coated with gold and analyzed using a Hitachi S-4200 scanning electron microscope. Digital images were obtained using Quartz PCI image management software (Hitachi, Pleasanton, CA).

Mechanical testing of the biocomposites

Compression testing was performed using an MTS 858 Bionix Servohydraulic Test System. Cylindrical specimens (6 mm diameter × 12 mm high) were conditioned in PBS at room temperature for 24 hr immediately before testing. The dimensions and mass of the samples before and after hydration were used to determine dry and wet density as well as water uptake patterns of the composites. Next, the specimens were pre-loaded to approximately 12 N, followed by continuous compression until failure at a rate of 25 mm min^{-1}. The load and position were recorded every 0.01 sec. The compressive stress was calculated by dividing the load by the initial cross-sectional area of the wet samples and reported in MPa. The compressive modulus was calculated as the slope of the initial linear section of the stress-strain curve and the compressive strength corresponded to the maximum stress tolerated by the material before failure.

Samples for torsion testing were prepared by potting ~5 mm at each end of 6-mm diameter cylinders into Technovit 4000 (Heraeus Kulzer) resulting in a central gauge length of about 10 mm. The potting material was prepared by mixing the powder:syrup I:syrup II using a ratio of 2:2:1 following the manufacturer's instructions. After potting, the torsion samples were hydrated for 24 hrs in PBS and then tested using an Instron DynaMight 8841 machine equipped with a 1.7 Nm torque cell. The potted ends were gripped using the Instron clamps in a horizontal setup (such that the residual torque was minimal). During testing, the clamps were rotated at an angular speed of 2°/s until failure. The measured torque and rotation angle were used to determine torsional stress using the equation [26, 27]:

$$\tau = [\theta(dT/d\theta) + 3T]/(2\pi r^3) \quad (4.1)$$

where r is the radius of the cylinder, $\theta = \alpha/L$ is the rotation angle per gauge unit length, and T is the measured torque. The derivative $dT/d\theta$ was determined by fitting the T vs. θ data to a 5^{th} order polynomial (between zero up to the maximum torque or ultimate point). Torsional strain (γ) was determined as $\gamma = \theta r$, and the shear modulus calculated from the linear region of the stress-strain curve $G = \tau/\gamma$. Toughness was calculated as the corresponding area under the stress-strain curve from zero to the maximum stress.

Osteoblast precursor cell culture and differentiation

Samples for cell culture were obtained by cutting thin disks from composite cylinders using an IsoMet Low Speed Saw (Buehler). Samples were sterilized with ethanol and conditioned with complete media (α-MEM with 10%FBS and 1% P/S) in a 48-well plate overnight. MC3T3 cells were cultured in complete media at 37°C in a humidified incubator with 5% CO_2 enriched atmosphere. $1.5x10^4$ MC3T3 cells were seeded on the materials and cultured in the presence of 0.5 ml of complete media. To determine the viability of MC3T3 cells seeded on the composites, the media was removed after 2 days of culture, the cells were gently rinsed with PBS, and live-dead reagent was added to the wells according to manufacturer's instructions. The surface of the materials was imaged and the percentage of cells stained green (live) was determined from the total population (which included dead cells stained red). Differentiation of MC3T3 cells seeded on the composites was monitored through the expression of active alkaline phosphatase (ALP). After 2 days of culture, the medium was changed to differentiating media (α-MEM with 2.5% FBS, 1% P/S, 100 μg/ml ascorbic acid, and 10 mM β-glycerophosphate) and culture continued for up to 7 days, with media change on

day 5. At days 2 and 7, cells were washed with PBS, removed from the materials using trypsin, centrifuged, re-suspended in 100 μl of 0.1% Triton-X, and frozen at -80°C. The Triton-X solutions were freeze-thawed 3 times to completely lyse the cells. 20 μl of the lysate were mixed with 100 μl of substrate buffer (1.5M alkaline buffer solution pH 10 [Sigma A9226], 16mM magnesium chloride, 2mg/ml phosphatase substrate [Sigma P4744], de-ionized water) and incubated at 37°C for 30 min, followed by measuring the absorbance of the solution at 405 nm. A standard curve with varying p-nitrophenol (product from the reaction of ALP with the substrate) concentrations was used to determine ALP activity at each time point. ALP activity was further normalized by total protein in the samples, measured using the Pierce BCA kit according to manufacturer's instructions.

Osteoclast precursor cell culture and differentiation

Samples for osteoclastic cell culture were cut, sterilized, and conditioned as detailed in the previous section. Osteoclast precursors were obtained from bone marrow cells extracted from the tibia and femoral head of 4-7 week old c57bl wild type mice. After extraction, CD11b+ osteoclast precursors present in the bone marrow [28] were labeled with microbeads, and separated from the non-labeled cells using an AutoMacs magnetic separator (Vanderbilt University Flow Cytometry Core). cD11b+ cells were seeded onto composite and dentin (control) samples at a density of $1.8x10^5$ cells/ml. Complete medium was supplemented with 50 ng/mL RANKL and 25 ng/mL MCSF. Cells were cultured for up to 21 days with media changes every 2-3 days.

Tartrate Resistant Acid Phosphatase (TRAP) is a histochemical marker of both, differentiating and active osteoclasts [29, 30]. In addition, extracellular release of TRAP by osteoclasts has been found to correlate with resorptive activity both *in vitro* [31, 32] and *in vivo* [33, 29]. Thus, to verify differentiation of the osteoclast precursors seeded on each material, cells were fixed and stained for intracellular TRAP activity (Sigma kit 387A). Furthermore, media removed from the wells during each change was collected and frozen at -80°C. Secreted TRAP into the media was quantified using napthol ASBI-phosphate as the substrate [34]. 50 μl of diluted media samples (such that the reading was located in the range of the total protein calibration curve) were mixed with 150 μl of reaction buffer (100 mM sodium acetate, 50 mM sodium tartrate, 2.5 mM Napthol ASBI-Phosphate in 4% 2-methoxyethanol [ethylene glycol monomethyl ether – EGME]) in a 96-well plate, followed by incubation at 37°C for 35 min. The reaction was stopped with the addition of 0.6 M NaOH and fluorescence was read at 405 nm (excitation), 520 nm (emission). Fluorescence units of secreted TRAP were further normalized to total protein per day and are presented relative to dentin controls.

Statistical analysis

Statistical analyses were performed using One-Way ANOVA followed by Tukey-Kramer tests to identify differences in XPS ratios, contact angles, mechanical properties, ALP activity, and secreted TRAP between groups. For all experiments, $p<0.05$ was considered statistically significant. Analyses were run using JMP 9.0.

Results

Characterization of matrix particles

Surface treatment of β-TCP particles led to changes in particle size, density, surface area, and composition (Figure 4.1). As shown in Figure 4.1A-B, the particle size distribution of TCP shifted towards lower diameters after surface modification. This shift took place mainly during the protonation step under continuous mixing in 5% phosphoric acid to obtain p-TCP particles. The decrease in particle size was accompanied by a decrease in density and a significant increase in surface area.

A

Filler particle properties		TCP	p-TCP	TCP-PCL
Diameter (μm)	90% finer	322.3	114.6	102.3
	50% finer	195.6	23.4	20.3
	10% finer	5.6	1.0	1.6
Density (g cm^{-3})		3.088	2.657	2.712
Surface Area ($m^2 g^{-1}$)		5.62	-	9.99
Grafted polymer content (mass %)		-	-	6.0 ± 0.9
Grafted polymer Mn (kDa)		-	-	15.2 ± 3.0
Grafted polymer PDI (Mw Mn^{-1})		-	-	1.34 ± 0.21

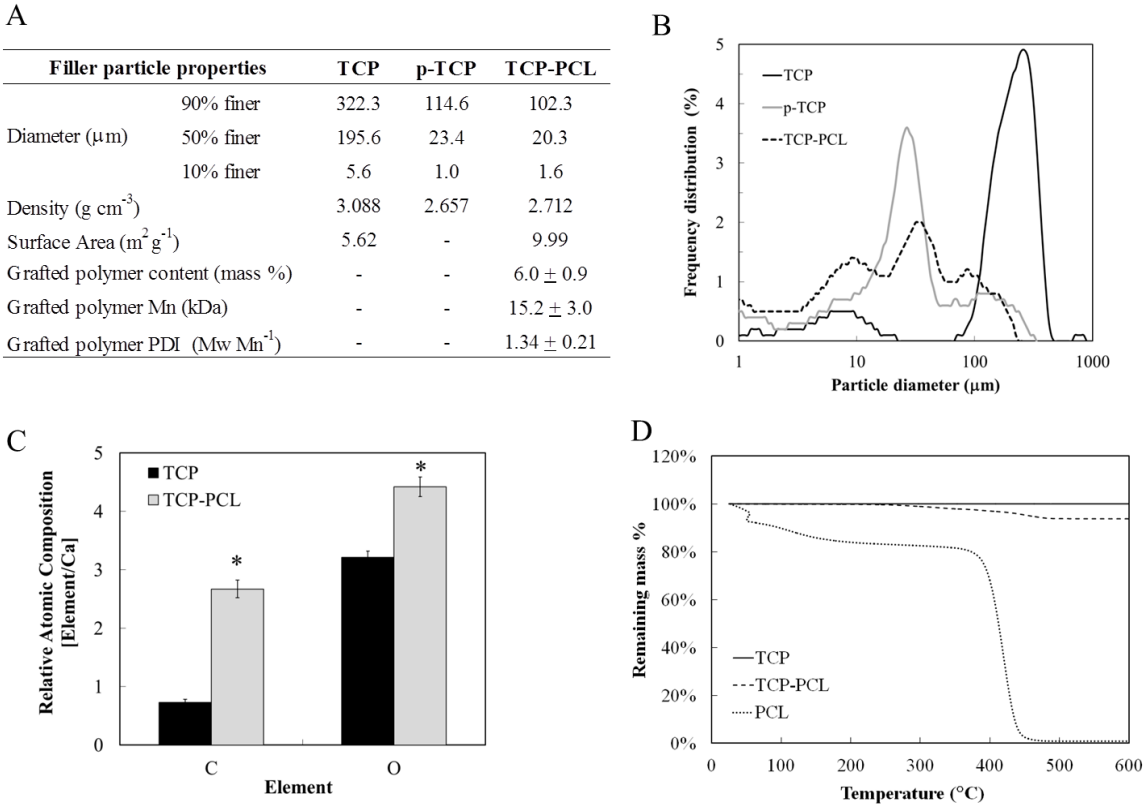

Figure 4.1. Characterization of matrix particles. (A) Matrix particle properties. (B) Frequency particle size distributions measured for TCP, p-TCP, and TCP-PCL. (C) Relative atomic composition at the surface of TCP, p-TCP, and TCP-PCL measured by XPS. (D) Thermogravimetric analysis (TGA) of TCP, TCP-PCL, and PCL.

Changes in surface composition were assessed using XPS and TGA. Relative atomic surface compositions quantified with XPS are shown in Figure 1C. Significantly higher C/Ca and O/Ca ratios were measured in TCP-PCL compared to TCP ($p<0.05$) which validate the presence of PCL on the surface of TCP-PCL. The amount of grafted polymer was quantified using TGA (Figure 4.1D). When exposed to the heating ramp up to 550ºC, the mass of TCP particles remained constant, while the mass of TCP-PCL particles decreased 6.0±0.9% at 500ºC due to degradation of the grafted PCL (as verified by the analysis of PCL recovered from the grafting reaction). The grafted PCL was further characterized using GPC and was found to have a number average molecular weight of 15.2±3.0 kDa and a polydispersity index of 1.34±0.21.

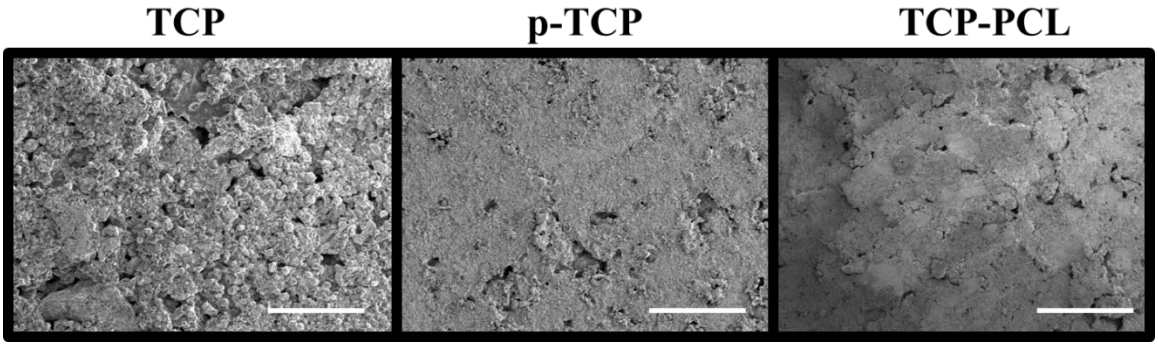

Figure 4.2. SEM images of TCP, p-TCP, and TCP-PCL composites. Scale bars correspond to 300 μm.

Composite interfacial interactions

Figure 4.2 presents cross-sectional images of composites with 56.7 vol% of modified and unmodified matrix particles. As shown by these images, the phase continuity of the composite improved as p-TCP and TCP-PCL particles were used as ceramic matrix. SEM images also show that porosity of the composites can be attributed to voids between the phases and not to pores created in the polymeric phase. Porosity was

measured gravimetrically [14] and determined to be between 19-27% for the TCP composite formulations and 7-16% for the composites with modified matrix (p-TCP or TCP-PCL). TCP composites show evidence of TCP particles and voids of varying size distributed throughout the material. Although TCP grains with original size (100-300 μm) remain, the images also show many smaller particles. These small particles may have been obtained by crushing during the hand-mixing steps. Due to the significant decrease in particle size, matrix particles are harder to identify in the p-TCP and TCP-PCL composites. Though voids were also present in the TCP-PCL composite, higher continuity of the phases was evident in the images, suggesting improved interaction between the polymeric and ceramic phases.

Further characterization of this interaction was conducted using contact angle measurements. The contact angle (θ) between a solid and a liquid can be used to calculate the work of adhesion (W_{Ad}) at the interface according to the Young-Dupré relationship where γ corresponds to the liquid surface tension [35]:

$$W_{Ad} = \gamma(1 + cos\theta) \quad (4.2)$$

An interface with strong interactions has high work of adhesion and low contact angle (good wetting). Non-reactive polymer was able to wet the TCP pellet surface with a contact angle of 29±2°. The reduced contact angle on TCP-PCL (26±2°) suggests a modest improvement in wetting due to PCL grafting, though no significant differences were observed between the TCP and TCP-PCL contact angles (n=5, p=0.057). Although water contact angles are a more common measure of changes in wettability of a surface, in this case, the treatment of the TCP pellets with acid during the protonation step

increased the porosity of the samples and water flowed through the TCP-PCL preventing the correct measurement of this parameter.

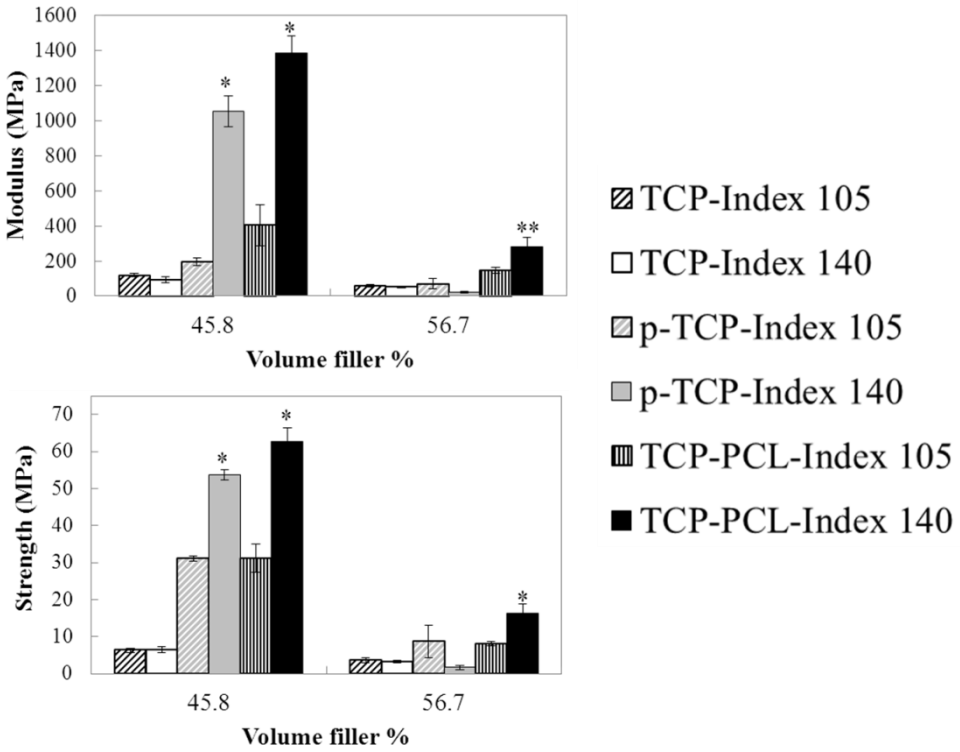

Figure 4.3. Wet mechanical properties of composites at different indexes A) modulus, B) compressive strength. Statistical analysis compares composites with the same filler but different indexes at each filler load; * $p<0.05$; ** $p=0.11$

Mechanical properties of composite scaffolds

Figure 4.3 presents the compressive mechanical properties of composites prepared with different matrices and isocyanate indices. While the mechanical properties of TCP composites were insensitive to index at both matrix contents evaluated, p-TCP and TCP-PCL composites exhibited increased mechanical properties when formulated with excess isocyanate. At lower matrix loadings (45.8 vol.%), both lower particle size and higher index improved the mechanical properties of composites with modified particles. However, as the matrix loading approached random close packing (>55 vol.%),

mechanical properties were only improved for TCP-PCL composites with 40% excess isocyanate. Composites prepared for further mechanical and cell culture analysis were all formulated with index 140.

Water uptake of the composites as a function of matrix loading is presented in Figure 4.4A. After 24 hrs submerged in PBS, TCP-PCL composites absorbed the least amount of water independent of matrix loading (Figure 4A). p-TCP composites exhibited a similar behavior except at 61.3 vol.%, while TCP composites absorbed a significantly higher amount of water at all matrix loadings. Reduced water uptake is additional evidence of improved interfacial interactions between the phases in TCP-PCL composites which result in minimal available space inside the material for water to accumulate [35, 36].

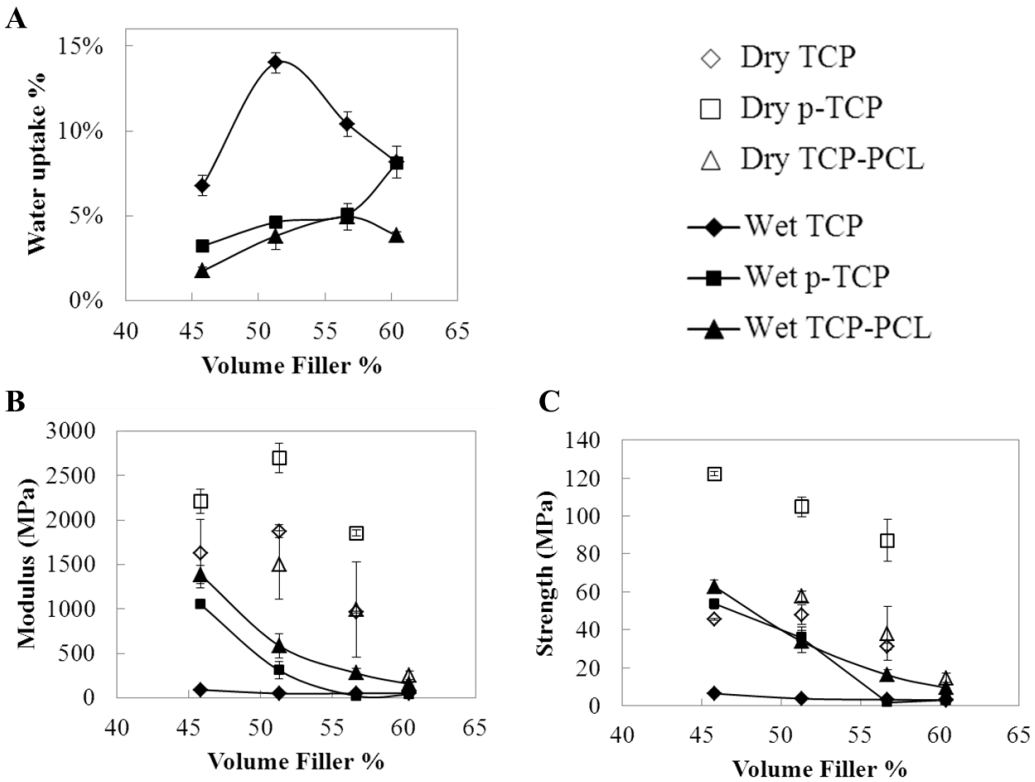

Figure 4.4. Compressive mechanical properties of scaffolds with index 140 as a function of matrix composition and loading. (A) Water uptake. (B) Compressive modulus under dry and wet conditions. (C) Compressive strength under dry and wet conditions.

The behavior of compressive (Figure 4.4B and C) and torsion (Table 4.1) properties under dry and wet conditions differed between the TCP treatment groups. Surface modification increased the compressive properties with respect to unmodified TCP. This can be attributed to a combined effect of reduced particle size and improved interfacial interactions. Composites with lower water uptake (TCP-PCL) had more stable modulus and strength under aqueous conditions. Increased matrix loading monotonically decreased the compressive properties of the composites. Mechanical properties under torsion were evaluated for composites with index 140 and 56.7 vol% of TCP or TCP-PCL. This matrix content was chosen to maximize the amount of matrix without compromising the compressive mechanical properties to values below that of trabecular bone. As expected, torsion is a more demanding mode of failure, and the measured properties for modified and unmodified particles are below the trabecular bone reference.

Table 4.1. Torsion mechanical properties for TCP and TCP-PCL composites

	TCP		**TCP-PCL**		**Trabecular bone ***
	Dry	**Wet**	**Dry**	**Wet**	
G (MPa)	1009±191	6.8±0.9	628±244	32.2±6.8	263 - 366
Max stress (MPa)	7.5±0.94	0.7±0.1	10.7±7.3	1.2±0.2	3.1 - 7.7
Max. strain (%)	0.9±0.1	10.6±0.5	1.9±0.7	4.9±0.1	4.6±1.3[26]
Energy to failure (kJ/m^3)	48.2±3.2	40.8±6.1	155.3±128.2	34±6.3	-

***** Ranges from studies of human, canine, bovine, and ovine samples (references included in the text).

Osteoblastic and osteoclastic cell culture

Ceramic phases are included in bone tissue engineering composites to provide osteoconductivity and bioactivity to the polymer [7, 37]. Thus, it was important for this work to verify that the surface modification of the particles would not affect the attachment and differentiation of bone remodeling cells. Osteoblast and osteoclast precursors were

seeded on TCP and TCP-PCL composites (56.7 vol.% matrix) *in vitro*, and their differentiation was monitored over time. It was not possible to seed cells on p-TCP composites to isolate the effects of changes in particle size, given that the materials acidified the media and did not allow cells to attach.

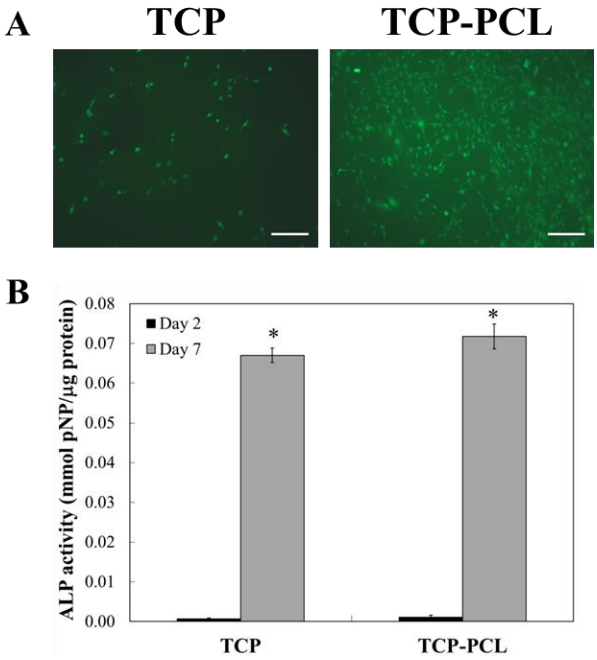

Figure 4.5. Osteoblastic cell culture of TCP, and TCP-PCL composites. (A) Live-Dead staining of MC3T3 cells seeded on composites after 2 days of culture (>95% viability). (B) The biocomposites support the differentiation of MC3T3 cells after 7 days of culture in differentiation media. White scale bars represent 200 um, * $p<0.05$ compared to Day 2.

Both osteoblast and osteoclast precursors attached and differentiated on the surface of TCP and TCP-PCL composites. Figure 4.5A shows images of live/dead staining of MC3T3 cells after being cultured 2 days. Viability of the cells was >95% for both formulations, suggesting minimal toxicity from the scaffolds. Furthermore, increased ALP activity in the cultured cells (Figure 4.5B) suggests that the cells differentiated into osteoblasts, and no significant differences were identified between the materials.

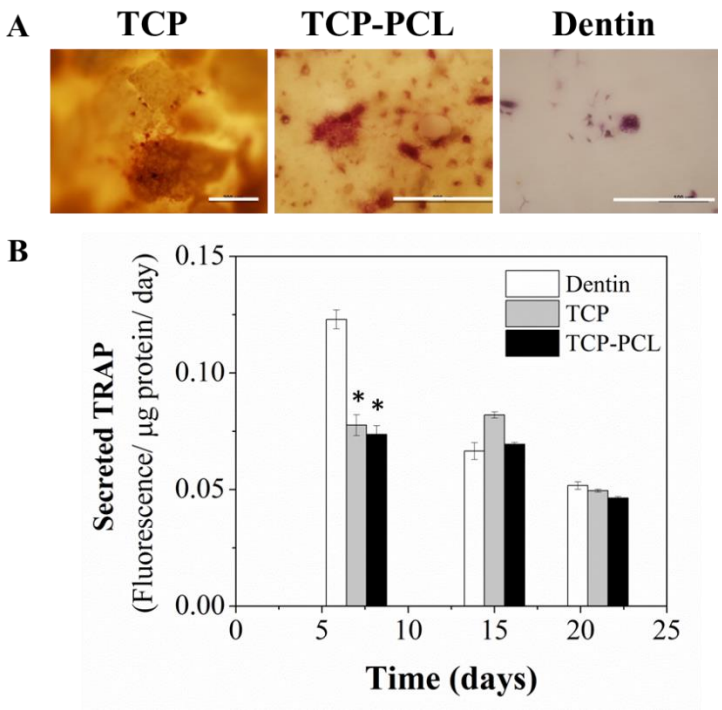

Figure 4.6. Osteoclastic cell culture of TCP, and TCP-PCL composites. (A) Positive TRAP staining of bone marrow cells cultured on the biocomposites for 15 days. (B) TRAP secreted into the media as a measure of osteoclastic resorption activity. * Significantly different from dentin at the same time point ($p<0.05$).

Similarly, positive staining for intracellular TRAP in osteoclast precursors cultured on composites and dentin controls for 15 days (Figure 4.6A) suggests that osteoclast differentiation was not hindered by surface modification of the matrix particles. It is evident that the positive cells on TCP composites, TCP-PCL composites, and dentin samples had different morphology, but this can be attributed to differences in surface topographies [38]. Quantification of secreted TRAP provided additional evidence of osteoclast differentiation *in vitro*. At early time points, osteoclasts cultured on dentin substrates had higher resorptive activity than those cultured on TCP and TCP-PCL composites. However, by 15 days of culture, osteoclast activity on the composites matched the activity on dentin. Combined, these observations suggest that the surface modification of TCP particles did not hinder the bioactivity of the ceramic matrix and

that the composite formulations developed in this work are candidates to undergo remodeling *in vivo*.

Discussion

Development of composite biomaterials for bone tissue engineering, in particular for load-bearing applications, has received increased attention in the past decade due to the improvements in handling, mechanical properties, and biological performance that arise when combining two or more phases [39, 7]. However, a recent review of the mechanical behavior of calcium phosphate/polymer composites reported that few formulations have strength and porosity comparable to trabecular bone [8]. To overcome this problem, compression molded composite formulations with polyurethane and calcium phosphates (hydroxyapatite and β-TCP) [9] or allograft bone particles [13] have been developed and tested *in vivo*. These low porosity composites achieved mechanical properties approaching those of cortical bone, and when implanted into femoral defects in rats and rabbits the materials supported cellular infiltration and promoted new bone deposition. Although these formulations have the potential to be applied as weight-bearing implants, they still require compaction with high pressures which limits their use in operating rooms. In this study, moldable and settable composites incorporating modified and unmodified β-TCP particles and lysine-derived polyurethanes were developed and characterized *in vitro*. The formulations can be easily prepared in the operating room by hand mixing, and delivered to bone defects using a straight-bore syringe. The β-TCP phase was included to increase osteoconductivity of the composite,

while the reactive polyurethane was anticipated to improve handling properties and reduce the brittleness of the calcium phosphate.

Incorporation of β-TCP particles into polymers has been reported to decrease the mechanical strength of composites due to incompatibility between phases [40]. Thus, the surface of β-TCP particles was modified with covalently grafted PCL chains to improve the interactions between the reactive polyurethane and ceramic phases. TGA and XPS analysis revealed successful polymer grafting (Figure 4.1C-D) on the surface, with a decrease in particle size as an additional effect of the protonation step. Contact angle measurements of non-reactive polyurethane on TCP and TCP-PCL pellets suggested a slight improvement in the interactions between the phases as evidenced by improved wetting of the TCP-PCL pellets. However, contact angle measurements were affected by changes in the surface topography and porosity of the pellets, as evidenced by the difficulty for measuring water contact angles on TCP-PCL samples. As a result, these measurements need to be complemented with additional characterization of the polymer-ceramic interface.

Interactions between polymer-coated particles and the polymeric matrix in composite materials not only depend on the surface chemistry of the particles but also on the arrangement of polymeric chains at the interface [41]. An important variable influencing the conformation of terminally anchored polymer chains is the surface grafting density (σ, chains/nm^2) [42]. Previous work studying the conformation of anchored polymer chains in the presence of a cross-linked network identified a critical value of grafting density:

$$\sigma_{crit} = \frac{1}{b^2 N} \quad (4.3)$$

where *b* corresponds to the Kuhn length of the polymer and *N* is the number of repeat units in the chain [43-45]. At low grafting densities ($\sigma < \sigma_{crit}$) the chains remain close to the surface without penetrating the network. On the other hand, if higher grafting densities are achieved ($\sigma > \sigma_{crit}$), the entropic cost of excluding the chains from the network is higher than the energy penalty associated to the network swelling due to interdigitation of the chains [44]. As a result, the chains extend away from the surface creating a brush layer capable of penetrating the network. The thickness of the resulting brush layer (*L*) can be estimated by assuming equilibrium at the interface such that the chemical potential of the polymer network is the same at the interface as in the bulk [43]. Mean-field theory has been used to calculate the free energy at the interface and defined the equilibrium condition in terms of α_0 (dimensionless layer thickness) as:

$$\alpha_0^3 - \frac{\left(1+\frac{1}{9}\emptyset_p^2\right)}{\alpha_0} = \frac{1}{6}z \qquad (4.4)$$

where *z* (0 under theta-conditions under which the polymer acts as ideal chains) is the ratio of excluded volume per chain to the volume occupied by the chain at ideal conditions [43]. $\emptyset_p = \frac{N\sigma w^{1/2}}{b}$ is the dimensionless surface density which takes into account three-body interactions of the chains through $w^{1/2} = \frac{MW_{RU}v}{NA}$, where MW_{RU} is the molecular weight of the repeating units, *v* is the specific volume (calculated from density values) and *NA* is Avogradro's number. After solving for α_0, the layer thickness can be calculated as $L = \alpha_0 N^{1/2} b$. Layer thickness has been reported to influence the interfacial adhesion energy at the interface of a polymeric layer anchored to a surface and an elastomeric network [41]. Deruelle et. al. characterized this relation using the JKR method (Johnson, Kendal, Roberts method [46]) and reported the interfacial adhesion energy

approaching a maximum value as the layer thickness approached 15 nm [41]. Even though other variables such as grafting procedure, and molecular weight between crosslinks of the elastomer changed the absolute value of the energy, the maximum value was always achieved at a similar thickness. The authors associated the enhancement of interfacial adhesion to penetration of the chains into the network.

The relations described above in combination with measured parameters for the modified particles, such as PCL surface content and molecular weight, were used to characterize the conformation of PCL chains at the surface of TCP-PCL in the presence of the PUR network assuming equilibrium and theta-conditions. These calculations provide a boundary condition of the system in which all the grafted chains act as active connectors between the ceramic surface and the network. The variables and results of these calculations are presented in Table 4.2.

Table 4.2. Interaction parameters between the ceramic and polymer network

Variable	Calculated value
PCL Kuhn length, *b* (nm)	0.7 [47]
Critical surface grafting density, σ_{crit} (chains nm^{-2})	0.015
Surface grafting density, $\sigma_{TCP\text{-}PCL}$ (chains nm^{-2})	0.238
Dimensionless layer thickness, α_0	1.61
Interfacial layer thickness, L (nm)	13.0

The calculated surface grafting density of the modified particles ($\sigma_{TCP-PCL}$) was higher than σ_{crit} suggesting that in presence of the PUR network the PCL grafted on the surface of TCP adopted a brush conformation, with a calculated layer thickness of 13 nm, close to the thickness with maximum adhesion energy reported by Deruelle et al.

Although the real layer thickness between the phases may have different dimensions, interpenetration of the chains is also favored by the low elasticity of the network [41] before the polyurethane completely sets.

SEM images and mechanical properties of the composites provided additional evidence of improved interactions between the modified TCP-PCL particles and the polyurethane binder. Compressive properties of formulations with 105 and 140 index including TCP, p-TCP, and TCP-PCL particles showed that while TCP composites were insensitive to changes in polyurethane index, p-TCP and TCP-PCL both had improved mechanical properties when excess isocyanate was present. This suggests that in addition to the strengthening mechanism of PCL interpenetration into the PUR network discussed previously, reactivity between hydroxyl groups at the surface of p-TCP and TCP-PCL with excess isocyanate groups can also improve interfacial interactions. While TCP composites exhibited a dramatic decrease (15-97%) of mechanical properties after 24 hrs in PBS, TCP-PCL composites had higher stability under water presenting a decrease in properties in the range of 35-61%. Reduction of mechanical properties of composites in an aqueous environment has been associated to a plasticizing effect of the absorbed water, degradation of the polymeric phase, and/or diffusion of water through the organic/inorganic interface [35, 40, 36]. Given that the polyurethane binder in our study had the same characteristics between the unstable TCP and more stable TCP-PCL composites, it is more likely that increased interfacial interactions in the TCP-PCL composites reduced water diffusion and enhanced the performance of the materials. In contrast to our results, previous studies incorporating ~10 vol% of modified TCP particles (with grafted poly(L-lactide) chains with molecular weight between 390 – 1,050 $g \cdot mol^{-1}$) in a

poly(D,L-lactide) matrix have reported improved coupling between phases (imaged with SEM) without any improvements in the mechanical properties when compared to composites with non-modified TCP particles [20]. However, for linear polymers, physical crosslinks due to chain entanglements result as the molecular weight of the polymer approaches the molecular weight for entanglements M_e [48], which for poly(lactide) is ~9,000 $g \cdot mol^{-1}$ [49]. Furthermore, models predicting the mechanical properties of filled polymers have shown that tensile strength of composites with significant interfacial interactions increases only when the filler volume fraction is above 15% [50]. In our case, the molecular weight of the grafted PCL was similar to the reported M_e for PCL (15,000 $g \cdot mol^{-1}$ [51]), and the filler loadings evaluated were above 45 vol%. It is important to highlight that the effect of filler surface modification was significant up to filler contents of 56.7 vol%. It is possible that above this value particle-particle instead of particle-polymer interactions become more significant due to changes in the packing distribution of the filler.

As shown in Figure 4.7, TCP-PCL composites developed in this work have higher mechanical properties than several calcium phosphate formulations recently reviewed [8]. TCP-PCL composites with high matrix loadings (>55 vol.%) exhibited compressive properties in the range of trabecular bone: compressive modulus of 100-500 MPa, and compressive strength of 4-12 MPa [8]. Since the mechanical properties of the composites are expected to decrease as initial degradation of the polymer takes place, TCP-PCL

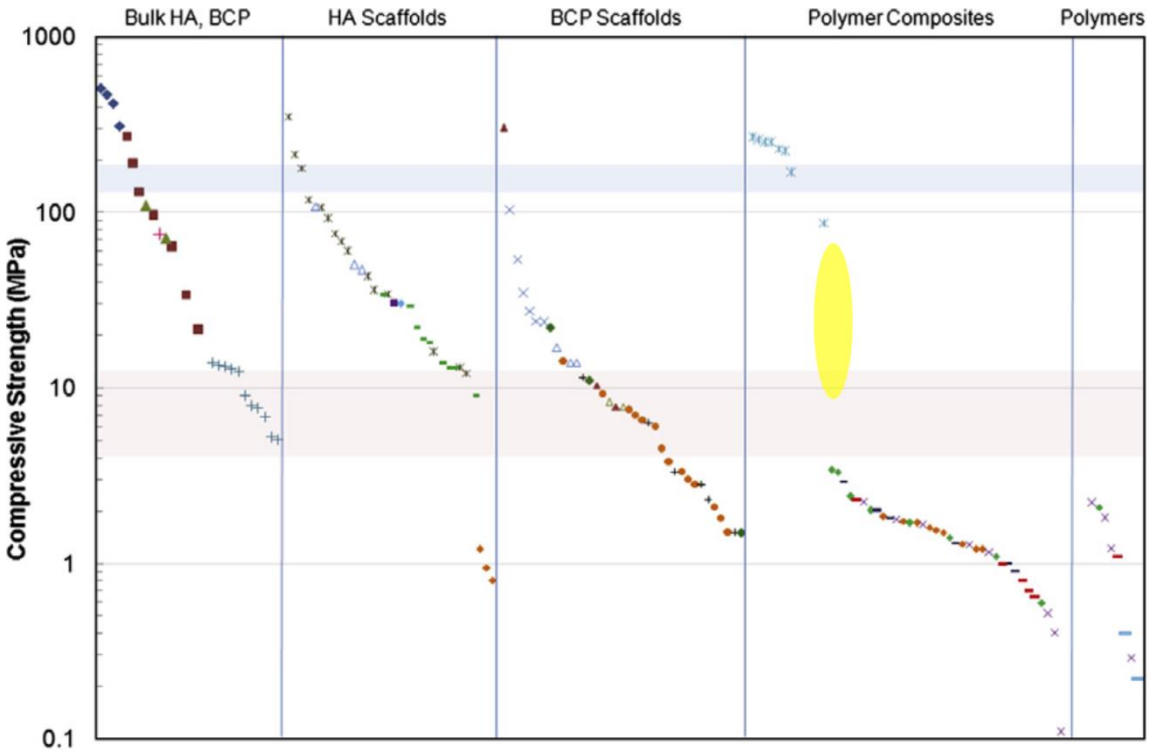

Figure 4.7. Compressive strength of calcium phosphates and calcium phosphates/polymer composites (modified with permission from [8]). Blue area: Cortical bone properties, Red area: Trabecular bone properties, Yellow area: properties of TCP-PCL composites developed in this study.

composites with initial strength between that of cortical and trabecular bone (<55 vol%) can support defects in trabecular bone as degraded polymer is replaced by new bone deposition [8]. However, when composites with 56.7 vol% of TCP or TCP-PCL were tested under torsion, their properties were significantly lower than those reported for human [26, 52], bovine [53, 54], canine [55], and ovine [56, 57] trabecular bone (Table 4.1). Due to limited reported data of calcium phosphate/polymer composites evaluated under torsion [58], comparison with other formulations was not possible. However, we have recently developed a polymeric biocomposite with surface modified bioactive glass particles which has compressive and torsional properties exceeding those of trabecular bone (unpublished results). This suggests that the surface modification of a stronger and less

brittle ceramic further improves the performance of polyurethane biocomposites under both, compression and torsion.

Low porosity polyurethane composites have been shown to support cellular infiltration and remodeling *in vivo* [9, 13, 18]. Composite formulations developed in this study are expected to remodel in a similar fashion, according to the *in vitro* characterization results which show that surface modification of ceramic surfaces allowed attachment and differentiation of osteoblast and osteoclast precursors. Even though compared to dentin controls the TCP and TCP-PCL composites had an initial lag in the activation of osteoclasts, the lag disappeared after 15 days of culture. Increased surface roughness and differences in mechanical properties between the composite phases influence the attachment and morphology of cells [38]. Thus it is possible that osteoclast precursors seeded on dentin samples were able to attach faster and start the differentiation process before the cells seeded on TCP-PCL materials. This small lag is not expected to pose problems for the *in vivo* remodeling of the composites. A limitation of the *in vitro* methods is that during the cutting of the samples for cell culture TCP-PCL grains are also cut through exposing non-modified surfaces which can promote cellular development. *In vivo* studies of hydroxyapatite/PCL composites with high and low levels of embedding of the ceramic by the polymer showed enhanced osteoconductive behavior in composites with low embedding of the hydroxyapatite (increased exposed surface) [37]. Thus, further *in vivo* studies should be completed to verify the ability of cells to infiltrate the low porosity composites developed in this study.

Conclusions

TCP-PCL/PUR composites with compressive mechanical properties between those of trabecular and cortical bone were developed. Improved interactions between β-TCP particles and the PUR phase were achieved by covalently grafting PCL to the surface of the filler. The resulting TCP-PCL composites had higher compressive mechanical properties and stability under aqueous conditions than TCP composites (non-modified). No significant effect of surface modification on cell differentiation or activity was identified *in vitro*. Thus, surface modification of ceramic particles is a suitable technique to improve the mechanical performance of settable composites for bone tissue engineering. The application of this technique with stronger and less brittle fillers is a promising alternative to develop formulations with initial weight-bearing capabilities.

References

1 J. A. Buckwalter, M. J. Glimcher, R. R. Cooper, and R. Recker, 'Bone Biology. I: Structure, Blood Supply, Cells, Matrix, and Mineralization', *Instr Course Lect,* 45 (1996), 371-86.

2 P. V. Giannoudis, H. Dinopoulos, and E. Tsiridis, 'Bone Substitutes: An Update', *Injury,* 36 Suppl 3 (2005), S20-7.

3 S. Kotani, Y. Fujita, T. Kitsugi, T. Nakamura, T. Yamamuro, C. Ohtsuki, and T. Kokubo, 'Bone Bonding Mechanism of Beta-Tricalcium Phosphate', *J Biomed Mater Res,* 25 (1991), 1303-15.

4 M. Neo, S. Kotani, Y. Fujita, T. Nakamura, T. Yamamuro, Y. Bando, C. Ohtsuki, and T. Kokubo, 'Differences in Ceramic-Bone Interface between Surface-Active Ceramics and Resorbable Ceramics: A Study by Scanning and Transmission Electron Microscopy', *J Biomed Mater Res,* 26 (1992), 255-67.

5 V. James Sammarco, and Laurette Chang, 'Modern Issues in Bone Graft Substitutes and Advances in Bone Tissue Technology', *Foot and Ankle Clinics of North America,* 7 (2002), 19-41.

6 Yusuf Khan, Michael J. Yaszemski, Antonios G. Mikos, and Cato T. Laurencin, 'Tissue Engineering of Bone: Material and Matrix Considerations', *J Bone Joint Surg Am,* 90 (2008), 36-42.

7 K. Rezwan, Q. Z. Chen, J. J. Blaker, and Aldo Roberto Boccaccini, 'Biodegradable and Bioactive Porous Polymer/Inorganic Composite Scaffolds for Bone Tissue Engineering', *Biomaterials,* 27 (2006), 3413-31.

8 A. J. Wagoner Johnson, and B. A. Herschler, 'A Review of the Mechanical Behavior of Cap and Cap/Polymer Composites for Applications in Bone Replacement and Repair', *Acta Biomater,* 7 (2011), 16-30.

9 T. Yoshii, J. E. Dumas, A. Okawa, D. M. Spengler, and S. A. Guelcher, 'Synthesis, Characterization of Calcium Phosphates/Polyurethane Composites for Weight-Bearing Implants', *Journal of Biomedical Materials Research Part B-Applied Biomaterials,* 100B (2012), 32-40.

10 Jian Ying Zhang, Eric J. Beckman, Nicholas P. Piesco, and Sudha Agarwal, 'A New Peptide-Based Urethane Polymer: Synthesis, Biodegradation, and Potential to Support Cell Growth in Vitro', *Biomaterials,* 21 (2000), 1247-58.

11 Jian Han, Bing Chen, Lin Ye, Ai-ying Zhang, Jian Zhang, and Zeng-guo Feng, 'Synthesis and Characterization of Biodegradable Polyurethane Based on Poly(E-Caprolactone) and L-Lysine Ethyl Ester Diisocyanate', *Frontiers of Materials Science in China,* 3 (2009), 25-32.

12 S. A. Guelcher, A. Srinivasan, J. E. Dumas, J. E. Didier, S. McBride, and J. O. Hollinger, 'Synthesis, Mechanical Properties, Biocompatibility, and Biodegradation of Polyurethane Networks from Lysine Polyisocyanates', *Biomaterials,* 29 (2008), 1762-75.

13 J. E. Dumas, T. Davis, G.E. Holt, T. Yoshii, D. S. Perrien, J. S. Nyman, T. Boyce, and S.A. Guelcher, 'Synthesis, Characterization, and Remodeling of Weight-Bearing Allograft Bone/Polyurethane Composites in the Rabbit', *Acta Biomaterialia,* 6 (2010), 2394-406.

14 J. E. Dumas, K. Zienkiewicz, S. A. Tanner, E. M. Prieto, S. Bhattacharyya, and S. A. Guelcher, 'Synthesis and Characterization of an Injectable Allograft Bone/Polymer Composite Bone Void Filler with Tunable Mechanical Properties', *Tissue Engineering Part A,* 16 (2010), 2505-18.

15 Ian C. Bonzani, Raju Adhikari, Shadi Houshyar, Roshan Mayadunne, Pathiraja Gunatillake, and Molly M. Stevens, 'Synthesis of Two-Component Injectable Polyurethanes for Bone Tissue Engineering', *Biomaterials,* 28 (2007), 423-33.

16 Raju Adhikari, Pathiraja A. Gunatillake, Ian Griffiths, Lisa Tatai, Malsha Wickramaratna, Shadi Houshyar, Tim Moore, Roshan T. M. Mayadunne, John Field, Margaret McGee, and Tania Carbone, 'Biodegradable Injectable Polyurethanes: Synthesis and Evaluation for Orthopaedic Applications', *Biomaterials*, 29 (2008), 3762-70.

17 J. E. Dumas, K. Zienkiewicz, S. A. Tanner, E. M. Prieto, S. Bhattacharyya, and S. A. Guelcher, 'Synthesis and Characterization of an Injectable Allograft Bone/Polymer Composite Bone Void Filler with Tunable Mechanical Properties', *Tissue Eng Part A*, 16, 2505-18.

18 J. E. Dumas, E. M. Prieto, K.J. Zienkiewicz, T. Guda, J. C. Wenke, J. Bible, G.E. Holt, and S.A. Guelcher, 'Balancing the Rates of New Bone Formation and Polymer Degradation Enhances Healing of Weight-Bearing Allograft/Polyurethane Composites in Rabbit Femoral Defects', *Tissue Eng Part A*, Not available - ahead of print (2013).

19 F. H. Norman-Taylor, N. Santori, and R. N. Villar, 'The Trouble with Bone Allograft', *BMJ*, 315 (1997), 498.

20 C. Kunze, T. Freier, E. Helwig, B. Sandner, D. Reif, A. Wutzler, and H. J. Radusch, 'Surface Modification of Tricalcium Phosphate for Improvement of the Interfacial Compatibility with Biodegradable Polymers', *Biomaterials*, 24 (2003), 967-74.

21 S. Guelcher, A. Srinivasan, A. Hafeman, K. Gallagher, J. Doctor, S. Khetan, S. McBride, and J. Hollinger, 'Synthesis, in Vitro Degradation, and Mechanical Properties of Two-Component Poly(Ester Urethane)Urea Scaffolds: Effects of Water and Polyol Composition', *Tissue Engineering*, 13 (2007), 2321-33.

22 Murat Barsbay, Olgun Güven, Martina H. Stenzel, Thomas P. Davis, Christopher Barner-Kowollik, and Leonie Barner, 'Verification of Controlled Grafting of Styrene from Cellulose Via Radiation-Induced Raft Polymerization', *Macromolecules*, 40 (2007), 7140-47.

23 Guelcher, 'Synthesis, Mechanical Properties, Biocompatibility, and Biodegradation of Polyurethane Networks from Lysine Polyisocyanates.', *Biomaterials* (2008).

24 ASTM, 'D4274: Standard Test Methods for Testing Polyurethane Raw Materials: Determination of Hydroxyl Numbers of Polyols', (1999).

25 ASTM, 'D2572: Standard Test Method for Isocyanate Groups in Urethane Materials or Prepolymers', (1997).

26 K. Bruyere Garnier, R. Dumas, C. Rumelhart, and M. E. Arlot, 'Mechanical Characterization in Shear of Human Femoral Cancellous Bone: Torsion and Shear Tests', *Med Eng Phys*, 21 (1999), 641-9.

27 C. M. Ford, and T. M. Keaveny, 'The Dependence of Shear Failure Properties of Trabecular Bone on Apparent Density and Trabecular Orientation', *J Biomech*, 29 (1996), 1309-17.

28 Hidetaka Hayashi, Ken-ichi Nakahama, Takahiro Sato, Takehiko Tuchiya, Yasuyuki Asakawa, Toshimitu Maemura, Masanobu Tanaka, Mineto Morita, and Ikuo Morita, 'The Role of Mac-1 (Cd11b/Cd18) in Osteoclast Differentiation Induced by Receptor Activator of Nuclear Factor-Kb Ligand', *FEBS Letters*, 582 (2008), 3243-48.

29 GregoryR Mundy, 'Regulatory Mechanisms of Osteoclast Differentiation and Function', *Journal of Bone and Mineral Metabolism*, 14 (1996), 59-64.

30 Steven L. Teitelbaum, 'Bone Resorption by Osteoclasts', *Science*, 289 (2000), 1504-08.

31 Anthony J. Janckila, Ranga N. Parthasarathy, Latha K. Parthasarathy, Ratnam S. Seelan, Yi-Cheung Hsueh, Jukka Rissanen, Sari L. Alatalo, Jussi M. Halleen, and Lung T. Yam, 'Properties

and Expression of Human Tartrate-Resistant Acid Phosphatase Isoform 5a by Monocyte-Derived Cells', *Journal of Leukocyte Biology,* 77 (2005), 209-18.

32 Barrie Kirstein, Timothy J. Chambers, and Karen Fuller, 'Secretion of Tartrate-Resistant Acid Phosphatase by Osteoclasts Correlates with Resorptive Behavior', *Journal of Cellular Biochemistry,* 98 (2006), 1085-94.

33 J. M. Halleen, H. Ylipahkala, S. L. Alatalo, A. J. Janckila, J. E. Heikkinen, H. Suominen, S. Cheng, and H. K. Väänänen, 'Serum Tartrate-Resistant Acid Phosphatase 5b, but Not 5a, Correlates with Other Markers of Bone Turnover and Bone Mineral Density', *Calcified Tissue International,* 71 (2002), 20-25.

34 Anthony J. Janckila, Karen Takahashi, Susan Z. Sun, and Lung T. Yam, 'Naphthol-Asbi Phosphate as a Preferred Substrate for Tartrate-Resistant Acid Phosphatase Isoform 5b', *Journal of Bone and Mineral Research,* 16 (2001), 788-93.

35 R. E. Neuendorf, E. Saiz, A. P. Tomsia, and R. O. Ritchie, 'Adhesion between Biodegradable Polymers and Hydroxyapatite: Relevance to Synthetic Bone-Like Materials and Tissue Engineering Scaffolds', *Acta Biomaterialia,* 4 (2008), 1288-96.

36 P. S. Uskokovic, C. Y. Tang, C. P. Tsui, N. Ignjatovic, and D. P. Uskokovic, 'Micromechanical Properties of a Hydroxyapatite/Poly-L-Lactide Biocomposite Using Nanoindentation and Modulus Mapping', *Journal of the European Ceramic Society,* 27 (2007), 1559-64.

37 S. Scaglione, E. Lazzarini, C. Ilengo, and R. Quarto, 'A Composite Material Model for Improved Bone Formation', *Journal of Tissue Engineering and Regenerative Medicine,* 4 (2010), 505-13.

38 Karen Fuller, Jade L. Ross, Kinga A. Szewczyk, Raymond Moss, and Tim J. Chambers, 'Bone Is Not Essential for Osteoclast Activation', *PLoS ONE,* 5 (2010), e12837.

39 R. Kruger, and J. Groll, 'Fiber Reinforced Calcium Phosphate Cements -- on the Way to Degradable Load Bearing Bone Substitutes?', *Biomaterials,* 33 (2012), 5887-900.

40 Blanca Vázquez, María Pau Ginebra, Xavier Gil, Josep Antón Planell, and Julio San Román, 'Acrylic Bone Cements Modified with -Tcp Particles Encapsulated with Poly(Ethylene Glycol)', *Biomaterials,* 26 (2005), 4309-16.

41 M. Deruelle, L. Leger, and M. Tirrell, 'Adhesion at the Solid-Elastomer Interface: Influence of the Interfacial Chains', *Macromolecules,* 28 (1995), 7419-28.

42 P. G. de Gennes, 'Conformations of Polymers Attached to an Interface', *Macromolecules,* 13 (1980), 1069-75.

43 W. B. Russel, D. A. Saville, and W. R. Schowalter, *Colloidal Dispersions* (Australia: Cambridge University Press, 1999).

44 M. Geoghegan, C. J. Clarke, F. Boué, A. Menelle, T. Russ, and D. G. Bucknall, 'The Kinetics of Penetration of Grafted Polymers into a Network', *Macromolecules,* 32 (1999), 5106-14.

45 K. P. O'Connor, and T. C. B. McLeish, '"Molecular Velcro": Dynamics of a Constrained Chain into an Elastomer Network', *Macromolecules,* 26 (1993), 7322-25.

46 K. L. Johnson, K. Kendall, and A. D. Roberts, 'Surface Energy and the Contact of Elastic Solids', *Proceedings of the Royal Society of London. A. Mathematical and Physical Sciences,* 324 (1971), 301-13.

47 Dinorah Herrera, Jean-Carlos Zamora, Alfredo Bello, Mario Grimau, Estrella Laredo, Alejandro J. Müller, and Timothy P. Lodge, 'Miscibility and Crystallization in Polycarbonate/Poly(E-

Caprolactone) Blends: Application of the Self-Concentration Model', *Macromolecules*, 38 (2005), 5109-17.

48 Hugh R. Brown, and Thomas P. Russell, 'Entanglements at Polymer Surfaces and Interfaces', *Macromolecules*, 29 (1996), 798-800.

49 John R. Dorgan, Joshua S. Williams, and David N. Lewis, 'Melt Rheology of Poly(Lactic Acid): Entanglement and Chain Architecture Effects', *Journal of Rheology (1978-present)*, 43 (1999), 1141-55.

50 Lawrence E. Nielsen, 'Simple Theory of Stress-Strain Properties of Filled Polymers', *Journal of Applied Polymer Science*, 10 (1966), 97-103.

51 Alper Gurarslan, Jialong Shen, and Alan E. Tonelli, 'Behavior of Poly(E-Caprolactone)S (Pcls) Coalesced from Their Stoichiometric Urea Inclusion Compounds and Their Use as Nucleants for Crystallizing Pcl Melts: Dependence on Pcl Molecular Weights', *Macromolecules*, 45 (2012), 2835-40.

52 M. Halawa, A. J. C. Lee, R. S. M. Ling, and S. S. Vangala, 'Shear-Strength of Trabecular Bone from Femur, and Some Factors Affecting Shear-Strength of Cement-Bone Interface', *Archives of Orthopaedic and Trauma Surgery*, 92 (1978), 19-30.

53 J. L. Stone, G. S. Beaupre, and W. C. Hayes, 'Multiaxial Strength Characteristics of Trabecular Bone', *J Biomech*, 16 (1983), 743-52.

54 R. B. Ashman, J. D. Corin, and C. H. Turner, 'Elastic Properties of Cancellous Bone: Measurement by an Ultrasonic Technique', *J Biomech*, 20 (1987), 979-86.

55 S. K. Eswaran, M. R. Allen, D. B. Burr, and T. M. Keaveny, 'A Computational Assessment of the Independent Contribution of Changes in Canine Trabecular Bone Volume Fraction and Microarchitecture to Increased Bone Strength with Suppression of Bone Turnover', *J Biomech*, 40 (2007), 3424-31.

56 D. Mitton, C. Rumelhart, D. Hans, and P. J. Meunier, 'The Effects of Density and Test Conditions on Measured Compression and Shear Strength of Cancellous Bone from the Lumbar Vertebrae of Ewes', *Med Eng Phys*, 19 (1997), 464-74.

57 M. Kasra, and M. D. Grynpas, 'On Shear Properties of Trabecular Bone under Torsional Loading: Effects of Bone Marrow and Strain Rate', *J Biomech*, 40 (2007), 2898-903.

58 M. Bohner, 'Design of Ceramic-Based Cements and Putties for Bone Graft Substitution', *Eur Cells Mater*, 20 (2010), 1-12.

CHAPTER V

BALANCING THE RATES OF NEW BONE FORMATION AND POLYMER DEGRADATION ENHANCES HEALING OF WEIGHT-BEARING ALLOGRAFT/POLYURETHANE COMPOSITES IN RABBIT FEMORAL DEFECTS

Introduction

Periarticular fractures involve a weight-bearing joint and often have depressed portions that require extensive open reduction and internal fixation along with subchondral grafting to maintain articular congruence. Maintenance of articular reduction and joint congruity are important for both bone healing and articular alignment, since lack of articular congruence after fractures increases the likelihood of osteoarthritis [1]. While autograft remains the standard of care for bone healing, calcium phosphate (CaP) cements (CPCs) have proven to be superior to autograft for maintaining articular congruence of tibial plateau fractures [2]. A recent retrospective study has reported that 61% of patients treated with buttress plating and autograft experienced loss of reduction after one year compared to 23% of patients treated with a hydroxyapatite (HA) bone cement [3]. However, HA bone cement does not extensively remodel and is not replaced by new bone. Moreover, the brittleness and low shear strength of CPCs adversely impact their ability to bear mechanical loads, requiring the use of large, mechanically rigid internal fixation devices (such as buttress plating), which has been suggested to increase complications [4].

Settable, weight-bearing bone grafts ideally exhibit both initial bone-like mechanical properties and also remodel with minimal resorption gaps such that the

strength of the graft exceeds that of host bone during all stages of healing. Injectable bone void fillers (BVFs) include non-setting allograft [5] and non-allogenic pastes [6], which are typically delivered using viscous carriers (e.g., sodium hyaluronate [7], glycerol [8], or dextran [9]) resulting in weak mechanical properties. Resorbable CPCs [10-13], such as β-TCP (slowly resorbed by osteoclasts) or calcium sulfate (CSH) and brushite (undergo dissolution), have also been used to enhance bone healing. Tri-phasic CPCs comprising CSH, brushite, and granular β-TCP have been shown to heal metaphyseal defects in preclinical [14] and clinical studies [15]. However, rapid dissolution of CSH and brushite at rates exceeding that of new bone formation can result in loss of mechanical strength [16], as well as the appearance of a fibrous resorption gap between the ingrowing new bone and the resorbing cement [17, 18]. While the initial compressive strength of CPCs is comparable to that of trabecular bone, they undergo brittle fracture at strains less than the yield strain of trabecular bone, resulting in failure due to fatigue under physiologically relevant cyclic loads where the shear component is significant [19, 6]. Reinforcement with polymeric, bioactive glass, or ceramic fibers has been reported to enhance strength and ductility of CPCs, resulting in strengths approaching 50 MPa for poly(lactic-co-glycolic acid) (PLGA) fibers [20] and 130 MPa for magnesium alloy fibers [21].

Despite the growing interest in weight-bearing settable bone grafts, there is a paucity of studies investigating *in vivo* remodeling in preclinical models. While several studies have reported that weight-bearing grafts heal and form new bone [22-25], there is limited understanding of the mechanisms by which these grafts remodel *in vivo*, which is essential for designing grafts that ideally maintain bone-like strength during the entire healing process [26]. It has been suggested that the degradation rates of the polymer and

ceramic phases must be balanced to optimize healing, which is a challenging problem due to the fundamentally different mechanisms by which polymers and ceramics degrade [26]. In this study, we investigated the effects of the rates of new bone formation, matrix resorption, and polymer degradation on healing of settable, weight-bearing polyurethane (PUR) composites comprising approximately equivalent volume fractions of polymer and matrix. Based on our previous study reporting that allograft bone particles (ABP) embedded in a degradable lysine-derived PUR network remodel by creeping substitution [22], we investigated ABP as the reinforcing particulated matrix phase. We hypothesized that matching the rate of new bone formation to that of polymer degradation would optimize healing. To test this hypothesis, we augmented the ABP/PUR composites with either 105 or 420 μg cm^{-3} recombinant human bone morphogenetic protein-2 (rhBMP-2), which was anticipated to increase the rate of new bone formation. Further, rhBMP-2 has been reported to promote zero-order degradation of the PUR network [27], resulting in more closely balanced rates of bone formation and PUR degradation. The composites were injected into cylindrical defects in the femoral condyles of rabbits and evaluated by micro-computed tomography (μCT) and histomorphometry at 0, 6, and 12 weeks.

Experimental

Materials

LTI-PEG prepolymer (23.6% NCO), poly(ε-caprolactone-*co*-D.L-lactide-*co*-glycolide) triol [162 mg KOH/g and M_n = 1393 g/mol (measured by gel permeation chromatography)], and rabbit allograft mineralized bone particles (ABP, 180 ± 70 μm) were received as a gift from Medtronic, Inc. (Memphis, TN) [28]. Triethylenediamine

(TEDA) catalyst was received as a gift from Goldschmidt (Hopewell, VA), and recombinant human bone morphogenetic protein (rhBMP-2) was purchased from R&D systems (Minneapolis, MN). Trehalose dehydrate, heparin sodium salt, acetonitrile, and trifluoroacetic acid (TFA) were purchased from Sigma Aldrich (St. Louis, MO).

Preparation of rhBMP-2

The rhBMP-2 was supplied as a solution comprising 35% acetonitrile and 0.1% TFA. A separate acetonitrile/TFA solution was prepared containing a ratio of 10:1 of trehalose dehydrate:heparin sodium. The rhBMP-2 and trehalose mixtures were combined such that the ratio of rhBMP-2 to trehalose was 1:125. The resulting mixture was distributed in glass vials and frozen at -80^{o}C in preparation for freeze-drying, which produced a powder.

Synthesis of ABP/PUR Biocomposites

The appropriate amounts of polyester triol, ABP, and LTI-PEG prepolymer were added to a mixing cup and mixed by hand for 90 s. The index (ratio of NCO:OH equivalents x 100) was 130. The resulting paste and the catalyst (5500 ppm TEDA) were then added to the rhBMP-2 vial and mixed for 60 s. The filler content (ABP and rhBMP-2 powder) was maintained at 70 wt% (56.7 vol%) for each biocomposite (BC) treatment group (Table 5.1). Two rhBMP-2 doses were investigated: 420 μg cm^{-3} and 105 μg cm^{-3}, corresponding to 100% and 25% of the dose recommended for the absorbable collagen sponge (ACS) for rabbits [29]. The porosities of the composites (measured

gravimetrically[27]) were 5.7 ± 2.0% (0 μg rhBMP-2 cm^{-3}), 2.7 ± 0.6% (105 μg rhBMP-2 cm^{-3}), and 1.6 ± 0.4% (420 μg rhBMP-2 cm^{-3}).

Table 5.1. Treatment groups evaluated in the rabbit femoral condyle plug defect study.

Treatment Group	rhBMP-2 (μg/mL)	6 weeks	12 weeks
Empty	0	6	6
ABP	0	6	6
Biocomposite (BC)	0	9	10
BC + BMP-L	105	9	10
BC + BMP-H	420	9	8

Rheological properties

The curing profile of the BC without rhBMP-2 (n=4) was determined using a TA Instruments AR2000ex rheometer. The reactive biocomposite was loaded between 25 mm diameter disposable plates and compressed to a gap of 1.5 mm. Measurements of storage (G') and loss (G") moduli were performed using an oscillatory time sweep method with a frequency of 1 Hz and amplitude of 1% strain. The working time of the BC, defined as the time from the start of mixing until cure, was determined as the G'-G" cross-over point. The flow characteristics of the BC were analyzed by removing the catalyst from the formulation (n=3). Non-setting samples were poured between 40mm cross-hatched parallel plates, compressed to a gap of 1.5 mm, and subjected to a dynamic frequency sweep (0.1 to 100 rad sec^{-1}) at 25°C with controlled strain amplitude of 0.02%. A Cox-Merz transformation was applied to the dynamic data to obtain the steady state viscosity (η, Pa*s) as a function of shear rate (γ, s^{-1}). The data were fit to the Herschel-Bulkley model, which relates the viscosity and shear rate of solid-filled suspensions with high solids content [30], to estimate the yield stress (τ_Y, Pa) of the material:

$$\eta = \tau_Y \dot{\gamma}^{-1} + K\dot{\gamma}^{(n-1)} \quad (5.1)$$

where K is the consistency index of the composite (constant) and n is the power-law index of the suspending polymer, which in this case is the non-reactive mixture of polyester triol and LTI-PEG prepolymer.

Mechanical properties

Cylindrical (6-mm diameter) samples of each treatment group were prepared for mechanical testing. The reactive paste was transferred into cylindrical plastic cups and a 1-lb weight (20.7 psi) was placed on the material for 10 min. Cylinders were cured in a vacuum oven at 37^{o}C overnight, removed from the plastic cups, and cut using a Buehler saw to a length of 12 mm. After 24 hours of hydration in phosphate buffered saline (PBS), the samples were tested using an MTS 898 by preloading to 12N followed by compression at a rate of 25mm/min until failure. The original cross sectional area of the cylinders was used to calculate compressive stress. The ultimate properties reported in this article correspond to the point where maximum stress was achieved. To prepare samples for torsion testing, ~5 mm at each end of 6-mm diameter cylinders was potted into Technovit 4000 (Heraeus Kulzer) resulting in a central gauge length of about 10 mm. The potting material was prepared by mixing the powder:syrup I:syrup II using a ratio of 2:2:1 following the manufacturer's instructions. After potting, the torsion samples were hydrated for 24 hrs in PBS and then tested using an Instron DynaMight 8841 machine equipped with a 1.7 Nm torque cell. The potted ends were gripped using the Instron clamps in a horizontal setup (such that the residual torque was minimal). During testing,

the clamps were rotated at an angular speed of 2°/s until failure. The measured torque and rotation angle were used to determine torsional stress using the equation [31, 32]:

$$\tau = [\theta(dT/d\theta) + 3T]/(2\pi r^3) \quad (5.2)$$

where r is the radius of the cylinder, $\theta = \alpha/L$ is the rotation angle per gauge unit length, and T is the measured torque. The derivative $dT/d\theta$ was determined by fitting the T vs. θ data to a 5th order polynomial (between zero up to the maximum torque or ultimate point). Torsional strain (γ) was determined as $\gamma = \theta r$, and the shear modulus calculated from the linear region of the stress-strain curve $G = \tau/\gamma$. Toughness was calculated as the corresponding area under the stress-strain curve from zero to the maximum stress.

Animal Study

Forty-two New Zealand White (NZW) rabbits weighing between 3.8 and 4.1 kg were used in this study. All surgical and care procedures were carried out under aseptic conditions per the approved Institutional Animal Care Use Committee (IACUC) protocol. The ABP/PUR putty components were gamma irradiated using a dose of ~25 kGY. Glycopyrrolate was administered at 0.01 mg/kg intramuscularly (IM) followed by ketamine at 40 mg/kg IM. Bilateral defects of ~6 mm diameter by 11 mm in depth were drilled in the lateral metaphysis of the distal femurs of each rabbit. ABP/PUR plugs from each treatment group (Table 5.1) were subsequently injected into each defect using a 1 mL syringe (modified by cutting the needle hub adapter). Treatment groups for each composite were dispersed randomly among the rabbits with rhBMP-2 treatment groups paired in each rabbit to eliminate systemic effects. The wound was closed approximately

3 minutes after injection. The rabbits were euthanized at both 6 and 12 week time points using Fatal-plus (2.2 mL/10 kg) intra-venously.

μCT Analysis

A μCT40 (SCANCO Medical) was used to acquire images of the extracted femurs post implantation at 6 and 12 weeks. In addition, femurs from NZW rabbits that were part of other experimental protocols which did not affect the skeleton (same age, sex, and similar weight to the rabbits used in this study) were scanned and analyzed as host bone controls. Subsequently, cylindrical defects (6 mm x 11 mm) were created in the host bone controls and filled with the BC formulation. The injected material was left to cure under PBS for 24 hrs before submerging the bone in formalin for further scanning as BC controls (BC, 0w). μCT scans were performed in formalin at 70 kVp energy, 114 μA source current, 1000 projections per rotation, 300 ms integration time, and an isotropic voxel size of 36 μm. A 0.1 mm thick aluminum foil filter was employed to reduce beam hardening. Axial images were reconstructed using manufacturer-provided software. Further beam hardening correction was performed during image reconstruction using the manufacturer's 1200 mg HA cm^{-3} algorithm. Attenuation values were converted to tissue mineral density (TMD) through calibration with hydroxyapatite (HA) phantoms with densities between 0 and 780 mg HA cm^{-3} (calibration of the instrument was checked weekly). Using the cortical borders of the defect for alignment, the reconstructed image stack was re-oriented such that the depth of the defect was parallel to the z-axis. A radial analysis of the morphometric parameters was conducted from the core of the implant to the interphase with host bone. Four concentric annular volumes of interest with thickness

of 1 mm and approximate length of 11mm (from the outer cortical surface of the femur) were defined for each sample. The 3 inner regions incorporated the BCs, while the outer region provided information about the interphase with host bone. Ossified tissue was segmented from soft tissue using a threshold of 480 mg·HA·cm^{-3} and Gaussian noise filter settings of sigma 0.2 and support 2. The threshold conditions were chosen visually and kept constant for the analysis of all the samples. Morphometric parameters within the annular volumes were calculated for each region, grouped by treatment and time point, and plotted versus the mean radial distance from the core of the defect R_m ($R_m=(R_o+R_i)/2$, where R_o and R_i correspond to the outer and inner radius of each region, respectively). Bone volume/total volume (BV/TV), tissue mineral density (TMD, density of the ossified tissue), connectivity density (Conn.D.), trabecular number (Tb.N.), trabecular thickness (Tb.Th.), and trabecular separation (Tb.Sp.) within the regions of interest were computed using SCANCO's Medical microCT systems software.

Histology and histomorphometry

Rabbit femora were placed in a solution of 10% formalin for two weeks followed by a series of ethanol dehydrations. After fixation, the femurs were embedded in poly(methyl methacrylate) and 200-μm sections were cut from the resulting blocks using an Exakt band saw. The sections were then ground and polished using an Exakt grinding system to less than 100 μm and stained with Sanderson's rapid bone stain counterstained with van Gieson. Residual allograft bone particles stained light brown, residual polymer stained black, new bone stained pink with dark blue osteocytes within the matrix, red blood cells stained torquiose, and other cells stained a lighter blue. The sections were

imaged at 10X magnification with an Olympus camera (DP71) using an Olympus BX60 microscope with and without polarizing the light. Residual ABPs, new bone formation, and remaining polymer were quantified in an area of interest 1.5 mm high × 6 mm wide located in the center of the defect. To analyze the radial remodeling of the scaffolds in time, the rectangular area of interest was further subdivided into 3 concentric annular regions (each 1 mm thick): A1, representing the area of the defect in contact with the host bone and up to 1 mm away from the edge of the defect; A2, representing the mid-region of the defect; and A3, representing the core of the defect. Residual allograft was differentiated from new bone by meeting the following three criteria: (i) acellularity, (ii)angular in shape, and (iii) ilumination under polarized light. Metamorph (Version 7.0.1) was utilized to perform histomorphometry using a color thresholding and an image layering technique to quantify the number of pixels of each layer and compare it to the total pixels in the area of interest.

Statistical analysis

Three-way ANOVA, performed in JMP 9.0, was used to determine whether statistical differences existed between treatment groups, area, and time. Comparissons of individual sample groups were performed using a Tukey HSD test. For all experiments $p<0.05$ was considered statistically significant.

Results

Rheological properties

Figure 5.1A shows a representative plot of the storage and loss moduli of the BC without rhBMP-2 during cure. The onset of the curve in Figure 5.1A is delayed due to the time (~9 min) required to set the gap and start data collection after mixing. Initially, the BC exhibits viscoelastic behavior as evidenced by its permanent deformation in response to applied stress, but when the working is reached (G'-G" crossover point at 13.7 ± 3.5 min), it becomes more elastomeric.

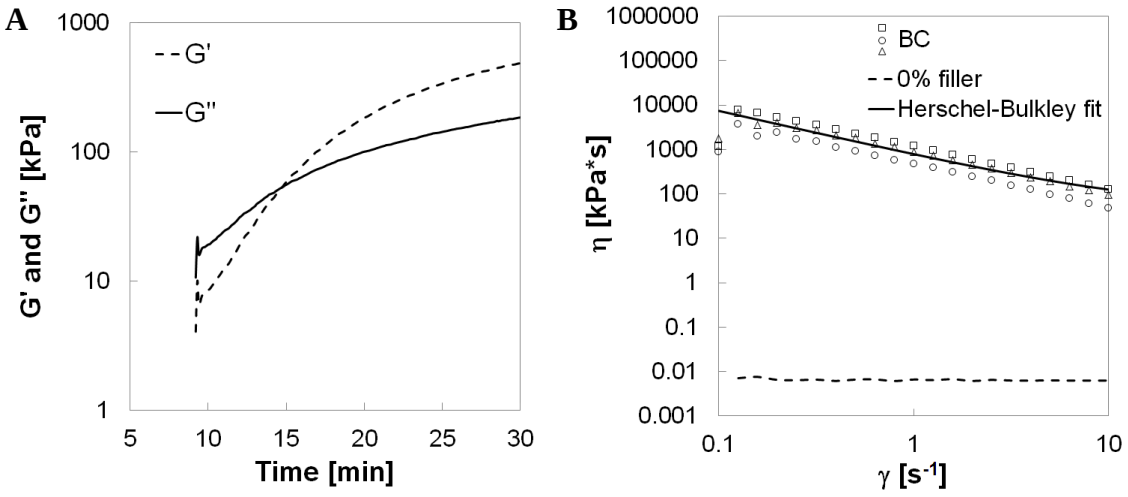

Figure 5.1. Rheological properties of the BC measured by rheometry. (A) *G'* represents the storage modulus and *G''* the loss modulus. The *G'-G''* crossover point is assumed to be the working time of the BC. (B) Viscosity versus shear rate plot illustrating calculation of the yield stress using the Herschel-Bulkley model.

The yield stress τ_Y of a solid-filled suspension can be defined as the minimum stress required for the material to deform [33]. Among the models developed to calculate τ_Y, the Herschel-Bulkley provides the best fit of the data for the non-reactive BC (Figure 5.1B). The suspending polymer (0% ABP) exhibits Newtonian behavior (dotted line)

over the range of shear rates investigated (0.1 – 10 s^{-1}). Consequently, the power-law index *n* (Equation 5.1) of the suspending polymer is equal to unity, and fitting the η vs. γ data to the resulting expression results in τ_Y = 738 kPa. Additionally, the viscosity of the material at 5 s^{-1} (the recommended shear rate at which the viscosity of an injectable material should be reported [34]) is 179 kPa·s. The high initial viscosity suggests that the material is not flowable; however, up to the working time the BC can be molded to conform to the contours of the defect.

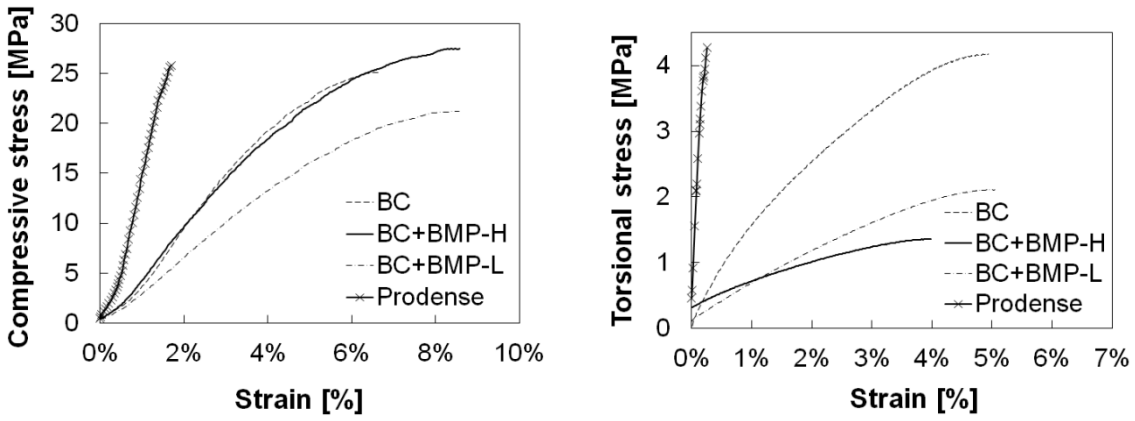

Figure 5.2. Representative stress-strain curves for the BCs and CaP cement under compression and torsion.

Mechanical properties

Representative compression and torsion stress-strain curves measured for the BCs with and without rhBMP-2 are shown in Figure 5.2 and compared to a tri-phasic CPC comprising 75% CSH and 25% brushite/granular β-TCP (ProDense®, Wright Medical) [6]. The Young's modulus, ultimate stress, ultimate strain, and toughness (area under the stress-strain curve) measured under compression and torsion are listed in Table 5.2.

Table 5.2. Mechanical properties of the injectable biocomposites (BC) and the calcium phosphate cement (CPC) measured under compressive and torsional loads. Data are reported as the mean ± Standard error of the mean (SEM).

(A) Compression

Property	CPC	BC	BC+BMP-L	BC+BMP-H
Young's modulus, MPa	1689 ± 197	503 ± 122	452 ± 103	524 ± 68
Stress at failure, MPa	19.9 ± 5.1	24.0 ± 4.8	24.7 ± 6.4	28.3 ± 3.2
Strain at failure, %	1.67 ± 0.03	7.39 ± 0.64	8.41 ± 0.11	8.12 ± 0.28
Energy-to-failure, kJ m^{-3}	168 ± 27	1072 ± 292	1188 ± 180	1395 ± 113

(B) Torsion

Property	CPC	BC	BC+BMP-L	BC+BMP-H
Young's modulus, MPa	2051 ± 45	121 ± 18	56.0 ± 9.5	40.0 ± 6.7
Stress at failure, MPa	2.90 ± 1.38	3.60 ± 1.05	1.80 ± 0.36	1.70 ± 0.20
Strain at failure, %	0.20 ± 0.08	5.0 ± 1.2	4.0 ± 0.6	5.0 ± 0.6
Energy-to-failure, kJ m^{-3}	4.0 ± 3.0	123 ± 53	55.0 ± 16.3	58.0 ± 7.4

Under compression, the modulus of the CPC (1689 MPa) was significantly higher than that of the BCs (450 – 524 MPa), but the strength of the CPC (19.9 MPa) was comparable to that of the BCs (24 – 28 MPa). However, due to the significantly higher ultimate strain for the BCs (7.4 – 8.1%) compared to the CPC (1.7%), the toughness was approximately an order of magnitude greater for the BCs. Addition of rhBMP-2 did not have a significant effect on the mechanical properties of the BCs under compressive loading. Under torsional loading, the modulus of the CPC (2051 MPa) was substantially greater than that of the BCs (40 – 121 MPa). However, the torsional strength of the CPC (2.9 MPa) was comparable to that of the BCs (1.7 – 3.6 MPa). Similar to the results for compression, the ultimate strain was dramatically higher for the BCs (4.0 – 5.0%) compared to the CPC (0.2%). Consequently, the toughness was more than an order of magnitude greater for the BCs. In contrast to the results under compression, the torsional properties decreased when rhBMP-2 was added to the formulations.

μCT Data

Representative μCT images of the BC and control groups after 6 and 12 weeks post-implantation are presented in Figure 5.3. Minimal new bone formation, primarily in the region of the femoral cortex, was observed for the empty and ABP-treated groups at 6 and 12 weeks. These observations suggest that the empty defects did not heal extensively, and that in the absence of the settable PUR binder to maintain the structure of the graft, the allograft particles had resorbed. All BC treatment groups showed evidence of resorption of allograft particles (irregularly shaped bright white particles with sharp edges) and remodeling.

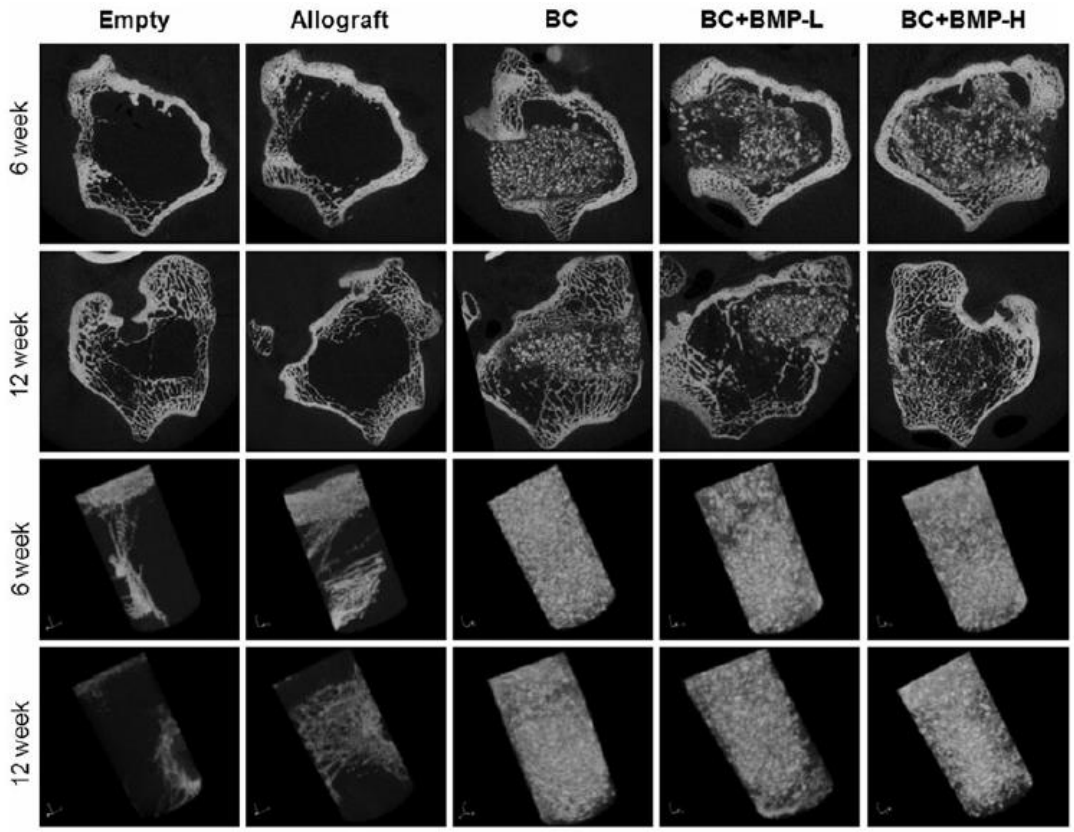

Figure 5.3. Representative images of the empty defects filled with the allograft bone particles, BC, BC+BMP-L, BC+BMP-H at 6 and 12 weeks. Longitudinal sections of the femur and 3D reconstructions of the cylindrical defect region of interest.

Considering that the BCs remodel by creeping substitution of ABPs initiated at the host bone/BC interface, the radial distribution of key morphometric parameters [35] was measured by μCT as shown in Figure 5.4. The defect was divided into four annular regions (Figure 5.4A) extending for 11 mm and the morphometric parameters BV/TV, TMD, Conn.D., Tb.N., Tb.Th., and Tb.Sp were measured for each region. The measured parameters of the samples were compared to those of the BC controls (BC, 0w) and healthy host trabecular bone controls (Host bone control).

As shown in Figure 5.4B, TMD showed minimal variation as a function of radial distance, while the values for all groups were slightly higher at 12 weeks compared to 6 weeks. At 6 weeks, BV/TV (Figure 5.4C) was relatively constant at ~50 vol% for the BC and BC+BMP-H groups, while BV/TV dropped below 40 vol% in the outer regions (e.g., near the bone/BC interface) of the BC+BMP-L group. By 12 weeks, BV/TV (Figure 5.4D) decreased monotonically from the inner core (~50%) to the outer interfacial region (30-45%) for all groups. At 12 weeks, the BC group showed the largest radial change in BV/TV, ranging from values comparable to the BC control ($51\pm0.4\%$) at the inner core to values comparable to host trabecular bone ($30\pm1\%$) at the bone-composite interface. None of the groups showed resorption gaps where BV/TV dropped below that of host trabecular bone.

In addition to TMD and BV/TV, several standard morphometric parameters [35], including mean trabecular thickness (Tb.Th.), mean trabecular separation (Tb.Sp.), trabecular number (Tb.N.), and connectivity density (Conn.D.), were plotted as a function R_m. Values for each treatment group were compared to measured values for BC controls (0 weeks) and host trabecular bone.

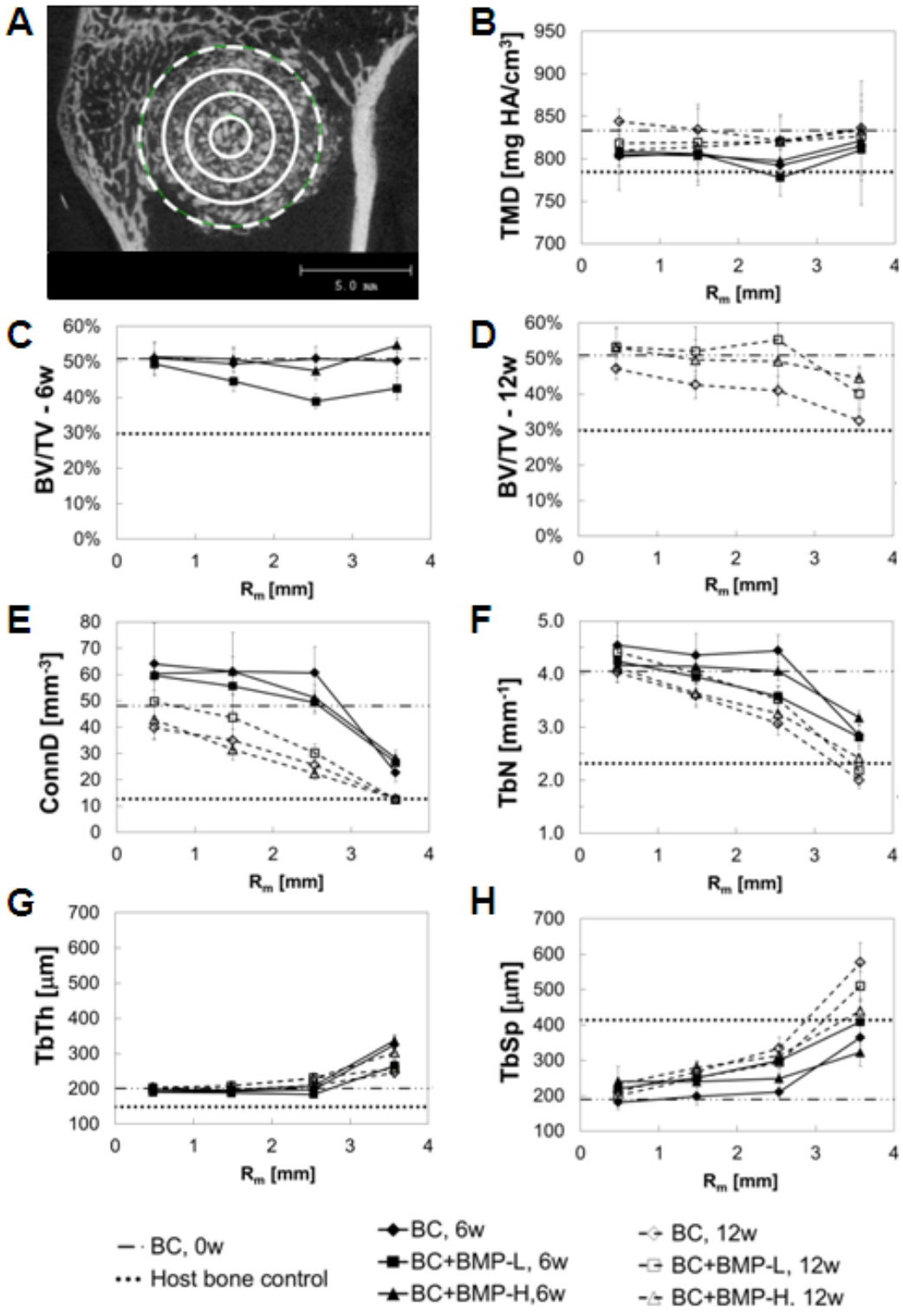

Figure 5.4. Radial distribution of morphometric parameters measured by µCT at 6 and 12 weeks. (A) Representative image highlighting subdivision of the defect into four annular shells each 1mm thick. (B)-(H) Morphometric parameters evaluated are plotted versus the mean radial distance from the core (Rm).

As shown in Figure 5.4E, F, and H, Conn.D., Tb.N., and Tb.Sp. progressed monotonically from values comparable to that of the BC control in the inner core region to values comparable to that of the host trabecular bone in the outer annular region. At each point in space and time, the differences between each rhBMP-2 dose were modest. However, values of Conn.D. and Tb.N. decreased from 6 to 12 weeks at each distance and rhBMP-2 dose, while Tb.Sp. increased. Similar to BV/TV, Conn.D., Tb.N., and Tb.Sp. did not drop below values measured for host bone in any region for any of the groups. Interestingly, Tb.Th. exhibited an opposite trend in which the parameter did not converge to the value measured in the host bone as the radial distance increased. Instead, Tb. Th. increased monotonically from values close to that of the BC controls (201$\pm$4μm) in the inner core region to 240–340 μm in the outer annular region compared to 149$\pm$2.6 μm for the host bone.

Histology and histomorphometry

Histological sections of the empty defects at 6 weeks (Figure 5.5) show minimal new bone formation, which is consistent with the μCT data. However, histological sections of the BC treatment groups (Figure 5.6) reveal evidence of cellular infiltration (CI), allograft (A) resorption, and new bone formation (NB). High magnification views show regions of active remodeling, osteoid formation, appositional growth of new bone on residual allograft particles, and bridging of allograft particles by new bone, suggesting that the biocomposites remodel by creeping substitution [22, 28, 27]. In contrast, allograft-treated defects supported minimal ingrowth of new bone, which is consistent with the notion that the continuous polymer phase is essential for supporting new bone formation.

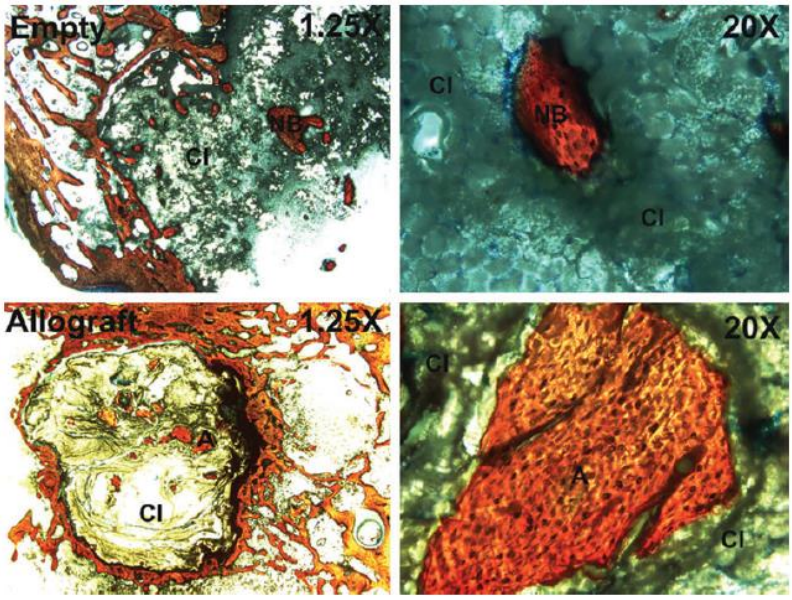

Figure 5.5. Low (1.25x) and high (20x) magnification images of histological sections of untreated (empty – top) and allograft-filled (bottom) defects at 6 weeks. CI: Cellular infiltration, A: Allograft particles.

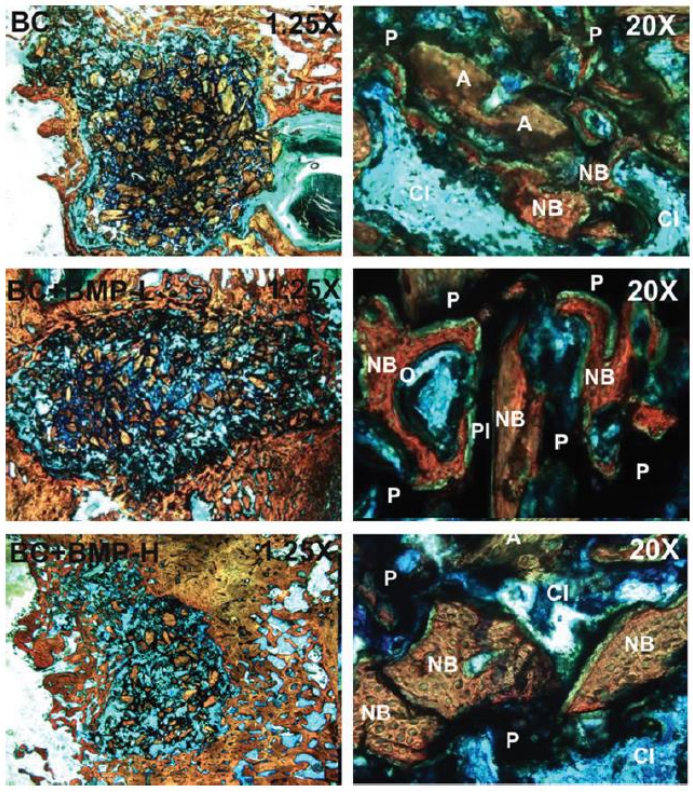

Figure 5.6. (A) Low (1.25x) and high (20x) magnification images of histological sections of the biocomposite treatment groups at 6 weeks. P: residual polymer, O: Osteoid, NB: New bone formation.

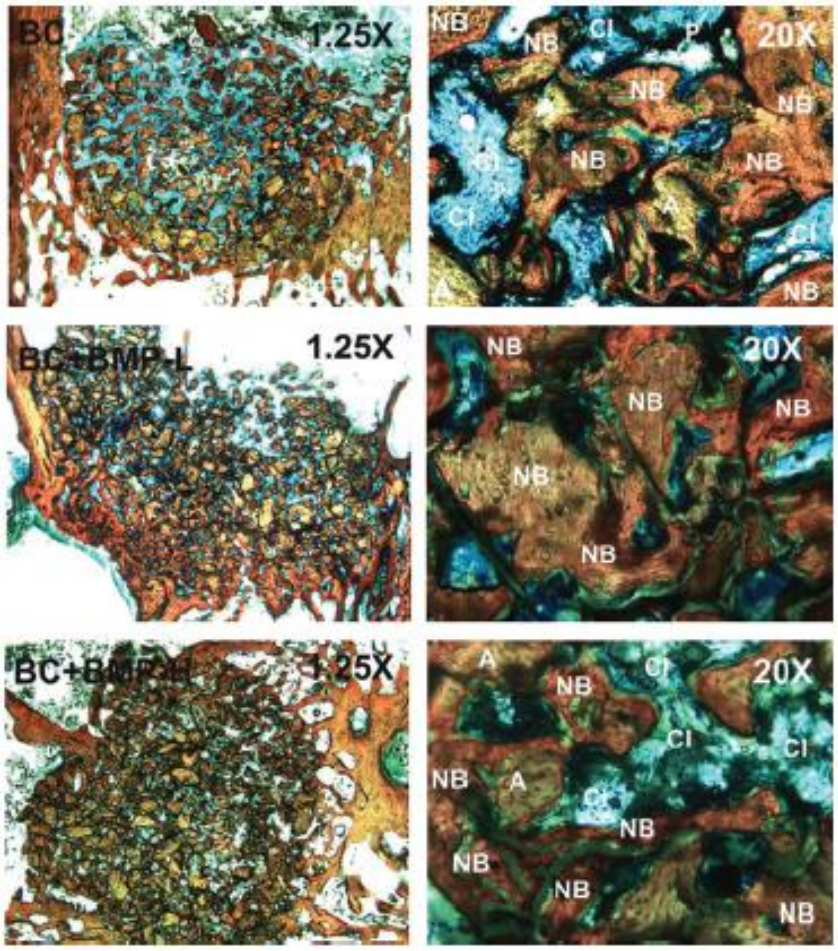

Figure 5.6 (continued). (B) Low (1.25x) and high (20x) magnification images of histological sections of the biocomposite treatment groups at 12 weeks. P: residual polymer, O: Osteoid, NB: New bone formation.

Histomorphometric analysis of each area of interest (labeled A1, A2, and A3 in Figure 5.7A) revealed an increase in new bone formation for all BC treatment groups between 6 and 12 weeks (Figure 5.7B-D). Differences over time within a specific area were significant only for A1 in the BC+BMP-L and BC+BMP-H groups, and differences between areas at each time point were not significant for any groups. Area% new bone formation data were fit to the following empirical equation ($R^2 \sim 1$ for all fits):

$$\%B = \frac{at}{(1+bt)} \tag{5.3}$$

where a and b are fitting parameters (Table 5.3). In the outer region (A1), $b \rightarrow 0$ for all groups, suggesting that ingrowth of new bone near the host bone interface is a zero-order process. Thus, bone forms at an approximately constant rate $r_B = d(\%B)/dt$ = mineral apposition rate, which has been reported as ~4 μm·day^{-1} for the distal femur of rabbits [36]. However, b = 0.307 in the inner region of group BC (Figure 5.7B), indicating that the rate of new bone formation decreased from 6 to 12 weeks. As anticipated, augmentation with rhBMP-2 increased the rate of new bone formation, but differences between the high and low dose were not significant. In the inner region, the parameter b is lower for the BC+BMP-L (Figure 5.7C) and BC+BMP-H (Figure 5.7D) groups compared to the BC group, suggesting that the rate of new bone formation in the interior of the graft is decreasing less in the presence of rhBMP-2.

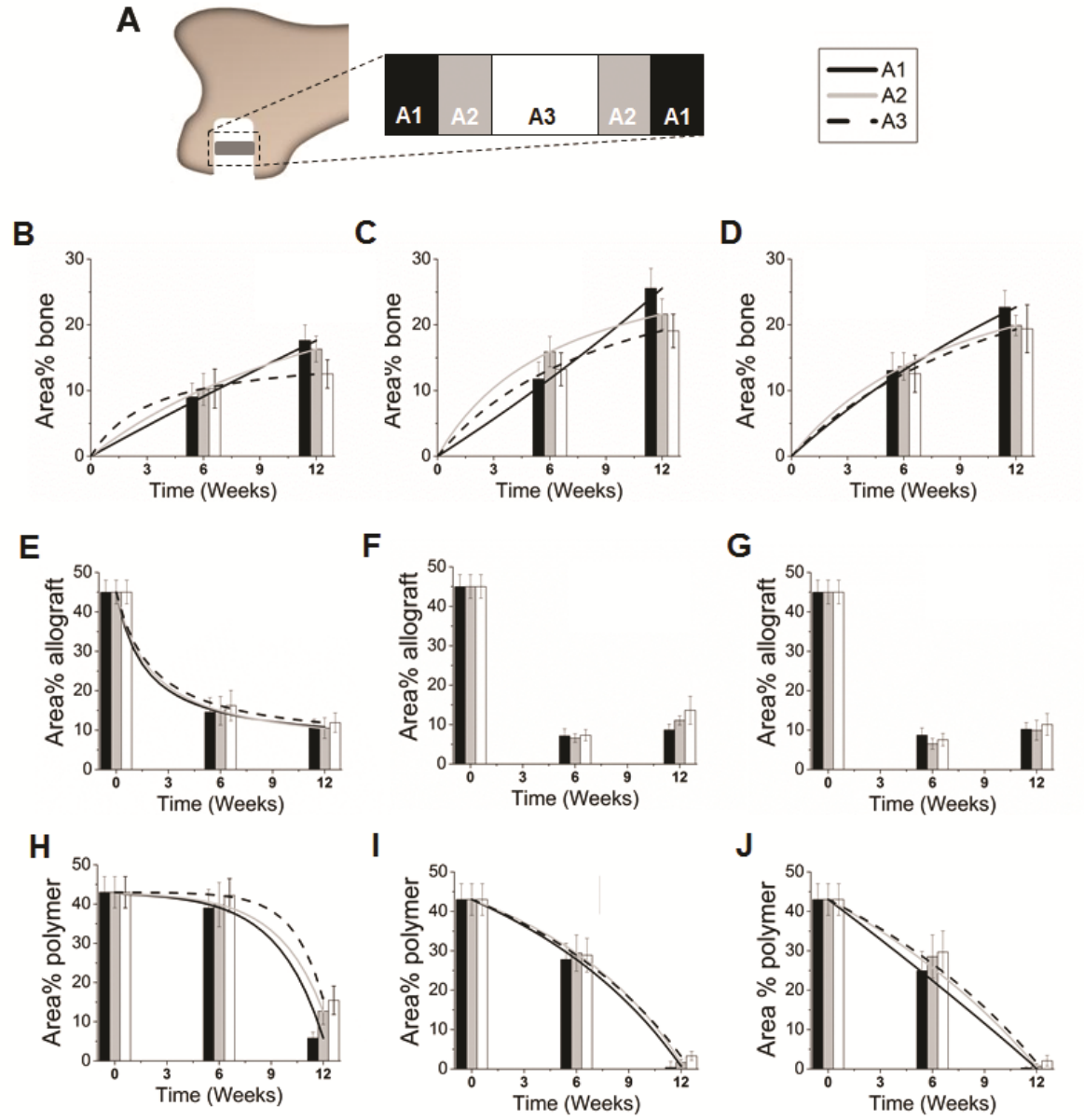

Figure 5.7. Histomorphometric evaluation of remodeling of the biocomposite scaffolds. (A) Diagram showing the areas of interest. Area% new bone, Area % remaining allograft particles, and Area% remaining polymer for (B,E,H) BC, (C,F,I) BC+BMP-L, and (D,G,J) BC+BMP-H

Table 5.3. Fitting parameters for bone (B) histomorphometry data, which were fit to area% B = $at/(1+bt)$.

	A1		A2		A3	
Group	***a***	***b***	***a***	***b***	***a***	***b***
BC	1.57	0.0059	2.27	0.0560	4.88	0.307
BC+BMP-L	1.82	-0.0121	5.02	0.149	3.56	0.103
BC+BMP-H	2.58	0.0304	3.66	0.101	3.00	0.072

Histomorphometry data for residual allograft are presented for each area in Figure 5.7E-G. Area% allograft (A) data for the BC group (Figure 5.7E) were fit to the following equation:

$$\%A = A_{A,i} - \frac{at}{(1+bt)} \tag{5.4}$$

where $A_{A,i}$ is the initial area% allograft in the sample at t = 0. Values of the fitting parameters *a* and *b* for each group are listed in Table 5.4. As anticipated, for the BC group the area% allograft decreased with time due to osteoclast-mediated resorption [27, 22, 28], but the differences between 6 and 12 weeks were not significant for any group. The half-life varied from 2.3 – 2.9 weeks. In the presence of rhBMP-2, the area% residual allograft was significantly less than in the BC group at 6 weeks, suggesting that rhBMP-2 accelerated allograft resorption at early time points. Interestingly, no significant changes in allograft area% were observed in the rhBMP-2 treatment groups from 6 to 12 weeks. Due to the transient resorption of allograft at 6 weeks, it was not possible to fit the area% allograft data to eq (5.4) in the presence of rhBMP-2.

Table 5.4. Fitting parameters for allograft (A) histomorphometry data, which were fit to area% A = $A_{A,i}$ - *at*/(1+*bt*) for the BC group. The parameter $A_{A,i}$ is the initial area% allograft measured by histomorphometry. Data for BC+BMP-L and BC+BMP-H groups could not be accurately fit to the exponential or rational functions.

	A1			**A2**			**A3**		
Group	***a***	***b***	**$t_{1/2}$ (wk)**	***a***	***b***	**$t_{1/2}$ (wk)**	***a***	***b***	**$t_{1/2}$ (wk)**
BC	22.8	0.583	2.3	0.318	0.380	2.6	0.023	0.590	2.9

Polymer degradation was affected by both time and rhBMP-2 dose (Figure 5.7H-J). Differences between 6 and 12 weeks were significant within a specific area for all

groups, but differences between areas were not significant. Area% polymer (P) data for the BC group (Figure 5.7H) were fit to the following equation:

$$\%P = A_{P,i} - \alpha \exp^{\beta t} \tag{5.5}$$

where $A_{P,i}$ is the initial area% polymer in the sample at t = 0. The half-life of the polymer ranged from 10.5 – 11.5 weeks, which is substantially longer than that of the allograft but slightly shorter than $t_{1/2}$ = 14 weeks reported *in vitro* [37]. Similar to observations from *in vitro* studies, the degradation profile of the poly(ester urethane) is consistent with an autocatalytic mechanism [37] and does not follow the first-order kinetics associated with ester hydrolysis [38]. Local delivery of rhBMP-2 (Figure 5.7I-J) changed the shape of the area% polymer curve, which was fit to an equation similar to the one used for new bone:

$$\%P = A_{P,i} - \frac{at}{(1+bt)} \tag{5.6}$$

Table 5.5. Fitting parameters for polymer (P) histomorphometry data, which were fit to area% P = $A_{P,i}$ - at/(1+bt) for BC+BMP-L and BC+BMP-H groups and to area% P = $A_{P,i}$ – αexp(βt) for the BC group. The parameter $A_{P,i}$ is the initial area% polymer measured by histomorphometry.

	A1			A2			A3		
Group	***a* (α)**	***b* (β)**	**$t_{1/2}$ (wk)**	***a* (α)**	***b* (β)**	**$t_{1/2}$ (wk)**	***a* (α)**	***b* (β)**	**$t_{1/2}$ (wk)**
BC	0.408	0.376	10.5	0.318	0.380	11.0	0.023	0.590	11.5
BC+BMP-L	1.98	-0.0365	6.4	1.69	-0.0425	8.3	1.83	-0.0373	8.2
BC+BMP-H	3.30	-0.0062	6.3	2.44	-0.0258	7.2	2.24	-0.0292	7.5

As evidenced by the values of $b \rightarrow 0$ (Table 5.5), the process of PUR degradation in the presence of rhBMP-2 is nearly zero-order (i.e., constant rate). Augmentation with rhBMP-2 also accelerated PUR degradation, as evidenced by $t_{1/2}$ = 6.4 – 8.3 weeks for BC+BMP-L and $t_{1/2}$ = 6.3 – 7.5 weeks for BC+BMP-H. Differences in residual polymer were significant between the BC group and the BC+BMP-L and –H groups at 6 weeks,

but not at 12 weeks. Thus, rhBMP2 both altered the mechanism of PUR degradation and also increased the degradation rate.

Discussion

Weight-bearing bone grafts have generated considerable interest in recent years, but the mechanisms by which they remodel, while maintaining their initial bone-like strength are poorly understood. In this study, we investigated the effects of the rate of new bone formation, the rate of reinforcing matrix (allograft) resorption, and the mechanism of polymer degradation on healing of ABP/PUR composites in femoral condyle plug defects in rabbits. The initial compressive strength (24–28 MPa) and toughness (1070–1400 $kJ \cdot m^{-3}$) of the composites were comparable to or exceeding those of trabecular bone (6 MPa and 1050 $kJ \cdot mm^{-3}$, respectively [39]). When injected into femoral condyle plug defects in NZW rabbits, new bone formation and healing progressed in both space and time for up to 12 weeks. Polymer degradation was autocatalytic and new bone formation was approximately zero-order in the absence of rhBMP-2, resulting in incomplete healing in the inner core of the graft at later time points. In contrast, local delivery of rhBMP-2 increased the rate of new bone formation, and promoted approximately zero-order degradation of the continuous polymer phase, resulting in improved healing at later time points. Thus, balancing the rates of new bone formation and polymer degradation was observed to improve healing.

The settable composites exhibited a working time of 13.7 ± 3.5 min, which is longer than the value of 4.5 min reported for an injectable, flowable bone void filler (36 vol% ABP [27]) and the working times of 6–10 min reported for CPCs [40, 41]. A proposed

criterion for injectability of CPCs dictates that the material can be administered from a syringe by applying a force < 100 N [6]. Consequently, a syringe with diameter >13-mm would be required to inject the BC due to its high yield stress (738 kPa). Similarly, the viscosity of the BC at 5 s^{-1} is substantially higher (18×10^3 Pa·s) than that of other injectable bone grafts, such the flowable ABP void filler (170 Pa·s [27], 35 vol% ABP) or flowable CPCs (5 – 10 Pa·s, 35 – 39 vol% solids [34]). Thus, while the BC has higher initial viscosity and yield stress compared to other BVFs due to its high solids content (57 vol%), it is moldable and settable within a clinically relevant time frame, which enables the surgeon to conform the graft to the contours of the bone defect [42].

The initial compressive strength (24.0 ± 4.8 MPa) and modulus (503 ± 122 MPa) of the BCs exceed values reported for trabecular bone, which range from 3.7–8.4 MPa and 104–300 MPa, respectively [43, 44, 39, 45]. Similarly, the ultimate strain of the BCs (7.3±0.6%) exceeds that of trabecular bone in human femora (1.05±0.46%) [46]), while the toughness (1072±292 kJ·m^{-3}) is comparable to that of trabecular bone (1000 kJ·m^{-3} [39]). Under torsional deformation, the strength and modulus of the BCs are 2.9±1.4 MPa and 121±18 MPa, respectively, which are close to values reported for human [31, 47], bovine [48, 49], canine [43], and ovine [50, 51] trabecular bone ranging from 3.1 to 7.7MPa and 263 to 366MPa, respectively. However, the ultimate strain of the BC (5.0±1.2%) is comparable to a previous study reporting strain at failure of 4.6±1.3% for trabecular bone [31]. Taken together, these observations suggest that the initial mechanical properties of the BCs are comparable to those of trabecular bone under compression and slightly weaker under torsion.

Recent studies have reported that the poor mechanical properties of CPCs under the physiologically relevant conditions of cyclic loading with a significant shear component [52] limit their use to non-load-bearing applications [19, 6]. The weak shear and torsional properties of these materials have been attributed to their inherent brittleness; however, there are limited toughness and fatigue data. Therefore, we compared the toughness of the BCs to an injectable tri-phasic CPC that supports bone healing in both preclinical models [14] and patients [53]. The toughness of the CPC was ~6 times less than that of the BC and trabecular bone under compression, while under torsion the toughness of the CPC was ~30 times less than that of the BC. The reduced toughness of the CPC is attributed in part to its lower ultimate strain compared to the BC and trabecular bone under compression (1.7%) and torsion (0.2%). While the area under the stress-strain curve is a convenient estimate of toughness, it is not a true material property [19], and thus the fatigue properties, fracture toughness, and/or other measures of reliability (such as the Weibull modulus) must be characterized to assess the potential of the BC to promote healing in weight-bearing bone defects.

While incorporation of calcium phosphate has been reported to increase osteoconductivity for some polymers [54], a recent review has reported that in most studies it does not increase the strength of polymer/ceramic composites [19]. As an exception to this trend, HA/poly(lactic acid) (HA/PLLA) composites incorporating negligible porosity and ~20 vol% HA particles exhibited bending strengths up to 280 MPa. However, since bridging between the ceramic particles and host bone was dependent upon the degradation of PLLA [55], the rate of remodeling was slow, as evidenced by the fact that 4% of the composite implanted in rabbit femora remained after 7 years [56]. Furthermore,

the resorption zone near the host bone interface resulting from phagocytosis of the implant by histocytes [56] is anticipated to reduce its strength. Compression-molded ABP/PUR BCs incorporating 68 vol% ABP exhibited compressive strengths ranging from 100 to 170 MPa and supported extensive cellular infiltration at 6 weeks in rabbit femoral condyle defects [22]. However, only modest new bone formation (~2%) was observed at 6 weeks. The grafts remodeled by creeping substitution, a process characterized by resorption of allograft particles by osteoclasts [27] followed by infiltration of osteoblasts into the newly formed pore [27, 22, 28]. Subsequent new bone formation was observed on the surfaces of both the polymer and also the residual allograft particles. However, as the polymer degraded the grafts filled with fibrous tissue due to the lack of a continuous surface for new bone growth. In the present study, the ABP control group with no polymer exhibited extensive resorption of allograft particles and minimal new bone formation away from the cortex. These observations underscore the need for a continuous polymer phase to persist throughout the interior of the BC until the defect has almost fully healed.

To overcome the limitations of previous studies, settable ABP/PUR composites were designed to incorporate 43% polymer, which formed a continuous phase. New bone formation in the outer region of all grafts progressed at a nearly constant rate (Figure 5.7B-D)). However, $r_B = d(\%B)/dt$ in the inner regions decreased with time, suggesting that mass-transfer limitations associated with infiltration of cells from the host bone into the interior of the scaffold slowed bone formation. Recently, a diffusion model for bone formation in osteoconductive scaffolds has been proposed [57]:

$$\frac{\partial c}{\partial t} = \alpha \Delta c \qquad (5.7)$$

where c denotes BV/TV, Δ is the Laplacian, and α ($mm^2 \cdot day^{-1}$) is the scaffold osteoconduction coefficient. Incorporation of ABPs, which resorb by osteoclastic resorption (fast) rather than dissolution (slow), at loadings sufficiently high to present a percolated phase resulted in relatively rapid ($t_{1/2} < 3$ weeks) resorption of the reinforcing matrix. However, the μCT radial analysis (Figure 5.4) shows that BV/TV progressed monotonically toward values approaching those of host bone near the interface, with no evidence of extensive resorption gaps. These observations point to the potential utilization of α as an independent design parameter that can be controlled by varying either the intrinsic resorption rate or loading of the reinforcing matrix.

Local delivery of rhBMP-2 increased the rate of bone formation and had a transient effect on allograft resorption at 6 weeks. These observations are consistent with *in vitro* and preclinical studies reporting that BMP-2 upregulates osteoclast differentiation and activity [58-61] and drives osteoclast-mediated resorption at high doses [62]. Similar observations have been made for rhBMP-2 released from an absorbable collagen sponge (ACS) implanted in femoral condyle plug defects in sheep [62]. However, transient allograft resorption observed in previous studies has generally been associated with doses of rhBMP-2 considerably higher than the recommended values. Exogenous rhBMP-2 also modified the degradation kinetics of the poly(ester urethane) network [27, 63]. While the mechanism of polymer degradation in the presence of rhBMP-2 is not well understood, rhBMP-2 has been reported to recruit monocytes [64] that degrade lysine-derived PUR scaffolds by an oxidative mechanism [65]. Thus, the zero-order polymer degradation kinetics observed in the presence of rhBMP-2 may be macrophage-mediated.

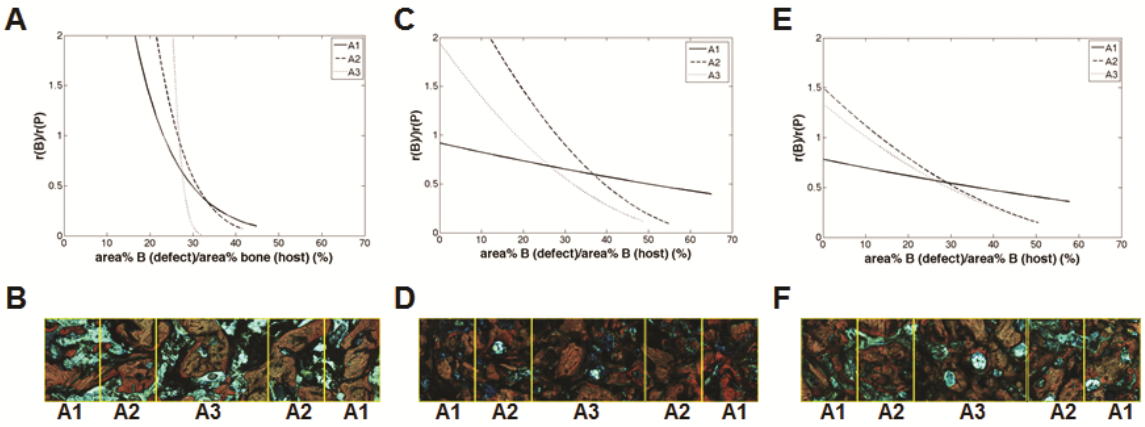

Figure 5.8. Analysis of histomorphometric data. The ratio of the rate of new bone formation (r_B) to that of polymer degradation (r_P) was calculated for each group by differentiating the equations expressing area% new bone and area% polymer as a function of time. Representative images of histological sections with highlighted areas of interest. (A-B) BC, (C-D) BC+BMP-L, and (E-F) BC+BMP-H

The histomorphometry data were further analyzed in Figure 5.8 to gain insight into the design criteria for weight-bearing bone grafts. The rate of new bone formation r_B relative to the rate of polymer degradation ($r_P = -d(\text{area\% P})/dt$) is plotted versus the parameter f_H, which approximates the fractional healing of the defect:

$$f_H = \frac{\text{area\% bone in defect}}{\text{area\% bone in host bone}} \qquad (5.8)$$

The area% bone in the host bone was measured by histomorphometry to be 39.3±1.9%. For the BC at early stages of healing, $r_B/r_P >> 1$ but it decreased dramatically with time (Figure 5.8A). A representative histological section (Figure 5.8B) shows poor surface connectivity at 12 weeks, characterized by isolated islands of polymer and allograft. The consequences of mismatched rates of new bone formation and polymer degradation are particularly acute in the inner region, where $r_B/r_P \rightarrow 0$ at $f_H = 32\%$ healing, at which time the surface is likely insufficiently interconnected to continue to support cellular infiltration and consequent new bone formation. Thus, autocatalytic degradation

of the PUR network driven by carboxylic acid groups formed after hydrolysis of ester bonds does not match the zero-order kinetics of new bone formation [66], resulting in poor healing in the inner region.

In the presence of exogenous rhBMP-2, the rates of new bone formation and polymer degradation were more balanced. Although r_B/r_P monotonically decreased with time in the presence of rhBMP-2 (Figure 5.8C,E), the effect was substantially weaker than in the BC group, and in the outer region r_B/r_P was nearly constant. The relative rate r_B/r_P approached values <0.2 in the inner regions, but by this time (12 weeks) healing had progressed to f_H>50%. The representative histological sections from the BC+BMP-L (Figure 5.8D) and BC+BMP-H (Figure 5.8F) groups show a more connected surface in the inner regions (A2 and A3) for continued bone growth at 12 weeks. Taken together, the data in Figure 5.8 suggest that to optimize bone healing, the polymer must persist until a sufficient amount of new bone has formed to provide a continuous surface, and that the rate of degradation of the continuous polymeric phase should be matched to the rate of new bone formation. While a polyester with a longer half-life [37] is anticipated to delay the onset of rapid polymer degradation until later stages of healing, autocatalytic degradation of these materials could result in unpredictable outcomes. In contrast, polymers that degrade at a constant rate, for example by enzymatic degradation, are anticipated to more closely match the rate of new bone formation [26].

Settable weight-bearing bone grafts could potentially transform the management of tibial plateau fractures, screw augmentation, vertebroplasty, and other orthopaedic indications, but their success is predicated on the ability to maintain sufficient bone-like strength while actively remodeling. Weight-bearing composites generally comprise a

resorbable reinforcing matrix (e.g., short fibers [20, 21] or particles [22, 56]) dispersed in a continuous phase (e.g., polymers or ceramics). A recent review highlighting the challenges associated with the design of weight-bearing composites has suggested that the rates of degradation of the reinforcing matrix and the continuous phase should be matched to ensure adequate healing [26]. In this study, we found that early resorption of the reinforcing matrix does not affect healing at later time points, but the continuous phase must persist until sufficient new bone has formed. Hydrolytically degradable polymers undergo autocatalytic degradation, resulting in poor healing in the interior of the graft due to transport limitations associated with ingrowth of new bone [57]. Closely balancing the rates of new bone formation and polymer degradation, accomplished by local delivery of rhBMP-2 in this study, allowed healing to progress to later stages (up to f_H=70%). A limitation of this study is that none of the areas healed >70% over the 12-week time course. However, our findings point to the importance of both maintaining a continuous surface for bone healing as well as balancing the rates of new bone formation and continuous phase degradation as a strategy for maintaining sufficient bone-like strength over the lifetime of the graft. Polymers that undergo cell-mediated degradation [26] are anticipated to promote balanced remodeling at all stages of healing, which should be assessed by long-term studies.

Conclusions

Moldable, settable ABP/PUR biocomposites exhibited initial mechanical properties comparable to those of trabecular bone. When implanted in plug defects in rabbit femoral condyles, morphometric analysis of both histological sections and μCT

reconstructions revealed that new bone formation and healing progressed in both space and time from the outer region near the host bone interface to the inner core for up to 12 weeks. However, the unbalanced rates of autocatalytic polymer degradation and zero-order new bone formation resulted in incomplete healing in the interior of the composite. Augmentation of the composites with rhBMP-2 increased the rate of new bone formation and induced approximately zero-order degradation of the polymer. The consequent balance of new bone formation and polymer degradation resulted in more extensive healing at later time points in all regions of the graft, including the interior. These observations underscore the importance of both maintaining a continuous polymer surface for new bone growth, as well as matching the rate of new bone formation to that of polymer degradation to promote healing of settable weight-bearing bone grafts that maintain bone-like strength while actively remodeling.

References

1 D. D. Anderson, C. Van Hofwegen, J. L. Marsh, and T. D. Brown, 'Is Elevated Contact Stress Predictive of Post-Traumatic Osteoarthritis for Imprecisely Reduced Tibial Plafond Fractures?', *J Orthop Res,* 29 (2011), 33-9.

2 T. A. Russell, and R. K. Leighton, 'Comparison of Autogenous Bone Graft and Endothermic Calcium Phosphate Cement for Defect Augmentation in Tibial Plateau Fractures. A Multicenter, Prospective, Randomized Study', *J Bone Joint Surg Am,* 90 (2008), 2057-61.

3 D. Simpson, and J. F. Keating, 'Outcome of Tibial Plateau Fractures Managed with Calcium Phosphate Cement', *Injury,* 35 (2004), 913-8.

4 J. A. Hall, M. J. Beuerlein, and M. D. McKee, 'Open Reduction and Internal Fixation Compared with Circular Fixator Application for Bicondylar Tibial Plateau Fractures. Surgical Technique', *J Bone Joint Surg Am,* 91 Suppl 2 Pt 1 (2009), 74-88.

5 Z. Schwartz, M. Goldstein, E. Raviv, A. Hirsch, D. M. Ranly, and B. D. Boyan, 'Clinical Evaluation of Demineralized Bone Allograft in a Hyaluronic Acid Carrier for Sinus Lift Augmentation in Humans: A Computed Tomography and Histomorphometric Study', *Clin Oral Implants Res,* 18 (2007), 204-11.

6 M. Bohner, 'Design of Ceramic-Based Cements and Putties for Bone Graft Substitution', *Eur Cell Mater,* 20 (2010), 1-12.

7 M. Chazono, T. Tanaka, H. Komaki, and K. Fujii, 'Bone Formation and Bioresorption after Implantation of Injectable Beta-Tricalcium Phosphate Granules-Hyaluronate Complex in Rabbit Bone Defects', *J Biomed Mater Res A,* 70 (2004), 542-9.

8 F. P. Cammisa, Jr., G. Lowery, S. R. Garfin, F. H. Geisler, P. M. Klara, R. A. McGuire, W. R. Sassard, H. Stubbs, and J. E. Block, 'Two-Year Fusion Rate Equivalency between Grafton Dbm Gel and Autograft in Posterolateral Spine Fusion: A Prospective Controlled Trial Employing a Side-by-Side Comparison in the Same Patient', *Spine (Phila Pa 1976),* 29 (2004), 660-6.

9 C. Chan, I. Thompson, P. Robinson, J. Wilson, and L. Hench, 'Evaluation of Bioglass/Dextran Composite as a Bone Graft Substitute', *Int J Oral Maxillofac Surg,* 31 (2002), 73-7.

10 C. D. Friedman, P. D. Constantino, S. Takagi, and L. C Chow, 'Bonesource™ Hydroxyapatite Cement: A Novel Biomaterial for Craniofacial Skeletal Yissue Engineering and Reconstruction', *J Biomed Mater Res,* 43 (1998), 428-32.

11 H. Chim, and A. K. Gosain, ' Biomaterials in Craniofacial Surgery Experimental Studies and Clinical Application ', *J Craniofac Surg,* 20 (2009), 29-33.

12 G. Gasparini, R. Boniello, A. Moro, G. Tamburrini, C. Di Rocco, and S. Pelo, 'Cranial Reshaping Using Methyl Methacrylate:Technical Note', *J Craniofac Surg,* 20 (2009), 184-90.

13 A. Moreira-Gonzalez, I. T. Jackson, T. Miyawaki, K. Barakat, and V. DiNick, 'Clinical Outcome in Cranioplasty: Critical Review in Long-Term Follow-Up', *J Craniofac Surg,* 14 (2003), 144-53.

14 R. M. Urban, T. M. Turner, D. J. Hall, N. Inoue, and S. Gitelis, 'Increased Bone Formation Using Calcium Sulfate-Calcium Phosphate Composite Graft', *Clin Orthop Relat Res,* 459 (2007), 110-7.

15 S Gitelis, R. M. Urban, T M Turner, R Heck, and A D Parameswaran, 'Outcomes in the Treatment of Benign Bone Lesions Using an Engineering Ceramic: Preclinical and Clinical Results', in *Materials and Processes for Medical Devices Conference*, ed. by J Gilbert (Minneapolis, MN: 2009).

16 M. Ikenaga, P. Hardouin, J. Lemaitre, H. Andrianjatovo, and B. Flautre, 'Biomechanical Characterization of a Biodegradable Calcium Phosphate Hydraulic Cement: A Comparison with Porous Biphasic Calcium Phosphate Ceramics', *J Biomed Mater Res*, 40 (1998), 139-44.

17 R. M. Urban, T. M. Turner, D. J. Hall, S. Infanger, N. Cheema, and T. H. Lim, 'Healing of Large Defects Treated with Calcium Sulfate Pellets Containing Demineralized Bone Matrix Particles', *Orthopedics*, 26 (2003), s581-5.

18 Y. E. Greish, and P. W. Brown, 'Phase Evolution During the Formation of Stoichiometric Hydroxyapatite at 37.4 Degrees C', *J Biomed Mater Res B Appl Biomater*, 67 (2003), 632-7.

19 A. J. Wagoner Johnson, and B. A. Herschler, 'A Review of the Mechanical Behavior of Cap and Cap/Polymer Composites for Applications in Bone Replacement and Repair', *Acta Biomater*, 7 (2011), 16-30.

20 R. Kruger, and J. Groll, 'Fiber Reinforced Calcium Phosphate Cements -- on the Way to Degradable Load Bearing Bone Substitutes?', *Biomaterials*, 33 (2012), 5887-900.

21 R. Kruger, J. M. Seitz, A. Ewald, F. W. Bach, and J. Groll, 'Strong and Tough Magnesium Wire Reinforced Phosphate Cement Composites for Load-Bearing Bone Replacement', *J Mech Behav Biomed Mater*, 20 (2013), 36-44.

22 J E Dumas, T E Davis, T Yoshii, J Nyman, G E Holt, D S Perrien, T M Boyce, and S A Guelcher 'Synthesis of Allograft Bone/Polymer Composites and Evaluation of Remodeling in a Rabbit Femoral Condyle Model', *Acta Biomaterialia*, 6 (2010), 2394–406.

23 Q. Lian, D. C. Li, J. K. He, and Z. Wang, 'Mechanical Properties and in-Vivo Performance of Calcium Phosphate Cement-Chitosan Fibre Composite', *Proc Inst Mech Eng H*, 222 (2008), 347-53.

24 J. Kim, S. McBride, M. Fulmer, R. Harten, Z. Garza, D. D. Dean, V. L. Sylvia, B. Doll, T. L. Wolfgang, E. Gruskin, and J. O. Hollinger, 'Fiber-Reinforced Calcium Phosphate Cement Formulations for Cranioplasty Applications: A 52-Week Duration Preclinical Rabbit Calvaria Study', *J Biomed Mater Res B Appl Biomater*, 100 (2012), 1170-8.

25 Z. Pan, and P. Jiang, 'Assessment of the Suitability of a New Composite as a Bone Defect Filler in a Rabbit Model', *J Tissue Eng Regen Med*, 2 (2008), 347-53.

26 J. R. Jones, 'Review of Bioactive Glass: From Hench to Hybrids', *Acta Biomater*, 9 (2013), 4457-86.

27 J. E. Dumas, P. B. Brownbaer, E. M. Prieto, T. Guda, R. G. Hale, J. C. Wenke, and S. A. Guelcher, 'Injectable Reactive Biocomposites for Bone Healing in Critical-Size Rabbit Calvarial Defects', *Biomed Mater*, 7 (2012), 024112.

28 J. E. Dumas, K. Zienkiewicz, S. A. Tanner, E. M. Prieto, S. Bhattacharyya, and S. Guelcher, 'Synthesis and Characterization of an Injectable Allograft Bone/Polymer Composite Bone Void Filler with Tunable Mechanical Properties', *Tissue Eng Part A*, 16 (2010), 2505-18.

29 D. M. Smith, A. M. Afifi, G. M. Cooper, M. P. Mooney, K. G. Marra, and J. E. Losee, 'Bmp-2-Based Repair of Large-Scale Calvarial Defects in an Experimental Model: Regenerative Surgery in Cranioplasty', *J Craniofac Surg*, 19 (2008), 1315-22.

30 A J Poslinski, Ryan M E, Gupta R K, Seshadri S G, and Frechette F J, 'Rheological Behavior of Filled Polymeric Systems I. Yield Stress and Shear-Thinning Effects', *Journal of Rheology*, 32 (1988), 703-35.

31 K. Bruyere Garnier, R. Dumas, C. Rumelhart, and M. E. Arlot, 'Mechanical Characterization in Shear of Human Femoral Cancellous Bone: Torsion and Shear Tests', *Med Eng Phys,* 21 (1999), 641-9.

32 C. M. Ford, and T. M. Keaveny, 'The Dependence of Shear Failure Properties of Trabecular Bone on Apparent Density and Trabecular Orientation', *J Biomech,* 29 (1996), 1309-17.

33 P.J. Carreau, and P. A. Lavoie, 'Rheological Properties of Filled Polymers', *Macromolecular symposia,* 108 (1996), 111-26.

34 G. Baroud, E. Cayer, and M. Bohner, 'Rheological Characterization of Concentrated Aqueous Beta-Tricalcium Phosphate Suspensions: The Effect of Liquid-to-Powder Ratio, Milling Time, and Additives', *Acta Biomater,* 1 (2005), 357-63.

35 M. L. Bouxsein, S. K. Boyd, B. A. Christiansen, R. E. Guldberg, K. J. Jepsen, and R. Muller, 'Guidelines for Assessment of Bone Microstructure in Rodents Using Micro-Computed Tomography', *J Bone Miner Res,* 25 (2010), 1468-86.

36 A. Cacchioli, F. Ravanetti, L. Soliani, and P. Borghetti, 'Preliminary Study on the Mineral Apposition Rate in Distal Femoral Epiphysis of New Zealand White Rabbit at Skeletal Maturity', *Anat Histol Embryol,* 41 (2012), 163-9.

37 AE Hafeman, B Li, T Yoshii, KL Zienkiewicz, JM Davidson, and SA Guelcher, 'Injectable Biodegradable Polyurethane Scaffolds with Release of Platelet-Derived Growth Factor for Tissue Repair and Regeneration', *Pharm Res,* 25 (2008), 2387-99.

38 T. J. Lehtonen, J. U. Tuominen, and E. Hiekkanen, 'Resorbable Composites with Bioresorbable Glass Fibers for Load-Bearing Applications. In Vitro Degradation and Degradation Mechanism', *Acta Biomater,* 9 (2013), 4868-77.

39 M. R. Allen, H. A. Hogan, W. A. Hobbs, A. S. Koivuniemi, M. C. Koivuniemi, and D. B. Burr, 'Raloxifene Enhances Material-Level Mechanical Properties of Femoral Cortical and Trabecular Bone', *Endocrinology,* 148 (2007), 3908-13.

40 G Lewis, 'Percutaneous Vertebroplasty and Kyphoplasty for the Stand-Alone Augmentation of Osteoporosis-Induced Vertebral Compression Fractures: Present Status and Future Directions', *J Biomed Mater Res Part B : Appl Biomater,* 81B (2007), 371-86.

41 O M Clarkin, D Boyd, S Madigan, and M R Towler, 'Comparison of an Experimental Bone Cement with a Commercial Control, Hydroset[tm]', *J Mater Sci: Mater Med,* 20 (2009), 1563 - 70.

42 J. D. Kretlow, S. Young, L. Klouda, M. Wong, and A. G. Mikos, 'Injectable Biomaterials for Regenerating Complex Craniofacial Tissues', *Adv Mater Deerfield,* 21 (2009), 3368-93.

43 S. K. Eswaran, M. R. Allen, D. B. Burr, and T. M. Keaveny, 'A Computational Assessment of the Independent Contribution of Changes in Canine Trabecular Bone Volume Fraction and Microarchitecture to Increased Bone Strength with Suppression of Bone Turnover', *J Biomech,* 40 (2007), 3424-31.

44 E. F. Morgan, and T. M. Keaveny, 'Dependence of Yield Strain of Human Trabecular Bone on Anatomic Site', *J Biomech,* 34 (2001), 569-77.

45 C. Du, H. Ma, M. Ruo, Z. Zhang, X. Yu, and Y. Zeng, 'An Experimental Study on the Biomechanical Properties of the Cancellous Bones of Distal Femur', *Biomed Mater Eng,* 16 (2006), 215-22.

46 T. A. Burgers, J. Mason, G. Niebur, and H. L. Ploeg, 'Compressive Properties of Trabecular Bone in the Distal Femur', *J Biomech,* 41 (2008), 1077-85.

47 M. Halawa, A. J. Lee, R. S. Ling, and S. S. Vangala, 'The Shear Strength of Trabecular Bone from the Femur, and Some Factors Affecting the Shear Strength of the Cement-Bone Interface', *Arch Orthop Trauma Surg,* 92 (1978), 19-30.

48 J. L. Stone, G. S. Beaupre, and W. C. Hayes, 'Multiaxial Strength Characteristics of Trabecular Bone', *J Biomech,* 16 (1983), 743-52.

49 R. B. Ashman, J. D. Corin, and C. H. Turner, 'Elastic Properties of Cancellous Bone: Measurement by an Ultrasonic Technique', *J Biomech,* 20 (1987), 979-86.

50 D. Mitton, C. Rumelhart, D. Hans, and P. J. Meunier, 'The Effects of Density and Test Conditions on Measured Compression and Shear Strength of Cancellous Bone from the Lumbar Vertebrae of Ewes', *Med Eng Phys,* 19 (1997), 464-74.

51 M. Kasra, and M. D. Grynpas, 'On Shear Properties of Trabecular Bone under Torsional Loading: Effects of Bone Marrow and Strain Rate', *J Biomech,* 40 (2007), 2898-903.

52 A. Gisep, S. Kugler, D. Wahl, and B. Rahn, 'Mechanical Characterisation of a Bone Defect Model Filled with Ceramic Cements', *J Mater Sci Mater Med,* 15 (2004), 1065-71.

53 J T Watson, J Borrelli, T G Weber, R H Choplin, S A Persohn, R White, and E M Haglund, 'A Prospective Functional Analysis of Proximal Tibia Fractures Using a Calcium Sulfate/Calcium Phosphate Composite Graft with an Early Weight Bearing Protocol', in *Orthopaedic Trauma Association* (Baltimore, MD: 2010), p. 55.

54 S. S. Kim, M. Sun Park, O. Jeon, C. Yong Choi, and B. S. Kim, 'Poly(Lactide-Co-Glycolide)/Hydroxyapatite Composite Scaffolds for Bone Tissue Engineering', *Biomaterials,* 27 (2006), 1399-409.

55 Yasuo Shikinami, Yoshitaka Matsusue, and Takashi Nakamura, 'The Complete Process of Bioresorption and Bone Replacement Using Devices Made of Forged Composites of Raw Hydroxyapatite Particles/Poly L-Lactide (F-U-Ha/Plla)', *Biomaterials,* 26 (2005), 5542-51.

56 S. Hasegawa, S. Ishii, J. Tamura, T. Furukawa, M. Neo, M. Matsusue, Y. Shikinami, M. Okuno, and T. Nakamura, 'A 5-7 Year in Vivo Study of High-Strength Hydroxyapatite/Poly(L-Lactide) Composite Rods for the Internal Fixation of Bone Fractures', *Biomaterials,* 27 (2006), 1327-32.

57 A. Roshan-Ghias, A. Vogel, L. Rakotomanana, and D. P. Pioletti, 'Prediction of Spatio-Temporal Bone Formation in Scaffold by Diffusion Equation', *Biomaterials,* 32 (2011), 7006-12.

58 T. Smoljanovic, I. Bojanic, G. Bicanic, and D. Delimar, 'Re: Toth Jm, Boden Sd, Burkus Jk, Et Al. Short-Term Osteoclastic Activity Induced by Locally High Concentrations of Recombinant Human Bone Morphogenetic Protein-2 in a Cancellous Bone Environment. Spine 2009;34:539-50', *Spine (Phila Pa 1976),* 35 (2010), 597; author reply 97-8.

59 E. D. Jensen, L. Pham, C. J. Billington, Jr., K. Espe, A. E. Carlson, J. J. Westendorf, A. Petryk, R. Gopalakrishnan, and K. Mansky, 'Bone Morphogenic Protein 2 Directly Enhances Differentiation of Murine Osteoclast Precursors', *J Cell Biochem,* 109 (2010), 672-82.

60 H. Kaneko, T. Arakawa, H. Mano, T. Kaneda, A. Ogasawara, M. Nakagawa, Y. Toyama, Y. Yabe, M. Kumegawa, and Y. Hakeda, 'Direct Stimulation of Osteoclastic Bone Resorption by Bone Morphogenetic Protein (Bmp)-2 and Expression of Bmp Receptors in Mature Osteoclasts', *Bone,* 27 (2000), 479-86.

61 K. Itoh, N. Udagawa, T. Katagiri, S. Iemura, N. Ueno, H. Yasuda, K. Higashio, J. M. Quinn, M. T. Gillespie, T. J. Martin, T. Suda, and N. Takahashi, 'Bone Morphogenetic Protein 2 Stimulates Osteoclast Differentiation and Survival Supported by Receptor Activator of Nuclear Factor-Kappab Ligand', *Endocrinology,* 142 (2001), 3656-62.

62 J. M. Toth, S. D. Boden, J. K. Burkus, J. M. Badura, S. M. Peckham, and W. F. McKay, 'Short-Term Osteoclastic Activity Induced by Locally High Concentrations of Recombinant Human Bone Morphogenetic Protein-2 in a Cancellous Bone Environment', *Spine (Phila Pa 1976),* 34 (2009), 539-50.

63 G. Wu, Y. Liu, T. Iizuka, and E. B. Hunziker, 'The Effect of a Slow Mode of Bmp-2 Delivery on the Inflammatory Response Provoked by Bone-Defect-Filling Polymeric Scaffolds', *Biomaterials,* 31 (2010), 7485-93.

64 N.S. Cunningham, V. Paralkar, and A.H. Reddi, 'Osteogenin and Recombinant Bone Morphogenetic Protein 2b Are Chemotactic for Human Monocytes and Stimulate Transforming Growth Factor Beta-1 Mrna Expression', *Proc. Natl. Acad. Sci., USA,* 89 (1992), 11740-44.

65 A. E. Hafeman, K. J. Zienkiewicz, A. L. Zachman, H. J. Sung, L. B. Nanney, J. M. Davidson, and S. A. Guelcher, 'Characterization of the Degradation Mechanisms of Lysine-Derived Aliphatic Poly(Ester Urethane) Scaffolds', *Biomaterials,* 32 (2011), 419-29.

66 D Eglin, D Mortisen, and M Alini, 'Degradation of Synthetic Polymeric Scaffolds for Bone and Cartilage Tissue Repairs', *Soft Matter,* 5 (2009).

CHAPTER VI

EFFECTS OF PARTICLE SIZE, LOADING, AND MINERAL CONTENT ON THE *IN VIVO* REMODELING OF SETTABLE ALLOGRAFT BONE/POLYURETHANE COMPOSITES

Introduction

Established clinical approaches to treat critical-sized bone defects include the implantation of autograft or allograft bone, ceramic scaffolds, or metallic devices [1]. While these materials offer a temporal solution to large bone loss, none of them fulfills all the identified requirements for successful bone scaffolds, namely being osteoconductive, biocompatible, resorbable, porous, and having mechanical properties comparable to those of the surrounding host bone [2-4]. In addition to providing structure for new bone development, ideal bone scaffolds should also act as a reservoir of signaling molecules to promote cellular recruitment, differentiation, and/or activation.

Current efforts in bone tissue engineering focus on developing composite scaffolds to replace bone, a natural nanocomposite. Biodegradable polymers are biocompatible, and have tailorable mechanical, degradation, and handling properties. However, their bioactivity (defined as the ability to induce a specific biological activity [5]) is usually low. Ceramics provide bioactivity and osteoconductivity, although slow degradation rates and brittle mechanical properties reduce their effectiveness in promoting bone remodeling (particularly for weight-bearing applications). Composite bone scaffolds combining different ceramic phases and/or polymers offer improved

mechanical stability [6] and tissue interaction [2, 3], in addition to injectability [7, 8], settability, and even weight-bearing capabilities [9, 10].

Lysine-derived polyurethane-ceramic composites have been developed as bone scaffolds and tested in femoral plug bone defects in rats [11, 12], rabbits [13, 9], and sheep [8]. The scaffolds generate a minimal and transient inflammatory response, support cellular infiltration, and degrade to non-cytotoxic compounds. Low-porosity polyurethane (PUR) composites with allograft bone particles (ABP) as the ceramic matrix have been shown to remodel by creeping substitution [13]. In the absence of interconnected pores, osteoclasts infiltrate the material through the mineralized particles' surface, followed by new bone deposition. While these materials offer stability, biocompatibility, and support new bone formation, further studies detailing the progression of scaffold remodeling *in vivo* are needed to identify target design parameters that improve healing outcomes.

The polymeric and ceramic phase degradation rate within composite scaffolds has been identified as a critical design parameter influencing healing progression. Recently, it has been suggested that the two phases should have a similar degradation rate to that of new tissue formation [6]. Furthermore, a detailed analysis of the remodeling of low-porosity PUR-ABP composites in rabbits highlighted improved healing outcomes by both maintaining a continuous phase supporting new bone deposition, and balancing the rates of polymer degradation and new bone formation (which was achieved delivering bone morphogenetic protein) [9]. This study continues to improve understanding of the healing mechanisms of composites in bone defects. Here, we have investigated the effects that ceramic matrix loading, matrix particle size, and mineralization of matrix particles have on the remodeling progression of composite PUR-ABP scaffolds. We expected enhanced

mechanical properties from the composites with smaller matrix particles, increased osteoinductive character provided by the addition of demineralized bone particles (DBM), and improved scaffold infiltration and remodeling in composites with higher matrix content (approaching a continuous allograft phase). Injectable and moldable formulations were implanted into femoral plug defects in rabbits and remodeling progression was analyzed at 6 and 12 weeks using micro-computed tomography and histomophometry.

Experimental

Materials

Lysine-triisocyanate prepolymer (LTI-PEG, 21.7% NCO), and poly(ε-caprolactone-*co*-D-L-lactide-*co*-glycolide) triol (187 mg KOH/g) were provided by Medtronic, Inc. (Memphis, TN). The backbone of the polyester triol contained 70% ε-caprolactone, 20% glycolide, and 10% D-L lactide. Rabbit allograft mineralized bone particles and demineralized bone matrix (DBM) were also received from Medtronic, Inc. Allograft particles and DBM were frozen and lyophilized before use to minimize water content. Triethylenediamine (TEDA) catalyst and dipropylene glycol (DPG) were purchased from Aldrich (St Louis, MO) and mixed to obtain a 10% (w/v) solution of TEDA in dry DPG.

Synthesis of injectable and moldable composites

Table 6.1 summarizes the settable formulations included in this study, which are divided into injectable (I, 47 wt% allograft) and moldable (M, 67 wt% allograft) composites. All biocomposites were prepared by loading a mixing cup with the

appropriate amounts of polyester triol, LTI-PEG, catalyst, and allograft particles followed by hand-mixing for 1 min. The index (ratio of isocyanate:hydroxyl equivalents x 100) for the injectable and moldable formulations was 115 and 130, respectively. Injectable biocomposites contained 3400 ppm of TEDA catalyst, and moldable biocomposites were prepared with 5500 ppm TEDA. The effect of allograft particle size on the performance of the injectable and moldable biocomposites was measured by using large (L, 105-500 μm) and small (S, <105 μm) allograft bone particles. In addition, a portion of the allograft component was replaced with DBM for some injectable formulations (D) to evaluate its osteoinductive effect. Poor handling properties and lack of cohesiveness precluded the use of DBM in the moldable composites. Injectable biocomposites contained the maximum amount of allograft that allowed the material to be delivered by injection into the defect. The DBM content was chosen as the maximum amount that did not affect the cohesion of the composite. Moldable composites were formulated with high loading of allograft particles to provide a pathway for cells to infiltrate the composites through creeping substitution [13, 14].

Table 6.1. Composition and physical properties of injectable and moldable composites

Treatment group	Category	Allograft (wt%)	DBM (wt%)	Particle size (μm)	Working time (min)	Viscosity at $5s^{-1}$ (kPa*s)	Non-reactive yield stress (kPa)
Empty	Control	N/A	N/A	N/A	N/A	N/A	N/A
IDL	Injectable	37.4	9.6	105-500	9.3±0.1[a]	30.2±4.5[a]	129±12[a]
IDS	Injectable	37.4	9.6	<105	9.5±0.3[a]	0.073	N/A
IS	Injectable	47	0	<105	8.7±0.1	0.017	N/A
ML	Moldable	67	0	105-500	5.3±0.1	8.1±3.6	34±17
MS	Moldable	67	0	<105	5.9±0.1	28.7±0.01[a]	119±4[a]

[a] Groups with the same letter are statistically the same ($p>0.05$)
Reported error corresponds to the standard error of the mean.

Rheological analysis: initial viscosity and working time

The curing profile of the biocomposites was determined using a TA Instruments AR2000ex rheometer. Reactive biocomposites were loaded between 25 mm diameter disposable plates and compressed to a gap of 1.5 mm. Measurements of storage (G') and loss (G") moduli were performed using an oscillatory time sweep method with a frequency of 1 Hz and amplitude of 1% strain. The working time of the formulations, defined as the time from the start of mixing until cure, was determined as the G'-G" cross-over point.

The initial flow characteristics of the biocomposites were analyzed by removing the catalyst from the formulation (n=3). Non-setting samples were poured between 40 mm cross-hatched parallel plates, compressed to a gap of 1.5 mm, and subjected to a dynamic frequency sweep (0.1 to 100 rad-sec^{-1}) at 25°C with controlled strain amplitude of 0.02%. A Cox-Merz transformation was applied to the dynamic data to obtain the steady state viscosity (η, Pa-s) as a function of shear rate (γ, s^{-1}). The data were fit to the Herschel-Bulkley model, which relates the viscosity and shear rate of solid-filled suspensions with high solids content [15], to estimate the yield stress (τ_Y, Pa) of the material:

$$\eta = \tau_Y \dot{\gamma}^{-1} + K\dot{\gamma}^{(n-1)} \qquad (6.1)$$

where K is the consistency index of the composite (constant) and n is the power-law index of the suspending polymer. In this case, the suspending polymer corresponds to the non-reactive mixture of polyester triol and LTI-PEG prepolymer and has been shown to exhibit a Newtonian behavior (n=1) [9].

In vitro characterization of the biomcomposites

Cylindrical samples of each formulation ($n \geq 3$) were prepared for characterization. To simulate the aqueous environment in the wounds, the formulations were loaded into 6 mm-diameter cylindrical plastic cups containing 250 μl of water and allowed to set at room temperature (cement formulations set under compression with a 1 lb weight [20.7 psi]). Cylinders were further cured in a vacuum oven at 37^{o}C overnight, removed from the plastic cups, and cut using a Buehler saw to a length of 12 mm (for mechanical testing) and ~2 mm (for scanning electron microscopy [SEM] imaging). Thin sections of cured biocomposite samples were sputter coated with gold and imaged using a Hitachi S-4200 SEM (Finchampstead, UK). SEM images were analyzed for pore size using MetaMorph 7.1 image analysis software. The porosity of the mechanical testing samples was calculated from the composite density which was measured gravimetrically [11]. After 24 hours of hydration in phosphate buffered saline (PBS), mechanical properties were measured using an MTS 898 by preloading the samples to 12 N followed by compression at a rate of 25 mm/min until failure. The original cross sectional area of the cylinders was used to calculate compressive stress. The strength reported corresponds to the point where maximum stress was achieved, and compressive modulus was calculated as the slope of the linear portion of the stress-strain curve.

Animal Study

Twenty-eight New Zealand White (NZW) rabbits were used in this study. All surgical and care procedures were carried out at IBEX Preclinical Research, Inc. (Logan, UT) under aseptic conditions per the approved IACUC protocol. The biocomposite

individual components were gamma-irradiated using a dose of 25 kGY. Bilateral critical-sized defects of 5 mm diameter by 6-8 mm in depth were drilled in the lateral femoral condyles of each rabbit. Metal wires were placed in the distal-most aspect of the defects to aid in location. Defects were filled with injectable or moldable formulations (n = 4 defects per formulation) according to a randomized experimental design (different formulations were placed in contralateral defects). Control defects were left untreated (Empty). Femoral specimens were harvested after 6 and 12 weeks and placed in 10% neutral buffered formalin for fixation.

Micro-computed tomography (μCT) analysis

A μCT80 (SCANCO Medical, Basserdorf, Switzerland) was used to acquire images of the extracted femurs post-implantation at 6 and 12 weeks. In addition, femurs from NZW rabbits which were part of other experimental protocols that did not affect the skeleton (same age, sex, and similar weight to the rabbits used in this study) were scanned and analyzed as host bone controls. μCT scans were performed in formalin at 70 kVp energy, 114 μA source current, 250 projections per rotation, 400 ms integration time, and an isotropic voxel size of 36 μm. Axial images were reconstructed using manufacturer-provided software. Attenuation values were converted to tissue mineral density (TMD) through calibration with hydroxyapatite (HA) phantoms with densities between 0 and 780 mg-HA-cm^{-3} (calibration of the instrument was checked weekly). Using the cortical borders of the defect for alignment, the reconstructed image stack was re-oriented such that the depth of the defect was parallel to the z-axis. A radial analysis of morphometric parameters was conducted from the core of the implant to the interface

with host bone. Three concentric annular volumes of interest with thickness of 1 mm and a cylindrical core with diameter of 1 mm, all with approximate length of 7 mm (from the outer cortical surface of the femur) were defined for each sample. The 3 inner regions covered the defect volume, while the outer region provided information about the interface with host bone. Ossified tissue was differentiated from soft tissue using lower and upper thresholds of 140 mg-HA-cm^{-3} and 254 mg-HA-cm^{-3} respectively, as well as Gaussian noise filter settings of sigma 0.2 and support 2. Threshold conditions were chosen visually and kept constant for the analysis of all the samples. An upper threshold was included to avoid the selection of the metal wires as ossified tissue. Morphometric parameters within the annular regions were calculated, grouped by treatment and time point, and plotted versus the mean radial distance (R_m) from the core of the defect ($R_m=(R_o+R_i)/2$, where R_o and R_i correspond to the outer and inner radius of each region, respectively). Bone volume/total volume (BV/TV), trabecular number (Tb.N.), trabecular thickness (Tb.Th.), and trabecular separation (Tb.Sp.) within the regions of interest were computed using SCANCO's Medical microCT systems software.

Histology

After fixation in formalin, femur specimens were trimmed and embedded in methyl methacrylate. Thin sections were cut in a longitudinal plane through the approximate center of each defect. Care was taken to ensure that the orientation was as similar as possible between specimens. Sections of parallel planes were stained with Goldner's trichrome stain and Hematoxylin and Eosin (H&E) stain to evaluate the *in vivo*

response of the different formulations. H&E sections were evaluated for inflammation and the presence of giant cells (GC's).

Histomorphometry

For quantitative analysis, Goldner's trichrome stained sections were imaged at 10x magnification with an Olympus camera (DP71) using an Olympus BX60 microscope. Residual allograft bone particles, newly formed bone, and residual polymer were quantified in an area of interest 1 mm high × 5 mm wide located in the center of the defect. To analyze the radial remodeling of the scaffolds in time, the rectangular area of interest was further subdivided into 3 concentric annular regions (each 0.83 mm thick) representing (1) the area of the defect in contact with the host bone, (2) the mid-region of the defect, and (3) the core of the defect. Mineralized tissue was stained green, and to differentiate between the new bone and the residual allograft, the allograft particles were identified as meeting the following two criteria: (1) acellular, and (2) angular shape. In the stained sections remaining polymer appeared white, newly deposited osteoid stained red/fucsia, cellular nuclei stained blue, and red blood cells stained orange/red. For histomorphometric analysis, Metamorph (Version 7.0.1) was utilized to color threshold each phase, quantify the number of pixels of each material and compare it to the total pixels in the area of interest. Similar to the μCT data, the content of new bone, allograft bone, and residual polymer was plotted as a function of the mean radial distance from the core of the defect (R_m). Goldner's trichrome stain did not reveal DBM particles, so these were not included in the histomorphometric analysis. Initial content of allograft bone and polymer in each formulation was determined from histological sections of scaffolds

prepared in the laboratory and processed as described in the previous section. These values were used to calculate rates of allograft resorption and polymer degradation throughout remodeling.

Statistical analysis

A one-way analysis of variance (ANOVA) was performed to compare the rheological and mechanical properties, as well as the pore size of different treatment groups. Statistical significance was considered for $p < 0.05$.

Results

Biocomposite characterization

Rheological characterization of the non-reactive and reactive formulations provided information about their initial handling properties. Moldable biocomposites had the lowest working times, and addition of DBM slightly delayed the setting of injectable formulations. Figure 6.1 shows representative curves for moldable and injectable biocomposites' initial viscosity as a function of shear rate. Injectable formulations with small particles exhibited Newtonian behavior at shear rates below ~3 s^{-1} (initial plateau), followed by power-law behavior at larger shear rates. While these groups showed minimal evidence of yield stress (minimal resistance to flow during the rheological analysis as well as during injection), the Herschel-Bulkley model [15] was used to calculate the yield stress for the IDL and moldable groups (Table 6.1). The IDL, ML, and MS groups exhibited power law behavior even at low shear rates. The addition of DBM

increased the initial viscosity of the formulations (reported at 5 s^{-1} for injectable biomaterials [16]).

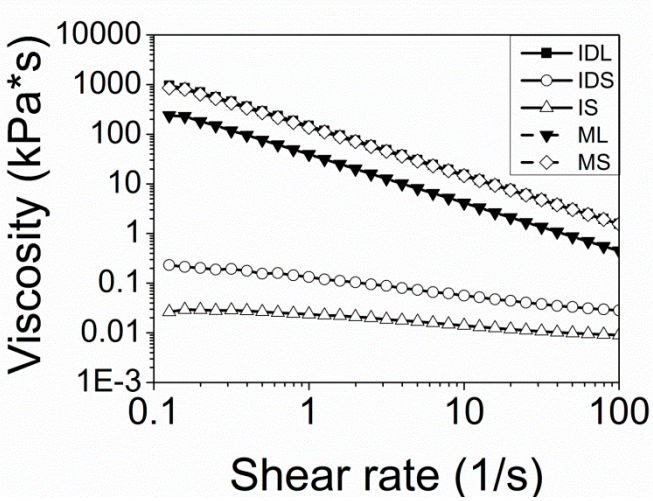

Figure 6.1. Initial viscosity of PUR/allograft composites. Non-reactive formulations were poured between 40mm cross-hatched parallel plates, compressed to a gap of 1.5 mm, and subjected to a dynamic frequency sweep (0.1 to 100 rad sec^{-1}) at 25°C with controlled strain amplitude of 0.02% (n=3). Dynamic data was transformed steady state viscosity (η, Pa*s) as a function of shear rate (g, s^{-1}) using a Cox-Merz transformation (geometric figures). Data were fit to the Herschel-Bulkley model (lines) to determine yield stress in the case of the IDL, MS, and ML formulations.

As expected, moldable biocomposites had lower porosity than injectables. Representative images of the materials (Figure 6.2) show that porosity of moldable formulations was associated with voids present between allograft particles, or between allograft particles and polyurethane (the size of the voids was not measured due to their irregular shapes). Instead, foaming of the polyurethane binder was the main contributor of porosity for injectables. Both particle size and DBM influenced the porous structure of injectable biocomposites. Comparison of IDL to IDS suggests increased porosity and pore size for formulations with large allograft particles. Moldables followed a similar trend. While addition of DBM had minimum effect on the total porosity, it promoted the generation of some larger pores, resulting in a larger average pore size.

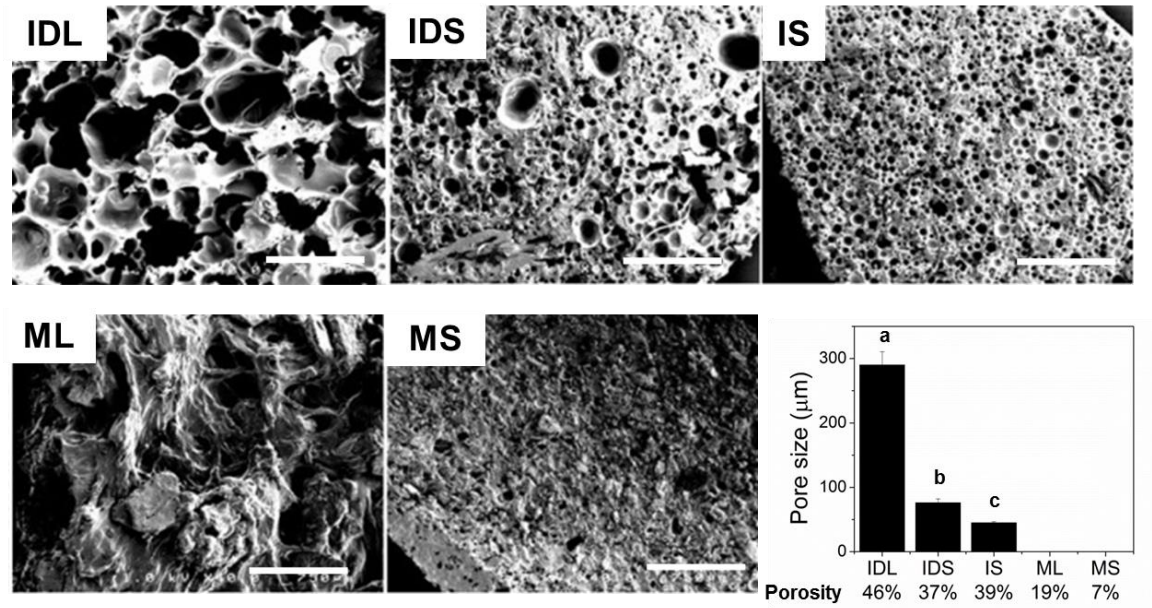

Figure 6.2. Scanning electron microscopy images and porosity of ABP-PUR biocomposites. Scale bars represent 750 μm. Statistical significant differences between groups with different letter.

A summary of the measured compressive properties of the injectable and moldable formulations is presented in Figure 6.3. Among the injectable treatment groups, compressive modulus remained constant between 20-25 MPa, and strength doubled from 3.1 MPa to ~6 MPa when small particles were used as fillers. Addition of DBM did not affect the mechanical properties of the injectable formulations. In general, moldable groups had higher mechanical properties than the injectable formulations. Small particles in moldables generated a 30% increase in strength and a 26% decrease in compressive modulus when compared to moldables with large particles.

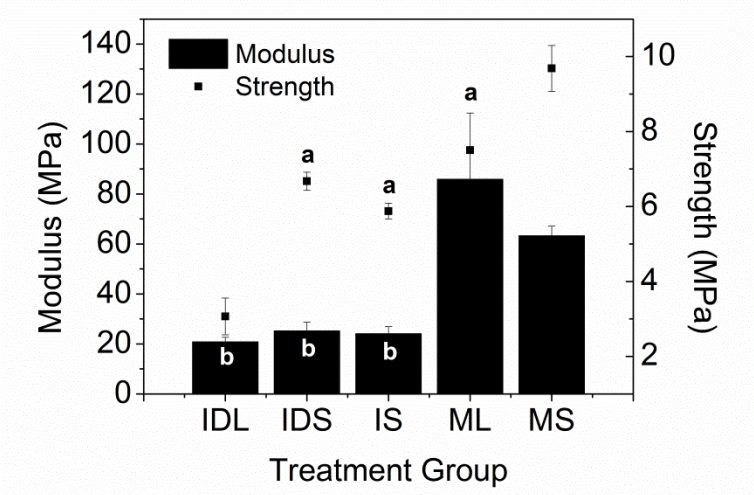

Figure 6.3. Compressive strength and modulus of settable ABP-PUR biocomposites. No statistical significant difference between groups with the same letter. (a) strength, (b) modulus.

μCT analysis

Representative μCT images of all the treatment groups after 6 and 12 weeks in the rabbits are presented in Figure 6.4A. Empty defects did not heal in time, and only showed new bone formation towards the femoral cortex. Large particles could be identified in the images, particularly at 6 weeks (irregularly shaped radiolucent particles). Visual changes between the 6 and 12 week images of the biocomposites suggest ongoing remodeling.

Allograft/polyurethane composites remodel by creeping substitution as cells infiltrate the scaffold from the host bone-scaffold interface to the core [13]. Thus, morphometric parameters evaluated by μCT were plotted as a function of the mean radial distance from the core of the defect to monitor the remodeling process in time and space (Figure 6.4B). The cylindrical volume of the defect was divided into three concentric regions (cylindrical core of 1 mm diameter and two annular regions with thickness of 1 mm). An additional concentric annular region extending 1 mm from the outer surface of the defect was included to evaluate changes in host bone near the interface. Measured

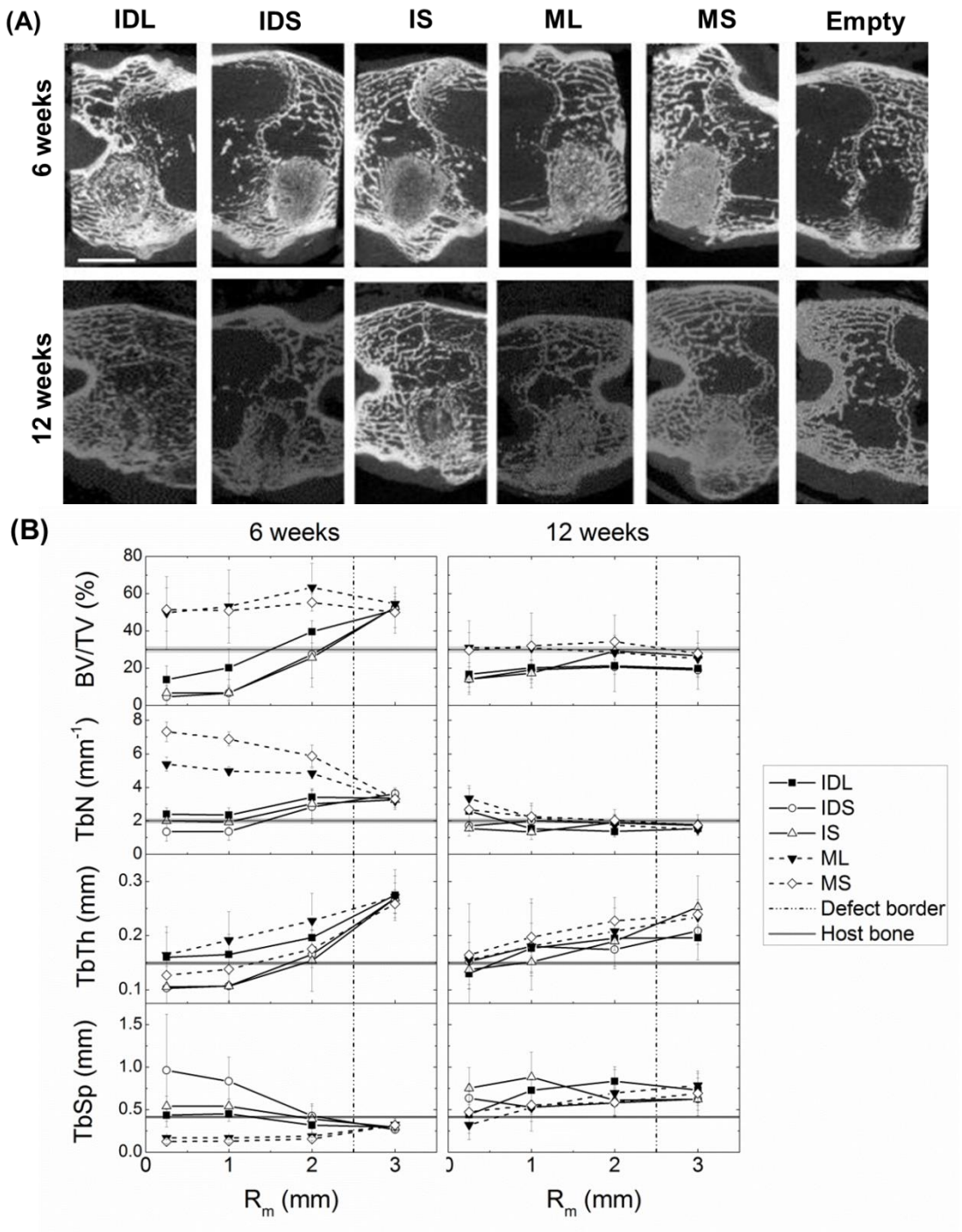

Figure 6.4. μCT analysis of mineralized tissue in ABP-PUR biocomposites. (A) Representative images at 6 and 12 weeks. (B) Morphometric parameters: BV/TV, Tb.N., Tb.Th., and Tb.Sp., all measured as a function of radial distance from the center line of the defect at 6 and 12 weeks and compared to host bone values measured separately.

values of the morphometric parameters were compared to the host bone control data collected from scans of femurs excised from healthy rabbits.

As a measure of the total content of mineralized tissue (including both residual allograft and new bone), BV/TV at 6 weeks showed differences between the injectable and moldable formulations. The radial distribution of BV/TV was constant for the moldable composites (dashed lines) at values close to 50%, including near the interface, suggesting densification of the neighboring host bone in response to grafting with the biocomposite. For the injectables (solid lines), BV/TV monotonically increased from values close to 10% at the core to ~50% near the host bone interface. For both injectables and moldable groups, large matrix particles tended to have higher BV/TV at 6 weeks. Ongoing remodeling at 6 weeks was suggested by the mineralized content different from the host bone controls (29.7$\pm$1.3%). By 12 weeks, BV/TV of all the groups approached host bone values although it was radially uniform for the moldable formulations at ~ 30%, balanced for the IDL formulation at ~20%, and had a radial increase from the core towards the interface of host bone for the remaining injectable formulations (IDS, IS).

Analysis of trabecular parameters provides additional information about the remodeling mechanism of the polyurethane/allograft composites. Tb.N and Tb.Th take into account remaining allograft particles and new trabeculae or bone being formed, while Tb.Sp measures the space between the trabeculae that can be occupied by polymer, pores, or soft tissue. Tb.N (average number of trabeculae per unit length [17]) is initially a measure of the matrix volume fraction. Thus, moldable formulations initially have higher Tb.N than injectables. The radial distribution of Tb.N at 6 weeks has opposite trends between moldables and injectables, although both approach host bone values. Moldable

formulations show a radial decrease in Tb.N from the core to the host interface, which suggests either allograft resorption or increased connectivity of the matrix particles at the border of the defect. In contrast, Tb.N of injectable formulations increases radially, suggesting the creation of new trabeculae near the host bone interface. At 12 weeks, the IDS and IS groups had uniform Tb.N with values between 1.5 and 2 mm^{-1}, while the ML, MS, and IDL groups had a slightly higher Tb.N only at the core (~2.5-3.3 mm^{-1}). Differences in Tb.Th (mean thickness of trabeculae [17]) between moldables and injectables at 6 weeks can be associated with differences in matrix particle size. Tb.Th increases for all the groups from the core to the interface, suggesting new bone deposition as cells infiltrate the materials. Between 6 and 12 weeks, Tb.Th for composites with large particles showed minimal changes, while Tb.Th increased throughout the defect for formulations with small particles. The final trabecular parameter, Tb.Sp (mean distance between trabeculae [17]), at 6 weeks trends with volume fraction of pores and polymer: injectable formulations have higher Tb.Sp than moldables, particularly near the core where less new bone deposition is expected. The radial increase in Tb.N and Tb.Th for the injectable groups results in less space between trabeculae and thus a radial decrease in Tb.Sp. Opposite radial trends in Tb.N and Tb.Th of moldable materials result in a uniform radial distribution of Tb.Sp at 6 weeks. Radial differences in Tb.Sp resolve after 12 weeks for all of the groups. Interestingly, similar to the BV/TV results, values of Tb.N and Tb.Th higher than the host bone control at 6 weeks in the outer region support the idea of initial densification of the surrounding host bone.

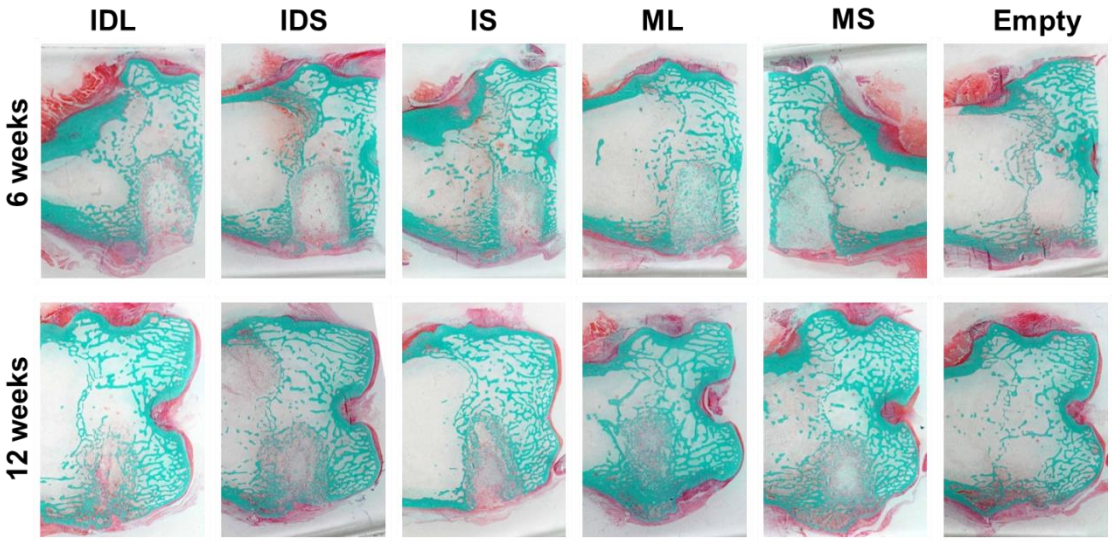

Figure 6.5. Low-magnification images of histological sections of ABP-PUR biocomposites at 6 and 12 weeks. Goldner's trichrome stain, original maginification 1X.

Histology

Figure 6.5 shows representative low magnification histological images of all the treatment groups at 6 and 12 weeks. Similar to the μCT results, the histological sections suggest that empty defects did not heal and were largely filled with fatty bone marrow surrounded by a shell of bone. Low magnification images of the treated defects suggest that large allograft particles promoted more balanced remodeling in time (approaching host bone architecture in the defect area at 12 weeks). Histological sections stained for H&E revealed that none of the treatment groups generated acute inflammation at 6 or 12 weeks (data not shown). In general, small numbers of inflammatory cells were present at 6 weeks and decreased with time. GCs present were associated with remaining allograft matrix and contained intracellular material (Figure 6.6-IDS 6 weeks).

High magnification histological images (Figures 6.6 and 6.7) reveal active remodeling of the implanted scaffolds in time. At 6 weeks, bone formation was ongoing predominantly at the periphery of treated defects, while the central area remained largely

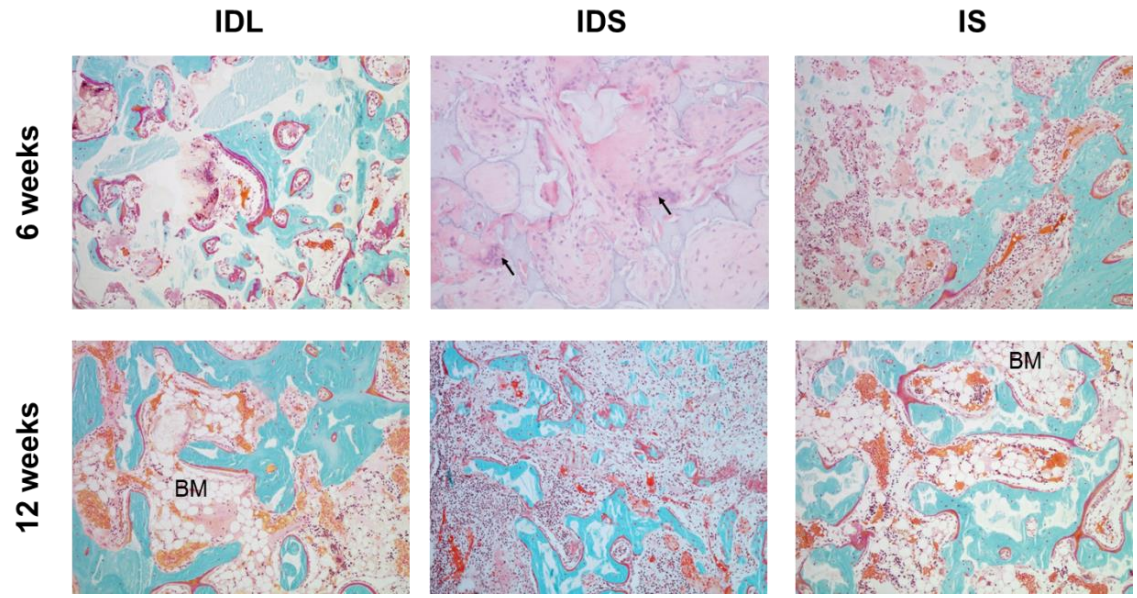

Figure 6.6. High-magnification images of histological sections of defects treated with injectable ABP-PUR biocomposites. All of the images show sections stained with Goldner's trichrome, except for IDS at 6 weeks, which is stained with H&E. Original magnification 70X. With Goldner's trichrome stain: *white*- remaining polymer; *light green particles with angled shapes*- remaining allograft particles; *green with cells inside*- new mineralized bone with osteocytes; *red*- osteoid; *orange*- red blood cells; *purple*- nuclei; BM- bone marrow. Arrows in the IDS-6 weeks section point to giant cells.

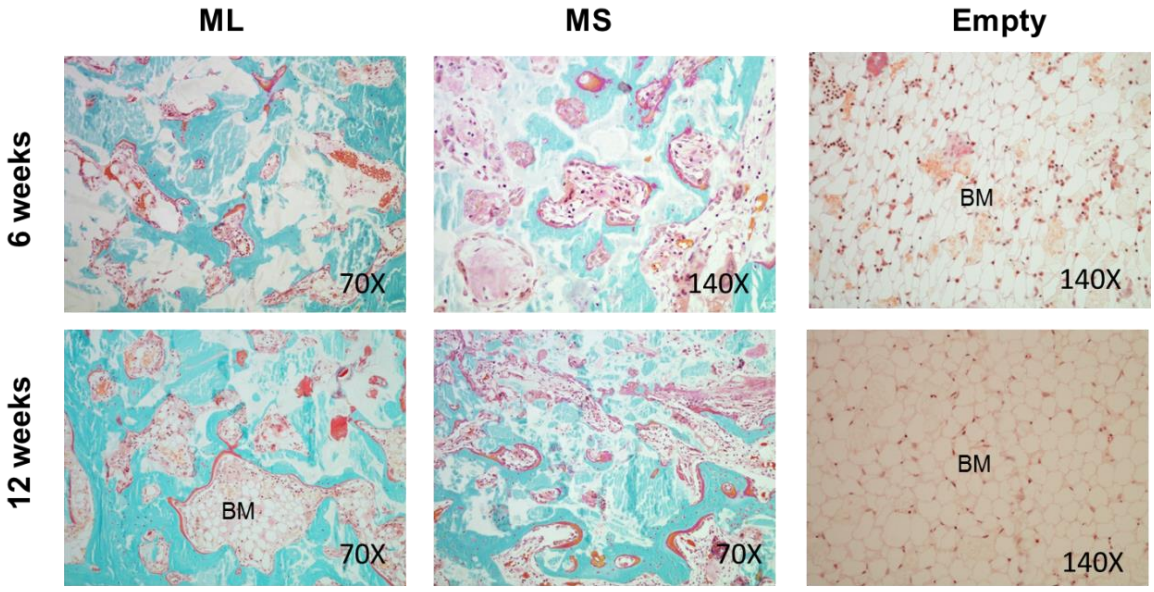

Figure 6.7. High-magnification images of histological sections of empty defects and defects treated with moldable ABP-PUR biocomposites. Goldner's trichrome stain. Original magnification reported in each image. With Goldner's trichrome stain: *white*- remaining polymer; *light green particles with angled shapes*- remaining allograft particles; *green with cells inside*- new mineralized bone with osteocytes; *red*- osteoid; *orange*- red blood cells; *purple*- nuclei; BM- bone marrow.

acellular. New bone was deposited appositionally mostly by intramembranous ossification, except at the periphery of the defects where some endochondral ossification was present (in particular at 6 weeks). New bone deposited at early time points had woven structure for all the treatment groups. This resolved for the ML group at 12 weeks with lamellar bone present in the defect (Figure 6.7-ML 12 weeks). After 12 weeks, remaining allograft particles were incorporated with new bone and this was more evident in scaffolds with large particles. An interesting difference between injectable and moldable materials was that at 6 weeks injectable scaffolds showed evidence of new bone growing not only on top of allograft particles but also on the surface of the polymer (center of Figure 6.6-IDL 6 weeks). Most new bone formation in moldable materials initiated at the surface of allograft particles (center of figure 6.7-ML 6 weeks).

Histomorphometry

Histomorphometric analysis enabled radial quantification of new bone formation, allograft resorption, and polymer degradation for each treatment group (Figure 6.8). Differences between the groups at different locations and time points were generally not statistically significant due to small sample size. As a result, analysis of the histomorphometry data focused on trends and rates instead of absolute values of each parameter.

While μCT analysis provided information about the mineral phase in the defects, histology was used to differentiate new bone from residual allograft, as well as to monitor remaining polymer at each time point and location. The total mineralized content measured by histomorphometry [NB+A(%) in Figure 6.8] showed similar trends to

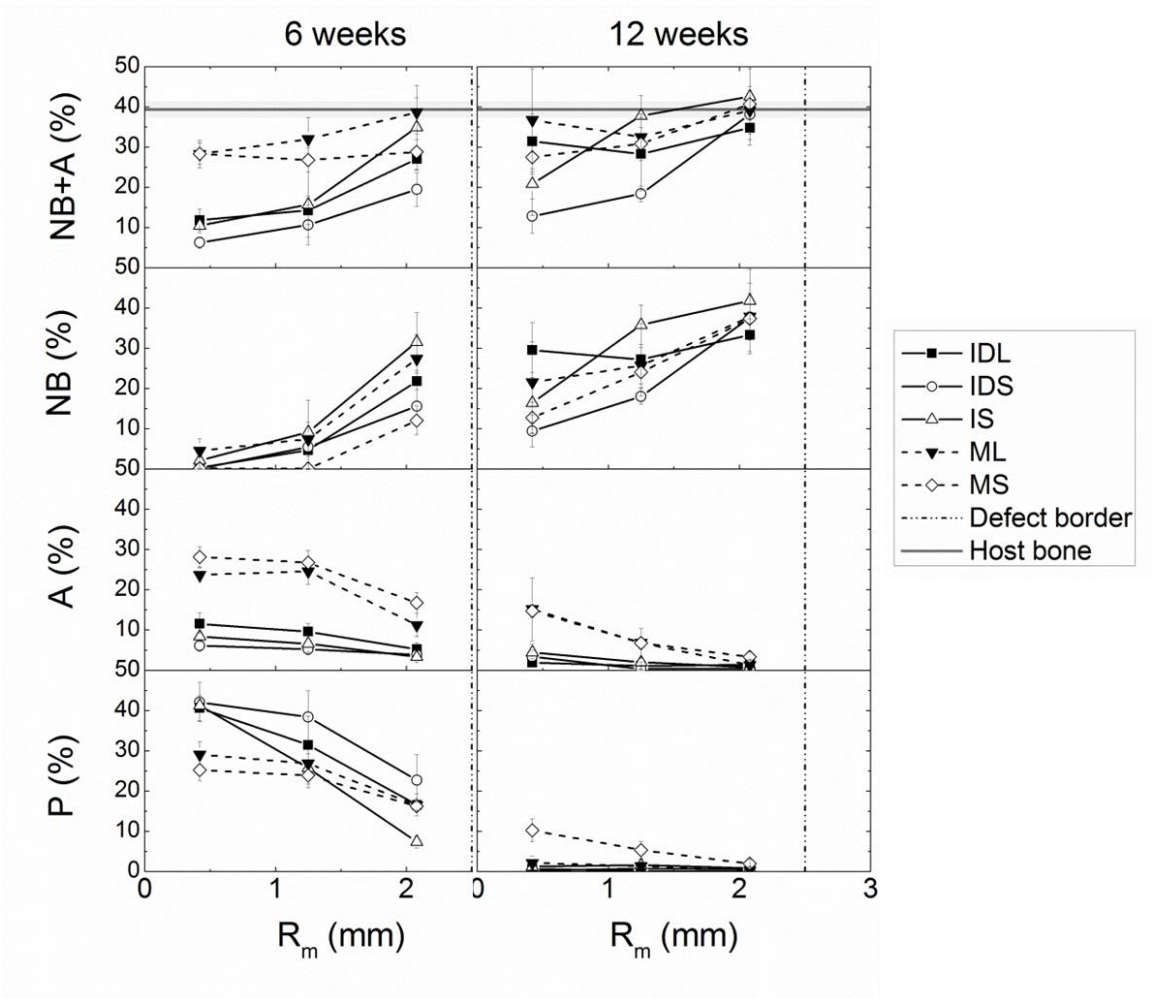

Figure 6.8. Histomorphometric analysis of new bone formation of ABP-PUR biocomposites at 6 and 12 weeks. Mineral content (including new bone and allograft), New bone (NB), remaining allograft (A), and polymer (P) data are plotted as a function of radial distance from the center line of the defect.

BV/TV measured by μCT although the values differed. At 6 weeks, all of the treatment groups showed increased new bone formation towards the border of the defect and minimal new bone formation at the core, matching the histological observations of acellular cores. Increased new bone formation near the host bone interface was complemented by minimal allograft resorption and increased polymer degradation for injectable formulations. Instead, moldable formulations showed increased allograft resorption and reduced polymer degradation in the region where new bone was deposited.

At 12 weeks, all of the treatment groups achieved a similar amount of new bone deposition at the edge of the defect. However, formulations with large particles showed a reduced radial gradient in new bone deposition, suggesting a more balanced remodeling throughout the defects. After 12 weeks, remaining polymer throughout the defects was minimal except at the core of the MS group.

Discussion

The golden standard of care for the treatment of bone defects continues to be the use of autograft bone. However, unlimited availability and donor site morbidity have motivated the search for bone substitute materials that also promote healing. As a biocompatible and osteoconductive alternative for autograft bone, surgeons have been using allograft bone for more than 20 years [18, 19]. Our group has developed injectable [20, 7, 11], moldable [9], and compression molded [13] composites incorporating allograft bone particles and biodegradable, lysine-derived polyurethanes. These materials have been shown to promote cellular infiltration, allograft resorption, and new bone deposition when implanted *in vivo.* Recently we reported an enhancement in healing progression of ABP-PUR composites promoted by balancing the rates of new bone formation and polymer degradation [9]. The aim of the present work was to further improve the understanding of the remodeling mechanisms of ABP-PUR biocomposites by evaluating the effects of allograft particle size, loading, and mineral composition on the healing of femoral plug defects in rabbits.

Characterization of the biocomposites in the lab suggested several effects of the variables of interest on their handling, structural, and mechanical properties. All the

treatment groups in our study contained similar volume fraction of polymer, and were classified into 2 general categories: injectable and moldable biocomposites. Injectable formulations were porous and had 47 wt% allograft particles. Instead, moldables had low porosity and high filler loading (67 wt%) such that the close proximity of the particles could provide a pathway for cellular infiltration. As their label suggest, injectable biocomposites could be delivered to the bone defect using a syringe. Interestingly, even though the IDL and MS groups exhibited the same rheological behavior under non-reactive conditions, and ML had lower viscosity and yield stress, the moldable formulations could not be injected. Most likely, the longer working time of IDL allowed the formulation to be loaded into the syringe and injected before the material completely transitioned from a viscoelastic to an elastomeric behavior. Addition of DBM increased the viscosity of injectable formulations. This observation correlates with studies reporting an increase in the resistance of polymers to flow as a consequence of clustering of incompatible fillers [21]. Our results align with reports of mechanical properties of particulate-polymer composites depending on particle loading and size [22, 23]: higher filler loading reduced the porosity of the biocomposites and resulted in improved compressive modulus; smaller particle size improved the strength of injectable and moldable composites. An additional effect of small particles over the structure of the ABP-PUR biocomposites was the significant reduction in pore size. While this was an unexpected result, it is possible that the increased number of small versus large allograft particles generated a more tortuous path for the foaming gas to escape, thus resulting in more and smaller pores.

Contrary to our expectations, the addition of DBM to injectable formulations hindered remodeling of the rabbit femoral plug defects. DBM has been reported to be osteoinductive and to stimulate defect healing in dogs [24, 25], rabbits [26], and humans [27]. However, multiple recent studies have reported variability in the osteoinductive character of DBM [28, 29], even among lots of the same formulation [30]. Factors that influence the effectiveness of DBM include: the technique to obtain the bone from human donors, donor age and gender, differences in preparation and processing methods for bone, and sterilization protocols among others [29]. Our results further support the idea that not all DBM is osteoinductive and as a result its use should be highly regulated.

Previous studies have reported a particle size effect on the remodeling of allograft bone particles *in vivo*. In combination with autogenous bone marrow, allograft particles with size in the range of 100-300 μm promoted significantly more new bone formation than larger particles (1000-2000 μm) when placed in the femurs of Rhesus monkeys for 8 weeks [31]. Another study in rabbit calvaria reported a greater amount of osteoid tissue and little fibrous tissue formation when allograft particles with size <450 μm were implanted instead of particles with larger size (up to 1000 μm) [32]. Both these studies also reported enhanced resorption and incorporation of allograft when particles smaller than 450 μm were used. The results of our *in vivo* study agree with these observations. Independent of the porosity, ABP-PUR biocomposites with particles in the size range of 105-500 μm achieved improved balanced remodeling throughout the defect after 12 weeks, as well as deposition of more mature bone. Kluppel et. speculated that the improved osteoinductive character of the small particles (within the size range studied) could be the result of the higher surface area exposed for resorption and new bone deposition [32]. While this was

our initial expectation when including smaller ABP in the formulations, our results contradict this hypothesis. Reduction of particle size below 105 μm did not favor improved remodeling. However, the particle size range of 100-500 μm seems to be ideal for new bone deposition.

Combined analysis of our μCT and histomorphometry data suggests interesting differences in the remodeling mechanism of injectable and moldable formulations. Previously, we and others have demonstrated that bone defects remodel from the periphery to the interior of the scaffolds as cells infiltrate the materials [9, 33]. Thus, the remodeling progression of the biocomposites was evaluated by comparing the radial distribution of morphometric parameters. The decrease of BV/TV and Tb.N between 6 and 12 weeks for the moldable groups suggested active allograft resorption throughout the scaffold. The radial increase in Tb.Th for this group at 6 weeks suggested new bone deposition on the surface of allograft particles, which was verified by histological images. Together, these observations suggest that the low-porosity moldable biocomposites remodel by creeping substitution: osteoclasts resorb the surface of allograft particles and are followed by other cells including osteoblasts which deposit new bone. On the other hand, Tb.N and Tb.Th of injectable formulations increased radially at 6 weeks. This suggested formation of new trabeculae, and growth of old and new trabeculae from the host bone interface towards the interior of the scaffold. Careful inspection of histological images revealed that indeed new bone was deposited on the surface of the PUR phase, and we believe that this corresponds to the new trabeculae detected by μCT. As a result, our data suggests that injectable composites remodel as cells infiltrate the pores and deposit new bone on the pore walls as well as on the surface of allograft particles.

Interconnected porosity has long been considered a fundamental requirement for the success of bone scaffolds [34, 4]. However, as discussed above, our results show that composites with high and low porosity remodel in femoral plug defects, although they achieve this through different mechanisms. From these observations we propose that a more important parameter for the successful remodeling of bone scaffolds is the persistence of a continuous phase. Visual inspection of the histological images obtained in this work suggests higher continuity in the groups that achieved better remodeling outcomes (ML, IDL). A method to quantify the continuity or the connectivity of an image is through the calculation of the Euler number defined as:

$$E = C - H \tag{6.2}$$

where *C* corresponds to the number of connected objects, and *H* to the number of holes[35]. As such, E=1 represents an image without holes, E>>1 an image with low connectivity, and E<<1 a highly connected image with holes. For the remodeling studies, the connected objects in the defect can be selected as allograft particles, new bone, and remaining polymer. As a result, connectivity will depend on several parameters such as filler particle size and loading, scaffold porosity, polymer stability, and filler resorbability. We hypothesize that a scaffold with increased connectivity (E<<1) will provide a pathway for cells to infiltrate the scaffold resulting in improved remodeling. Preliminary Euler number calculations for a single sample of each treatment group (at 6 weeks) are promising: IDS, IS, and MS had the highest Euler values (2001, 361, and 71 respectively), while IDL and ML (the formulations that achieved more balanced healing) had the lowest Euler values representing higher connectivity (-214 and -81 respectively). A recent publication studying the effect of particle size on the osteointegration of silicate-

substituted calcium phosphates (Si-CaP) reported enhanced performance of particles with size in the range of 250-500 μm [36]. Similar to our study, the authors found that smaller particles (90-125 μm) promoted a less favorable healing outcome. However, the formulation tested was a combination of high loading of particles with slower resorption rates than allograft, and fast polymer degradation (no evidence of polymer after 4 weeks in femoral plug defects in sheep). In contrast to the best candidate formulations from this work (IDL and ML), the Si-CaP will result in high Euler numbers as remodeling progresses, and as shown by the authors, this state can also promote remodeling of the defect. Further work is needed to verify these propositions, and this is discussed in the future work section of this dissertation.

Conclusions

Moldable and injectable ABP-PUR biocomposites supported cellular infiltration, and remodeling when implanted in rabbit femoral plug defects, although through different remodeling mechanisms. Moldable biocomposites remodeled by creeping substitution with new bone being deposited on the surface of allograft particles; cells infiltrated injectable formulations through the pores and deposited new bone on the surface of the polymer and allograft particles. Evaluation of the effect of filler mineral composition on the remodeling of injectable formulations, suggested improved performance of mineralized allograft particles without the addition of DBM. Formulations incorporating 105-500 μm sized allograft particles promoted deposition of more mature bone throughout the defects in a radially balanced progression. The results

presented point to connectivity and distance between filler particles as possible influential parameters in the remodeling progression of composite bone scaffolds.

References

1 M. A. Woodruff, C. Lange, J. Reichert, A. Berner, F. L. Chen, P. Fratzl, J. T. Schantz, and D. W. Hutmacher, 'Bone Tissue Engineering: From Bench to Bedside', *Materials Today*, 15 (2012), 430-35.

2 K. Rezwan, Q. Z. Chen, J. J. Blaker, and A. R. Boccaccini, 'Biodegradable and Bioactive Porous Polymer/Inorganic Composite Scaffolds for Bone Tissue Engineering', *Biomaterials*, 27 (2006), 3413-31.

3 S. Scaglione, E. Lazzarini, C. Ilengo, and R. Quarto, 'A Composite Material Model for Improved Bone Formation', *Journal of Tissue Engineering and Regenerative Medicine*, 4 (2010), 505-13.

4 S. Bose, M. Roy, and A. Bandyopadhyay, 'Recent Advances in Bone Tissue Engineering Scaffolds', *Trends in Biotechnology*, 30 (2012), 546-54.

5 M. Bohner, and J. Lemaitre, 'Can Bioactivity Be Tested in Vitro with Sbf Solution?', *Biomaterials*, 30 (2009), 2175-79.

6 J. R. Jones, 'Review of Bioactive Glass: From Hench to Hybrids', *Acta Biomater*, 9 (2013), 4457-86.

7 J. M. Page, E. M. Prieto, J. E. Dumas, K. J. Zienkiewicz, J. C. Wenke, P. Brown-Baer, and S. A. Guelcher, 'Biocompatibility and Chemical Reaction Kinetics of Injectable, Settable Polyurethane/Allograft Bone Biocomposites', *Acta Biomaterialia*, 8 (2012), 4405-16.

8 R. Adhikari, P. A. Gunatillake, I. Griffiths, L. Tatai, M. Wickramaratna, S. Houshyar, T. Moore, R. T. M. Mayadunne, J. Field, M. McGee, and T. Carbone, 'Biodegradable Injectable Polyurethanes: Synthesis and Evaluation for Orthopaedic Applications', *Biomaterials*, 29 (2008), 3762-70.

9 J. E. Dumas, E. M. Prieto, K.J. Zienkiewicz, T. Guda, J. C. Wenke, J. Bible, G.E. Holt, and S.A. Guelcher, 'Balancing the Rates of New Bone Formation and Polymer Degradation Enhances Healing of Weight-Bearing Allograft/Polyurethane Composites in Rabbit Femoral Defects', *Tissue Eng Part A*, Not available - ahead of print (2013).

10 R. Kruger, and J. Groll, 'Fiber Reinforced Calcium Phosphate Cements -- on the Way to Degradable Load Bearing Bone Substitutes?', *Biomaterials*, 33 (2012), 5887-900.

11 J. E. Dumas, K. Zienkiewicz, S. A. Tanner, E. M. Prieto, S. Bhattacharyya, and S. A. Guelcher, 'Synthesis and Characterization of an Injectable Allograft Bone/Polymer Composite Bone Void Filler with Tunable Mechanical Properties', *Tissue Engineering Part A*, 16 (2010), 2505-18.

12 T. Yoshii, J. E. Dumas, A. Okawa, D. M. Spengler, and S. A. Guelcher, 'Synthesis, Characterization of Calcium Phosphates/Polyurethane Composites for Weight-Bearing Implants', *Journal of Biomedical Materials Research Part B-Applied Biomaterials*, 100B (2012), 32-40.

13 J. E. Dumas, T. Davis, G.E. Holt, T. Yoshii, D. S. Perrien, J. S. Nyman, T. Boyce, and S.A. Guelcher, 'Synthesis, Characterization, and Remodeling of Weight-Bearing Allograft Bone/Polyurethane Composites in the Rabbit', *Acta Biomaterialia*, 6 (2010), 2394-406.

14 Michael J. Eagan, and David R. McAllister, 'Biology of Allograft Incorporation', *Clinics in Sports Medicine*, 28 (2009), 203-14.

15 A J Poslinski, Ryan M E, Gupta R K, Seshadri S G, and Frechette F J, 'Rheological Behavior of Filled Polymeric Systems I. Yield Stress and Shear-Thinning Effects', *Journal of Rheology*, 32 (1988), 703-35.

16 G. Baroud, E. Cayer, and M. Bohner, 'Rheological Characterization of Concentrated Aqueous Beta-Tricalcium Phosphate Suspensions: The Effect of Liquid-to-Powder Ratio, Milling Time, and Additives', *Acta Biomaterialia*, 1 (2005), 357-63.

17 Mary L. Bouxsein, Stephen K. Boyd, Blaine A. Christiansen, Robert E. Guldberg, Karl J. Jepsen, and Ralph Müller, 'Guidelines for Assessment of Bone Microstructure in Rodents Using Micro–Computed Tomography', *Journal of Bone and Mineral Research*, 25 (2010), 1468-86.

18 Carlos E. A. Ferreira, Arthur B. Novaes, Violet I. Haraszthy, Márcio Bittencourt, Carolina B. Martinelli, and Sonia M. Luczyszyn, 'A Clinical Study of 406 Sinus Augmentations with 100% Anorganic Bovine Bone', *Journal of Periodontology*, 80 (2009), 1920-27.

19 Francesco Pieri, Giuseppe Corinaldesi, Milena Fini, Nicolò Nicoli Aldini, Roberto Giardino, and Claudio Marchetti, 'Alveolar Ridge Augmentation with Titanium Mesh and a Combination of Autogenous Bone and Anorganic Bovine Bone: A 2-Year Prospective Study', *Journal of Periodontology*, 79 (2008), 2093-103.

20 J.E. Dumas, P.B. BrownBaer, E.M. Prieto, T. Guda, R.G. Hale, J.C. Wenke, and S.A. Guelcher, 'Injectable Reactive Biocomposites for Bone Healing in Critical-Size Rabbit Calvarial Defects', *Biomedical Materials*, 7 (2012), 024112.

21 Joshua Qingsong Li, and Ronald Salovey, 'Model Filled Polymers: The Effect of Particle Size on the Rheology of Filled Poly(Methyl Methacrylate) Composites', *Polymer Engineering & Science*, 44 (2004), 452-62.

22 Shao-Yun Fu, Xi-Qiao Feng, Bernd Lauke, and Yiu-Wing Mai, 'Effects of Particle Size, Particle/Matrix Interface Adhesion and Particle Loading on Mechanical Properties of Particulate–Polymer Composites', *Composites Part B: Engineering*, 39 (2008), 933-61.

23 Kin-tak Lau, Chong Gu, and David Hui, 'A Critical Review on Nanotube and Nanotube/Nanoclay Related Polymer Composite Materials', *Composites Part B: Engineering*, 37 (2006), 425-36.

24 JJ Tiedeman, JF Connolly, BS States, and L Lipiello, 'Treatment of Nonunion by Percutaneous Injection of Bone Marrow and Demineralized Bone Matrix. An Experimental Study in Dogs.', *Clin Orthop Relat Res.*, 268 (1991), 294-302.

25 SR Frenkel, R Moskovich, J Spivak, ZH Zhang, and AB Prewett, 'Demineralized Bone Matrix. Enhancement of Spinal Fusion.', *Spine (Phila Pa 1976)*, 18 (1993), 1634-9.

26 CJ Damien, JR Parsons, AB Prewett, F Huismans, E C Shors, and R E Holmes, 'Effect of Demineralized Bone Matrix on Bone Growth within a Porous Ha Material: A Histologic and Histometric Study.', *J Biomater Appl.*, 9 (1995), 275-88.

27 M Simion, C Dahlin, P Trisi, and A Piatelli, 'Qualitative and Quantitative Comparative Study on Different Filling Materials Used in Bone Tissue Regeneration: A Controlled Clinical Study.', *Int J Periodontics Restorative Dent.* , 14 (1994), 198-215.

28 Lingfei Wei, Richard J. Miron, Bin Shi, and Yufeng Zhang, 'Osteoinductive and Osteopromotive Variability among Different Demineralized Bone Allografts', *Clinical Implant Dentistry and Related Research* (2013), n/a-n/a.

29 Elliott Gruskin, Bruce A. Doll, F. William Futrell, John P. Schmitz, and Jeffrey O. Hollinger, 'Demineralized Bone Matrix in Bone Repair: History and Use', *Advanced Drug Delivery Reviews*, 64 (2012), 1063-77.

30 Hyun W. Bae, Li Zhao, Linda E. A. Kanim, Pamela Wong, Rick B. Delamarter, and Edgar G. Dawson, 'Intervariability and Intravariability of Bone Morphogenetic Proteins in Commercially

Available Demineralized Bone Matrix Products', *Spine*, 31 (2006), 1299-306 10.097/01.brs.0000218581.92992.b7.

31 Cary A. Shapoff, Gerald M. Bowers, Bernard Levy, James T. Mellonig, and Raymond A. Yukna, 'The Effect of Particle Size on the Osteogenic Activity of Composite Grafts of Allogeneic Freeze-Dried Bone and Autogenous Marrow*†', *Journal of Periodontology*, 51 (1980), 625-30.

32 Leandro Eduardo Klüppel, Fernando Antonini, Sérgio Olate, Frederico Felipe Nascimento, José Ricardo Albergaria-Barbosa, and Renato Mazzonetto, 'Bone Repair Is Influenced by Different Particle Sizes of Anorganic Bovine Bone Matrix: A Histologic and Radiographic Study in Vivo', *Journal of Craniofacial Surgery*, 24 (2013), 1074-77 10.97/SCS.0b013e318286a0a3.

33 Megan E. Oest, Kenneth M. Dupont, Hyun-Joon Kong, David J. Mooney, and Robert E. Guldberg, 'Quantitative Assessment of Scaffold and Growth Factor-Mediated Repair of Critically Sized Bone Defects', *Journal of Orthopaedic Research*, 25 (2007), 941-50.

34 A. J. Wagoner Johnson, and B. A. Herschler, 'A Review of the Mechanical Behavior of Cap and Cap/Polymer Composites for Applications in Bone Replacement and Repair', *Acta Biomater*, 7 (2011), 16-30.

35 WK Pratt, *Digital Imaging Processing* (Canada: John Wiley & Sons, 2001).

36 Melanie J. Coathup, Qian Cai, Charlie Campion, Thomas Buckland, and Gordon W. Blunn, 'The Effect of Particle Size on the Osteointegration of Injectable Silicate-Substituted Calcium Phosphate Bone Substitute Materials', *Journal of Biomedical Materials Research Part B: Applied Biomaterials*, 101B (2013), 902-10.

CHAPTER VII

EFFECT OF SUBSTRATE COMPOSITION ON THE *IN VITRO* DIFFERENTIATION OF OSTEOCLAST PRECURSORS AND RESORPTIVE ACTIVITY OF OSTEOCLASTS

Introduction

Developing scaffolds that deliver living cells and/or biologically active molecules to promote the repair and regeneration of injured bone has been the focus of bone tissue engineering. To this end, organic/inorganic composite formulations that combine the mechanical and biological advantages of polymers and ceramics have been produced [1, 2]. Polymeric phases include saturated aliphatic polyesters [3-6], polypropylene fumarates [7-10], and polyurethanes [11-13], among others. Examples of synthetic ceramic phases are bioactive glasses [14], and calcium phosphates [1], while non-synthetic ceramics include autograft and allograft bone [15].

The natural process of bone remodeling is a combination of bone resorption by osteoclasts, followed by new bone deposition by osteoblasts. In order to mimic this phenomenon in bone defects, effective third generation composite biomaterials (those that stimulate specific cellular responses at the cellular level) must combine resorbability and bioactivity [16]. Much attention has been devoted to the bioactivity requirement of biocomposites, and several formulations have been shown to promote cellular infiltration and new bone deposition *in vivo* [17-19, 15, 20, 21]. On the other hand, composite degradation has been mostly associated with hydrolytic degradation of polymers and the dissolution of calcium phosphates at rates dependent on their solubility. In order for biocomposites to be effectively integrated into the remodeling cycle, it has been suggested that they

must undergo active resorption at a similar rate of new bone formation [22]. Consequently, detailed understanding of osteoclasts' effect on different materials is critical information for the design of bone-regenerating biocomposites.

In vitro models can be used to characterize the response of different materials to the action of osteoclasts. Although these models do not take into account all the interactions present *in vivo*, they allow the isolation of specific parameters of interest and serve as a screening tool to identify materials for future animal testing. Previous *in vitro* studies of osteoclasts on ceramics have reported the presence of differentiated cells on bioactive glasses [23-25], calcium phosphates [26-29], and dentin (used as an approximation to bone) [30, 31]. Several of these studies also include evidence of resorbed areas on the surface of the different matrices. While this confirms that osteoclasts can attach and modify ceramics, few studies have focused on osteoclastic resorption rates. Furthermore, studies measuring *in vitro* resorptive rates of selected calcium phosphates and dentin have been completed with methods that i) are coupled with the differentiation of precursor cells, ii) only include one time point, and/or iii) have based the rate calculations on 2D measurements [32, 33].

This study's purpose was to determine the effects of different materials on the differentiation of osteoclast precursors and the resorptive activity of differentiated osteoclasts. In order to decouple the processes of precursor differentiation and osteoclastic resorption, two culture protocols were implemented.

The first protocol was used to study the differentiation progression of osteoclast precursors. CD11b+ mononuclear monocyte/macrophages (which differentiate into functional osteoclasts [34, 35]) were isolated from murine bone marrow cells and cultured on

the different matrices. Tartrate Resistant Acid Phosphatase (TRAP) is a histochemical marker of differentiating and active osteoclasts [36, 37]. Additionally, extracellular release of TRAP by osteoclasts has been found to correlate with resorptive activity both *in vitro* [38, 39] and *in vivo* [36, 40]. Thus, intracellular and extracellular TRAP levels were monitored in time to verify the differentiation progression of the seeded precursors on different matrices. The expression of osteoclastic genes in time was monitored using quantitative real time PCR to identify different stages of osteoclastic differentiation. Given that TRAP is expressed both by osteoclast precursors and differentiated cells [41], it served as an early marker of differentiation. The vacuolar ATPase subunit d2 (ATP6V0d2) has been reported to regulate cell fusion during osteoclast differentiation, and to be an essential component of the proton pump that mediates osteoclastic acidification of the resorption pit [42]. Thus, ATP6V0d2 (labeled as ATP) was hypothesized to represent a mid- and late-stage differentiation marker. Cathepsin-K (CTSK) is a lysosomal protease used by osteoclasts to degrade the organic component of bone [37]. Therefore, expression of CTSK was expected to increase as osteoclasts became active resorbers.

A second protocol was used to quantify the resorptive activity of osteoclasts independently from the differentiation process. Bone marrow osteoclast precursors were first differentiated on tissue culture plastic and then cultured on different matrices. Scanning electron microscopy and confocal imaging techniques were used to characterize osteoclast attachment and morphology. Quantification of resorbed volume of dentin at different time points enabled the calculation of its volumetric resorption rate.

An additional objective of this work was to study the effects of bone morphogenetic protein 2 (BMP-2) on the differentiation of osteoclast precursors and the

resorptive activity of osteoclasts in the presence of mineralized matrices. Our lab has previously reported that delivery of recombinant human BMP-2 in rabbit femoral plug defects stimulated new bone formation, allograft resorption and promoted changes in the degradation mechanism of the polymer [43, 44]. The latter two observations, in combination with *in vitro* and pre-clinical studies reporting enhanced osteoclast differentiation and activity in the presence of BMP-2 [45-48] suggested that BMP-2 could be directly influencing osteoclasts at different stages. The two culture protocols described above were used to characterize the behavior of precursor and differentiated osteoclasts seeded on mineralized matrices in the presence of BMP-2.

Experimental

Materials

Dentin (ivory) was kindly provided by Dr. Julie Sterling (Vanderbilt Center for Bone Biology [VCBB]), and used as a mineralized surface control. Melt-derived 45S5 bioactive glass rods (diameter 10 mm) were purchased from Mo-Sci Health Care (Rolla, MO). β-tricalcium phosphate pellets (48-well compatible) were obtained from 3D Biotek (Hillsborough,NJ). α-minimal essential medium (α-MEM), fetal bovine serum (FBS), Penicillin/Streptomycin solution (P/S), Dulbecco's phosphate-buffered salt without calcium and magnesium (PBS), and the Pierce BCA Protein kit were purchased from Fisher Scientific (Pittsburgh, PA). Osteoclast growth factors (recombinant mouse macrophage colony stimulating factor (MCSF) and receptor activator of NF-kB Ligand (RANKL), transforming growth factor beta (TGF-β), and interleukin-1 alpha (IL-1α)), were purchased from R&D Systems (Minneapolis, MN). CD11b MicroBeads used in the

purification of osteoclast precursors were obtained from Miltenyi Biotec (Auburn, CA). Chemicals for intracellular (Sigma kit 387A) and extracellular staining of tartrate resistance acid phosphatase (TRAP), as well as the glutaraldehyde (25% in water) and osmium tetroxide (4% in water) solutions for electron microscopy, and Triton X-100 were obtained from Sigma-Aldrich (St. Louis, MO). Recombinant human bone morphogenetic protein-2 (BMP-2) was received from Dr. Josh Wenke (Institute of Surgical Research, San Antonio, TX). The BMP-2 was provided in a solution with 1:100 BMP-2:sucrose in weight, 2.5% w/v glycine, 0.5% w/v sucrose, 0.1% v/v Tween80, and 0.5 mM glutamic acid (R&D Systems). This solution was aliquoted into small quantities for cell culture and stored at -80°C. Rhodamine phalloidin was purchased from Life Technologies (Carlsbad, CA) to stain actin filaments of differentiated osteoclasts.

Preparation of matrices for cell culture

Dentin pieces were cut into square chips (~1 mm thick, and cross-sectional area compatible with a 24-well plate) and bioactive rods were cut into disks (~2 mm thick) using an IsoMet Low Speed Saw (Buehler). The surface of bioactive glass disks was polished using wet silicon carbide paper. The resulting material (BG) had a surface roughness lower than 1μm (measured with a Veeco Dektak 150 Stylus Surface profilometer [Plainview, NY]). After polishing, BG disks were cleaned to ensure homogeneous surface activity [49]. Disks were sonicated for 5 min in a solution of acetone and deionized (DI) water (5:95 volume ratio), followed by washing with DI water under sonication for an additional 5 min. After repeating three washings the clean bioactive glass (CBG) was either sterilized for cell culture or further modified in the presence of

simulated body fluid (SBF, prepared according to published techniques [50]). CBG disks were submerged in 15 ml of SBF in a conical plastic tube making sure that the polished surface of the disk was exposed to the solution. The tube was incubated at 37°C for 3 days. Modified disks (SBG) were removed from the solution and gently rinsed with DI water. Polyurethane disks were prepared by mixing polyester polyol (900Da MW), LTI-PEG prepolymer (formulation index: 130), and 7800 parts per million (ppm) triethylenediamine catalyst as a 10% solution in dipropylene glycol. All the reagents were loaded into a 5 ml cup and mixed at low speed using a Hauschild SpeedMixer. The resulting viscous polymer mixture was loaded into plastic cups (diameter of 14 mm) up to a height of ~5 mm and allowed to cure overnight. The polyurethane disks (PUR) removed from the plastic cups had a flat (in contact with the base of the cup) and a concave surface. Surface characterization and cell seeding was completed on the flat surface. Mineralized matrices and polyurethane disks were sterilized with ethanol and conditioned with complete media (α-MEM with 10% FBS and 1% P/S) in an incubator at 37°C in 5% CO_2 overnight. During the entire process, care was taken to ensure that the working surface of the materials was facing up.

Differentiation of osteoclast precursors on different materials

The differentiation of osteoclast precursors cultured on different materials was assessed using CD11b+ mouse bone marrow cells. In each experimental run additional material samples were incubated with complete media (no cells) as controls.

Primary bone marrow cells were extracted from the tibiae and femurs of 4-8 week old c57bl mice. Mice were sacrificed by cervical dislocation following ethical guidelines.

Femurs and tibiae were dissected, followed by complete removal of the surrounding soft tissue. The bone ends (away from the knee) were cut and the bones were submerged in PBS and centrifuged to collect the bone marrow. Centrifuged cells were re-suspended in complete media. Osteoclast precursors were labeled with CD11b microbeads and separated from the bone marrow population using an AutoMacs magnetic separator (Miltenyi Biotec) according to manufacturer's instructions. CD11b+ cells were seeded onto materials and tissue culture plastic at a density of $1.8x10^5$ cells/ml (per well of a 24-well plate – density equivalent to $9x10^4$ cells/cm^2). To seed the cells, conditioning media was removed from all the wells and the samples were air dried inside the sterile hood. A concentrated drop of complete media (~15 μl) containing the cells was located on top of the materials and cells were allowed to sediment for ~20 min. 1 ml of complete medium supplemented with RANKL (50 ng/ml) and MCSF (25 ng/ml) was carefully added to each well and cells were cultured for up to 28 days. Media was replenished every 3-4 days. Previous studies have reported the synergetic effect of BMP-2 with suboptimal levels of RANKL (<<60 ng/ml) on the *in vitro* differentiation of osteoclast precursors [46]. Thus, to study the effect of BMP-2 over the differentiation progression of CD11b+ cells seeded on different mineralized surfaces, complete media was supplemented with MCSF (25 ng/ml), RANKL (30 ng/ml), and BMP-2 (30 ng/ml).

Intracellular and extracellular TRAP staining

To verify differentiation of the osteoclast precursors seeded on each material, cells were fixed and stained for intracellular TRAP activity (Sigma kit 387A). Furthermore, media removed from the wells during each change was collected and frozen at -80°C.

Secreted TRAP into the media was quantified using napthol ASBI-phosphate as the substrate [51]. 50 μl of media were mixed with 150 μl of reaction buffer (100 mM sodium acetate, 50 mM sodium tartrate, 2.5 mM Napthol ASBI-Phosphate in 4% 2-methoxyethanol [ethylene glycol monomethyl ether – EGME]) in a 96-well plate, followed by incubation at 37°C for 35 minutes. The reaction was stopped with the addition of 0.6 M NaOH solution and fluorescence was read at 405 nm (excitation), 520 nm (emission). Fluorescence from control wells (no cells) was subtracted from fluorescence values of the corresponding materials with cells. Fluorescence units of secreted TRAP were further normalized to total protein in the sample.

Quantitative real-time PCR (qPCR) of osteoclast gene markers

Total RNA was isolated from cultured primary cells using the QIAShredder and RNeasy kits from Qiagen. RNA from minimum 4 samples per treatment group was pooled together to obtain enough genetic material for an accurate concentration measurement. cDNA synthesis was performed with the iScript cDNA synthesis kit (BioRad). Quantitative real time PCR of 9-25 ng cDNA/well was performed using the IQ Real Time SybrGreen PCR Supermix (Biorad) and 500 nM of primer mix (250 nM forward, 250 nM reverse). qPCR was completed in a CFX96 system (BioRad) using a 2 step amplification protocol (with annealing temperature of 62°C) followed by a melt curve analysis. Gene expression was normalized to GAPDH. Primer sequences used are summarized in Table 7.1. Primer optimization was completed by the Molecular Cell Biology Resource (MCBR) Core at Vanderbilt University.

Table 7.1. Primer sequences for osteoclastic genes

Gene	Approved nomenclature	Primer sequence	T_A (°C)	Accession number
TRAP	Acp5	*Forward*: CAAGAGGTTCCAGGAGAC *Reverse*: TTTCCAGCCAGCACATAC	55-62	NM_007388
CTSK	Ctsk	*Forward*: ATAACAGCAAGGTGGATG *Reverse*: CACTTCTTCACTGGTCAT	62	NM_007802
ATP	Atp6v0d2	*Forward*: GAAGCTGTCAACATTGCAGA *Reverse*: TCACCGTGATCCTTGCAGAAT	60	NM_175406.3
GAPDH	Gapdh	*Forward*: GAGAAACCTGCCAAGTATG *Reverse*: GGAGTTGCTGTTGAAGTC	55-63	NM_008084

T_A – Annealing temperature

Culture to study the resorptive activity of differentiated osteoclasts

Fully differentiated osteoclasts are capable of polarizing their cell body and forming a tight junction between the basal membrane and the bone surface to delimit a sealed resorption compartment [41]. Thus, resorptive activity of osteoclasts can only be quantified after the precursors have achieved differentiation. In order to de-couple the effects of matrix chemistry over the differentiation of osteoclastic precursors and the resorptive activity of osteoclasts, osteoclasts precursors were completely differentiated on tissue culture plastic and then cultured on different matrices to evaluate their resorptive activity. Osteoclasts were obtained by inducing differentiation of non-adherent MCSF-dependent bone marrow cells according to published methods [52]. Stromal cells were removed from the bone marrow cell population by culturing the cell suspension in a T150 flask at a density of $3x10^5$ cells/ml for 24 hrs with complete media supplemented with 5 ng/ml of MCSF. Media (containing the non-adherent cells) was collected and centrifuged. $7.2x10^6$ non-adherent cells/dish were seeded in 90-mm-diameter cell culture dishes and

cultured with 25 ml of complete media containing MCSF (50 ng/ml), RANKL (30 ng/ml), and TGF-β (0.1 ng/ml). 15 ml of culture medium were replaced every 2-3 days. Cultures were incubated for 5-7 days monitoring the formation of multinucleated cells. When osteoclast formation was maximal, the media was removed from the dishes and the cells were washed 3 times with PBS. While active osteoclasts formed on plastic are resistant to EDTA removal, initial EDTA treatment reduces substrate adhesion and facilitates the removal of functional multinucleated cells with a cell scraper [52]. Thus, 6 ml of 0.02% EDTA (Sigma Aldrich) were added to each dish and the cells were incubated for 20 min at room temperature. EDTA was then removed and replaced with 6 ml of PBS. Cells were carefully scraped from the plastic using a cell scraper, suspended in PBS and counted. $1.8x10^5$ cells/ml (per well of a 24-well plate – density equivalent to $9x10^4$ cells/cm^2) were seeded onto materials and tissue culture plastic. To seed the cells, conditioning media was removed from the wells, and 1 ml of complete media containing the cells was added drop-wise to each well. The cells were allowed to sediment onto the materials for 25 min while being incubated at 37°C and 5% CO_2. Next, the samples were transferred to new plates (or media was removed in case of the tissue culture plastic samples), and 1 ml of complete media supplemented with MCSF (50 ng/ml), RANKL (30 ng/ml), IL-1α (10 ng/ml), and in some cases BMP-2 (30 ng/ml) was carefully added to the wells. Cells were cultured at 37°C and 5% CO_2 for up to 48 hrs.

Morphology characterization of differentiated osteoclasts on different materials

Scanning electron (SEM) and confocal microscopy were used to characterize the morphology of seeded osteoclasts on different matrices. Samples for SEM were washed

with PBS and fixed in a 5% glutaraldehyde solution in DI water for 2 hrs. Samples were then rinsed with DI water and submerged in 1% osmium tetroxide for 15 min as a secondary fixation step. Next, the samples were washed 3 times with DI water, and sequentially dehydrated using increasing concentrations of ethanol. Fixed samples were dried, sputter-coated with gold and imaged using a Hitachi S-4200 SEM (Finchampstead, UK). Confocal microscopy was used to verify the presence of actin rings, characteristic of active osteoclasts, on differentiated cells seeded on dentin. After cell culture, samples were washed twice with PBS, fixed with 10% formalin for 10 min at room temperature, and washed again with PBS. Cells were then permeabilized with 0.1% Triton X-100 in PBS for 5 min, followed by washing with PBS. Cells were incubated with 5 μl of reconstituted methanolic rhodamine phalloidin stock solution per 200 μl of PBS (1% bovine serum album was added to avoid non-specific binding) for 45 min at 37°C protected from light. Samples were washed with PBS, air dried, and cells were imaged using a Zeiss LSM 510 META inverted microscope using a HeNe1 laser at 543 and 633 nm wavelengths, and 20x magnification.

Quantification of volumetric resorption rates

After 24 or 48 hrs culturing on dentin, active osteoclasts were carefully removed from the surface using a cell scraper and the samples were air dried overnight. 3D images of the surface of dentin were obtained using a Zeta instruments Zeta-20 True Color 3D Optical Profiler (San Jose, CA). Images were collected using a Z-range of 42-48 μm and 200 steps resulting in a Z-step size of 0.211-0.239 μm. 20x magnification (field of view: 474x356 μm^2) was used to image at least 3 different areas per sample (total samples: 2).

Roughness of the dentin surface with and without cell treatment was measured using the Zeta 3D imaging software. Zeta Feature Detection Software was used to detect resorption pits on the surface. A reference surface was established on the non-resorbed areas of dentin. Deviations from this baseline with depth >1μm were selected by the software as features of interest (resorption pit), and volume of each feature was reported. The total resorbed volume per image was normalized to the cross sectional area analyzed.

Results

Differentiation of CD11b+ osteoclast precursors mineralized matrices and tissue culture plastic

Figure 7.1 shows images of CD11b+ osteoclast precursors fed with differentiating growth factors and cultured on tissue culture plastic and TCP surfaces. After 28 days, differentiated precursors fused and stained positive for intracellular TRAP (cells cultured on dentin and BG were also TRAP+). Cells with a wide range of size and number of nuclei were identified on tissue culture plastic (Figure 7.1A-B). While cells seeded on mineralized matrices also stained positive for intracellular TRAP, the size of the cells was significantly smaller (Figure 7.1C). Culture of osteoclast precursors with only MCSF generated no positive staining for TRAP which confirmed the lack of committed osteoclasts in the initial cell population (Figure 7.1D).

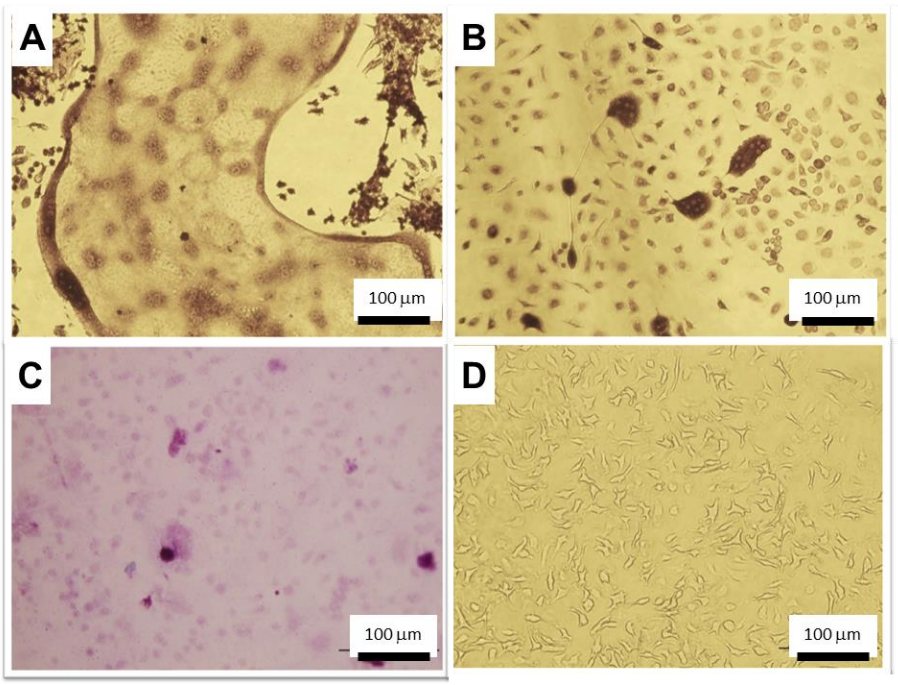

Figure 7.1. Intracellular TRAP staining of osteoclast precursors cultured for 28 days on A,B,D) on tissue culture plastic, and C) TCP. Cell culture media consisted of complete media supplemented with MCSF (25ng/ml) and RANKL (50ng/ml) for A-C, or MCSF (25ng/ml) for D.

Differentiation progression of osteoclast precursors seeded on tissue culture plastic (well), dentin, and BG was monitored in time by measuring their gene expression and secretion of TRAP into the media (Figure 7.2). Expression of all the genes was higher for cells cultured on wells. Cells differentiated on dentin and BG had similar TRAP, and CTSK gene expression, while ATP expression was more similar between cells seeded on wells and dentin. However, the measured trends did not match the expected profile of gene expression in time, and this was true for all the materials.

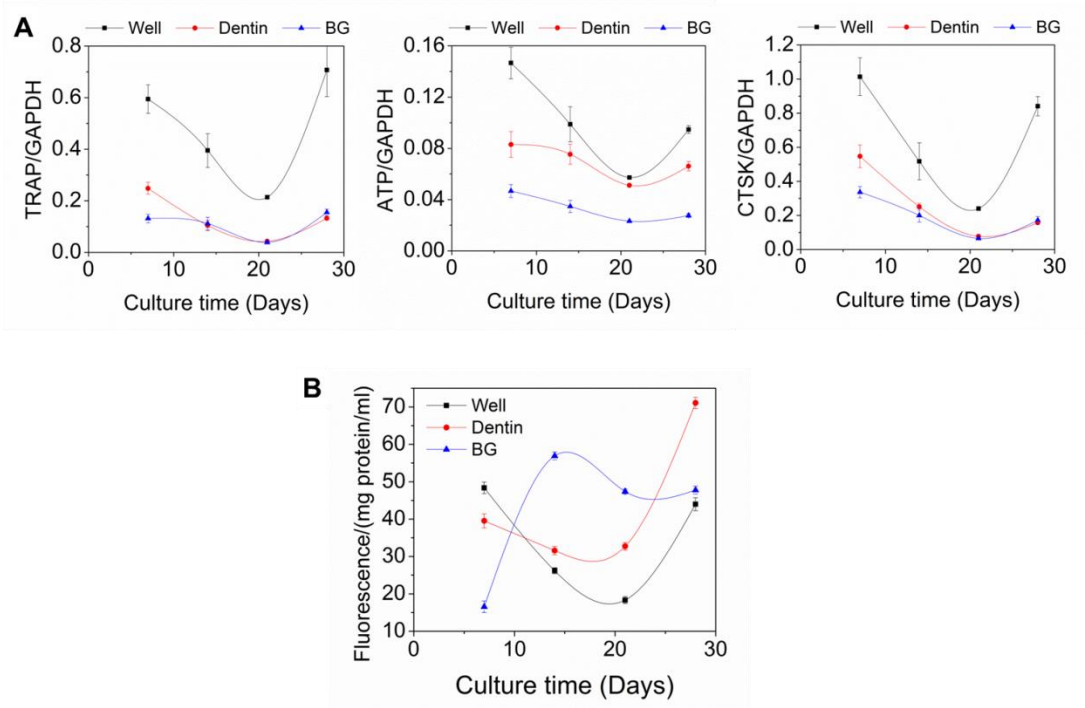

Figure 7.2. Longitudinal characterization of the differentiation of osteoclast precursors cultured on tissue culture plastic (well), dentin, and BG. A) Gene expression, B) Quantification of secreted TRAP

In contrast to gene expression, after 7 days of culture, cells differentiated on wells secreted the least amount of TRAP into the media. Since secreted TRAP is associated with resorptive activity of the osteoclasts, these results indicate that differentiation markers are not good predictors of resorptive activity. Furthermore, as improved differentiation was promoted on tissue culture plastic while secreted TRAP (associated with resorptive activity) was higher on cells cultured on mineralized matrices, osteoclastic differentiation and resorption might be modulated by different factors.

Gene expression and secreted TRAP in time were also evaluated for cells cultured on mineralized matrices in the absence or presence of BMP-2 (Figure 7.3). The obtained results have high variability between runs, hence additional work is required to optimize the experimental methods. However, when comparing treatment effects in each run, it

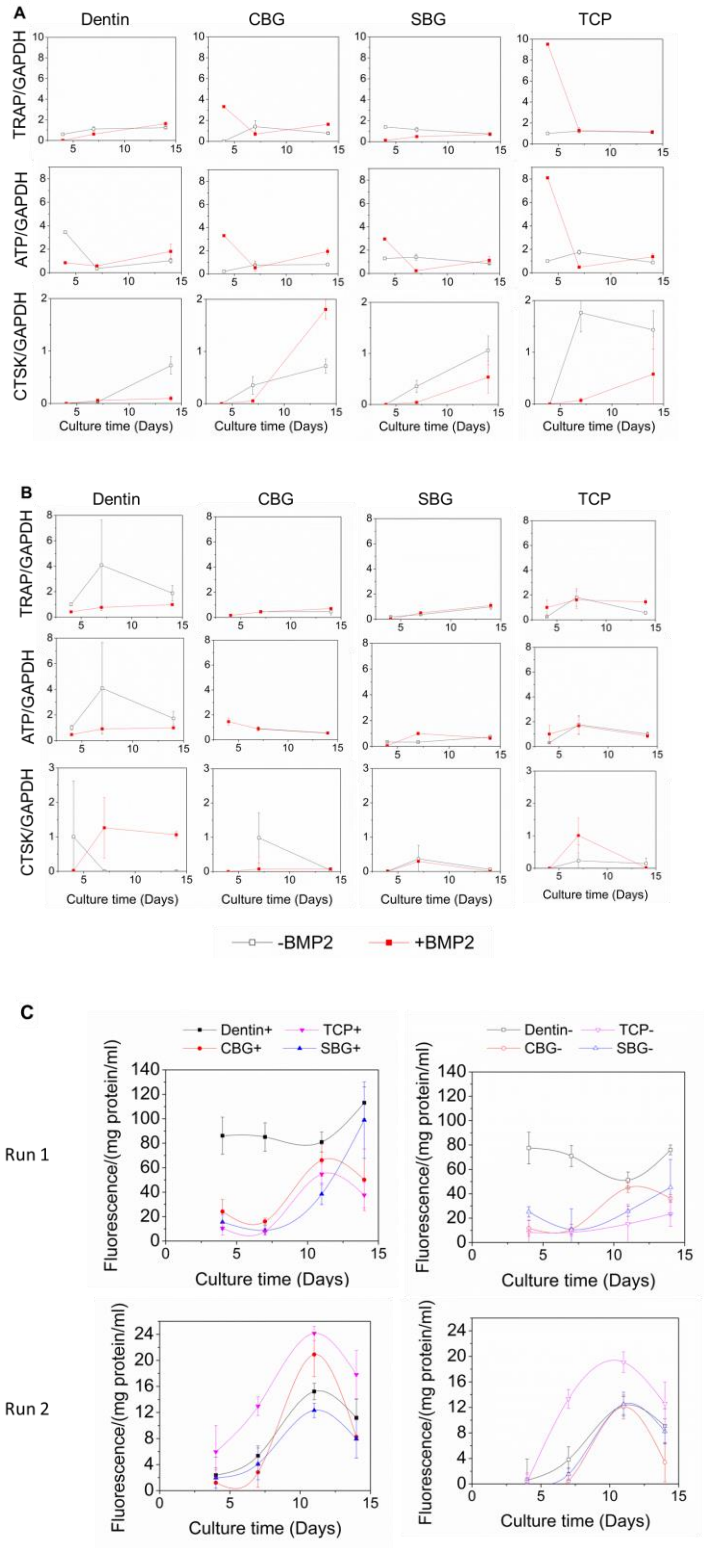

Figure 7.3. Longitudinal characterization of the differentiation of osteoclast precursors cultured on dentin, CBG, SBG and TCP with and without addition of exogenous BMP-2. A) Gene expression quantified in run 1, B) Gene expression quantified in run 2, C) Quantification secreted TRAP in run 1 and 2.

can be concluded that the addition of BMP-2 (even at non-optimal concentrations of RANKL) did not modify the differentiation progression or resorptive activity of osteoclast precursors.

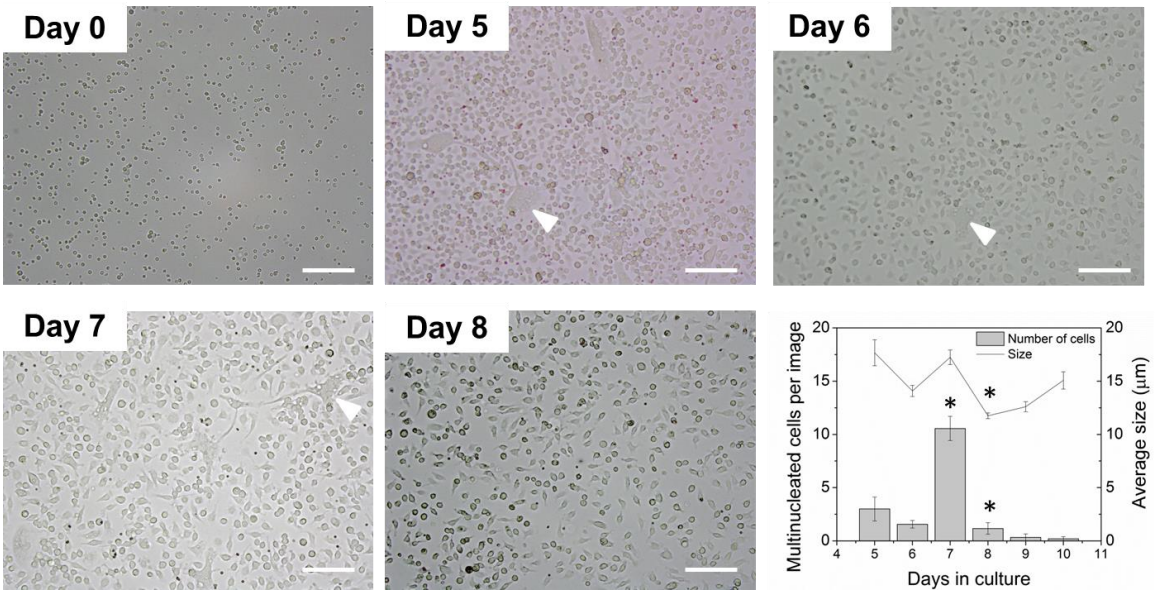

Figure 7.4. Differentiation of non-adherent bone marrow osteoclast precursors. Day 0-8: Representative images of the cells during the differentiation process. White arrowheads point to an example of multinucleated cells in each image. Scale bars represent 100 um. Graph: summarizes the number and average size of multinucleated cells during the differentiation process. These variables were monitored to decide when to stop the experiment to collect differentiated osteoclasts. * Significantly different ($p<0.05$) from the value quantified the day before.

Differentiation of non-adherent osteoclast precursors on tissue culture plastic

Bone marrow osteoclast precursors were successfully differentiated into multinucleated osteoclasts. Figure 7.4 shows representative images of the cells at different time points during the differentiation process. The number of multinucleated cells increased in time until it achieved a maximum value between days 5 and 7. Due to the variation of this parameter between experimental runs, the total number of multinucleated cells per field of view and the average size of cells per field of view were

evaluated as variables to identify the time point at which the differentiation process should be stopped and osteoclasts collected. As shown in Figure 7.4, there was a peak in the number of multinucleated cells (day 7 in that particular run) followed by a significant decrease. This behavior was replicated in each run. On the other hand, average cell size per field of view only showed a significant change compared to the previous day when the number of multinucleated cells had already significantly decreased. According to these results, differentiation of bone marrow precursors should be stopped the day in which a significant increase in number of multinucleated cells is observed.

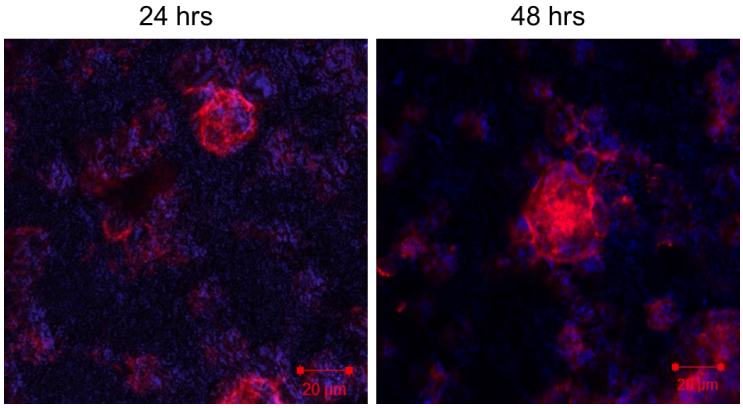

Figure 7.5. Confocal images of osteoclasts seeded on dentin

Morphology of differentiated osteoclasts seeded on different materials

Differentiated osteoclasts were lifted into suspension and seeded onto various surfaces according to the seeding procedure described in the experimental section. The cells obtained exhibited characteristics of active osteoclasts: formation of actin rings when seeded on dentin (Figure 7.5), and positive TRAP staining after being cultured on tissue culture plastic (well), dentin, and PUR, for 24 and 48 hrs (Figure 7.6). Previously, the Chambers research group reported minimal changes in osteoclast-like multinuclear

cells during the first 6 incubation hours on bone slices [52], indicating the cells were already competent for bone resorption when they were sedimented onto bone. In our studies however, the number and size of large multinucleated cells on wells and dentin significantly increased between 24 and 48 hrs of culture (Figure 7.6E). Thus the resorptive activity of the cells was evaluated during longer periods of time (up to 48 hrs compared to 6 hrs by the Chambers group) to ensure full activity of the seeded cells.

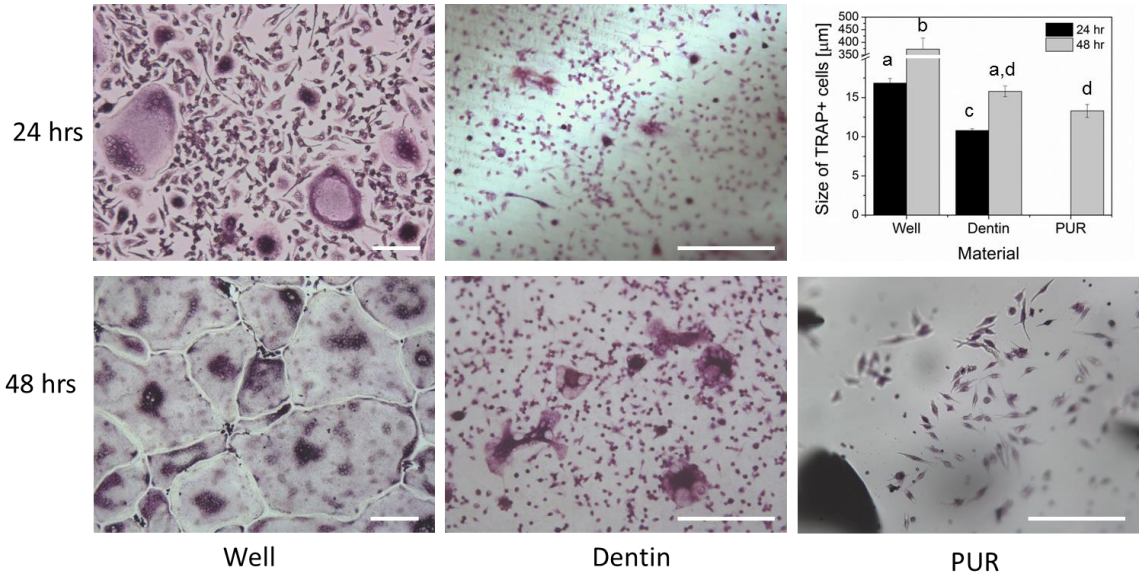

Figure 7.6. Intracellular TRAP stain of osteoclasts seeded on different matrices. Inset graph presents size of the +TRAP cells as a function of material. Scale bars represent 200µm.

An interesting observation from the images in Figure 7.6 is that even though the cells seeded on the different materials were obtained from the same differentiation batch, they adopted different morphologies when exposed to different materials. As expected, all the cells were TRAP+ differentiated osteoclasts. Cells cultured on tissue culture plastic expanded and fused at a higher rate compared to cells cultured on dentin and PUR.

Furthermore, after 48 hrs in culture, large (>350 μm) multinucleated cells completely covered the well surface.

In the case of dentin, at 24 hrs the differentiated cells were smaller than those on the wells. By 48 hrs, the cells increased in size due to fusion of smaller cells (Figure 7.6D). Compared to dentin and wells, a significantly lower number of osteoclasts attached to the surface of PUR. The cells that attached expanded and by 48 hrs their average size was similar to that of cells on dentin, although no large multinucleated cells were present. It has been reported that large osteoclasts are more active resorbers than small osteoclasts [53]. Thus, these results suggest that even cells with the same extent of differentiation might have different resorptive performance on matrices of different nature.

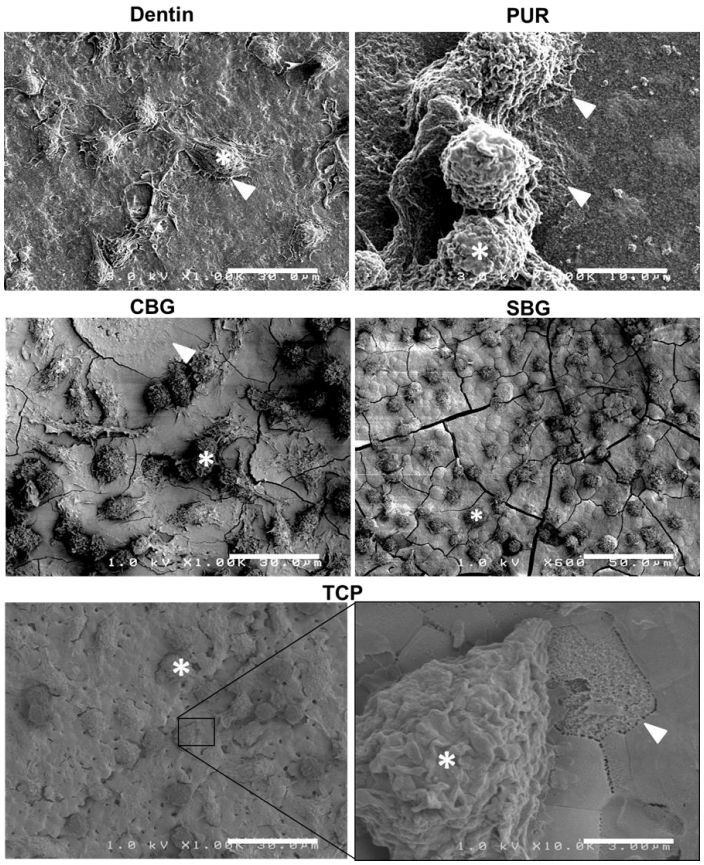

Figure 7.7. Morphology of osteoclasts cultured on different materials observed by SEM.

SEM images of osteoclasts cultured on different matrices for 24 hrs confirm differences in cell size and provide evidence of resorptive activity on each matrix (Figure 7.7). On dentin, cells had a more extended morphology and larger cells (up to 25 μm) were identified in comparison to PUR, CBG, SBG, and TCP. Images show polarized cells with ruffled membranes towards the surface of dentin which suggest active resorption. On PUR, cells were smaller (~9 μm) and rounder. Some cells were fusing, and underneath them changes on the surface of the material were evident. Osteoclasts cultured on CBG and SBG had similar size to cells cultured on PUR, although a significantly higher number of cells attached to the bioactive glass surfaces. Cells cultured on CBG and SBG had protrusions extending towards the surface of the materials (similar to cells on dentin) suggesting stronger attachment to the surface than the cells on PUR. At the top of the SEM image of Figure 7.7 corresponding to CBG a large cell (~30 μm) was removed during the processing. The CBG surface that was underneath the cell shows evidence of etching towards the center of the cell and of extended protrusions towards the border where the cell formed the sealing zone of the resorption pit. Images of SBG with osteoclasts show the characteristic hydroxyapatite nodules surrounded by osteoclasts. No differences between the morphology of osteoclasts cultured on CBG and SBG were identified, although active resorption areas were not easily identified on the SBG materials. Osteoclasts cultured on TCP adopted a small (~7μm) and round configuration on the materials. Extended protrusions towards the surface were not present on most of the cells. Higher magnification images revealed areas in close proximity to osteoclasts with exposed "micro-needled" crystals. Other groups have reported similar results in which these areas are generated by acid etching of the TCP surface [30].

Volumetric resorption rate of dentin

The surface topography of dentin was characterized before and after 24 and 48 hr of osteoclast culture. Cells were removed from the surface and line roughness measurements were completed. Roughness (R_a) of dentin was initially <1μm, and this parameter significantly increased after osteoclast culture (Figure 7.8A). 3-dimensional images of the surface suggest that this increase in roughness was associated with the creation of resorption pits by osteoclasts (Figure 7.8B). Figure 7.8C summarizes the characteristics of the resorption pits at different time points. Total resorbed volume normalized to cross-sectional area constantly increased between 0 and 48 hr. Initially (first 24 hr), this increase was generated by the creation of resorption pits with relatively constant cross-sectional area. In the second 24 hr period, the cells continued to resorb the surface by expanding the area of a fraction of the pits (thus increasing the variability of the pit area), as well as by increasing the excavations' depths. The dependence of resorbed volume on time in these first 48 hr of culture can be approximated by a linear function as shown in Figure 7.8D. According to this, the volumetric resorption rate of dentin by murine osteoclasts *in vitro* corresponds to 0.032 $\mu m^3 \cdot \mu m^{-2} \cdot hr^{-1}$, or 0.768 $\mu m^3 \cdot \mu m^{-2} \cdot day^{-1}$.

Effect of BMP-2 on the volumetric resorption of dentin

In order to evaluate if BMP-2 influenced the resorptive activity of osteoclasts, differentiated cells were seeded onto dentin slices and 30 ng/ml of BMP-2 were added to the culture media. After 48 hr of culture, the resorbed volume and area % were measured

and no significant differences were identified between the groups treated with and without BMP-2, as shown in Figure 7.9.

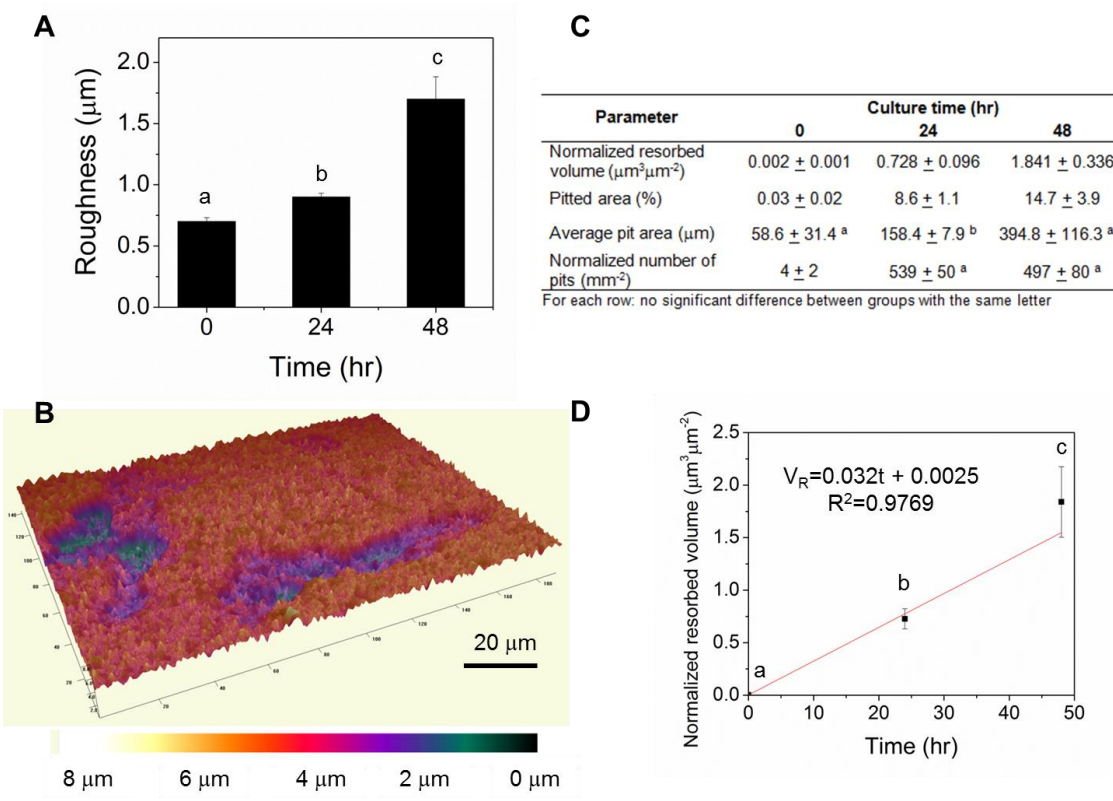

Parameter	Culture time (hr) 0	24	48
Normalized resorbed volume ($\mu m^3 \mu m^{-2}$)	0.002 ± 0.001	0.728 ± 0.096	1.841 ± 0.336
Pitted area (%)	0.03 ± 0.02	8.6 ± 1.1	14.7 ± 3.9
Average pit area (µm)	58.6 ± 31.4 [a]	158.4 ± 7.9 [b]	394.8 ± 116.3 [a,b]
Normalized number of pits (mm^{-2})	4 ± 2	539 ± 50 [a]	497 ± 80 [a]

For each row: no significant difference between groups with the same letter

Figure 7.8. Resorption for 2 days with BMP2. (A) Roughness of the surface before and after cell culture, (B) 3D view of dentin surface after resorption, (C) Characteristics of the resorption pits generated by osteoclasts on dentin, (D) Quantification of dentin's volumetric resorption rate.

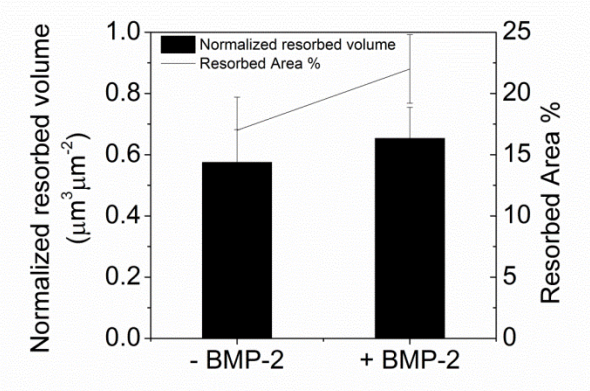

Figure 7.9. Effect of BMP-2 on the volumetric resorption of dentin.

Discussion

Osteoclasts have been reported to differentiate and generate resorption pits when cultured on different mineralized matrices, and our results further support these observations. While analysis at only one time point suggests that all the materials support osteoclast precursor attachment and differentiation, it does not provide information about when this happens. Thus, to monitor the differentiation process in time, osteoclastic gene expression was quantified after 7, 14, 21, and 28 days of culture. Three genes were identified as possible markers of state changes of differentiating osteoclasts [41, 37, 42]: TRAP (early marker), ATP (mid and late marker), and CTSK (late marker). According to studies of osteoclast precursors obtained from human peripheral blood mononuclear cells (PBMC), the cells only began resorbing dentin after 3 weeks of culture [33]. This suggests that resorptive capabilities develop after the cells differentiate on top of the materials. We expected to capture this change in behavior by monitoring gene expression. However, as shown in Figures 2 and 3, gene expression did not follow the expected profiles. No consistent changes could be identified in the gene expression profiles of cells cultured on different materials in time. One possible explanation for this is that the profiled genes start being expressed earlier than day 7 in culture. Indeed, detailed analysis of the transcriptional program of mouse osteoclasts has suggested that pre-osteoclasts express almost all genes necessary for differentiation [54]. Another possibility for not detecting changes of gene expression in time is that the protocol needs to be further optimized. Suggestions to improve the characterization of the differentiation process in time are presented in the future work section of this dissertation.

Osteoclastic differentiation and function are regulated by different humoral agents [52]. Maintaining these agents constant in cell culture, our goal was to characterize the resorptive activity of osteoclasts when exposed to matrices of different nature. Thus, the differentiation protocol of murine non-adherent bone marrow cells into osteoclasts on tissue culture plastic was fully characterized. During differentiation, a significant increase in the number of multinucleated osteoclasts signals that the cells should be collected for further activity studies. Following the described protocol, functional TRAP+ osteoclasts that generate characteristic actin rings when seeded on dentin were obtained (Figures 7.4-7.5).

Microscopy analysis of differentiated osteoclasts cultured on wells, dentin, PUR, CBG, SBG, and TCP surfaces revealed morphological variances that could be related to differences in their resorptive activity (Figures 7.5-7.6). Although the seeding procedure for all the materials was the same, a lower number of cells attached to the PUR disks. The cells that did attach remained small and round without a polarized cell body characteristic of actively resorbing osteoclasts (Figure 7.6-PUR). A similar cell body was evident for the osteoclasts seeded on TCP, although higher number attached to this surface (Figure 7.6-TCP). However, areas with evidence of changes on the substrate surface were present in close proximity of cells seeded on these materials (PUR and TCP). The changes on the surface correspond to that reported as resorption of TCP by other authors [27, 28], and were shallow and localized. In contrast, osteoclasts cultured on dentin and bioactive glass surfaces (CBG and SBG) had a polarized structure with extensive protrusions towards the substrate away from the apical region (Figure 7.6- Dentin, CBG, SBG). The extended protrusions of cells cultured on dentin, CBG, and SBG suggest tighter attachment to these

substrates than to PUR and TCP, and correlate with observations of other groups reporting different modes of resorption for cells with various sizes [55] or on materials with different chemistries [32]. Against a widely accepted consensus in the field about osteoclasts recognizing bone as a substrate for resorption due to the bone mineral content, it has recently been reported that "bone is not essential for osteoclast activation", and that resorptive activity is induced by $\alpha_v\beta_3$ ligands (vitronectin) which have high affinity for bone [56]. Since cell culture in this work was completed using 10% FBS in the media, it is possible that vitronectin present in the serum adhered to the substrates and influenced the cellular behavior. As suggested in the future work section, it would be worthwhile to quantify the affinity of vitronectin to the surface of the mineralized matrices and PURs analyzed in this work to verify if this is the controlling factor that promotes different resorption rates of materials *in vivo*.

Measurement of the resorbed volume in time enabled the determination of the *in vitro* volumetric resorption rate of dentin as 0.768 $\mu m^3 \cdot \mu m^{-2} \cdot day^{-1}$. This value is much higher than that reported for calcium phosphate ceramics as 0.01 $\mu m^3 \cdot \mu m^{-2} \cdot day^{-1}$ [32]. The difference between these resorption rates is in line with *in vivo* observations of calcium phosphates remaining in the body even after years of implantation [57]. However, the analysis of calcium phosphates was conducted using human cells (which have lower metabolic activity than mice cells), as well as a protocol that includes the period of osteoclast differentiation in the calculation. Thus, it is important to use the same *in vitro* protocol described in this work to characterize and compare the resorptive rates of synthetic matrices. A challenge associated with the measurement of resorption rates of the synthetic matrices is that these contain pits even before cell culture. We have tested

polishing the materials before culture, but due to the porosity of the materials, polishing exposes pits on the final surface. To overcome this, the pit volume of each sample should be quantified before and after cell culture, and the resulting difference used to calculate the corresponding resorption rates.

Addition of BMP-2 to the culture media did not significantly change osteoclastic differentiation or resorptive activity on mineralized matrices. These results contrast to previous reports of BMP-2 stimulating the direct differentiation of osteoclasts *in vitro.* However, this stimulation took place under very specific culture conditions: on tissue culture plastic and suboptimal doses of RANKL [46]. It is possible that the addition of a matrix to the protocol modified the behavior of the cells, and even masked the effect of BMP-2. Evidence of the impact that the substrate has on the behavior of the cells is present in Figure 7.5 which shows significant differences in the size of differentiated osteoclasts cultured on several substrates. An additional observation to keep in mind for future experiments is that for the experimental runs measuring resorptive activity in the presence of BMP-2, the cell seeding procedure used was the one described for the differentiation studies. As a result, the seeded cells were concentrated on a section of the materials instead of being homogeneously distributed among the whole area. Consequently, the normalized resorbed volume is lower than that measured for the resorption rate calculations. While the normalized resorbed volumes should not be directly compared between these experiments, comparisons between groups in the same experiment are valid. For future experiments however, the preferred seeding procedure is the one described for the activity studies since it generates a homogeneous distribution of the cells on the materials. The preferred seeding procedure removes bias from the results

since it allows the experimenter to image random areas of the sample instead of having to locate the specific area where the cells were initially seeded.

Conclusions

In vitro cell culture methods enabled the characterization of the differentiation and resorptive activity of osteoclast precursors cultured on different substrates. Pre-osteoclasts attached and differentiated on mineralized surfaces. BMP-2 did not have a direct effect on osteoclastic differentiation or activity. When differentiated osteoclasts where cultured on dentin, CBG, SBG, TCP, and PUR, they exhibited different morphology. It is expected that differences in morphology will be associated to different resorption rates, and this remains to be studied in future work. The results from this work suggest that differentiation of osteoclast precurors is not sufficient for effective resorption. While this has been reported in the past and associated with lack of expression of specific genes in the cells [37], we have shown that even equally differentiated cells behave differently depending on the substrate for culture. The *in vitro* cell culture protocol to study the resorptive activity of murine bone marrow cells on different matrices introduced in this work was used to determine the volumetric resorptive rate of dentin. The application of this method for the quantitation and direct comparison between volumetric resorptive rates of synthetic matrices provides a useful screening tool in the design of effective biocomposite bone scaffolds.

References

1 K. Rezwan, Q. Z. Chen, J. J. Blaker, and A. R. Boccaccini, 'Biodegradable and Bioactive Porous Polymer/Inorganic Composite Scaffolds for Bone Tissue Engineering', *Biomaterials,* 27 (2006), 3413-31.

2 A. J. Wagoner Johnson, and B. A. Herschler, 'A Review of the Mechanical Behavior of Cap and Cap/Polymer Composites for Applications in Bone Replacement and Repair', *Acta Biomater,* 7 (2011), 16-30.

3 C. Mauli Agrawal, and Robert B. Ray, 'Biodegradable Polymeric Scaffolds for Musculoskeletal Tissue Engineering', *Journal of Biomed Mater Res,* 55 (2001), 141-50.

4 Zhen Pan, and Jiandong Ding, 'Poly(Lactide-Co-Glycolide) Porous Scaffolds for Tissue Engineering and Regenerative Medicine', *Interface Focus,* 2 (2012), 366-77.

5 Xiaohua Liu, and Peter X. Ma, 'Polymeric Scaffolds for Bone Tissue Engineering', *Annals of Biomedical Engineering,* 32 (2004), 477-86.

6 Lakshimi S. Nair, and Cato T. Laurencin, 'Biodegradable Polymers as Biomaterials', *Progress in Polymer Science,* 32 (2007), 762-98.

7 Elizabeth M. Christenson, Wafa Soofi, Jennifer Holm, L., Neil Cameron, R., and Antonios G. Mikos, 'Biodegradable Fumarate-Based Polyhipes as Tissue Engineering Scaffolds', *Biomacromolecules,* 8 (2007), 3806-14.

8 S He, MD Timmer, MJ Yaszemski, AW Yasko, PS Engel, and AG Mikos, 'Synthesis of Biodegradable Poly(Propylene Fumarate) Networks with Poly(Propylene Fumarate)-Diacrylate Macromers as Crosslinking Agents and Characterization of Their Degradation Products', *Polymer,* 42 (2001), 1251.

9 R. S. Moglia, J. L. Holm, N. A. Sears, C. J. Wilson, D. M. Harrison, and E. Cosgriff-Hernandez, 'Injectable Polyhipes as High-Porosity Bone Grafts', *Biomacromolecules,* 12 (2011), 3621-28.

10 X Shi, and AG Mikos, 'Poly(Propylene Fumarate)', in *An Introduction to Biomaterials*, ed. by SA Guelcher and JO Hollinger (Boca Raton: CRC Press, 2006), pp. 205-18.

11 R. Adhikari, P. A. Gunatillake, I. Griffiths, L. Tatai, M. Wickramaratna, S. Houshyar, T. Moore, R. T. M. Mayadunne, J. Field, M. McGee, and T. Carbone, 'Biodegradable Injectable Polyurethanes: Synthesis and Evaluation for Orthopaedic Applications', *Biomaterials,* 29 (2008), 3762-70.

12 S Gogolewski, and K Gorna, 'Biodegradable Polyurethane Cancellous Bone Graft Substitutes in the Treatment of Iliac Crest Defects', *J Biomed Mater Res,* 80A (2007), 94.

13 SA Guelcher, 'Biodegrabable Polyurethanes: Synthesis and Applications in Regenerative Medicine', *Tissue Engineering: Part B,* 14 (2008), 3-17.

14 J. R. Jones, 'Review of Bioactive Glass: From Hench to Hybrids', *Acta Biomater,* 9 (2013), 4457-86.

15 J. E. Dumas, T. Davis, G.E. Holt, T. Yoshii, D. S. Perrien, J. S. Nyman, T. Boyce, and S.A. Guelcher, 'Synthesis, Characterization, and Remodeling of Weight-Bearing Allograft Bone/Polyurethane Composites in the Rabbit', *Acta Biomaterialia,* 6 (2010), 2394-406.

16 Larry L. Hench, and Julia M. Polak, 'Third-Generation Biomedical Materials', *Science,* 295 (2002), 1014-17.

17 T. Yoshii, J. E. Dumas, A. Okawa, D. M. Spengler, and S. A. Guelcher, 'Synthesis, Characterization of Calcium Phosphates/Polyurethane Composites for Weight-Bearing Implants', *Journal of Biomedical Materials Research Part B-Applied Biomaterials,* 100B (2012), 32-40.

18 J. Kim, S. McBride, M. Fulmer, R. Harten, Z. Garza, D. D. Dean, V. L. Sylvia, B. Doll, T. L. Wolfgang, E. Gruskin, and J. O. Hollinger, 'Fiber-Reinforced Calcium Phosphate Cement Formulations for Cranioplasty Applications: A 52-Week Duration Preclinical Rabbit Calvaria Study', *J Biomed Mater Res B Appl Biomater,* 100 (2012), 1170-8.

19 J Kim, MHR Magno, H Waters, B Doll, S McBride, P Alvarez, A Darr, A Vasanji, J Kohn, and JO Hollinger, 'Bone Regeneration in a Rabbit Critical-Sized Calvarial Model Using Tyrosine-Derived Polycarbonate Scaffolds', *Tissue Engineering: Part A,* 18 (2012), 1132-39.

20 JP Fisher, JWM Vehof, D Dean, JPCM van der Waerden, TA Holland, A Mikos, and JA Jansen, 'Soft and Hard Tissue Response to Photocrosslinked Poly(Propylene Fumarate) Scaffolds in a Rabbit Model', *J Biomed Mater Res,* 59 (2002), 547-56.

21 S. Scaglione, E. Lazzarini, C. Ilengo, and R. Quarto, 'A Composite Material Model for Improved Bone Formation', *Journal of Tissue Engineering and Regenerative Medicine,* 4 (2010), 505-13.

22 ArndtF Schilling, Sandra Filke, Silja Brink, Heike Korbmacher, Michael Amling, and JohannesM Rueger, 'Osteoclasts and Biomaterials', *European Journal of Trauma,* 32 (2006), 107-13.

23 Eileen Gentleman, Yann C. Fredholm, Gavin Jell, Nasrin Lotfibakhshaiesh, Matthew D. O'Donnell, Robert G. Hill, and Molly M. Stevens, 'The Effects of Strontium-Substituted Bioactive Glasses on Osteoblasts and Osteoclasts in Vitro', *Biomaterials,* 31 (2010), 3949-56.

24 Y. M. Zhao, Y. M. Zhang, Y. T. Zhao, Y. R. Cai, F. Monchau, A. Lefevre, and H. F. Hildebrand, 'Osteoclast Behaviour on Synthetic Bioglasses with Different Crystallinity in Vitro', in *BIOmaterialien* (2005), p. 281.

25 Swati Midha, Wouter van den Bergh, Taek B. Kim, Peter D. Lee, Julian R. Jones, and Christopher A. Mitchell, 'Bioactive Glass Foam Scaffolds Are Remodelled by Osteoclasts and Support the Formation of Mineralized Matrix and Vascular Networks in Vitro', *Advanced Healthcare Materials,* 2 (2013), 490-99.

26 C. M. Botelho, R. A. Brooks, G. Spence, I. McFarlane, M. A. Lopes, S. M. Best, J. D. Santos, N. Rushton, and W. Bonfield, 'Differentiation of Mononuclear Precursors into Osteoclasts on the Surface of Si-Substituted Hydroxyapatite', *Journal of Biomedical Materials Research Part A,* 78A (2006), 709-20.

27 Rainer Detsch, Susannne Schaefer, Ulrike Deisinger, Guenter Ziegler, Hermann Seitz, and Barbara Leukers, 'In Vitro -Osteoclastic Activity Studies on Surfaces of 3d Printed Calcium Phosphate Scaffolds', *Journal of Biomaterials Applications,* 26 (2011), 359-80.

28 S. Yamada, D. Heymann, J. M. Bouler, and G. Daculsi, 'Osteoclastic Resorption of Biphasic Calcium Phosphate Ceramic in Vitro', *Journal of Biomedical Materials Research,* 37 (1997), 346-52.

29 S. Yamada, D. Heymann, J.M. Bouler, and G. Daculsi, 'Osteoclastic Resorption of Calcium Phosphate Ceramics with Different Hydroxyapatite/B-Tricalcium Phosphate Ratios', *Biomaterials,* 18 (1997), 1037-41.

30 Zahi Badran, Paul Pilet, Elise Verron, Jean-Michel Bouler, Pierre Weiss, Gaël Grimandi, Jérôme Guicheux, and Assem Soueidan, 'Assay of in Vitro Osteoclast Activity on Dentine, and Synthetic Calcium Phosphate Bone Substitutes', *Journal of Materials Science: Materials in Medicine,* 23 (2012), 797-803.

31 Karen Fuller, Jade L. Ross, Kinga A. Szewczyk, Raymond Moss, and Timothy J. Chambers, 'Bone Is Not Essential for Osteoclas Activation', *PLoS one*, 5 (2010), 1-14.

32 T. Winkler, E. Hoenig, R. Gildenhaar, G. Berger, D. Fritsch, R. Janssen, M. M. Morlock, and A. F. Schilling, 'Volumetric Analysis of Osteoclastic Bioresorption of Calcium Phosphate Ceramics with Different Solubilities', *Acta Biomaterialia*, 6 (2010), 4127-35.

33 Arndt F. Schilling, Wolfgang Linhart, Sandra Filke, Matthias Gebauer, Thorsten Schinke, Johannes M. Rueger, and Michael Amling, 'Resorbability of Bone Substitute Biomaterials by Human Osteoclasts', *Biomaterials*, 25 (2004), 3963-72.

34 Hidetaka Hayashi, Ken-ichi Nakahama, Takahiro Sato, Takehiko Tuchiya, Yasuyuki Asakawa, Toshimitu Maemura, Masanobu Tanaka, Mineto Morita, and Ikuo Morita, 'The Role of Mac-1 (Cd11b/Cd18) in Osteoclast Differentiation Induced by Receptor Activator of Nuclear Factor-Kb Ligand', *FEBS Letters*, 582 (2008), 3243-48.

35 Kosuke Mizutani, Sudha Sud, and Kenneth J. Pienta, 'Prostate Cancer Promotes Cd11b Positive Cells to Differentiate into Osteoclasts', *Journal of Cellular Biochemistry*, 106 (2009), 563-69.

36 GregoryR Mundy, 'Regulatory Mechanisms of Osteoclast Differentiation and Function', *Journal of Bone and Mineral Metabolism*, 14 (1996), 59-64.

37 Steven L. Teitelbaum, 'Bone Resorption by Osteoclasts', *Science*, 289 (2000), 1504-08.

38 Anthony J. Janckila, Ranga N. Parthasarathy, Latha K. Parthasarathy, Ratnam S. Seelan, Yi-Cheung Hsueh, Jukka Rissanen, Sari L. Alatalo, Jussi M. Halleen, and Lung T. Yam, 'Properties and Expression of Human Tartrate-Resistant Acid Phosphatase Isoform 5a by Monocyte-Derived Cells', *Journal of Leukocyte Biology*, 77 (2005), 209-18.

39 Barrie Kirstein, Timothy J. Chambers, and Karen Fuller, 'Secretion of Tartrate-Resistant Acid Phosphatase by Osteoclasts Correlates with Resorptive Behavior', *Journal of Cellular Biochemistry*, 98 (2006), 1085-94.

40 J. M. Halleen, H. Ylipahkala, S. L. Alatalo, A. J. Janckila, J. E. Heikkinen, H. Suominen, S. Cheng, and H. K. Väänänen, 'Serum Tartrate-Resistant Acid Phosphatase 5b, but Not 5a, Correlates with Other Markers of Bone Turnover and Bone Mineral Density', *Calcified Tissue International*, 71 (2002), 20-25.

41 William J. Boyle, W. Scott Simonet, and David L. Lacey, 'Osteoclast Differentiation and Activation', *Nature*, 423 (2003), 337-42.

42 Haiping Wu, Guoliang Xu, and Yi-Ping Li, 'Atp6v0d2 Is an Essential Component of the Osteoclast-Specific Proton Pump That Mediates Extracellular Acidification in Bone Resorption', *Journal of Bone and Mineral Research*, 24 (2009), 871-85.

43 J. E. Dumas, E. M. Prieto, K.J. Zienkiewicz, T. Guda, J. C. Wenke, J. Bible, G.E. Holt, and S.A. Guelcher, 'Balancing the Rates of New Bone Formation and Polymer Degradation Enhances Healing of Weight-Bearing Allograft/Polyurethane Composites in Rabbit Femoral Defects', *Tissue Eng Part A*, Not available - ahead of print (2013).

44 J.E. Dumas, P.B. BrownBaer, E.M. Prieto, T. Guda, R.G. Hale, J.C. Wenke, and S.A. Guelcher, 'Injectable Reactive Biocomposites for Bone Healing in Critical-Size Rabbit Calvarial Defects', *Biomedical Materials*, 7 (2012), 024112.

45 Jeffrey M. Toth, Scott D. Boden, J Kenneth Burkus, Jeffrey M. Badura, Steven M. Peckham, and William F. McKay, 'Short-Term Osteoclastic Activity Induced by Locally High Concentrations of Recombinant Human Bone Morphogenetic Protein–2 in a Cancellous Bone Environment', *Spine*, 34 (2009), 539-50 10.1097/BRS.0b013e3181952695.

46 E. D. Jensen, L. Pham, C. J. Billington, Jr., K. Espe, A. E. Carlson, J. J. Westendorf, A. Petryk, R. Gopalakrishnan, and K. Mansky, 'Bone Morphogenic Protein 2 Directly Enhances Differentiation of Murine Osteoclast Precursors', *J Cell Biochem,* 109 (2010), 672-82.

47 H. Kaneko, T. Arakawa, H. Mano, T. Kaneda, A. Ogasawara, M. Nakagawa, Y. Toyama, Y. Yabe, M. Kumegawa, and Y. Hakeda, 'Direct Stimulation of Osteoclastic Bone Resorption by Bone Morphogenetic Protein (Bmp)-2 and Expression of Bmp Receptors in Mature Osteoclasts', *Bone,* 27 (2000), 479-86.

48 K. Itoh, N. Udagawa, T. Katagiri, S. Iemura, N. Ueno, H. Yasuda, K. Higashio, J. M. Quinn, M. T. Gillespie, T. J. Martin, T. Suda, and N. Takahashi, 'Bone Morphogenetic Protein 2 Stimulates Osteoclast Differentiation and Survival Supported by Receptor Activator of Nuclear Factor-Kappab Ligand', *Endocrinology,* 142 (2001), 3656-62.

49 E. Verne, C. Vitale-Brovarone, E. Bui, C. L. Bianchi, and A. R. Boccaccini, 'Surface Functionalization of Bioactive Glasses', *Journal of Biomedical Materials Research Part A,* 90A (2009), 981-92.

50 T. Kokubo, and H. Takadama, 'How Useful Is Sbf in Predicting in Vivo Bone Bioactivity?', *Biomaterials,* 27 (2006), 2907-15.

51 Anthony J. Janckila, Karen Takahashi, Susan Z. Sun, and Lung T. Yam, 'Naphthol-Asbi Phosphate as a Preferred Substrate for Tartrate-Resistant Acid Phosphatase Isoform 5b', *Journal of Bone and Mineral Research,* 16 (2001), 788-93.

52 Karen Fuller, Barrie Kirstein, and Timothy J. Chambers, 'Murine Osteoclast Formation and Function: Differential Regulation by Humoral Agents', *Endocrinology,* 147 (2006), 1979-85.

53 Morris F. Manolson, Hesheng Yu, Weimin Chen, Yeqi Yao, Keying Li, Rita L. Lees, and Johan N. M. Heersche, 'The A3 Isoform of the 100-Kda V-Atpase Subunit Is Highly but Differentially Expressed in Large (≥10 Nuclei) and Small (≤5 Nuclei) Osteoclasts', *Journal of Biological Chemistry,* 278 (2003), 49271-78.

54 David Cappellen, Ngoc-Hong Luong-Nguyen, Sandrine Bongiovanni, Olivier Grenet, Christoph Wanke, and Mira Šuša, 'Transcriptional Program of Mouse Osteoclast Differentiation Governed by the Macrophage Colony-Stimulating Factor and the Ligand for the Receptor Activator of Nfκb', *Journal of Biological Chemistry,* 277 (2002), 21971-82.

55 OkHee Jeon, SuHo Jeong, Yeong-Min Yoo, KyungHwan Kim, DaeSung Yoon, and ChiHyun Kim, 'Quantification of Temporal Changes in 3d Osteoclastic Resorption Pit Using Confocal Laser Scanning Microscopy', *Tissue Engineering and Regenerative Medicine,* 9 (2012), 29-35.

56 Karen Fuller, Jade L. Ross, Kinga A. Szewczyk, Raymond Moss, and Tim J. Chambers, 'Bone Is Not Essential for Osteoclast Activation', *PLoS ONE,* 5 (2010), e12837.

57 T. Kraal, M. Mullender, J. H. D. de Bruine, R. Reinhard, A. de Gast, D. J. Kuik, and B. J. van Royen, 'Resorbability of Rigid Beta-Tricalcium Phosphate Wedges in Open-Wedge High Tibial Osteotomy: A Retrospective Radiological Study', *The Knee,* 15 (2008), 201-05.

CHAPTER VIII

CONCLUSIONS

The research presented in this dissertation describes the development and characterization of biodegradable lysine-derived polyurethane (PUR) formulations that actively participate in the bone healing process. Findings and conclusions presented in the previous chapters have provided insight into structure-property-performance relations of PUR foams and composites.

To our knowledge, Chapter III demonstrates the first biofilm-dispersive scaffold capable of reducing bacterial burden within infected wounds.[1] *In vitro* studies on biofilms of clinical isolates of *Staphylococcus Aureus* identified D-Methionine (D-Met), D-Phenylalanine (D-Phe), D-Proline (D-Pro), and D-Tryptophan (D-Trp) as D-Amino Acids (D-AA) highly effective at dispersing and preventing biofilm formation. Incorporation of a free-base D-Met:D-Pro:D-Trp mixture (1:1:1 mass ratio) into a porous PUR formulation had minimal effects over scaffold porosity and pore size. It did however reduce the compressive mechanical properties of the materials due to the solid particles creating defects on the pore walls. The D-AA mixture was released by diffusion controlled mechanisms for up to 4 weeks, with minimal scaffold degradation. When implanted into segmental rat defects contaminated with an osteomyelitis bacterial strain (UAMS-1), PUR foams augmented with ≥5% D-AA mixture significantly reduced bacterial burden. These results highlight the capability of porous PUR scaffolds to act as

delivery vehicles that modify the wound environment and improve the conditions for future bone remodeling.

PUR composites incorporating β-tricalcium phosphate (TCP) particles exhibited mechanical properties between those of cortical and trabecular bone. Improved interfacial interactions between the ceramic and PUR phases were promoted by the covalent grafting of polycaprolactone (PCL) to the surface of TCP particles. As a result, composites incorporating surface modified particles had reduced water absorption and improved stability under aqueous conditions as confirmed by the measured mechanical properties. When tested *in vitro*, no differences were observed between the differentiation of osteoblasts and osteoclasts seeded on the composites with modified and unmodified particles. These results suggest that surface modification of ceramic fillers is a suitable technique to improve the mechanical performance of settable bone composites. However, in the case of the TCP particles, a side effect of surface modification was a significant decrease in particle size. *In vitro* studies have shown that small particles of hydroxyapatite (<20 μm) generate a strong and cytotoxic inflammatory response.[2] To avoid this response *in vivo*, surface modification of less brittle and stronger ceramic fillers should be considered. An example is the use of surface modified bioactive glass particles, which in turn provide initial weight-bearing capabilities to the PUR scaffolds (ongoing work in the lab).

Settable ABP-PUR biocomposites exhibited initial mechanical properties comparable to those of trabecular bone. Independent of allograft particle size, loading, mineral content, porosity, or BMP-2 dose, all the studied formulations promoted new bone deposition and progressive healing in time from the host bone interface towards the

core of the defects. However, the extent to which healing was achieved varied according to the parameters listed above.

BMP-2 addition to ABP-PUR biocomposites not only increased the rate of new bone formation, but also altered the polymer degradation mechanism to approximate a zero-order process.[3] The resulting similar rates of both new bone formation and polymer degradation resulted in more extensive healing at later time points throughout the graft. These observations underscore the importance of balancing new bone formation and polymer degradation rates so as to promote healing of settable weight-bearing bone composite grafts that maintain bone-like strength while actively remodeling.

Care should be taken with the incorporation of demineralized bone matrix (DBM) in to bone grafts. Contrary to our initial expectations, when DBM was included in ABP-PUR composites, healing progression slowed. We associate this with reported variability of the osteoinductive character of DBM.[4-6] This property is affected by several factors such as donor age and gender, processing, and sterilization protocols.[5] However, there are currently no target properties or standards to describe the osteoinductive capacity of DBM. Consequently, caution should be exercised by surgeons when incorporating DBM as part of a treatment, and by scientists when they aim to pose conclusions in studies utilizing DBM.

In contrast, particle size had a strong effect on the porosity and pore size of ABP-PUR biocomposites. Both these parameters were reduced upon incorporation of allograft particles with size <105 μm. Furthermore, particle size proved to have an effect on the healing progression of plug defects. After 12 weeks, particles in the size range of 100-500 μm promoted more balanced radial remodeling throughout the defects than particles <105

μm. Particles in the effective size range also stimulated the deposition of higher quality bone.

Combined analysis of μCT and histomorphometry data suggests interesting differences in the remodeling mechanism of injectable and moldable ABP-PUR formulations. Moldable composites (<20% porosity, 67 wt% filler) remodeled by creeping substitution: osteoclasts resorbed the surface of allograft particles and generated new pores for cellular inflitration. As part of the infiltrating cells, osteoblasts followed and deposited new bone on the surface of the remaining allograft particles. In comparison, injectable composites (37-47% porous, 47 wt% filler) remodeled as cells infiltrated through the pores and deposited new bone on both the pore walls and the surface of allograft particles. These observations suggest a fully interconnected osteoconductive surface is required for bone graft healing. Although porosity might promote faster initial bone deposition, it also reduces the bone grafts' mechanical properties. Such reductions pose significant limitations for weight-bearing applications in which a slower remodeling progression can favor the appropriate incorporation of the bone graft.

In addition to the *in vivo* characterization of the various ABP-PUR formulations, an *in vitro* cell culture protocol that independently studied the differentiation and resorptive activity of murine bone marrow cells in the presence of different matrices was introduced. Pre-osteoclasts attached and differentiated on mineralized matrices. However, differentiated osteoclasts cultured on dentin, bioactive glass, TCP, and PUR disks exhibited different morphology. These differences are expected to be associated with different resorption rates, and this remains to be studied with the implementation of the developed protocol. Given that osteoclasts were simulateously differentiated and then

seeded on the different materials, our observations suggest that osteoclastogenesis (differentiation) might not be sufficient for effective resorption of matrices. The *in vitro* cell culture protocol to study osteoclastic resorptive activity on different matrices was implemented to determine volumetric resorptive rate of dentin (0.768 $\mu m^3 \cdot \mu m^{-2} \cdot day^{-1}$). Future application of this method to quantify and compare volumetric resorptive rates of synthetic matrices will provide a useful screening tool to design effective biocomposite bone scaffolds.

References

1 Carlos J. Sanchez Jr, Edna M. Prieto, Chad A. Krueger, Katarzyna J. Zienkiewicz, Desiree R. Romano, Catherine L. Ward, Kevin S. Akers, Scott A. Guelcher, and Joseph C. Wenke, 'Effects of Local Delivery of D-Amino Acids from Biofilm-Dispersive Scaffolds on Infection in Contaminated Rat Segmental Defects', *Biomaterials*, 34 (2013), 7533-43.

2 JS Sun, HC Liu, WH Chang, J Li, FH Lin, and HC Tai, 'Influence of Hydroxyapatite Particle Size on Bone Cell Activities: An in Vitro Study', *J Biomed Mater Res*, 39 (1998), 390-7.

3 J. E. Dumas, E. M. Prieto, K.J. Zienkiewicz, T. Guda, J. C. Wenke, J. Bible, G.E. Holt, and S.A. Guelcher, 'Balancing the Rates of New Bone Formation and Polymer Degradation Enhances Healing of Weight-Bearing Allograft/Polyurethane Composites in Rabbit Femoral Defects', *Tissue Eng Part A*, Not available - ahead of print (2013).

4 Lingfei Wei, Richard J. Miron, Bin Shi, and Yufeng Zhang, 'Osteoinductive and Osteopromotive Variability among Different Demineralized Bone Allografts', *Clinical Implant Dentistry and Related Research* (2013), n/a-n/a.

5 Elliott Gruskin, Bruce A. Doll, F. William Futrell, John P. Schmitz, and Jeffrey O. Hollinger, 'Demineralized Bone Matrix in Bone Repair: History and Use', *Advanced Drug Delivery Reviews*, 64 (2012), 1063-77.

6 Hyun W. Bae, Li Zhao, Linda E. A. Kanim, Pamela Wong, Rick B. Delamarter, and Edgar G. Dawson, 'Intervariability and Intravariability of Bone Morphogenetic Proteins in Commercially Available Demineralized Bone Matrix Products', *Spine*, 31 (2006), 1299-306 10.097/01.brs.0000218581.92992.b7.

CHAPTER IX

SUGGESTIONS FOR FUTURE WORK

In addition to identifying and describing useful structure-property-performance relations of PUR foams and composite formulations, the results presented in this work have generated several new and interesting questions. The following are suggestions for future work that address these new research avenues and continue advancing the PUR technology as a viable therapeutic treatment for bone defects.

Biofilm-dispersive PUR scaffold

The promising results obtained with the diffusion controlled release of D-AAs from PUR scaffolds in contaminated wounds open exciting avenues of research in the area of dual-purpose bone grafts. While augmentation with ≥5 wt% D-AA mixture reduced bacterial colonization of scaffolds implanted for 2 weeks in rats, it is not clear if this could further be improved using a different release profile. Effective treatment of MRSA osteomyelitis includes antibiotic treatment for up to 8 weeks.[1] However, the optimal release profile of D-AA remains unknown and merits further investigation. Several strategies could be explored to modify the release profile of the D-AA: a) deliver the D-AAs as hydrochloride salts to accelerate release due to increased solubility,[2] b)encapsulate D-AAs in PLGA microspheres to slow down release, [3] and c) decrease the PUR scaffolds's porosity to slow D-AA diffusion. Given the non-bactericidal character of D-AAs, their effectiveness is enhanced when used as an adjuvant therapy with antibiotics

(unpublished results from our collaborators at the Institute of Surgical Research in San Antonio, TX). Consequently, dual delivery of antibiotics and D-AA could be explored with PUR as the delivery vehicle. This would localize the action of both molecules in the wound. Furethermore, optimization of the antibiotic and D-AA release profile should still be completed. A final suggestion is to replace D-Tryptophan for D-Phenylalanine due to the lower *in vitro* cytotoxicity of the latter.

Remodeling mechanisms of PUR biocomposites

Chapter V presented the strong dependence of wound healing extent on the relative rates of new bone formation and polymer degradation. In this study, these rates were modulated by the addition of rhBMP-2. However, different strategies can be implemented to modify these rates: a) incorporation of mineralized fillers that promote different rates of new bone deposition and resorption (for example, bioactive glass particles), b) development of enzyme-degradable polymers (including for example cathepsin k sensitive peptides in the backbone [4]) which are anticipated to more closely match the constant rate of new bone formation.[5]

Chapters V and VI both suggest that maintaining a continuous surface in the scaffold during bone healing is important to achieve improved remodeling. This observation has been mostly based on histological observations. In order to provide quantifiable evidence, it is suggested to study the relationship between the extent of healing and the samples' connectivity. Thus, histological sections analyzed by histomorphometry can be further processed to calculate their Euler number (eq. 6.2).[6] We speculate that formulations with consistently low Euler numbers (<1, high connectivity)

during remodeling will achieve improved healing at earlier time points compared to those with Euler numbers approaching or higher than unity.

Preliminary work characterizing the new bone formation and polymer degradation rates, as well as the Euler number distribution by areas in the samples studied in Chapter VI, shows promising results. Figures 9.1 and 9.2 plot the histomorphometry values for new bone, and remaining allograft and polymer in the injectable and moldable formulations respectively. Similar to the analysis conducted in Chapter V, data for new bone, allograft, and polymer content were fit to equations 5.3, 5.4, and 5.6 respectively (connecting lines in Figures 9.1 and 9.2). However, given that no new bone formation is present in the acellular cores of injectable materials at 6 weeks, we speculate that new bone formation in this area would be best modeled by an expression that includes a time lag. Currently, new bone formation is suggested to rapidly increase between 6 and 12 weeks. However, we believed the observed profile is an artifact of the fit since the materials are not delivering any growth factor that could promote this response. Figure 9.3 presents the relative rates of new bone formation and polymer degradation as a function of healing extent. In addition, the preliminary Euler number (E) for one sample of each formulation is presented with each graph. These plots show that indeed, samples with lower Euler number achieved a more balanced remodeling throughout the defect (close to balanced rates of new bone formation and polymer degradation, and all the areas achieved >50% healing). Instead, samples with higher Euler numbers exhibited variations in each area's healing extent. To fully characterize the effect of connectivity on healing extent, it is recommended to quantify the Euler number by areas and compare it to the measured rates in time. It is important to note that this preliminary data set includes estimated, as

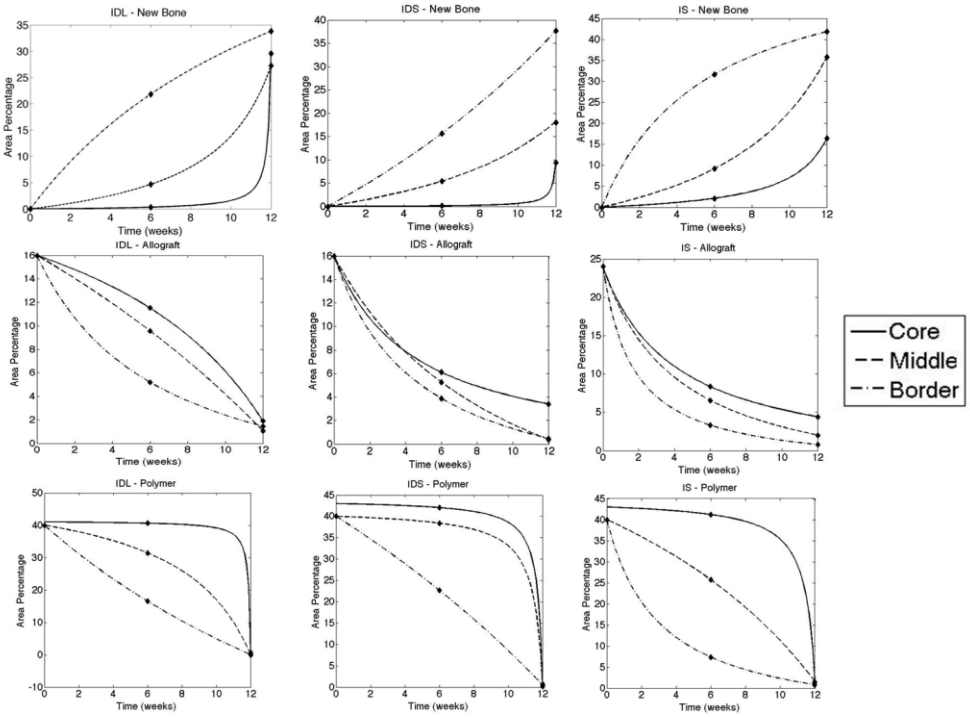

Figure 9.1. Histomorphometric evaluation of remodeling in the injectable scaffolds described in Chapter VI, as a function of time and location.

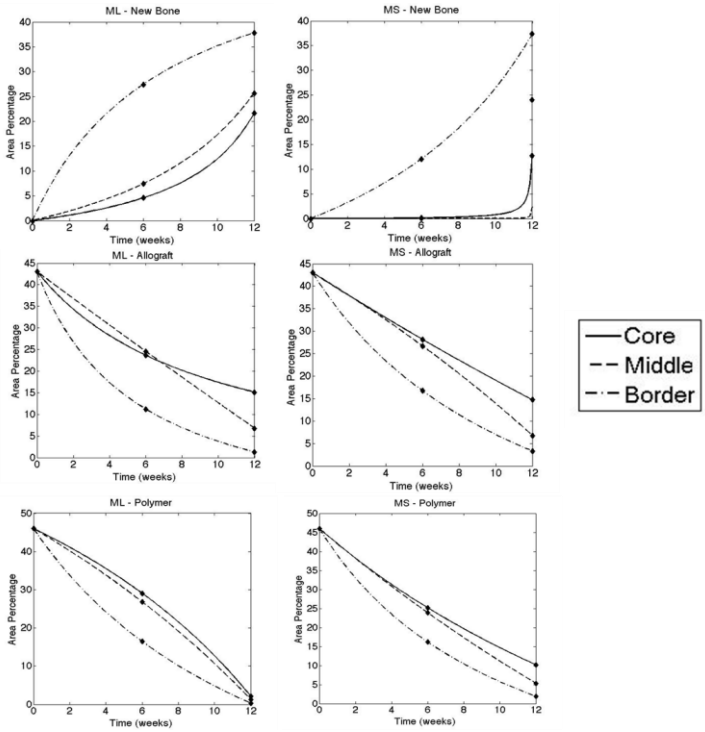

Figure 9.2. Histomorphometric evaluation of remodeling in the moldable scaffolds described in Chapter VI, as a function of time and location.

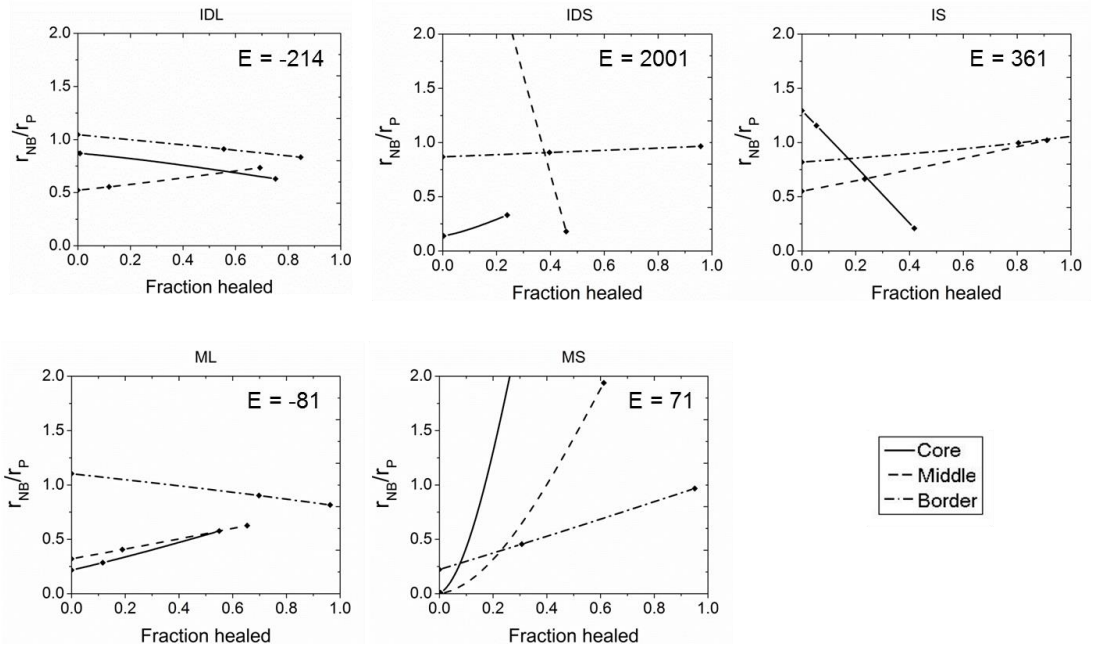

Figure 9.3. Relative rates of new bone formation and polymer degradation for the injectable and moldable formulations described in Chapter VI, as a function of fraction healed and location. E corresponds to the Euler number calculated from a single section for each group at 6 weeks.

opposed to measured, initial values of allograft and polymer (t=0). Thus, in order to ensure proper modeling of the remodeling progression it is necessary to quantify by histomorphometry the initial area % of allograft and polymer in each formulation using samples that were not implanted into the animals (ongoing work in the lab).

Osteoclastic resorption of mineralized matrices

The protocol developed in Chapter VII offers the possibility to independently monitor differentiation of osteoclast precursors and resorptive activity of osteoclasts *in vitro.* Keeping in mind the results from Chapters V and VI which demonstrate high connectivity of the scaffolds as a remodeling requirement, comparing different materials' volumetric resorptive rates *in vitro* will identify the best candidate materials to incorporate in formulations with balanced new bone formation and scaffold degradation

rates. To start, the protocol should be implemented to quantify and compare the volumetric resorptive rates of different mineralized matrices used in our lab (TCP, bioactive glass). While studies have reported osteoclastic effects on the surface of these materials,[8-14] our preliminary studies have shown that these changes are very shallow and seem to be of significantly smaller volumes than the changes on dentin's surface. This also correlates to the observed morphological differences of the cells seeded on each of these materials. Thus, it is speculated that the volumetric resorption rate of the synthetic mineralized matrices will be significantly lower than that measured for dentin, and it will most likely be larger for bioactive glass than for TCP. Rate quantification for these synthetic matrices poses challenges not present with the dentin samples. In contrast to dentin, TCP and bioactive glass disks contain pits on the surface even before cells are cultured on them. To overcome this, the pit volume of each sample should be quantified before and after cell culture and the resulting difference used to calculate the corresponding resorption rates. The samples should be very well labeled to avoid confusion when subtracting initial pitted volumes. Given the location variability of the initial pits, the subtraction of average initial volume should be avoided to reduce error.

Now that the protocol to quantify volumetric resorption rates is in place, it can be used to answer questions related to PUR biocomposite formulation for improved healing. For example, it has recently been reported that the way osteoclasts recognize bone for resorption is due to its high affinity to vitronectin (an $\alpha_v\beta_3$ ligand).[15] Thus, it would be interesting to quantify the affinity of vitronectin to the different matrices of interest. A possible way to do this would be by submerging samples of the same size into a set protein solution volume. At several time points, the samples could be removed from the

solution and incubated in a solution with a set vitronectin antibody set concentration, followed by incubation with a secondary horseradish peroxidase (HRP)-conjugated antibody. Further incubation with a solution containing ABTS (an HRP substrate) and quantification of the optical density at 405 mm would allow determining the total amount of vitronectin adsorbed on the material's surface. A follow up question to answer will be: does the forced adsorption (by drying a known amount of protein on the surface of the materials) of vitronectin improve the volumetric resorption rates of the matrices? Do improvements depend on matrix composition? The answers to these questions will aid in the selection of matrices to further incorporate in PUR biocomposites for *in vivo* testing.

The polymers used so far in the PUR biocomposite formulation have mostly undergone hydrolytic degradation *in vivo*. Results from this work and other research projects in our lab have shown that a better option would be for the polymers to undergo cellular degradation. Thus, the protocol developed in Chapter VII can also be implemented to study the effect that rigidity, as well as oxidative and proteolytic degradation might have on the volumetric resorptive rates of different polymeric formulations.

References

1 C. Liu, A. Bayer, S. E. Cosgrove, R. S. Daum, S. K. Fridkin, R. J. Gorwitz, S. L. Kaplan, A. W. Karchmer, D. P. Levine, B. E. Murray, J. Rybak M, D. A. Talan, and H. F. Chambers, 'Clinical Practice Guidelines by the Infectious Diseases Society of America for the Treatment of Methicillin-Resistant Staphylococcus Aureus Infections in Adults and Children: Executive Summary', *Clin Infect Dis,* 52 (2011), 285-92.

2 B. Li, K. V. Brown, J. C. Wenke, and S. A. Guelcher, 'Sustained Release of Vancomycin from Polyurethane Scaffolds Inhibits Infection of Bone Wounds in a Rat Femoral Segmental Defect Model', *J Control Release,* 145 (2010), 221 - 30.

3 B. Li, T. Yoshii, A. E. Hafeman, J. S. Nyman, J. C. Wenke, and S. A. Guelcher, 'The Effects of Rhbmp-2 Released from Biodegradable Polyurethane/Microsphere Composite Scaffolds on New Bone Formation in Rat Femora', *Biomaterials,* 30 (2009), 6768-79.

4 C. W. Hsu, R. M. Olabisi, E. A. Olmsted-Davis, A. R. Davis, and J. L. West, 'Cathepsin K-Sensitive Poly(Ethylene Glycol) Hydrogels for Degradation in Response to Bone Resorption', *Journal of Biomedical Materials Research Part A,* 98A (2011), 53-62.

5 J. R. Jones, 'Review of Bioactive Glass: From Hench to Hybrids', *Acta Biomater,* 9 (2013), 4457-86.

6 WK Pratt, *Digital Imaging Processing* (Canada: John Wiley & Sons, 2001).

7 Melanie J. Coathup, Qian Cai, Charlie Campion, Thomas Buckland, and Gordon W. Blunn, 'The Effect of Particle Size on the Osteointegration of Injectable Silicate-Substituted Calcium Phosphate Bone Substitute Materials', *Journal of Biomedical Materials Research Part B: Applied Biomaterials,* 101B (2013), 902-10.

8 Eileen Gentleman, Yann C. Fredholm, Gavin Jell, Nasrin Lotfibakhshaiesh, Matthew D. O'Donnell, Robert G. Hill, and Molly M. Stevens, 'The Effects of Strontium-Substituted Bioactive Glasses on Osteoblasts and Osteoclasts in Vitro', *Biomaterials,* 31 (2010), 3949-56.

9 Y. M. Zhao, Y. M. Zhang, Y. T. Zhao, Y. R. Cai, F. Monchau, A. Lefevre, and H. F. Hildebrand, 'Osteoclast Behaviour on Synthetic Bioglasses with Different Crystallinity in Vitro', in *BIOmaterialien* (2005), p. 281.

10 Swati Midha, Wouter van den Bergh, Taek B. Kim, Peter D. Lee, Julian R. Jones, and Christopher A. Mitchell, 'Bioactive Glass Foam Scaffolds Are Remodelled by Osteoclasts and Support the Formation of Mineralized Matrix and Vascular Networks in Vitro', *Advanced Healthcare Materials,* 2 (2013), 490-99.

11 C. M. Botelho, R. A. Brooks, G. Spence, I. McFarlane, M. A. Lopes, S. M. Best, J. D. Santos, N. Rushton, and W. Bonfield, 'Differentiation of Mononuclear Precursors into Osteoclasts on the Surface of Si-Substituted Hydroxyapatite', *Journal of Biomedical Materials Research Part A,* 78A (2006), 709-20.

12 Rainer Detsch, Susannne Schaefer, Ulrike Deisinger, Guenter Ziegler, Hermann Seitz, and Barbara Leukers, 'In Vitro -Osteoclastic Activity Studies on Surfaces of 3d Printed Calcium Phosphate Scaffolds', *Journal of Biomaterials Applications,* 26 (2011), 359-80.

13 S. Yamada, D. Heymann, J. M. Bouler, and G. Daculsi, 'Osteoclastic Resorption of Biphasic Calcium Phosphate Ceramic in Vitro', *Journal of Biomedical Materials Research,* 37 (1997), 346-52.

14 S. Yamada, D. Heymann, J.M. Bouler, and G. Daculsi, 'Osteoclastic Resorption of Calcium Phosphate Ceramics with Different Hydroxyapatite/B-Tricalcium Phosphate Ratios', *Biomaterials*, 18 (1997), 1037-41.

15 Karen Fuller, Jade L. Ross, Kinga A. Szewczyk, Raymond Moss, and Tim J. Chambers, 'Bone Is Not Essential for Osteoclast Activation', *PLoS ONE*, 5 (2010), e12837.

APPENDIX A

EXPERIMENTAL PROTOCOLS

Method based on the protocol reported in:
C. Kunze, T. Freier, E. Helwig, B. Sandner, D. Reif, A. Wutzler, and H. J. Radusch, 'Surface Modification of Tricalcium Phosphate for Improvement of the Interfacial Compatibility with Biodegradable Polymers', *Biomaterials*, 24 (2003), 967-74.

Materials

- ε-caprolactone (Sigma-Aldrich)
- Phosphoric acid (5% in distilled water prepared from concentrated acid bought from Sigma-Aldrich)
- Chloroform (Sigma-Aldrich)
- β-TriCalcium Phosphate particles (TCP - Berkeley, CA)
- Beaker
- Magnetic stirrer
- Three-necked flask and setup for continuous stirring
- Argon
- Ceramic funnel
- Filter paper

Protonation of TCP particles

1. In a beaker with a magnetic stirrer, add TCP particles and phosphoric acid (5% in distilled water) with a mass ratio of 1:2
2. Set up the mixing speed such that the TCP particles are well mixed with the acid
3. Mix for 1 hour
4. Stop mixing, allow the protonated TCP particles (p-TCP) to sediment, and remove the acid solution
5. Wash with distilled water at least three times
6. Filter and dry under vacuum at 40ºC overnight

Grafting reaction

1. Load the three-necked flask with p-TCP particles and ε-caprolactone using a mass ratio of 1:4 (molar ratio of 1:10)
2. Setup and start the continuous stirring and flow of argon
3. Heat the reaction flask to 150ºC and allow the reaction to proceed for 4 days
4. To stop the reaction, cool down the reaction flask below 60ºC and continue stirring

5. Add chloroform to the reaction flask to solubilize the polymerized polycaprolactone (PCL)

6. Transfer the content of the reaction flask (PCL and surface modified particles: TCP-PCL) into 50ml centrifuge tubes
    a. TIP: Transfer about 5-10 ml of the reaction content, and 40-45ml of chloroform to each centrifuge tube

7. Centrifuge for 5 min at 2500 rpm

8. Remove extra chloroform (save this material for further analysis of molecular weight of the grafted PCL – see note below), add fresh solvent, and mix well
    a. NOTE: The molecular weight of the grafted PCL can be measured by GPC. To do this, collect the chloroform used to wash the reaction flask. Using a rotavapor, evaporate the chloroform and collect the remaining polymer for further chromatography analysis

9. Repeat steps 7-8 until the chloroform appears clear after centrifugation.

10. Consolidate all the TCP-PCL powder in one centrifuge tube

11. Dry under vacuum at 40ºC overnight

The Euler number is a measure of the connectivity of an image and is calculated by:

$$E = C - H$$

Where 'C' corresponds to the number of connected objects, and 'H' to the number of holes in the image (Pratt, 2001). As such, E=1 represents an image without holes, E>>1 an image with low connectivity, and E<<1 a highly connected image with holes.

Materials

- Stained histology sections
- GIMP software
- ImageJ software
- MATLAB software

Procedure

1. Image the region of interest of the histology section

2. Using GIMP, manually color over the areas corresponding to new bone, allograft, and remaining polymer

3. When all the objects have been colored, use GIMP threshold to select the colored areas
    a. Colors → threshold
    b. Use this tool to only select the manually colored areas
    c. Export as a TIFF file

4. Convert the TIFF file generated in step 3 into a binary image using ImageJ
    a. Open the file using ImageJ
    b. Select Process → Binary → Make binary
    c. At this point, the colored areas should be white. If this is not the case, invert image using: Edit → Invert
    d. Save and replace the TIFF file

5. Use MATLAB to calculate the Euler number of the image
    a. Open MATLAB and import the image
    b. Use the function: bweuler()

Guelcher Lab
Preparation of 'bioactive glass' and 'surface modified bioactive glass' disks for cell culture

Materials

- Bioglass rods (Mo-Sci Health Care)
- IsoMet Low Speed Saw (Buehler)
- Silicon carbide paper or sandpaper (800, 1000, 1200 grade)
- Deionized Water
- X-Acto Knife

Procedure

1. Preparation: Clean saw blade with DI water.

2. Add water to the basin below the saw blade. Secure the bioglass rod and cut one disk at a speed of 6.5. Discard this disk.

3. Cut pieces of the same thickness. Use the micrometer on the saw to measure the thickness of each disk. After each cut, remove the disk from the water basin, dry the disk using a kimwipe, and continue to cut the next disk.

4. After all pieces are cut, polish one side of the disk using the three different sandpapers. Make sure to add DI water to the sandpaper before polishing
    - Polishing times for each roughness:
        - 800: 10 seconds
        - 1000: 10 seconds
        - 1200: 60 seconds

5. Dry the disk after polishing. Make a mark on the non-polished side of each disk using an x-acto knife

Materials

- Samples to sterilize (usually as disks)
- Sonicator
- Beaker
- DI water
- Sterile DI water (filtered for cell culture)
- 70% ethanol
- α-MEM (Fisher scientific)
- Fetal bovine serum (FBS – Fisher scientific)
- Penicillin/Streptomycin solution (Fisher scientific)

Procedure

1. Load the samples to sterilize into a beaker. If sterilizing several groups, prepare one beaker per group

2. Sonicate samples in deionized distilled water to remove any loose particles: 3 times, 7.5 min each time

3. Submerge in 70% ethanol for 5 min, 2 times

4. Wash with sterile deionized distilled water for 5 min, 2 times

5. Transfer samples to tissue culture plastic plates

6. Condition the sample in incomplete culture medium (αMEM) for 5 min, 2 times
    a. NOTE: Make sure that the sample is completely covered by the media – for example, if using a 24-well plate, add 1 ml of media

7. Incubate the sample in complete medium (αMEM containing 10% FBS and 1% Pen/Strep) overnight in cell culture incubator at 37°C
    a. NOTE: Make sure that the sample is completely covered by the media – for example, if using a 24-well plate, add 1 ml of media

8. After the incubation, remove the media and proceed to seed cells according to the specific experiment

Original method received from: Javier Esparza (Vanderbilt Center for Bone Biology)

Materials

- 1.5 ml centrifuge tubes
- 0.65ml centrifuge tubes
- PBS
- 70% ethanol
- Complete media: αMEM + 10% Fetal bovine serum + 1% antibiotics (Pen-Strep)
- Dissection instruments: forceps and scissors (Fine Science Tools)
- Pipettes (200 μl and 1 ml) and sterile pipette tips
- 6-well plate
- Ice box with ice
- c57bl male mice 4-8 weeks old

Preparations the day before

1. Using 18G needle, punch 2-3 holes at bottom of the 0.65 ml centrifuge tubes.

2. Introduce a 0.65 ml tube into a 1.5 ml tube. Two of these sets will be needed per mouse.

3. Autoclave the tube sets, as well as the forceps and scissors.

Procedure (work under the hood to maintain sterility)

1. Sedate mice using either isofluorane (sedated for minutes), or ketamine (~30 min sedated)
    a. Isofluorane machine settings: 2.5 Iso, 2.5 Oxygen
    b. Ketamine: intramuscular injections completed by personnel from the bone center

2. Sacrifice mice by cervical dislocation and excise femur and tibia keeping the whole bones
    a. TIP: keep the fur wet during all the process (using PBS)
    b. If removing bones from several mice, submerge the whole bones in PBS in a 6-well plate and remove the bones from all the mice. Then continue with the process below.

3. Remove soft tissue from bone

4. Dunk femur and tibia in 70% ethanol for 10sec.

5. Hold femur and tibia with forceps by the knee and using the scissors cut femur and tibia ends to expose bone marrow

6. Place bones, with the exposed ends towards the bottom, into the 0.65 ml tube inside the 1.5 ml tube

7. Add 500 μl PBS into the 0.65 ml tube to keep marrow from drying up
    a. Place samples on ice until centrifugation

8. Spin tubes at 12,000 rpm for 2 min

9. Discard 0.65 ml tube. Bone marrow cells should be at the bottom of the 1.5ml tube, in 500 μl PBS

10. Remove PBS; add 500 μl complete media to wash cells

11. Spin tube at 12,000 rpm for 2 min

12. Remove media and resuspend cells in (1-5 ml) complete media

13. Count cells:
    a. Transfer 50 μl of cell suspension into 450 μl of fresh complete media and mix well (1:10 dilution)
    b. Use the cell counter to count diluted cells

Method based on: instructions from Dr. James Edwards (Vanderbilt Center for Bone Biology), and adapted for the AutoMACS sorter in the Flow Cytometry Core at Vanderbilt.

Materials

- CD11b MicroBeads (human and mouse – Miltenyi Biotec, Cat. No. 130-049-601)
- Separation buffer (also called Running buffer – Miltenyi Biotec, Cat. No. 130-091-221)
- Rinsing solution (Miltenyi Biotec, Cat. No. 130-091-222)
- MACS separator (in the flow cytometry core – reserve time following the link: http://www.mc.vanderbilt.edu/root/vumc.php?site=flowcytometry)
- PBS (Fisher scientific)
- Complete media: αMEM + 10% Fetal bovine serum, 1% antibiotics (Pen-Strep)
- Ice box with ice
- 15 ml centrifuge tubes

Cell labeling (starting solution: cells in complete media)

1. Determine cell number
2. Centrifuge cells – 5 min / 1700 rpm
3. Remove media and wash with PBS
4. Centrifuge and obtain pellet – 5 min / 1700 rpm
5. Remove PBS
6. Re-suspend pellet in 90 µl of MACS Separation Buffer (or Running buffer) per 10^7 total cells
7. Add 10 µl of CD11b MicroBeads per 10^7 total cells and mix well by pipetting
8. Incubate for 15 min at 4-8ºC (on ice)
9. Wash cells with 1-2 ml of separation buffer per 10^7 total cells and centrifuge to obtain pellet – 10 min, 1200 rpm
10. Remove supernatant
11. Re-suspend up to 10^8 in 500 µl of separation buffer and proceed to magnetic separation

Magnetic separation using the AutoMACS Separator

1. Check the dates on the columns. The columns last ~2weeks. If they need to be changed look for a flow cytometry core administrator.
2. Run a CLEANING procedure. The run will end by priming the equipment with running buffer.
3. Place the magnetically labeled cells in the autoMACS separator, and choose the separation program: Positive selection – "POSSEL"

4. Collect positive cell fraction in a 15 ml centrifuge tube (outlet port pos1). This is the purified CD11b+ cell fraction.

5. When done, run a CLEANING procedure

6. Run the SLEEP program and wait until it is sleeping to remove the bottles

7. Turn off the equipment (button on the lower right)

8. Centrifuge, remove buffer

9. Add 1-5 complete media and count cells

10. Prepare a solution with appropriate cell density for seeding according to each experiment

Materials

- PBS (Fisher scientific)
- 5% glutaraldehyde solution in DI water
- DI water
- 1% Osmium tetroxide solution in DI water (concentrated Osmium tetroxide bought from Sigma-Aldrich) – TOXIC REAGENT
- 100%, 95%, 75%, 50%, 25% ethanol in DI water
- SEM stubs
- Double sided carbon tape
- Scanning electron microscope (VINSE)

Cell fixation

1. Wash with PBS

2. Fix in 5% glutaraldehyde solution for ~2 hrs at room temperature, or overnight at 4°C
    a. NOTE: Make sure the sample is completely covered with the solution

3. Rinse with DI water x3 times at room temperature

4. UNDER THE HOOD: Fix in 1% Osmium tetroxide for 15 min at room temperature

5. Wash with DI water x3 times at room temperature

6. Sequentially dehydrate sample in increasing concentrations of ethanol
    a. 25% ethanol – 1 hour
    b. 50% ethanol – 1 hour
    c. 75% ethanol – 30-45 min
    d. 95% ethanol – 1 hour
    e. 100% ethanol – 1 hour
    f. 100% ethanol – 1 hour
    g. 100% ethanol – 1 hour

7. Dry samples either at the critical point in the EM core (preferable) or under vacuum overnight

Stub preparation for SEM imaging

1. Cover the surface of the SEM stub with double sided carbon tape

2. Locate the sample on top of the carbon tape (making sure the side with the cells is on top)

3. If imaging disks, cut a thin and long strip of carbon tape and put it on top of the sample making sure it connects the surface of the disk and the metallic SEM stub (this will help reduce charging)

4. Leave the SEM stubs with samples under vacuum until further processing

5. Sputter-coat with gold (at VINSE)

6. Image

This protocol can be used to stain cells on tissue culture plastic or on disks of different materials.

Materials

- PBS (Fisher scientific)
- 10% formalin
- 0.1% Triton X-100 in PBS
- Rhodamine phalloidin (Life Technologies)
- Bovine Serum Albumin (BSA - optional)
- Mattek plates (for confocal imaging – Cat. # P50G-0-30-F)
- Confocal microscope (Cell Imaging Shared Resource)

Procedure

1. Wash cells 2 times with PBS

2. Fix cells in 10% formalin for 10 min at room temperature
    a. Make sure the cells are completely covered with the fixative

3. Wash cells 2 times with PBS

4. Permeabilize cells 0.1% Triton X-100 for 5 min

5. Wash cells 2 times with PBS

6. Incubate cells for 45 min at 37°C in 5 μl of the reconstituted methanolic stock solution of rhodamine phalloidin per 200 μl of PBS (prepare enough to completely cover the cells)
    a. Add 1% BSA to avoid non-specific binding

7. Wash with PBS

8. Air dry samples protected from light

9. Image using confocal microscope. Use Mattek plates (with glass center) to support the samples during imaging

This protocol is designed to monitor in time the differentiation process of osteoclast precursors seeded on matrices with different chemistries. Amounts are based on 24-well plates and disk samples with diameter of 10-12 mm.

Materials

- Matrices with different chemistries (ex. dentin, TCP, bioglass)
- Reconstituted MCSF (R&D Systems)
- Reconstituted RANKL (R&D Sytems)
- BMP-2 (R&D Systems)
- Complete media (α-MEM + 10% Fetal bovine serum + 1% Pen/Strep)
- Forceps
- 24-well plate

Procedure

1. Sterilize and condition matrix samples (according to protocol)
    a. Prepare 3 plates with replicates of the materials. Each plate will be stopped at a different time point for gene expression analysis

2. Extract bone marrow cells (according to protocol)

3. Select CD11b+ cells from bone marrow population (according to protocol)

4. Remove conditioning media from the sample wells

5. Slowly and drop-wise add 1 ml of complete media containing $1.8x10^5$ CD11b+ cells to each well

6. Allow the cells to sediment for 25 min in the incubator at 37°C

7. Carefully, transfer the samples to a new well plate

8. Using the walls of the wells carefully add 1 ml of complete media augmented with growth factors:
    a. *Optimal concentrations:* MCSF 25 ng/ml; RANKL 50 ng/ml
    b. *Concentrations to study the effect of BMP-2:* MCSF 25 ng/ml; RANKL 30ng/ml; BMP-2 30 ng/ml

9. Incubate the samples at 37°C for up to 14 days changing the media every 3-4 days.
    a. *To change the media of the plate that will be cultured for the longest time:* collect media from each well and freeze for future analysis of TRAP activity on culture supernatant (according to protocol) and replace with fresh complete media containing growth factors
    b. *To change the media of the other plates:* aspirate the media and replace with fresh complete media containing growth factors

10. At 3 different time points (for ex. Days 4,7,14 or 1,4,7): stop one of the plates and collect mRNA for gene expression (according to protocol)

11. After all plates are stopped analyze the TRAP activity on the collected media (protocol)

Materials

- RNAse Zap wipes
- Forceps
- 24-well plate to transfer samples
- 1.5 ml RNase free vials
- KIMWIPES (these are RNAse free)
- RNAse free tips
- Pipettes
- Centrifuge for 2 ml tubes
- 70% ethanol
- QIAShredder Kit (QIAGEN)
- RNeasy mini Kit (QIAGEN)
- Sterile Water- RNase free
- RNase-Free DNase set – (QIAGEN Cat #79254)

NOTE: Change gloves frequently during the process

Procedure

1. Prepare DNAse digestion mixture (1 column per group of pooled samples)
    a. Add 10 µl DNAase to 70 µl RDD buffer per column (include an extra column in your calculations to have enough material). Mix by GENTLE inversion. Reagents sensitive to mechanical force. Keep on ice.

2. COMPLETELY remove media from wells w/ pipette and wash with PBS or water

3. Move samples to empty well
    a. NOTE: To achieve enough mRNA you will need to pool samples together. To do this, either a) combine more than one sample into a clean well and continue with the steps below, or b) follow step 4 and transfer the RLT buffer to the next well with a sample; repeat this until the cells from all the wells of interest have been pooled together into the 700 µl of RLT buffer

4. Disrupt cells by adding 700 µl RLT Buffer/well (pipette around to mix). All the samples should be covered in buffer. Incubate at room temperature for about 5 min.

5. Transfer lysate into a QIAshredder spin column (PURPLE) in 2 ml collection tube (transfer maximum 700 µl to each column at a time).

6. Centrifuge at 2 min full speed (13200 rpm) and collect the homogenized lysate.

7. Repeat for remaining lysate

8. To the homogenized lysate, add volume equal to the total amount RLT buffer of 70% ethanol. Mix by pipetting, do not centrifuge.

9. Add 700 µl of lysate with ethanol to pink column in 2 ml collection tube (RNeasy kit)

10. Cetrifuge at ≥10,000 rpm for 15 s. DISCARD FLOW THROUGH

11. Repeat with the remaining lysate from the purple shredder columns (each time adding up to 700 µl per column)

12. Add 350 µl of wash RW1 to columns and centrifuge for 15 sec at 10,000 rpm. DISCARD FLOW THROUGH

13. Add 80 µl of DNA digestion mix to each column

14. Incubate at room temp for 15 min

15. Add 350 µl RW1 again and centrifuge for 15s at 10,000 rpm. Change collection tubes.

16. *****Make sure ethanol has been added to RPE buffer***** Add 500 µl Buffer RPE to the spin column. Centrifuge for 15s at 10,000 rpm. DISCARD FLOW THROUGH

17. Wash again with 500 µl RPE. Centrifuge for 2 min at full speed.

18. Centrifuge 1 min at max speed.

19. Transfer column to collection tube with top (1.5 ml)

20. Add 40 µl RNase free H20 to column. SOAK 10 min at room temperature

21. Centrifuge 10,000 rpm 1 min
    a. RNA will be collected in 40 µl water in tube.

22. Remove pink column, close the centrifuge tube and put it on ice.

23. Quantify the concentration of mRNA in each sample using the:
    a. Biophotometer and cuvettes (Eppendorf – in the room with the autoclave), or
    b. NanoDrop (in Dr. Jamey Young's lab)

24. Preferably: prepare cDNA immediately. If not possible, store mRNA at -80^{o}C

Materials

- RNAse Zap wipes
- 200 µl RNase free vials
- KIMWIPES (these are RNAse free)
- RNAse free tips
- Pipettes
- IQ Real Time SybrGreen PCR Supermix (Biorad) – Cat # 1708880
- Microseal 'B' adhesive tape for PCR plates – Cat #MSB1001
- PCR Plates – Cat #MLL9601
- Centrifuge for PCR plate
- Thermocycler
- Biorad PCR machine
- iScript cDNA Kit – Cat # 170-8890
- Sterile Water- RNase free
- IQ Real Time SybrGreen PCR Supermix (Biorad) – Cat # 1708880
- Specific primers

cDNA synthesis

Each tube for cDNA synthesis will contain a total of 20 µl mixture distributed as:

a) 4 µl reaction mix
b) 1 µl reverse transcriptase
c) X µl mRNA
d) Y µl nuclease free water

Where X+Y = 15 µl, and a,b,d are part of the iScript kit

1. From mRNA concentration measurements, determine the amount of mRNA to reverse-transcribe into cDNA per treatment group
    a. NOTE: the maximum amount possible will be that in 15 µl of mRNA solution

2. Prepare enough mixture of reaction mix and reverse transcriptase for the total amount of cDNA tubes + 1 extra (for ex. If you have 3 treatment groups, pre-mix 16 µl of reaction mix with 4 µl of reverse transcriptase)

3. Transfer into each cDNA tube
    a. 5 µl of reaction mix and reverse transcriptase pre-mix (prepared in step 2)
    b. X µl of mRNA (determined in step 1)
    c. Y µl nuclease free water (such that X+Y=15 µl)

4. Centrifuge 3,000 rpm for 3 minutes

5. Load into thermal cycler. Select iScript protocol (details below):
    a. 5 minutes at 25°C
    b. 30 minutes at 42°C
    c. 5 minutes at 85°C
    d. Hold at 4°C

6. Store the cDNA at -20°C

Real time qPCR

This information is to run the real time qPCR in 20 µl using a flat surface 96-well PCR plate in a CFX machine at the Molecular Biology Core at Vanderbilt. Reserve machine ahead of time using the Core ordering website.

1. Prepare primer mix (2 µl of primer mix are needed per well)
    a. For a final concentration of 500 nM of primer mix in the reaction well: Mix 95 µl water with 2.5 µl forward primer and 2.5 µl of reverse primer

2. Determine the cDNA template concentration per well

3. Dilute stored cDNA to desired concentration. Keep in mind that only 8 µl of cDNA solution will be transferred to each reaction well

4. Pre-mix supermix and primer mix enough for all the reaction wells and 1-2 extra ones
    a. 10 µl supermix/well
    b. 2 µl of primer mix/well (prepared in step 1)

5. While keeping the PCR plate on ice, load into each well:
    a. 12 µl of the premix prepared in step 4
    b. 8 µl of cDNA solution prepared in step 3
    c. NOTE: when transferring these amounts avoid making bubbles in the solutions and change tip for each well

6. Place sticker seal on top of plate making sure it is well sealed

7. Centrifuge at 3,000 rpm for 3 min

8. While on ice, take the plate to the core

9. On the reserved machine:
    a. Select the lab's profile → User: Guelcher Password: SG3-4977
    b. Go to protocol
    c. Select existing (unless you have a different protocol to use)
    d. Use CFX_2StepAmp+Melt Protocol (found under PCR protocols in sample files folder)
    e. Press: "Edit selected"
    f. Enter temperature information according to your experiment, and save the protocol
    g. Under USER PREFERENCES, make sure that your email is included so that results are sent to you at the end of the run
    h. Open machine by pressing OPEN LID (under start run menu)
    i. Place plate firmly on metal grid
    j. Close lid using the software by pressing CLOSE LID (under start run menu)
    k. Click START RUN

This method is for staining cells on tissue culture plastic or seeded on disks of materials

Materials

- Sigma kit 387A (contains citrate solution, fast Garnet GBC base solution, sodium nitrite solution, naphthol AS-BI phosphate solution, acetate solution, tartrate solution, and hematoxylin solution)
- Acetone
- Formaldehyde, 37%
- DI water

Procedure

The amounts below can be modified according to the number of samples as long as the proportions remain constant.

1. Pre-warm sufficient DI water for day's use to 37°C. Check temperature before use

2. Prepare fixative solution in a glass vial:
    a. 25 ml citrate solution + 65 ml acetone + 8 ml of formaldehyde 37%
    b. Cap tightly and allow to equilibrate at room temperature

3. In a glass vial prepare diazotized fast Garnet GBC solution:
    a. 0.5 ml fast Garnet GBC solution + 0.5 ml sodium nitrite solution
    b. Mix by gentle inversion for 30s and let stand 2 min

4. In a clean glass vial prepare staining solution by mixing well the following:
    a. 45 ml DI water at 37°C
    b. 1 ml diazotized fast Garnet GBC solution (from step 3)
    c. 0.5 ml Naphthol AS-BI phosphate solution
    d. 2 ml acetate solution
    e. 1 ml tartrate solution

5. Warm solution to 37°C in water bath or incubator

6. Remove media from wells and wash with DI water

7. Add fixative solution to wells (making sure all the cells are covered) and let stand for 30s.

8. Wash with DI water and do not allow cells to dry

9. Add warm staining solution (from step 5) to each well, making sure all the cells are covered

10. Incubate for 20 min at 37°C protected from light

11. Remove the solution and wash thoroughly with DI water

12. Air dry and evaluate microscopically

Secretion of tartrate resistant acid phosphatase (TRAP) 5b into the supernatant has been found to correlate with bone resorptive activity.

Biochemical measurement of TRAP activity in culture supernatant is typically conducted using either para-nitrophenylphosphate (pNPP) or naphthol-AS-BI phosphate (N-ASBI-P) as a substrate. Compared with nPP, N-AS-BI-P is a more specific substrate for TRAP 5b activity (Janckila et al., 2001). As opposed to nPP, N-ASBI-P is selectively hydrolyzed by the 5b isoform (Janckila et al., 2001). Vaughan et al. (1971) compared the fluorescent properties of various naphthol derivatives and concluded that AS-BI phosphate was the most effective substrate for both acid and alkaline phosphatase. Phosphatase hydrolyzes N-AS-BI-P to yield fluorescent N-AS-BI.

After quantifying the amount of TRAP in the media, total protein in the sample is used to normalize the results. Total protein is quantified using the BCA kit.

Materials

- Napthol AS-BI phosphate - -20°C freezer (in the HPLC lab – Sigma Cat. # N2125)
- Sodium Acetate
- Sodium Tartrate
- EGME (2-Methoxyethanol) (Refrigerator in the mixer lab)
- 0.6 M NaOH (prepare as needed)
- DI water
- 96-well plates (preferably with clear bottom, but all black also work)
- BCA Protein kit (Fisher Scientific)

Procedure

1. Thaw frozen media and vortex to mix

2. Prepare buffer
    a. Total = 150 µl * (# samples)
        i. Ex. = 0.150* 164= 24.6 ml. Make 27 ml

    b. To have a total of 2.5mM Napthol AS-BI Phosphate in 4% EGME in 27 ml of buffer:
        i. $(27x10^{-3}$ L)*$(2.5x10^{-3}$ mol/L)*(452.19 g/mol) = 0.031 g Napthol ASBI-P
        ii. Dissolve in 1 ml EGME (add it and vortex it. If it doesn't dissolve you can put it in the 37°C incubator for a few minutes and vortex again)

    c. To have a total of 100 mM sodium acetate in 27 ml of buffer:
        i. $(27x10^{-3}$ L)*$(100x10^{-3}$ mol/L)*(82.03 g/mol) = 0.221 g
        ii. Add 0.221 g Na Acetate to 13 ml DI water
        iii. ml DI water = (Total buffer ml – ml EGME)/2

    d. To have a total of 50 mM sodium tartrate in 27 ml of buffer
        i. $(27x10^{-3}$ L)*$(50x10^{-3}$ mol/L)*(230.08 g/mol) = 0.311 g
        ii. Add 0.311g Na Tartrate to 13 mL DI water
        iii. ml DI water = (Total buffer ml – ml EGME)/2

e. Measure pH of buffer. Aim for pH of 6.1-6.3

3. Add 150 µl buffer to each well (using a 96 well-plate)

4. Add 50 µl of sample to each well

5. Allow to react for 35 min at 37°C protected from light (Be sure all samples carry out reaction for the same amount of time)

6. Stop with addition of 50 µl 0.6 M NaOH per well

7. Check pH of one well. Need basic conditions

8. Measure fluorescence of the plate
   a. Go to the Molecular Biology core in Light Hall
   b. Set the fluorescence plate reader:
      i. Shake duration: 10s
      ii. Read From Top
      iii. Measure Fluorescence: 405 Excitation, 520 Emission
   c. Run the reading and save data

Total protein measurement

1. Prepare the BCA protein buffer (each sample well will need 200 µl of buffer)
   a. Solution A → ml = (Total ml)
   b. Solution B → ml = (Total ml)*0.02

2. Prepare the protein standards with the standard concentrations suggested by the BCA total protein assay kit:

Table 1. Preparation of Diluted Albumin (BSA) Standards

Dilution Scheme for Standard Test Tube Protocol and Microplate Procedure (Working Range = 20–2,000 µg/ml)			
Vial	**Volume of Diluent**	**Volume and Source of BSA**	**Final BSA Concentration**
A	0	300 µl of Stock	2,000 µg/ml
B	125 µl	375 µl of Stock	1,500 µg/ml
C	325 µl	325 µl of Stock	1,000 µg/ml
D	175 µl	175 µl of vial B dilution	750 µg/ml
E	325 µl	325 µl of vial C dilution	500 µg/ml
F	325 µl	325 µl of vial E dilution	250 µg/ml
G	325 µl	325 µl of vial F dilution	125 µg/ml
H	400 µl	100 µl of vial G dilution	25 µg/ml
I	400 µl	0	0 µg/ml = Blank
J	200µl	200 µl of vial H dilution	12.5 µg/ml
K	200µl	200 µl of vial J dilution	6.25 µg/ml

3. Add to each sample well:
   a. 5 µL sample media (or incomplete media for blank)
   b. 15 µL PBS (take into account this dilution when reporting total protein in each well)
   c. 200 µL buffer

4. To generate the calibration curve add:
    a. 20 µl of each standard
    b. 200 µl of the buffer

5. Incubate at room temperature protected from light for 30 min

6. Measure the absorbance at 562 nm (using the plate reader in the cell culture room)

7. Use the calibration curve to determine the total protein concentration in each well. If the absorbance reading of the samples is higher than the higher standard, repeat the experiment using an even more diluted sample.

Differentiation of osteoclast precursors based on published methods from: Karen Fuller, Barrie Kirstein, and Timothy J. Chambers, 'Murine Osteoclast Formation and Function: Differential Regulation by Humoral Agents', *Endocrinology*, 147 (2006), 1979-85.

In this method, osteoclast precursors are first differentiated into active osteoclasts, and then seeded on different matrices. After culturing the active osteoclasts on the matrices, they are removed, and the resorbed volume is quantified in time.

Materials

- Sterilized and conditioned matrices for analysis (according to protocol)
- Complete media: α-MEM + 10% Fetal bovine serum + 1% Pen/Strep (all from Fisher Scientific)
- PBS (Fisher Scientific)
- Reconstituted MCSF, RANKL, TGF-β, IL-1α (R&D Systems)
- 24-well plate (this can change depending on the size of the samples)
- T150 cell culture flasks (Fisher Scientific)
- 90-mm diameter cell culture dishes
- 0.02% EDTA solution (Sigma Aldrich)
- Cell scraper (Fisher scientific)
- Zeta-20 True Color 3D Optical Profiler (Zeta Instruments; located in the National Research Resource for Imaging Mass Spectrometry – 9th floor in MRB III)
- Forceps

Differentiation of non-adherent bone marrow cells

1. Extract murine bone marrow cells from c57bl male mice 4-8 weeks old (according to protocol)

2. Remove the stromal cells from the bone marrow cell population:
    a. Seed the bone marrow cells in a T150 cell culture flask at a density of $3x10^5$ cells/ml
    b. Feed with ~30 ml of complete media supplemented with 5 ng/ml MCSF
    c. Incubate for 24 hrs at 37°C and 5% CO_2
    d. Aspirate the media and centrifuge (3000 rpm for 3 min)
    e. Re-suspend in complete media and count

3. Seed and differentiate the non-adherent cells
    a. Seed $7.2x10^6$ cells/dish in 90-mm diameter cell culture dishes
    b. Feed with 25 ml of complete media augmented with 50 ng/ml MCSF, 30 ng/ml RANKL, and 0.1 ng/ml TGF-β
    c. Every 2-3 change 15 ml of the media per flask
    d. Incubate for 5-7 days at 37°C and 5% CO_2.
        i. NOTE: In order to know when to stop the culture, monitor the number of multinucleated cells each day (for ex. count the number of multinucleated cells in several regions each day). Stop the culture the day that the number of multinucleated cells significantly increases compared to the previous day.

4. Collect differentiated osteoclasts
    a. Remove media from cell culture dishes
    b. Wash 3 times with PBS
    c. Add 6 ml of 0.02% EDTA solution to each dish
    d. Incubate the cells for 20 min at room temperature
    e. Gently tap the dishes, and remove the EDTA solution.
    f. Add 6 ml of PBS to each dish
    g. Carefully scrape the cells using a cell scraper such that the cells are suspended in PBS
    h. Combine all the cells, pipette up and down, and count the cells

Culture of osteoclasts on matrices

1. Remove conditioning media from the sample wells

2. Slowly and drop-wise add 1 ml of complete media containing $1.8x10^5$ osteoclasts to each well (equivalent seeding density to $9x10^4$ cells/cm^2)

3. Allow the cells to sediment for 25 min in the incubator at 37°C

4. Carefully, transfer the samples to a new well plate

5. Using the walls of the wells carefully add 1 ml of complete media augmented with 50ng/ml MCSF, 30 ng/ml RANKL, 10 ng/ml IL-1α
    a. Depending on the experiment, other growth factors can also be included in the media

6. Culture the samples for up to 48 hrs at 37°C and 5%CO_2
    a. NOTE: Initially prepare enough samples to stop several wells at different time points. For example, stop some samples after 6, 24, 48 hrs of resorption. This will provide data in time to determine the volumetric resorption rate

Quantification of volumetric resorption rates

1. Stop several samples after different times of culture (for ex. 6, 24, 48 hrs)
    a. Remove media from sample wells
    b. Wash with PBS
    c. Carefully remove attached cells using a cell scraper
    d. Air dry samples overnight

2. Image the surface of the matrices (using the Zeta profiler)
    NOTE: For matrices with high roughness of the surface, this step should also be completed before cell culture. The pit volume before culture can be subtracted from the pit volume after culture to obtain the real resorbed volume.

    a. Open Zeta 3D software (icon on the desktop of the microscope computer)
    b. Enter Username: a, and Password: a
    c. Click OK to initialize Z and XY stages
    d. Make sure the objective with lowest magnification is being used
    e. Place the sample on the sample holder

f. On the 'Live Image" menu click: DOWN and follow instructions to lower the microscope head. This will lower the objectives to a set position, but you will still need to move them closer to the sample. To do this, position the mouse cursor on the 'Mouse Wheel' (found on the 'Scan Dialog' window). Use the scroll wheel to move the microscope head up and down. You can also use the buttons: PGUP and PGDN to move faster.

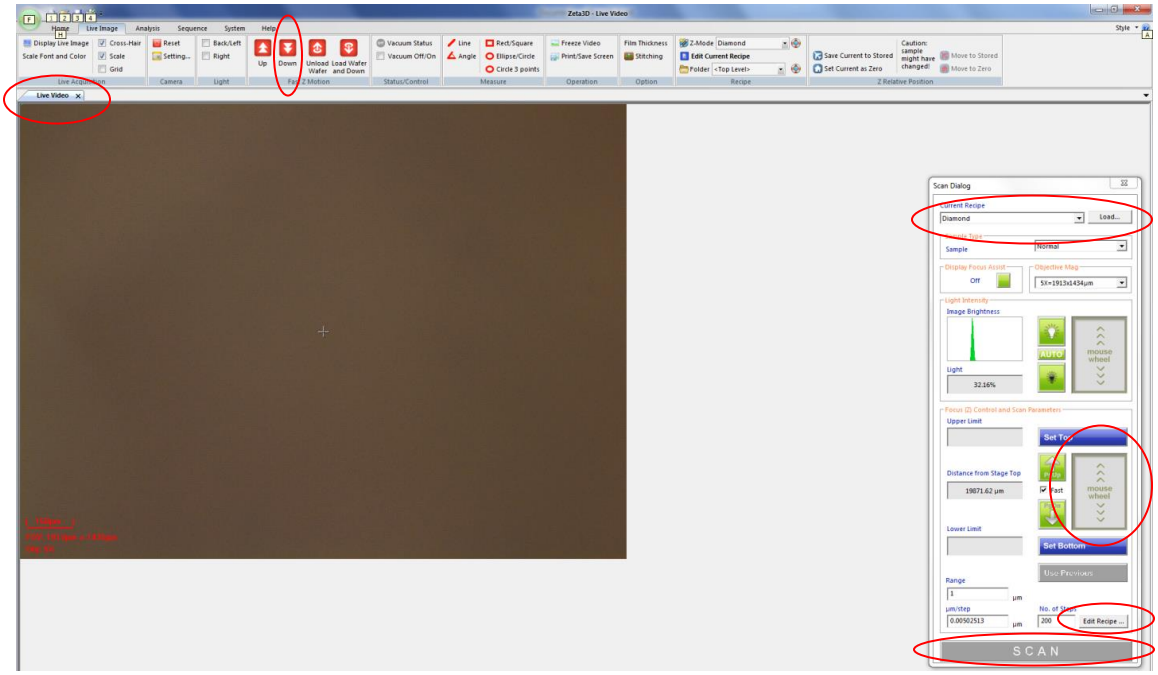

g. Find the height of the microscope in which most of the image appears focused on the screen
    i. NOTE: Here you can change magnification to the one you want to use for your analysis

h. From the focused position, move up and down to mark your lower and higher limits for the scan (*set bottom, set top*). These limits will determine the height of the scan.
    i. NOTE: When analyzing several samples try to keep this height and the magnification constant between samples such that the resolution of the analysis is the same

i. Click *Scan*

j. Save the image

k. Repeat until you have imaged several regions of the samples

3. Quantify the resorbed volume
    a. Using the Zeta 3D software, open the image to analyze

b. Go to 'Analysis' menu → click on 'Z 3D view' → uncheck 'True color'
    i. NOTE: This will provide a color map of height

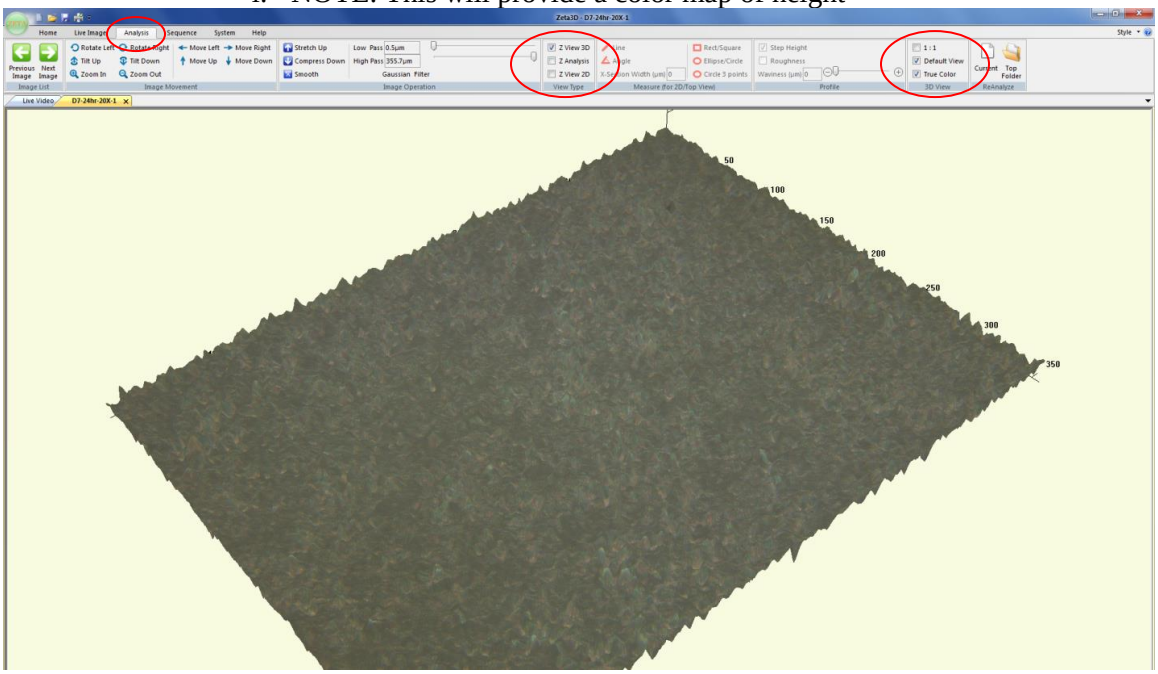

c. Check the image to see if it needs to be leveled. If so, go to 'View type', select 'Z Analysis', right click on the image, set a reference surface, and level the reference surface

d. In the 'Scan Dialog' window (found on the 'Live Video'- towards the right on the screenshot in the previous page) make sure that the Diamond recipe is loaded.
    i. If the Diamond recipe is not loaded, click 'Load' and locate the corresponding file: Program files → Zeta Instruments → zmm → Diamond.rcp

e. Towards the bottom of the 'Scan Dialog' window click on 'Edit recipe'

f. Under the 'Analysis' tab select the threshold selection method as Z (depth) and provide the threshold for detection (in μm)
    i. NOTE: To select pits input a negative value for the threshold for detection (ex. -1, would select all pits deeper than 1 μm). Positive values select structures above the surface.
    ii. NOTE: The software will automatically select any features that have a depth equal or larger to the threshold value.

g. Go back to the 'Z view 2D' image and the 'Z view 3D' to visually check the selected pits. Make changes to the threshold if necessary.

h. Save the data of the thresholded volumes by right clicking on the data table (lower left quadrant of the 'Z view 2D' window) and following the link to save the file